UNIVERSITÉ SORBONNE PARIS NORD

ÉCOLE DOCTORALE GALILÉE
Université Sorbonne Paris Nord

Doctorat de physique

Spécialité : Sciences des matériaux

Présentée par

Stéphane Chiroli

Elastic control of spin wave dynamics in magnonic crystals: experiments and numerical simulations

Soutenue publiquement le 10 décembre 2024 devant le jury composé de :

Yann Gallais	Président
Liliana Buda-Prejbeanu	Rapporteur
Grégoire de Loubens	Rapporteur
Adekunle O. Adeyeye	Examinateur
Denys Makarov	Examinateur
Damien Faurie	Directeur de thèse
Fatih ZIGHEM	Directeur de thèse

THESE

Université Sorbonne Paris Nord
Préparée au Laboratoire des Sciences des Procédés et des Matériaux (LSPM)
UPR CNRS 3407, 99 avenue J.-B. Clément, 93430 Villetaneuse, France

Elastic control of spin wave dynamics in magnonic crystals: experiments and numerical simulations

Doctorat de physique

Stéphane Chiroli

March 7, 2025

Université Sorbonne Paris Nord

Contents

Remerciements

On dit souvent que le temps file lorsqu'on s'amuse, et c'est l'impression que j'ai à l'issue de ces trois années de thèse. Je garderai longtemps en mémoire de nombreux moments et accomplissements, qu'ils soient d'ordre scientifique, personnel ou humain que j'ai pu partager avec mes collègues et amis au sein du LSPM.

Je souhaite en tout premier lieu remercier Fatih et Damien, qui n'ont jamais douté de moi, et qui m'ont laissé énormément de liberté dans la manière d'aborder mon travail. Je n'ai pas une seule seconde ressenti une quelconque hiérachie en leur présence en trois ans. On peut difficilement espérer meilleurs encadrants, et ce fut un réel plaisir de travailler avec eux dans cette ambiance amicale, toujours ponctuée d'humour. Cela fait maintenant sept ans que Fatih suit mon parcours, d'abord en tant qu'étudiant, puis padawan et maintenant ami, et j'imagine son soulagement de me voir enfin partir après avoir fait les frais de ma poisse légendaire.

Je souhaite remercier particulièrement le deuxième étage. Imane, Théo, Walid et mes plantes qui m'ont rejoint progressivement dans le bureau et qui ont rendu mes journées plus agréables. Merci à Éloi grâce à qui j'ai la main verte, à MARTIN pour sa bonne humeur et son savoir en acoustique et à Yves (alias 24/32) dont l'humour et les anecdotes me manqueront terriblement. Merci à Noël et à l'équipe du CISE pour leur aide au développement des expériences qui permettent de voir naître de nombreux projets, notamment la lithographie interférentielle. Merci à Nabil qui m'a beaucoup appris lors de mon stage et début de thèse, et qui m'a permis de trouver un logement.

Parce que la vie du laboratoire ne s'arrête pas à la recherche, j'aimerais saluer tous les amis du club apéro, du club jeu de société, et du club running avec qui j'ai passé des moments plus qu'agréables (et souvent arrosés).

J'aimerais finir par remercier mes proches. Mes parents (les meilleurs du monde) à qui je dois tout et qui ont toujours cru en moi; ma petite soeur, ma famille de Guadeloupe et de métropole, mes amis et frères de longue date, ainsi que ma compagne qui me supporte et m'accompagne depuis de nombreuses années maintenant.

Enfin, merci au LSPM pour son atmosphère bienveillante et chaleureuse, qui m'a tant apporté et où j'ai passé parmi les plus belles années de ma vie.

1 Introduction

Contents

This chapter explores the principles of magnetoelasticity, a phenomenon that links the mechanical and magnetic properties of materials. Initially discovered by James Prescott Joule in 1842, this effect has become essential in the development of electromechanical transducers and flexible magnetic systems. The focus is on magnonic crystals, which enable the control of spin wave propagation by adjusting their dispersion spectrum via an external magnetic field. This chapter also addresses magnetic straintronics, an emerging field that leverages the magnetoelastic properties of artificial multiferroic materials. Although research on spin waves under mechanical strain is still limited, preliminary studies show that static elastic strains can influence magnetization distribution, providing additional control over spin waves without the use of external magnetic fields. Furthermore, magphonic crystals are discussed for their ability to couple magnonic and phononic behaviors, paving the way for advanced applications in communication and information processing systems. The interactions between spin and acoustic waves, in connection with magnetoelastic effects, are also briefly presented.

1.1 Magnetoelasticity

Magnetoelastic effects were first discovered by James Prescott Joule in 1842 but did not draw much attention until the next century. His work was first presented on the 16th of February 1842 in a lecture entitled *On a New Class of Magnetic Forces,* at the Royal Victoria Gallery of Manchester which was then printed in *The Annals of Electricity, Magnetism, and Chemistry, and Guardian of Experimental Science, Vol.8, p.219.* He eventually published his results in 1847 in the paper *On the Effects of Magnetism upon the Dimensions of Iron and Steel Bars* in the Philosophical Magazine where he it made evident that magnetizing an iron bar induces an increase of its length (see figure 1.1) [1, 2].

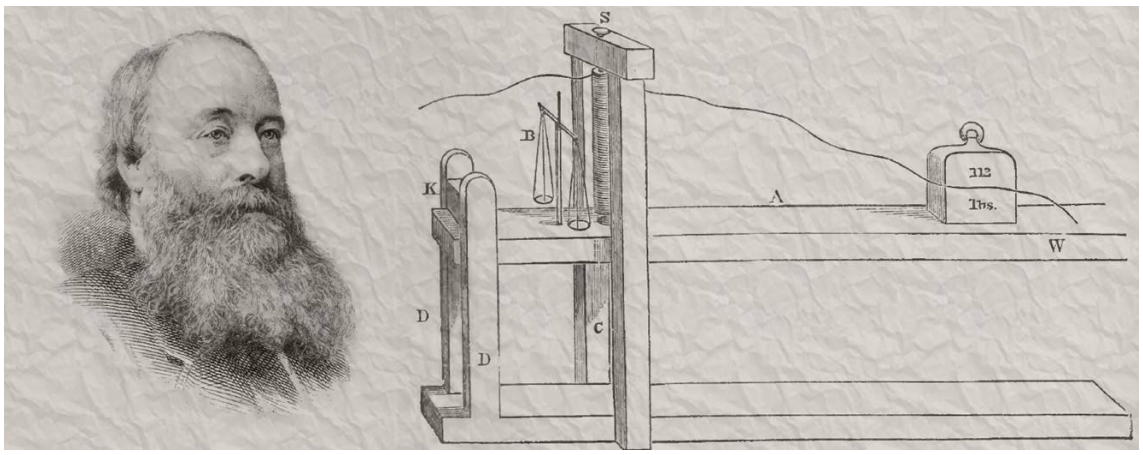

Figure 1.1: Illustration adapted from J.P. Joule's book published in 1842, which presents the experimental setup he utilized to measure direct magnetostriction. This setup was pivotal in advancing our understanding of the relationship between magnetism and mechanical deformation in materials [2].

He was indeed the first to observe what we now refer to as the direct magnetoelastic effect, often referred to as the Joule effect. This effect results in the appearance of a strain field inside a magnetic object that is influenced by the magnetization strength and direction. There also exists an inverse effect, also called the Villari effect, that influences the magnetization by applying strain to the magnetic object. These effects can be explained by the accommodation of electron orbitals in crystalline lattices which results in the creation of easier directions for the magnetization in the case of the inverse effect, and in a small change of the crystalline lattice dimensions in the case of the direct effect, as schematically presented in figure 1.2.

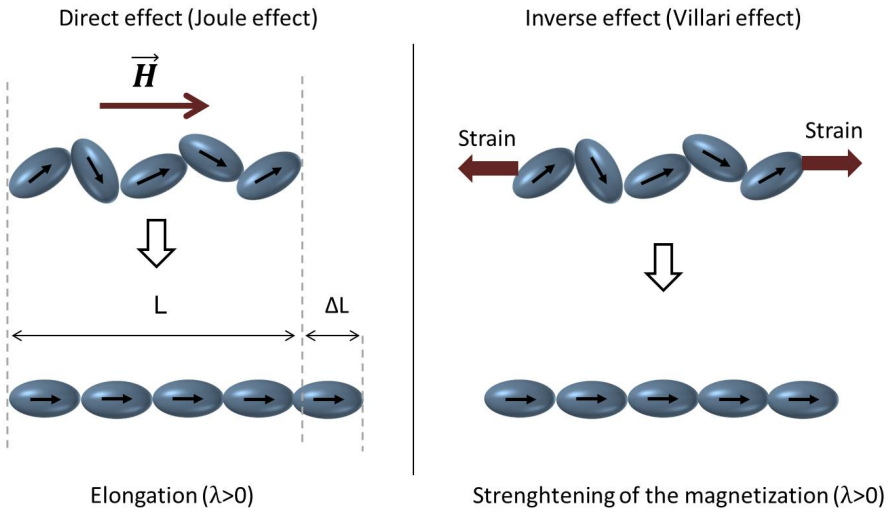

Figure 1.2: Diagram illustrating the schematic representation of the Joule and Villari effects, highlighting the relationship between magnetostriction and the magnetic properties of materials.

Several papers started to emerge during the 1930s attempting to understand and theorize these effects[3]. Ideas of potential applications quickly grew out of these early works. Among them we can mention electromechanical transducers and magnetostriction oscillators and filters [4]. Magnetostriction was also one of the main reasons for the use of permalloy in industry, to prevent changes of magnetic properties in component subjected to mechanical stress. Nowadays, with the progress of material engineering, micro- and nanofabrication and the emergence of giant magnetostriction [6, 7, 8], new opportunities have arisen in the fundamental study of magnetoelastic effects and the potential industrial applications involving them [5, 9, 10, 11]. As magnetoelasticity became more and more involved in the various topics of nanomagnetism, new fields of research appeared. For instance, we have seen the emergence of what can be called "magnetic-straintronics," [12, 13, 14, 15, 16] in which elastic (static) strains imposed on the system allow control of certain magnetic properties. To this purpose we can associate an even more emerging theme - the curvilinear magnetism which allows highlighting complex magnetic textures in systems presenting strong curvatures despite the fact that mechanical deformations are not yet taken into account in this theme [17, 18, 19, 20]. The influence of these magnetoelastic effects is also very much studied in flexible magnetic systems which are generally composed of a magnetic deposit on a polymer substrate with applications ranging from everyday gadgets to aerospace devices [21, 22, 20, 19, 26]. *In operando*, these devices will be subjected to complex strain fields that can modify their magnetic properties [27, 28, 29]. For these systems, magnetoelasticity can be undesirable, and it is therefore necessary to find solutions to limit its effects [17, 18]. Therefore, despite numerous experimental studies, it is of utmost importance to develop numerical tools to describe heterogeneous strain and magnetoelastic fields in nanoobjects [32, 33]. The numerical description of magnetic nanostructure behavior involves the resolution of the Landau-Lifshitz-Gilbert (LLG) equation. The commonly used software al-

low one to simulate the magnetic properties of nanostructures but are rarely used to take into account inhomogeneous strains [34, 35, 36, 37, 38]. The magnetoelastic coupling must be,therefore , fully described at the scale of these inhomogeneities. Therefore, in a context where very few groups try to describe precisely the magnetoelastic effects with fully coupled micromagnetic/mechanical numerical simulations [33, 39, 40, 41, 42, 43, 44, 45], one of the goals of the present thesis is to develop such tools and to relate them with some widespreaded caracterisation techniques such as ferromagnetic resonance and Brillouin light scattering.

In the following, we will briefly review the recent progress in the field of magnonic crystals [46, 47, 48], a topic of particular focus in this thesis. Indeed magnonic crystals are periodic magnetic structures that can control the propagation of spin waves, known as magnons [49, 50, 51, 52, 53, 54]. The presence of magnetoelastic effects in these crystals can give rise to a variety of intriguing phenomena. These effects depend on the nature of the applied mechanical strains: if the strains are static, they alter the magnetic properties in a way that is central to magnetic straintronics applications [17]. Conversely, if the mechanical strains are dynamic, they can induce a coupling between magnons and phonons [1, 2, 3, 4, 5], leading to a rich landscape of coupled excitations that can be exploited for advanced functionalities. This duality, arising from the interaction between mechanical and magnetic properties, underpins the potential of magnetoelastic effects in enhancing the performance and tunability of magnonic crystals.

1.2 Magnonic crystals

Over the past two decades, there has been a growing interest in the fundamental understanding of spin-wave propagation in magnonic crystals due to their immense potential for a variety of applications, including microwave resonators [60], filters [61], and spin-wave logic devices [62]. From a practical standpoint, one of the most appealing features of magnonic crystals is their ability to easily modify the dispersion spectrum of magnons through the application of an external magnetic field. Utilizing periodic magnetic nanostructures as a functional medium in magnonic devices offer distinct advantages over conventional charge-based devices. In magnonic systems, both the amplitude and the direction (phase) of magnetization can be harnessed for information encoding, contrasting with the scalar nature of charge. Encoding information in the amplitude of magnetization leads directly to the development of a spin-wave switch, a device capable of controlling the transmission or cessation of spin wave propagation. When information is encoded in phase, different frequencies can be employed as separate information channels, facilitating parallel data processing within the same structure. This capacity for multichannel information transmission and processing provides a significant advantage over traditional switch-based logic devices. Furthermore, the shape anisotropy in nano-confined geometries can serve as an effective biasing external field, enabling devices to operate at gigahertz frequencies with minimal or no external biasing required.

The spectra of spin-wave excitations in magnonic crystals differ significantly from those observed in uniform media. Thanks to the lateral periodic magnetic contrast, these spec-

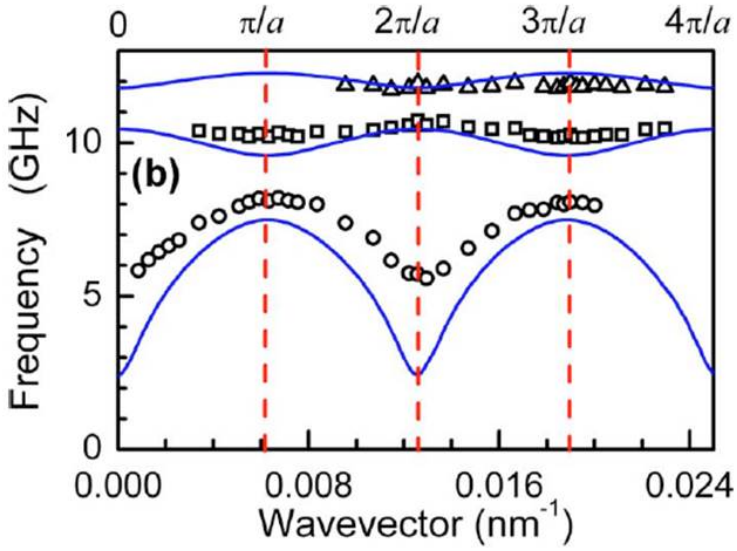

Figure 1.3: Dispersion relations of spin waves, the experimental data are denoted by symbols. The Brillouin zone boundaries $q = n/a$ are represented by dashed lines. The magnonic crystal is a 1D periodic array of alterned permalloy and cobalt nanowires. There is no applied magnetic field and the probed wave-vector k is transverse to the nanowires. Adapted from [49].

tra display characteristics such as tunable magnonic bandgaps, within which spin-wave propagation is completely suppressed. The presence of spin-wave bandgaps have been predicted for one-dimensional, two-dimensional, and three-dimensional systems [49, 50, 51, 52, 53, 54]. Furthermore, frequency bandgaps have been observed experimentally in wire-like structures consisting of shallow grooves etched into yttrium-iron-garnet films, a one-dimensional array of homogeneous $Ni_{80}Fe_{20}$ nanowires separated by an air gap [63], and synthetic nanostructures composed of periodic arrays of alternating $Ni_{80}Fe_{20}$ nanowires in direct contact with Co nanowires [49], also known as bi-component magnonic crystals. It has been clearly shown that the frequency bandgaps can be tuned by the application of a magnetic field and also by changing the lateral dimensions of the nanowires. For example, figure 1.3 illustrates the magnonic characteristics measured using BLS, as reported by Wang et al. [49]. In their study, they describe a magnonic crystal that exhibits tunable band gaps, which facilitate precise control over spin-wave generation and propagation in devices such as filters. The studied magnonic crystal was a 1D magnonic crystal in the form of a periodic array comprising alternating contacting cobalt and permalloy nanowires.

Additionally, the bandgap structure can also be adjusted by strain-induced magnetic effects, stemming from magnetoelastic energy. This tunability of the bandgap is a crucial property that could have significant applications in controlling the generation and propagation of information-carrying spin waves within devices utilizing these crystals. By varying the size of the bandgap, where spin-wave propagation is entirely prohibited, only modes capable of crossing the gap can propagate through the medium, enabling selective trans-

mission of specific spin-wave frequencies. Furthermore, the recent advancements in artificial spin-ice create new opportunities for harnessing spin-wave properties. Consequently, developing systems that exploit magnons represents a promising strategy for information processing in the coming decades. This brings us to the next section, which delves into magnetoelastic effects in magnonic crystals.

1.3 Magnetic straintronic (elastic static strain)

Magnetic straintronics represents a broad field of research that has gained significant traction since the early 21st century [12, 13, 14, 15, 16]. As modern information technology increasingly relies on electronic systems for data processing and transmission, the quest for more efficient methods of manipulating and storing information has become paramount. Current electronic technologies primarily depend on electrical signals, which often lead to substantial energy consumption—over 10% of global electricity consumption can be attributed to electronic devices. This underscores the need for innovative approaches that enhance energy efficiency while maintaining or improving performance. One promising approach in this context is the exploration of magnetoelastic properties in magnetostrictive multiferroic materials. These materials have the unique ability to couple magnetic and mechanical responses, enabling a new paradigm in information technology that exploits the interactions between magnetic fields and mechanical strains. However, the practical application of these materials is hindered by their scarcity, as few materials exhibit both ferromagnetic characteristics (typically found in metals) and ferroelectric properties (commonly associated with insulators) [66].

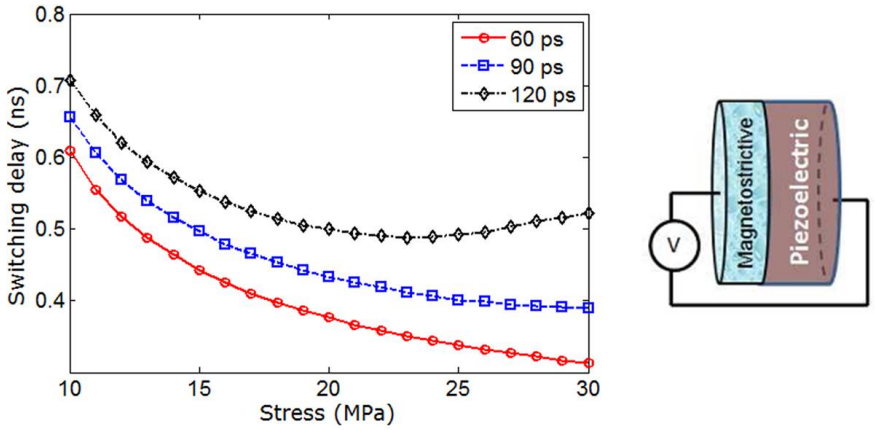

Figure 1.4: Switching delay versus stress for different stress ramp durations in a multiferroic system schematized on the right. Adapted from ref. [64].

This duality is crucial for the effective implementation of multiferroic applications in technology. To overcome this limitation, researchers have increasingly focused on the development of artificial multiferroics. These engineered systems combine ferromagnetic layers, often metallic, deposited on top of ferroelectric materials, creating a composite that

harnesses the advantageous properties of both constituents [67]. This layered approach not only facilitates the conversion of electric signals into mechanical strain but also allows for a more controlled interaction between the magnetic and electric domains. By applying a voltage to the ferroelectric layer, it is possible to generate strain that effectively modifies the magnetic characteristics of the ferromagnetic layer, leading to significant advancements in the control and manipulation of magnetic information. In recent years, the field of magnetic straintronics has become a focal point for developing advanced electronic devices with various applications. These include straintronic memory systems, which promise faster data storage and retrieval, energy-efficient switches that reduce power consumption, and innovative architectures for Boolean computing that leverage the unique properties of magnetic states [12]. The potential to create devices that operate with less energy and generate minimal heat is particularly appealing, especially as the demand for efficient computing solutions continues to rise. At the core of electronic computing lies the transistor, a device that encodes binary information as 0s and 1s based on its conductance state. Magnetic straintronics offers a novel approach to encoding these binary states by utilizing the manipulation of magnetic anisotropy through voltage application. By controlling the magnetic states in this manner, it becomes feasible to switch between distinct configurations that represent 0 or 1 with remarkable efficiency. This not only leads to reduced electrical consumption but also minimizes heat generation, which is a critical factor in the design of modern electronic devices. Figure 1.4 illustrates the relationship between the switching delay of magnetization and the voltage-induced stress. By associating this delay with the switching rate, we observe an order of magnitude approaching the gigahertz range, a speed comparable to the clock rates of contemporary CPU transistors. These results, reported by K. Roy et al. [64], highlight the remarkable potential of magnetization switching in magnetoelastic materials for high-speed applications. However, it is important to note that the results presented focus solely on successful switching events, which do not account for the errors that currently limit the practical application of these devices in Boolean computing. While the errors associated with switching events remain a challenge, they are not inherently detrimental in the context of straintronic energy-efficient memory systems. Existing error correction methods, commonly employed in memory chip technology, can effectively mitigate these issues, allowing for reliable data storage and retrieval despite occasional switching errors. This adaptability is crucial for the development of memory systems that prioritize energy efficiency alongside performance. In the system described, the switching mechanism relies on strain-induced anisotropy, meaning that the stored information is lost when the applied voltage is removed. This characteristic presents a limitation for non-volatile applications, where retaining information without a constant power supply is essential.

However, alternative device geometries and configurations may address this issue, paving the way for the implementation of non-volatile information systems such as magnetoelectric random access memories (MeRAM). MeRAM combines the advantages of both magnetic and electric functionalities, enabling data to be stored and retained even in the absence of power. This innovative approach not only enhances the robustness of memory systems but also offers the potential for further integration with existing semiconductor technologies. As research progresses, the exploration of diverse geometries and materials will be

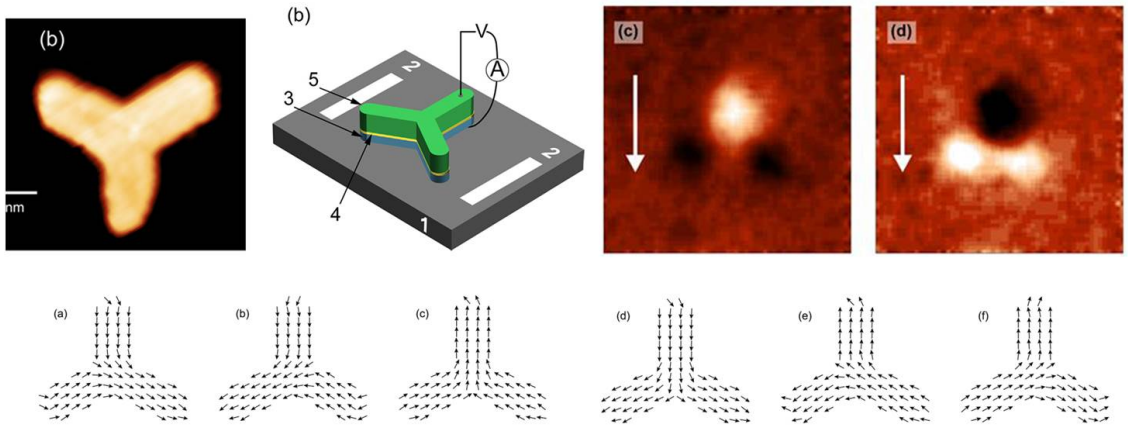

Figure 1.5: Strain control induce electrically of a Y-shaped object magnetization deposited on a piezoelectic substrate. Adapted from [65].

key to overcoming the limitations of current straintronic devices and unlocking their full potential in next-generation computing applications. Another example is presented in figure 1.5. These results obtained by A.A. Bukharaev et al. demonstrate that the "Y-shaped" TMR (tunneling magnetoresistance) structure exhibits multiple stable configurations due to shape anisotropy [65]. In their study, they successfully transitioned from one stable configuration to another by applying an external magnetic field, which could be alternatively replaced by a voltage-induced magnetoelastic field. In the following paragraph, we will provide an overview of magnonic crystals subjected to static mechanical strains. This discussion will encompass the fundamental principles governing their behavior under such conditions, the impact of mechanical strain on their magnonic band structure and the potential applications that arise from manipulating these properties.

1.4 Magnonic crystal under elastic strains

Studies on the propagation of spin waves in magnonic crystals under static mechanical deformations are still relatively scarce. However, past and future work on these crystals under deformation can be seen as part of magnetic straintronics. For example, Karboul et al. investigated spin waves in a thin Ni film, demonstrating that these waves can be controlled by applying mechanical strains. This is understandable, as the static magnetic configuration is influenced by deformation, thereby affecting the magnetization distribution. Consequently, it becomes feasible to manipulate spin waves through these strains. With respect to magnonic crystals under applied strain, the impact of external strain on the evolution of the magnonic band structure remains relatively unexplored [17]. Figure 1.6, based on the concept proposed in ref. [17], demonstrates strain control in a fictitious 2D square magnonic crystal, schematically represented in figure 1.6-a), with the magnonic bands projected along the high symmetry points of the first Brillouin zone. More precisely, figure 1.6-b) illustrates how applying controlled strain can modulate both the average posi-

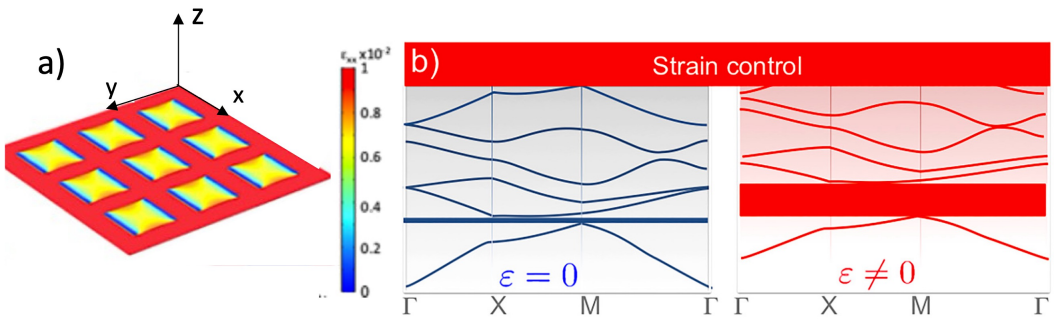

Figure 1.6: a) Schematic of an *ad hoc* 2D magnonic crystal formed by an array of square dots deposited on a stretchable substrate. A strain of 1% is applied to the substrate along x, the colors encode ε_{xx}. b) Concept demonstration showing the magnonic bands of a square 2D crystal (Γ, X, and M correspond to the high symmetry points of the first Brillouin zone) in the absence and presence of applied strains. The blue and red bands illustrate the evolution of the mean position and width of a magnonic bandgap.

tion and width of the magnonic bands. This adjustment can occur in the GHz range without the need for a magnetic field. Many perspectives and possibilities remain to be explored. Due to the geometry of nanostructures, strain heterogeneity can be significant within individual nanostructures because of the presence of free surfaces (as shown in figure 1.6-a)). In this case, different magnetic modes experience varying magnetoelastic fields, leading to a differentiated tunability of the magnonic bands based on the spatial localization of spin-wave modes within each nanostructure. This effect was recently proposed by Challab et al., who demonstrated that applying a weak strain to an $Ni_{60}Fe_{40}$ antidot system results in a significant variation in spin wave energy, reaching several tens of percent [68]. Such position-dependent tunability is challenging to achieve with an external magnetic field applied uniformly to an array of identical nanostructures. Furthermore, one could envision assemblies of nanostructures with varying lateral geometries (isotropic or anisotropic) or different thicknesses, offering a wide range of distinct strain fields across different types of nanostructures. Some of these possibilities will be explored in this thesis.

1.5 Towards magnon-phonon coupling in magphonic crystals

We previously discussed that dynamic mechanical strains can induce coupling between magnons and phonons [1, 2, 3, 4, 5], creating a rich landscape of coupled excitations that can be harnessed for advanced functionalities. In this context, some research groups have focused on so-called magphonic crystals [3, 4, 5]. A magphonic crystal is an artificial structure that simultaneously exhibits magnonic and phononic behaviors. It is designed as a periodic system for both spin and acoustic waves. For instance, the magnon and phonon dis-

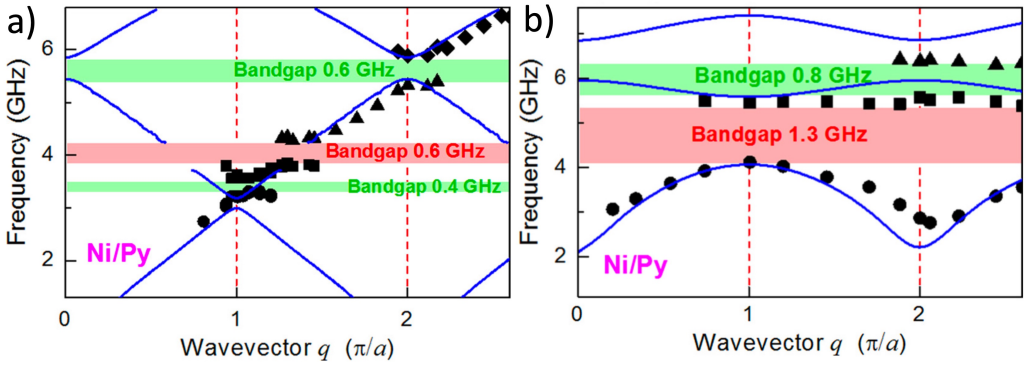

Figure 1.7: Magnon and phonon dispersion relations of $Ni/Ni_{80}Fe_{20}$ magphonic crystal. Experimental and theoretical data are denoted by symbols and continuous curves, respectively. Measured bandgaps are represented by shaded bands and Brillouin zone boundaries by vertical dashed lines.

persion relations in a 1D magphonic crystal (comprising alternating $Ni/Ni_{80}Fe_{20}$ nanowires fabricated on a SiO_2/Si substrate) have been experimentally measured using BLS [4, 5]. The dispersion relations are represented in figure 1.7. The dispersion relations reveal distinct magnonic and phononic band gaps, where neither spin waves nor acoustic waves can propagate. In addition, in their work, the authors do not detect the presence of coupling between magnons and phonons. However, due to the common frequency range, multiple intersections between spin and acoustic dispersion branches can occur as a result of the periodicity. These couplings are absent in homogeneous materials. In conventional crystals, the first phonon band gaps are far from the GHz range in which magnetostatic spin waves typically propagate. The coupling mechanism between spin and acoustic waves is magnetoelastic [3]. Dynamic magnetization generates a dynamic stress in the material *via* magnetostrictive effects, while the strain from the acoustic wave induces a dynamic magnetic field (inverse magnetostriction). If the frequency and wavelength of the stress field from the spin wave match the frequency of the magnetic field from the acoustic wave, the resonance condition for dynamic magnetoelastic coupling is met.

However, the magnon-phonon coupling in the same crystal (both magnonic and phononic) is not necessarily guaranteed because each magnonic and phononic band possesses its own width and mean frequency depending on the crystal's geometrical design. Thus, it is fundamental to control magnonic or phononic dispersion branches in order to study the coupling between them. Phononic bands are hardly tunable for a given system. Indeed, the acoustic wave velocity depends on intrinsic parameters (material mass density, elastic coefficients) and the geometrical features of the artificial crystal that are difficult to reversibly tune for a given system [69]. Some groups still managed to reversibly control the phononic bands by developing magnetoelastic phononic crystals [70, 71], electrorheological phononic crystals [72] or by using a thermal tuning of the phononic bands [73]. However, the amplitude of the frequency shifts is too low (a few MHz) to make interacting these phononic bands with the magnonic ones.

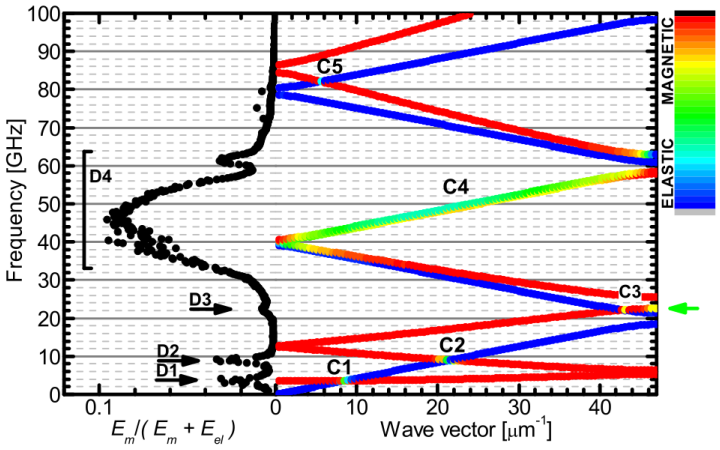

Figure 1.8: Dispersion relation for $Ni_{80}Fe_{20}$/CoFeB magphonic crystal. In the color scale, blue and red correspond to acoustic and spin waves, respectively. Green indicates coupled magnetoelastic waves. (left) Proportion of magnetic energy accumulated in the system in 1 ns of excitation by acoustic wave of a given frequency.

It is thus more thoughtful to master the magnonic bands in relation to phononic ones. As a consequence, the simplest way to tune the magnonic bands is the use of an applied magnetic field [49]. Indeed, the application of a few hundred Gauss leads to bandgap variations of the order of 1 GHz, depending on the magnetic intrinsic properties of the crystal (saturation magnetization, magnetic anisotropy, ...) and on the geometrical characteristics of the crystal [74]. This is sufficient to potentially induce and control a magnon-phonon coupling. However, as for more classical magnetic devices, such magnitudes of magnetic fields requires high electrical current, which is very energy intensive [75]. In summary, the most advanced results regarding these couplings in such crystals are likely those obtained by P. Graczyk and M. Krawczyk. In figure 1.8, the dispersion relation of a magphonic crystal is presented. Acoustic wave and spin wave branches cross at different frequencies . The third acoustic branch overlaps with the fifth spin wave branch throughout the Brillouin zone (labeled as C4). These dispersions show that the spin-wave and acoustic dispersions anti-cross at some points. In ref. [3], they conclude that magphonic crystals with such a property are promising candidates for spin wave generation. They can be used for efficient generation of spin waves by acoustic waves in a broad band of frequencies and wave vectors. The generated waves can have a nanometer wavelength much shorter than the source wave. We will revisit these coupling phenomena in the final chapter of this thesis.

1.6 Thesis manuscript overview

This thesis presents an investigation of magnetoelasticity, bridging mechanical and magnetic properties, particularly in the context of magnonic crystals and their applications. Chapter 1 discusses magnetoelasticity, which connects mechanical and magnetic proper-

ties. It highlights magnonic crystals for controlling spin waves and magnetic straintronics. Preliminary findings suggest that static elastic strains can influence magnetization and enhance spin wave control. Additionally, the chapter addresses magphonic crystals that couple magnonic and phononic behaviors and explores spin-acoustic wave interactions. Chapter 2 lays the groundwork in solid mechanics, focusing on linear elasticity and the behavior of isotropic and anisotropic crystals while preparing the reader for subsequent chapters addressing the intricate interplay between micromagnetic and mechanical/acoustic phenomena. Chapter 3 delves into micromagnetism, emphasizing the relevance of the Landau-Lifshitz-Gilbert (LLG) equation in understanding magnetic dynamics and its contributions from various energetic factors. The chapter also introduces the concept of magnonic crystals and their periodic structures, which significantly influence spin wave behavior.

In Chapter 4, our numerical method is detailed, fully coupling micromagnetism and solid mechanics using COMSOL Multiphysics®. This approach addresses the limitations of conventional micromagnetic software in simulating complex mechanical behavior and provides a robust framework for further investigation. Chapter 5 explores experimental techniques in ferromagnetic resonance (FMR) and Brillouin light scattering (BLS), fundamental for studying magnetization dynamics and spin wave interactions in nanostructures.

Subsequent chapters (6-9) investigate the magnetic properties of periodic nanostructures, including antidot arrays and modulated nanowires, under both static and dynamic strain. The experimental validation and numerical simulations reveal critical insights into spin wave dispersion and the effects of mechanical strain on magnonic properties, setting the stage for a deeper understanding of magnon-phonon interactions in Chapter 9.

The thesis culminates in Chapter 10, which synthesizes the findings, highlighting the integration of experimental and numerical methodologies. The conclusions affirm the potential of strain-induced control over spin wave dynamics, particularly in magnonic crystals, and outline future research directions, including the exploration of magnetic textures and nutation phenomena under strain.

Bibliography

[1] Joule, J. P. (1847). XVII. On the effects of magnetism upon the dimensions of iron and steel bars. The London, Edinburgh, and Dublin Philosophical Magazine and Journal of Science, 30(199), 76-87 1.1

[2] Joule, J. P. (1884). The Scientific Papers of James Prescott Joule (Vol. 1). The Society 1.1, 1.1, 10.2.3

[3] Smoluchowski, R. (1941). On the Theory of Volume Magnetostriction. Physical Review, 59(3), 309 1.1

[4] Lee, E. W. (1955). Magnetostriction and magnetomechanical effects. Reports on progress in physics, 18(1), 184 1.1

[5] Lapine, M., Shadrivov, I. V., Powell, D. A., & Kivshar, Y. S. (2012). Magnetoelastic metamaterials. Nature materials, 11(1), 30-33 1.1

[6] Engdahl, G., & Mayergoyz, I. D. (2000). Handbook of giant magnetostrictive materials (Vol. 107, pp. 1-125). San Diego: Academic press 1.1

[7] Hunter, D., Osborn, W., Wang, K., Kazantseva, N., Hattrick-Simpers, J., Suchoski, R., ... & Takeuchi, I. (2011). Giant magnetostriction in annealed Co1− xFex thin-films. Nature communications, 2(1), 518 1.1

[8] He, Y., Jiang, C., Wu, W., Wang, B., Duan, H., Wang, H., ... & Xu, H. (2016). Giant heterogeneous magnetostriction in Fe–Ga alloys: Effect of trace element doping. Acta Materialia, 109, 177-186 1.1

[9] Grimes, C. A., Roy, S. C., Rani, S., & Cai, Q. (2011). Theory, instrumentation and applications of magnetoelastic resonance sensors: a review. Sensors, 11(3), 2809-2844 1.1

[10] Ekreem, N. B., Olabi, A. G., Prescott, T., Rafferty, A., & Hashmi, M. S. J. (2007). An overview of magnetostriction, its use and methods to measure these properties. Journal of Materials Processing Technology, 191(1-3), 96-101 1.1

[11] Del Moral, A., Algarabel, P. A., Arnaudas, J. I., Benito, L., Ciria, M., De la Fuente, C., ... & De Teresa, J. M. (2002). Magnetostriction effects. Journal of magnetism and magnetic materials, 242, 788-796 1.1

[12] Bukharaev, A. A., Zvezdin, A. K., Pyatakov, A. P., & Fetisov, Y. K. (2018). Straintronics: a new trend in micro-and nanoelectronics and materials science. Physics-Uspekhi, 61(12), 1175 1.1, 1.3, 1.3

[13] Barangi, M., & Mazumder, P. (2015). Straintronics: A leap toward ultimate energy efficiency of magnetic random access memories. IEEE Nanotechnology Magazine, 9(3), 15-24 1.1, 1.3

[14] Biswas, A. K., Atulasimha, J., & Bandyopadhyay, S. (2015). The straintronic spin-neuron. Nanotechnology, 26(28), 285201 1.1, 1.3

[15] Roy, K. (2013, June). Ultra-low-energy straintronics using multiferroic composites. In Spin (Vol. 3, No. 02, p. 1330003). World Scientific Publishing Company 1.1, 1.3

[16] Cui, J., Hockel, J. L., Nordeen, P. K., Pisani, D. M., Liang, C. Y., Carman, G. P., & Lynch, C. S. (2013). A method to control magnetism in individual strain-mediated magnetoelectric islands. Applied Physics Letters, 103(23) 1.1, 1.3

[17] Makarov, D., & Sheka, D. D. (Eds.). (2022). Curvilinear micromagnetism: from fundamentals to applications (Vol. 146). Springer Nature 1.1

[18] Sheka, D. D. (2021). A perspective on curvilinear magnetism. Applied Physics Letters, 118(23) 1.1

[19] Makarov, D., Volkov, O. M., Kákay, A., Pylypovskyi, O. V., Budinská, B., & Dobrovolskiy, O. V. (2022). New dimension in magnetism and superconductivity: 3D and curvilinear nanoarchitectures. Advanced Materials, 34(3), 2101758 1.1

[20] Volkov, O. M., Kákay, A., Kronast, F., Mönch, I., Mawass, M. A., Fassbender, J., & Makarov, D. (2019). Experimental observation of exchange-driven chiral effects in curvilinear magnetism. Physical Review Letters, 123(7), 077201 1.1

[21] Karnaushenko, D., Makarov, D., Yan, C., Streubel, R., & Schmidt, O. G. (2012). Printable giant magnetoresistive devices. Advanced Materials, 24(33), 4518-4522 1.1

[22] Makarov, D., Melzer, M., Karnaushenko, D., & Schmidt, O. G. (2016). Shapeable magnetoelectronics. Applied Physics Reviews, 3(1). 1.1

[23] Cañón Bermúdez, G. S., & Makarov, D. (2021). Magnetosensitive E-Skins for Interactive Devices. Advanced Functional Materials, 31(39), 2007788 1.1, 8.2.4

[24] Karnaushenko, D., Karnaushenko, D. D., Makarov, D., Baunack, S., Schäfer, R., & Schmidt, O. G. (2015). Self-assembled on-chip-integrated giant magneto-impedance sensorics 1.1, 8.2.4

[25] Melzer, M., Makarov, D., & Schmidt, O. G. (2020). A review on stretchable magnetic field sensorics. Journal of Physics D: Applied Physics, 53(8), 083002.

[26] Melzer, M., Kaltenbrunner, M., Makarov, D., Karnaushenko, D., Karnaushenko, D., Sekitani, T., ... & Schmidt, O. G. (2015). Imperceptible magnetoelectronics. Nature communications, 6(1), 6080 1.1

[27] Makushko, P., Oliveros Mata, E. S., Cañón Bermúdez, G. S., Hassan, M., Laureti, S., Rinaldi, C., ... & Makarov, D. (2021). Flexible magnetoreceptor with tunable intrinsic logic for on-skin touchless human-machine interfaces. Advanced Functional Materials, 31(25), 2101089 1.1

[28] Faurie, D., Zighem, F., Garcia-Sanchez, A., Lupo, P., & Adeyeye, A. O. (2017). Fragmentation and adhesion properties of CoFeB thin films on polyimide substrate. Applied Physics Letters, 110(9) 1.1

[29] Merabtine, S., Zighem, F., Garcia-Sanchez, A., Gunasekaran, V., Belmeguenai, M., Zhou, X., ... & Faurie, D. (2018). Origin of relationship between ferromagnetic response and damage in stretched systems. Scientific Reports, 8(1), 13695 1.1

[30] Faurie, D., Adeyeye, A. O., & Zighem, F. (2021). Prospects toward flexible magnonic systems. Journal of Applied Physics, 130(15) 1.1, 1.4, 8.2.3, 8.2.4

[31] Zighem, F., & Faurie, D. (2021). A review on nanostructured thin films on flexible substrates: links between strains and magnetic properties. Journal of Physics: Condensed Matter, 33(23), 233002 1.1, 8.2.4

[32] Challab, N., Zighem, F., Faurie, D., Haboussi, M., Belmeguenai, M., Lupo, P., & Adeyeye, A. O. (2019). Local stiffness effect on ferromagnetic response of nanostructure arrays in stretchable systems. physica status solidi (RRL)–Rapid Research Letters, 13(2), 1800509 1.1

[33] Challab, N., Aboumassound, A. D., Zighem, F., Faurie, D., & Haboussi, M. (2019). Micromagnetic modeling of nanostructures subject to heterogeneous strain fields. Journal of Physics D: Applied Physics, 52(35), 355004 1.1

[34] https://math.nist.gov/oommf/ 1.1

[35] http://www.magpar.net 1.1

[36] http://mumax.github.io 1.1

[37] https://gitlab.com/magnum.np/magnum.np 1.1

[38] http://www.micromagus.de 1.1

[39] Liang, C. Y., Keller, S. M., Sepulveda, A. E., Bur, A., Sun, W. Y., Wetzlar, K., & Carman, G. P. (2014). Modeling of magnetoelastic nanostructures with a fully coupled mechanical-micromagnetic model. Nanotechnology, 25(43), 435701. 1.1

[40] Bur, A., Wu, T., Hockel, J., Hsu, C. J., Kim, H. K., Chung, T. K., ... & Carman, G. P. (2011). Strain-induced magnetization change in patterned ferromagnetic nickel nanostructures. Journal of Applied Physics, 109(12). 1.1

[41] De Jesús, M. G., Panduranga, M. K., Shirazi, P., Keller, S., Jackson, M., Wang, K. L., ... & Carman, G. P. (2022). Micro-magnetoelastic modeling of Terfenol-D for spintronics. Journal of Applied Physics, 131(23). 1.1

[42] Tiercelin, N., Dusch, Y., Preobrazhensky, V., & Pernod, P. (2011). Magnetoelectric memory using orthogonal magnetization states and magnetoelastic switching. Journal of Applied Physics, 109(7). 1.1

[43] Giordano, S., Dusch, Y., Tiercelin, N., Pernod, P., & Preobrazhensky, V. (2012). Combined nanomechanical and nanomagnetic analysis of magnetoelectric memories. Physical Review B—Condensed Matter and Materials Physics, 85(15), 155321. 1.1

[44] Graczyk, P., & Krawczyk, M. (2017). Coupled-mode theory for the interaction between acoustic waves and spin waves in magnonic-phononic crystals: Propagating magnetoelastic waves. Physical Review B, 96(2), 024407. 1.1

[45] K. Di, H. S. Lim, V. L. Zhang, S. C. Ng, M. H. Kuok, H. T. Nguyen and M. G. Cottam, J. Appl. Phys. 115, 053904 (2014) 1.1

[46] Di, K., Lim, H. S., Zhang, V. L., Ng, S. C., Kuok, M. H., Nguyen, H. T., & Cottam, M. G. (2014). Tuning the band structures of a one-dimensional width-modulated magnonic crystal by a transverse magnetic field. Journal of Applied Physics, 115(5). 1.1

[47] Nikitov, S. A., Tailhades, P., & Tsai, C. S. (2001). Spin waves in periodic magnetic structures—magnonic crystals. Journal of Magnetism and Magnetic Materials, 236(3), 320-330. 1.1

[48] Chumak, A. V., Serga, A. A., Hillebrands, B., & Kostylev, M. P. (2008). Scattering of backward spin waves in a one-dimensional magnonic crystal. Applied Physics Letters, 93(2). 1.1

[49] Wang, Z. K., Zhang, V. L., Lim, H. S., Ng, S. C., Kuok, M. H., Jain, S., & Adeyeye, A. O. (2009). Observation of frequency band gaps in a one-dimensional nanostructured magnonic crystal. Applied Physics Letters, 94(8). 1.1, 1.3, 1.2, 1.5, 10.2.3

[50] Gubbiotti, G., Tacchi, S., Madami, M., Carlotti, G., Adeyeye, A. O., & Kostylev, M. (2010). Brillouin light scattering studies of planar metallic magnonic crystals. Journal of Physics D: Applied Physics, 43(26), 264003. 1.1, 1.2

[51] Merbouche, H., Boventer, I., Haspot, V., Fusil, S., Garcia, V., Gouéré, D., ... & Anane, A. (2021). Voltage-controlled reconfigurable magnonic crystal at the sub-micrometer scale. ACS nano, 15(6), 9775-9781. 1.1, 1.2

[52] Beginin, E. N., Sadovnikov, A. V., Sakharov, V. K., Stognij, A. I., Khivintsev, Y. V., & Nikitov, S. A. (2019). Collective and localized modes in 3D magnonic crystals. Journal of Magnetism and Magnetic Materials, 492, 165647. 1.1, 1.2

[53] Barman, A., Gubbiotti, G., Ladak, S., Adeyeye, A. O., Krawczyk, M., Gräfe, J., ... & Winklhofer, M. (2021). The 2021 magnonics roadmap. Journal of Physics: Condensed Matter, 33(41), 413001. 1.1, 1.2

[54] Choudhury, S., Barman, S., Otani, Y., & Barman, A. (2017). Efficient modulation of spin waves in two-dimensional octagonal magnonic crystal. ACS nano, 11(9), 8814-8821. 1.1, 1.2

[55] Liao, L., Liu, J., Puebla, J., Shao, Q., & Otani, Y. (2024). Hybrid magnon-phonon crystals. npj Spintronics, 2(1), 47. 1.1, 1.5, 8.1, 9, 9.1.3, 9.1.3, 9.2.2

[56] Hatanaka, D., Asano, M., Okamoto, H., & Yamaguchi, H. (2023). Phononic crystal cavity magnomechanics. Physical Review Applied, 19(5), 054071. 1.1, 1.5, 8.1, 9

[57] Graczyk, P., & Krawczyk, M. (2017). Coupled-mode theory for the interaction between acoustic waves and spin waves in magnonic-phononic crystals: Propagating magnetoelastic waves. Physical Review B, 96(2), 024407. 1.1, 1.5, 1.5, 8.1, 9, 9.1.1, 9.2.2

[58] Pan, H., Zhang, V. L., Di, K., Kuok, M. H., Lim, H. S., Ng, S. C., ... & Adeyeye, A. O. (2013). Phononic and magnonic dispersions of surface waves on a permalloy/BARC nanostructured array. Nanoscale research letters, 8, 1-6. 1.1, 1.5, 8.1, 9, 9.2.2

[59] Zhang, V. L., Ma, F. S., Pan, H. H., Lin, C. S., Lim, H. S., Ng, S. C., ... & Adeyeye, A. O. (2012). Observation of dual magnonic and phononic bandgaps in bi-component nanostructured crystals. Applied Physics Letters, 100(16). 1.1, 1.5, 8.1, 9, 9.2.2

[60] Chumak, A. V., Serga, A. A., & Hillebrands, B. (2017). Magnonic crystals for data processing. Journal of Physics D: Applied Physics, 50(24), 244001. 1.2

[61] Sadovnikov, A. V., Gubanov, V. A., Sheshukova, S. E., Sharaevskii, Y. P., & Nikitov, S. A. (2018). Spin-wave drop filter based on asymmetric side-coupled magnonic crystals. Physical Review Applied, 9(5), 051002. 1.2

[62] Klingler, S., Pirro, P., Brächer, T., Leven, B., Hillebrands, B., & Chumak, A. V. (2015). Spin-wave logic devices based on isotropic forward volume magnetostatic waves. Applied Physics Letters, 106(21). 1.2

[63] Gubbiotti, G., Tacchi, S., Carlotti, G., Singh, N., Goolaup, S., Adeyeye, A. O., & Kostylev, M. (2007). Collective spin modes in monodimensional magnonic crystals consisting of dipolarly coupled nanowires. Applied Physics Letters, 90(9). 1.2

[64] Roy, K., Bandyopadhyay, S., & Atulasimha, J. (2012). Energy dissipation and switching delay in stress-induced switching of multiferroic nanomagnets in the presence of thermal fluctuations. Journal of Applied Physics, 112(2). 1.4, 1.3, 10.2.3

[65] Bukharaev, A. A., Bizyaev, D. A., Nurgazizov, N. I., Chuklanov, A. P., & Useinov, N. K. (2020). Ferromagnetic particles with the configuration anisotropy for straintronic memory cells. Journal of Magnetism and Magnetic Materials, 500, 166315. 1.5, 1.3, 10.2.3

[66] Martin, L. W., & Ramesh, R. (2012). Multiferroic and magnetoelectric heterostructures. Acta Materialia, 60(6-7), 2449-2470. 1.3

[67] Garcia, V., Bibes, M., & Barthélémy, A. (2015). Artificial multiferroic heterostructures for an electric control of magnetic properties. Comptes Rendus Physique, 16(2), 168-181. 1.3

[68] Challab, N., Faurie, D., Haboussi, M., Adeyeye, A. O., & Zighem, F. (2021). Differentiated strain-control of localized magnetic modes in antidot arrays. ACS Applied Materials & Interfaces, 13(25), 29906-29915. 1.4

[69] Gorishnyy, T., Ullal, C. K., Maldovan, M., Fytas, G., & Thomas, E. L. (2005). Hypersonic phononic crystals. Physical review letters, 94(11), 115501. 1.5

[70] Robillard, J. F., Matar, O. B., Vasseur, J. O., Deymier, P. A., Stippinger, M., Hladky-Hennion, A. C., ... & Djafari-Rouhani, B. (2009). Tunable magnetoelastic phononic crystals. Applied Physics Letters, 95(12). 1.5

[71] Bou Matar, O., Robillard, J. F., Vasseur, J. O., Hladky-Hennion, A. C., Deymier, P. A., Pernod, P., & Preobrazhensky, V. (2012). Band gap tunability of magneto-elastic phononic crystal. Journal of Applied Physics, 111(5). 1.5

[72] Yeh, J. Y. (2007). Control analysis of the tunable phononic crystal with electrorheological material. Physica B: Condensed Matter, 400(1-2), 137-144. 1.5

[73] Jim, K. L., Leung, C. W., Lau, S. T., Choy, S. H., & Chan, H. L. W. (2009). Thermal tuning of phononic bandstructure in ferroelectric ceramic/epoxy phononic crystal. Applied Physics Letters, 94(19). 1.5

[74] Wang, Z. K., Zhang, V. L., Lim, H. S., Ng, S. C., Kuok, M. H., Jain, S., & Adeyeye, A. O. (2010). Nanostructured magnonic crystals with size-tunable bandgaps. ACS nano, 4(2), 643-648. 1.5

[75] Wang, Z. K., Zhang, V. L., Lim, H. S., Ng, S. C., Kuok, M. H., Jain, S., & Adeyeye, A. O. (2010). Nanostructured magnonic crystals with size-tunable bandgaps. ACS nano, 4(2), 643-648. 1.5

2 Basics in solid mechanics

Contents

This chapter introduces the fundamental concepts of solid mechanics, laying the groundwork for the subsequent exploration of micromagnetic and mechanical/acoustic phenomena and their coupling. The first section covers linear elasticity, detailing stress and strain in both isotropic and anisotropic crystals, as well as polycrystalline models used in simulations. These models are essential for describing surface acoustic waves, such as Rayleigh and Love waves, which play a key role in the analyses presented later.

2.1 Linear elasticity

Solid mechanics is a vast and well-established field, encompassing a wide range of models depending on the material properties, the mechanical regime, and other factors. This work does not aim for perfect rigor but rather relies on common and simplified mechanical models to provide a practical foundation. This non-exhaustive theoretical background focuses primarily on strain and stress in isotropic materials, cubic crystals, and anisotropic crystals within the elastic regime, as considered in both simulations and analytical models. These equations will then serve to describe surface acoustic waves in solids, particularly Rayleigh and Love waves, which play a crucial role in the analyses presented in the final chapter of this thesis.

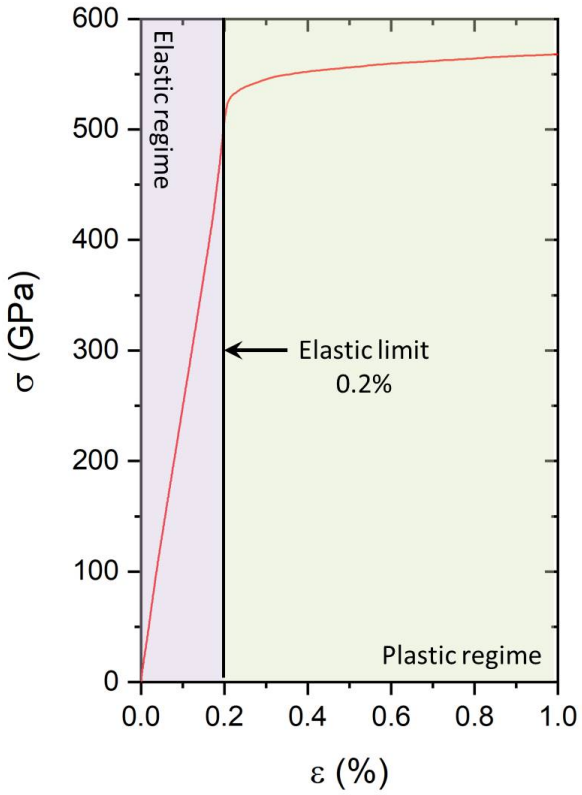

Figure 2.1: Uniaxial traction test realized during a master's practical work on a steel test piece witnessing the linear elastic behavior (pink area) and a non-linear plastic regime (green area) separated by the elastic limit at 0.2% of strain.

The elastic regime of a material refers to the reversible deformation a solid undergoes when subjected to a load. Within this regime, the material returns to its original shape once the load is removed, without any permanent deformation. This behavior is governed by Hooke's law, which establishes a linear relationship between stress and strain in elastic materials [1]:

$$\sigma = Y\varepsilon \tag{2.1}$$

The expression 2.1 is valid for isotropic materials subjected to uniaxial strain and depends on one single material property called the Young's modulus Y, expressed in Pa. This law reveals a linear dependency between the strain felt by the solid σ (in Pa) and the strain ε (dimensionless). The strain can be expressed as the relative elongation of the solid, and can be written as follows:

$$\varepsilon = \frac{\ell_f - \ell_i}{\ell_i} = \frac{u}{\ell_i} \tag{2.2}$$

where ℓ_i and ℓ_f are respectively the initial and final lengths of the object and u is the displacement. Hooke's law describe the elastic regime and therefore cannot be used to describe any mechanical behavior as shown in figure 2.1. The pink part of the traction test shows the domain described by Hooke's law, which expands until the elastic limit which is typically 0.2% for metals. Inside this region all the strain is reversible, meaning that when releasing the load, the solid will return in its original state. Above this limit, a nonlinear regime appears which corresponds the the plastic deformation which is permanent[2]. In the case of non-isotropic materials and non-isotropic loads, Hooke's law is generalized by this following form:

$$\sigma_{ij} = C_{ijkl}\varepsilon_{ij} \tag{2.3}$$

or :

$$\varepsilon_{ij} = S_{ijkl}\sigma_{ij} \tag{2.4}$$

where σ_{ij} and ε_{ij} (also noted $\overline{\overline{\sigma}}$ and $\overline{\overline{\varepsilon}}$) are respectively the stress and strain ij components of the stress and strain tensors (noted $\overline{\overline{\sigma}}$ and $\overline{\overline{\varepsilon}}$), and C_{ijkl} and S_{ijkl} are respectively stiffness and compliance $ijkl$ components of their respective tensors (noted $\overline{\overline{\overline{\overline{C}}}}$and $\overline{\overline{\overline{\overline{S}}}}$) which are material-based properties. The strain can be calculated from the displacement by:

$$\varepsilon_{ij} = \frac{1}{2}\left(\frac{\partial u_i}{\partial x_j} + \frac{\partial u_j}{\partial x_i}\right) \tag{2.5}$$

with u_i the component of the displacement vector and x_i the component of the space coordinate vector. Ultimately, the matrix forms of the stress and strain are as follows:

$$\overline{\overline{\sigma}} = \begin{pmatrix} \sigma_{11} & \sigma_{12} & \sigma_{13} \\ \sigma_{21} & \sigma_{22} & \sigma_{23} \\ \sigma_{31} & \sigma_{32} & \sigma_{33} \end{pmatrix} = \begin{pmatrix} \sigma_{11} & \tau_{12} & \tau_{13} \\ \tau_{21} & \sigma_{22} & \sigma_{23} \\ \tau_{31} & \tau_{32} & \sigma_{33} \end{pmatrix} \tag{2.6}$$

$$\overline{\overline{\varepsilon}} = \begin{pmatrix} \varepsilon_{11} & \varepsilon_{12} & \varepsilon_{13} \\ \varepsilon_{21} & \varepsilon_{22} & \varepsilon_{23} \\ \varepsilon_{31} & \varepsilon_{32} & \varepsilon_{33} \end{pmatrix} \tag{2.7}$$

It is important to note that those tensors are symmetric meaning that $\sigma_{ij} = \sigma_{ji}$ and $\varepsilon_{ij} = \varepsilon_{ji}$. The diagonal components of these tensors refer to normal stress and strain while the non-diagonal components correspond to tangential or shear stress (also noted τ) and strain. Concerning the stiffness and compliance tensors, they are initially composed of 81

components. However, taking into consideration homogeneous materials and the symmetry of the tensor, it can be reduced to only 36 material coefficients (with 21 independent coefficients). In this case, it is convenient to use a contracted notation for the strain and stress tensors given by table 2.1.

Stress tensor notation	Contracted stress notation	Strain tensor notation	Contracted strain notation
σ_{11}	σ_1	ε_{11}	ε_1
σ_{22}	σ_2	ε_{22}	ε_2
σ_{33}	σ_3	ε_{33}	ε_3
$\sigma_{12} = \sigma_{21}$	σ_4	$2\varepsilon_{12} = 2\varepsilon_{21}$	ε_4
$\sigma_{13} = \sigma_{31}$	σ_5	$2\varepsilon_{13} = 2\varepsilon_{31}$	ε_5
$\sigma_{23} = \sigma_{31}$	σ_6	$2\varepsilon_{23} = 2\varepsilon_{32}$	ε_6

Table 2.1: Tensor and contracted notation of stress and strain

This contraction allows one to write equations 2.3 and 2.4 as:

$$\begin{pmatrix} \sigma_1 \\ \sigma_2 \\ \sigma_3 \\ \sigma_4 \\ \sigma_5 \\ \sigma_6 \end{pmatrix} = \begin{pmatrix} C_{11} & C_{12} & C_{13} & C_{14} & C_{15} & C_{16} \\ C_{12} & C_{22} & C_{23} & C_{24} & C_{25} & C_{26} \\ C_{13} & C_{23} & C_{33} & C_{34} & C_{35} & C_{36} \\ C_{14} & C_{24} & C_{34} & C_{44} & C_{45} & C_{46} \\ C_{15} & C_{25} & C_{35} & C_{45} & C_{55} & C_{56} \\ C_{16} & C_{26} & C_{36} & C_{46} & C_{56} & C_{66} \end{pmatrix} \begin{pmatrix} \varepsilon_1 \\ \varepsilon_2 \\ \varepsilon_3 \\ 2\varepsilon_4 \\ 2\varepsilon_5 \\ 2\varepsilon_6 \end{pmatrix} \tag{2.8}$$

$$\begin{pmatrix} \varepsilon_1 \\ \varepsilon_2 \\ \varepsilon_3 \\ 2\varepsilon_4 \\ 2\varepsilon_5 \\ 2\varepsilon_6 \end{pmatrix} = \begin{pmatrix} S_{11} & S_{12} & S_{13} & S_{14} & S_{15} & S_{16} \\ S_{12} & S_{22} & S_{23} & S_{24} & S_{25} & S_{26} \\ S_{13} & S_{23} & S_{33} & S_{34} & S_{35} & S_{36} \\ S_{14} & S_{24} & S_{34} & S_{44} & S_{45} & S_{46} \\ S_{15} & S_{25} & S_{35} & S_{45} & S_{55} & S_{56} \\ S_{16} & S_{26} & S_{36} & S_{46} & S_{56} & S_{66} \end{pmatrix} \begin{pmatrix} \sigma_1 \\ \sigma_2 \\ \sigma_3 \\ \sigma_4 \\ \sigma_5 \\ \sigma_6 \end{pmatrix} \tag{2.9}$$

In elastic materials the strain energy per unit volume is given by[3]:

$$F_{el} = \frac{1}{2} C_{ij} \varepsilon_i \varepsilon_j \tag{2.10}$$

which can be expressed in a partial differentiation form as:

$$\mathrm{d}F_{el} = \sigma_i \mathrm{d}\varepsilon_i \tag{2.11}$$

Because of the stress-strain relations, the differentiated energy becomes:

$$\mathrm{d}F_{el} = C_{ij} \varepsilon_j \mathrm{d}\varepsilon_i \tag{2.12}$$

2.2 The cubic case

The complexity of the compliance and stiffness tensors very often reduces due to the geometry of the crystalline lattices. In the case of the cubic crystals, which is the most common cases, only 3 independent elastic constants are needed instead of 21 as $C_{11} = C_{22} = C_{33}$, $C_{44} = C_{55} = C_{66}$, and the only non-zero non-diagonal component is $C_{12} = C_{13} = C_{23}$. The tensor is finally:

$$\overline{\overline{\overline{C}}} = \begin{pmatrix} C_{11} & C_{12} & C_{12} & 0 & 0 & 0 \\ C_{12} & C_{11} & C_{23} & 0 & 0 & 0 \\ C_{12} & C_{12} & C_{11} & 0 & 0 & 0 \\ 0 & 0 & 0 & C_{44} & 0 & 0 \\ 0 & 0 & 0 & 0 & C_{44} & 0 \\ 0 & 0 & 0 & 0 & 0 & C_{44} \end{pmatrix}$$

Thus, using equation 2.10, one can calculate the elastic energy for a cubic material[3, 4]:

$$F_{el} = \frac{1}{2}C_{11}(\varepsilon_1^2 + \varepsilon_2^2 + \varepsilon_3^2) + C_{12}(\varepsilon_1\varepsilon_2 + \varepsilon_2\varepsilon_3 + \varepsilon_1\varepsilon_3) + \frac{1}{2}C_{44}(\varepsilon_4^2 + \varepsilon_5^2 + \varepsilon_6^2) \tag{2.13}$$

2.3 The case of an isotropic thin film

The systems studied in this thesis are either polycrystalline or amorphous. Polycrystalline thin films consist of aggregates of crystal grains with varying sizes and orientations, where the macroscopic properties are influenced by the characteristics of individual grains. For simplicity, we will assume that our polycrystalline films exhibit isotropic and homogeneous behavior in terms of elastic properties. At the microscopic level, the elastic strain and stress states of individual crystallites are governed by Hooke's law, subject to the applicable boundary conditions. In this context, homogenization methods are used to determine the effective elastic coefficients, which depend on the intrinsic elastic properties of single crystals. Among these, the Reuss and Voigt homogenization methods are the most fundamental approaches. They are widely recognized for providing bounds on the effective elastic coefficients. For instance, in the case of an isotropic thin film, the effective elastic coefficients in the Voigt model—denoted as ($\widetilde{C}_{11}$, $\widetilde{C}_{12}$ and $\widetilde{C}_{44}$)—are given by:

$$C = C_{11} - C_{12} - 2C_{44} \tag{2.14}$$

where C_{11}, C_{12} and $C_{44}$are the elastic constants of the single crystal.

$$\widetilde{C}_{11} = C_{11} - \frac{2}{5}C \tag{2.15}$$

$$\widetilde{C}_{12} = C_{12} + \frac{1}{5}C \tag{2.16}$$

$$\widetilde{C}_{44} = C_{44} + \frac{1}{5}C \tag{2.17}$$

while in the Reuss model they are given by (with $S = S_{11} - S_{12} - \frac{1}{2}S_{44}$):

$$\widetilde{C}_{11}^{-1} = C_{11}^{-1} - \frac{2}{5}S \tag{2.18}$$

$$\widetilde{C}_{12}^{-1} = C_{12}^{-1} + \frac{1}{5}S \tag{2.19}$$

$$\widetilde{C}_{44}^{-1} = C_{44}^{-1} + \frac{4}{5}S \tag{2.20}$$

$$\begin{bmatrix} \widetilde{C}_{11}+2\widetilde{C}_{44} & \widetilde{C}_{11} & \widetilde{C}_{11} & 0 & 0 & 0 \\ \widetilde{C}_{11} & \widetilde{C}_{11}+2\widetilde{C}_{44} & \widetilde{C}_{11} & 0 & 0 & 0 \\ \widetilde{C}_{11} & \widetilde{C}_{11} & \widetilde{C}_{11}+2\widetilde{C}_{44} & 0 & 0 & 0 \\ 0 & 0 & 0 & \widetilde{C}_{44} & 0 & 0 \\ 0 & 0 & 0 & 0 & \widetilde{C}_{44} & 0 \\ 0 & 0 & 0 & 0 & 0 & \widetilde{C}_{44} \end{bmatrix} \tag{2.21}$$

One can note here that only two independent coefficients are remaining ($\widetilde{C}_{11}$ and $\widetilde{C}_{44}$). The following relation is thus deduced:

$$\sigma_{ij} = \widetilde{C}_{11}\delta_{ij}\varepsilon_{kk} + 2\widetilde{C}_{44}\varepsilon_{ij} \tag{2.22}$$

From this relation $\sigma_{kk} = \left(3\widetilde{C}_{11} + 2\widetilde{C}_{44}\right)\varepsilon_{kk}$, we can rewrite the above formula as a function of the stresses:

$$\varepsilon_{ij} = \frac{1}{2\widetilde{C}_{44}}\sigma_{ij} - \frac{\widetilde{C}_{11}}{2\widetilde{C}_{44}(3\widetilde{C}_{11}+2\widetilde{C}_{44})}\sigma_{kk}\delta_{ij} \tag{2.23}$$

We can define the Young's modulus (Y) and the Poisson's ratio (ν) by considering a simple tensile mechanical test:

$$\sigma = \begin{pmatrix} \sigma & 0 & 0 \\ 0 & 0 & 0 \\ 0 & 0 & 0 \end{pmatrix}; \varepsilon = \begin{pmatrix} \varepsilon_L & 0 & 0 \\ 0 & \varepsilon_T & 0 \\ 0 & 0 & \varepsilon_T \end{pmatrix} \tag{2.24}$$

where ε_L and ε_T stand for the longitudinal and the transverse strains, respectively. They can be written as functions of $\widetilde{C}_{11}$ and $\widetilde{C}_{44}$:

$$\varepsilon_L = \frac{\widetilde{C}_{11}+\widetilde{C}_{44}}{\widetilde{C}_{44}(3\widetilde{C}_{11}+2\widetilde{C}_{44})}\sigma = \frac{1}{Y}\sigma \tag{2.25}$$

$$\varepsilon_T = -\frac{\widetilde{C}_{11}}{2\widetilde{C}_{44}(3\widetilde{C}_{11}+2\widetilde{C}_{44})}\sigma = -\nu\,\varepsilon_L \tag{2.26}$$

where the Young's modulus Y and the Poisson's ratio (ν) are given by:

$$Y = \frac{\widetilde{C}_{44}(3\widetilde{C}_{11}+2\widetilde{C}_{44})}{\widetilde{C}_{11}+\widetilde{C}_{44}} \tag{2.27}$$

$$\nu = \frac{\widetilde{C}_{11}}{2(\widetilde{C}_{11}+\widetilde{C}_{44})} \tag{2.28}$$

The equation 2.23 can be rewritten by introducing Y and ν:

$$\varepsilon_{ij} = \frac{1+\nu}{Y}\sigma_{ij} - \frac{\nu}{Y}\sigma_{kk}\delta_{ij} \tag{2.29}$$

$$\sigma_{ij} = \frac{Y}{1+\nu}\varepsilon_{ij} + \frac{\nu Y}{(1+\nu)(1-2\nu)}\varepsilon_{kk}\delta_{ij} \tag{2.30}$$

2.4 Elastic waves in solids

2.4.1 Basic formalism

he previously developed framework is typically applied at the macroscopic (or sometimes microscopic) scale. However, it does not fully describe the phenomena occurring at the atomic scale. When a force disturbs the equilibrium of a solid medium, elastic waves are generated and propagate as atoms oscillate harmonically. The formalism governing the propagation equations of acoustic waves is derived from Newton's second law of motion [5, 6, 8, 9]:

$$\vec{\nabla} \cdot \overline{\overline{\sigma}} + \vec{f_v} = \rho \frac{\partial^2 \vec{u}}{\partial t^2} \tag{2.31}$$

where $\vec{f_v}$ are the volume forces applied on the system, ρ the mass density and $\vec{u}$ the particle displacement vector. By combining Hooke's law (eq. 2.3) with Newton's second law (eq. 2.31), we obtain the wave equation:

$$\rho \frac{\partial^2 u_i}{\partial t^2} = C_{ijkl} \frac{\partial^2 u_l}{\partial x_j \partial x_k} \tag{2.32}$$

TThis equation describes the propagation of elastic waves, whose solutions determine the displacement of particles. By considering plane wave solutions, we can rewrite the wave equation in a new form known as Christoffel's equation:

$$\rho V_\phi^2 P_i = C_{ijkl} n_j n_k P_l = \Gamma_{il} P_l$$

where $\vec{n}$ is the propagation direction of the wave, $\vec{P}$ is the polarization of the displacement, V_ϕ is the phase velocity of the wave and $\overline{\overline{\Gamma}}$ is the Christoffel tensor. According to Christoffel's equation, the term ρV_ϕ^2 corresponds to the eigenvalues of the Christoffel tensor, leading to:

$$\left(\Gamma_{il} - \rho V_\phi^2 \delta_{il}\right) P_l = 0 \tag{2.33}$$

with δ_{il} the Kronecker coefficient. By considering solutions where all polarization components are nonzero, we obtain the trivial solution:

$$\Gamma_{il} = \rho V_\phi^2 \delta_{il} \tag{2.34}$$

This formulation provides a foundation for understanding elastic wave propagation in solids, particularly in anisotropic media, where the eigenvalues of the Christoffel tensor determine the phase velocities of different wave modes.

2.4.2 Rayleigh and Sezawa acoustic wave

Multiple types of elastic (or acoustic) waves can propagate in solids, each characterized by its polarization. Among them, the Rayleigh acoustic wave is a transverse surface wave with elliptical polarization in the sagittal plane. The primary component of its displacement is perpendicular to the surface of the solid, while the displacement in the propagation direction is relatively small. As a result, this wave is actually a combination of a transverse wave (major component) and a longitudinal wave (minor component).

A similar surface mode is the Sezawa wave, which is often regarded as an extension of the Rayleigh wave. However, the terminology is not universally adopted; many acoustics specialists refer to these higher-order surface waves as Rayleigh-$2, 3, \cdots n$. In this work, we use the Sezawa designation to refer specifically to waves with elliptical polarization in the sagittal plane, where the longitudinal component dominates, while the transverse component is minor. The polarization and displacement of the solid surface associated with Rayleigh and Sezawa waves are illustrated in figure 2.2[5, 6, 8, 10, 11, 12].

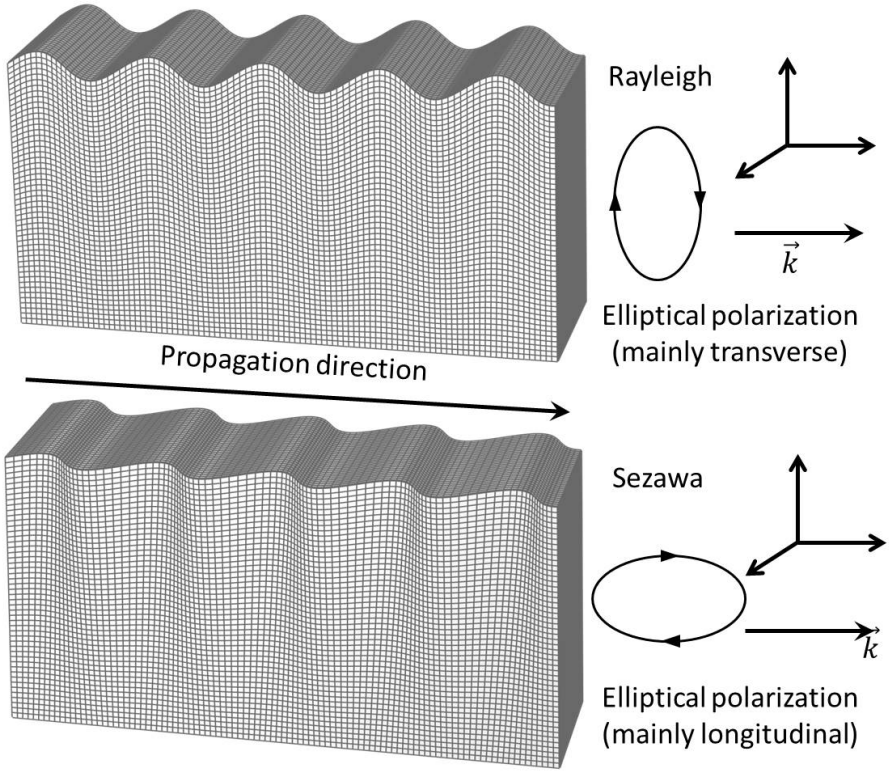

Figure 2.2: Schematic representation of the Sezawa and Rayleigh elastic waves modeled by using Comsol Multiphysics.

2.4.3 Love acoustic wave

The Love acoustic wave is a transverse surface wave with linear polarization that is parallel to the surface and perpendicular to the propagation direction. Unlike Rayleigh and Sezawa

waves, the Love wave does not induce any out-of-plane particle displacement. Its existence is particularly favored in multilayered media, especially when the propagating medium is supported by a softer substrate. A schematic representation of its polarization is shown in figure 2.3. In this thesis, the focus is primarily on surface acoustic waves; however, other types of volume waves also exist:

- Shear volume waves (S waves) exhibit longitudinal polarization,
- Compression waves (P waves) have transverse polarization,
- Lamb waves propagate within thin films where the thickness is comparable to the wavelength.

These volume waves play a role in certain applications but are not central to the analyses presented in this work [13].

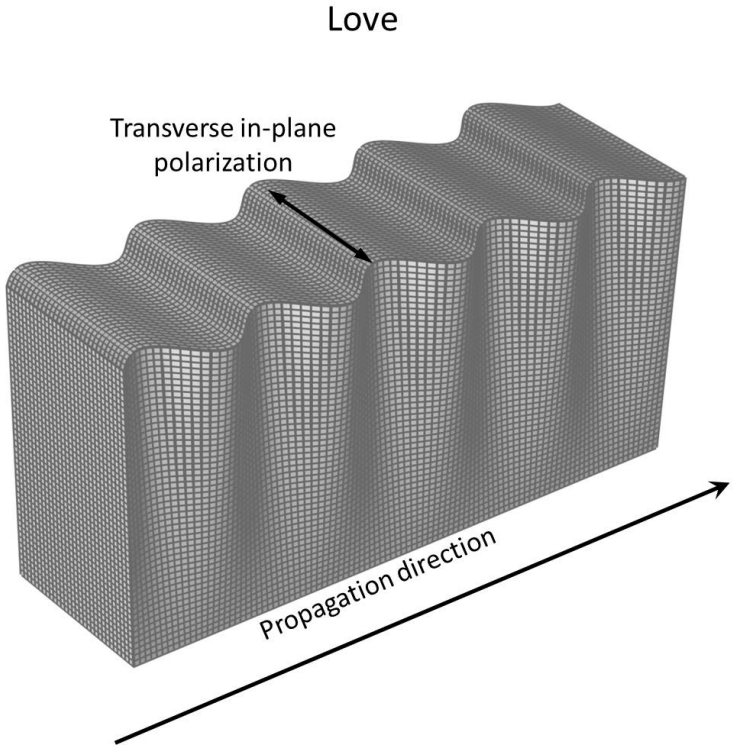

Figure 2.3: Schematic representation of the Love elastic wave modeled by using Comsol Multiphysics.

Bibliography

[1] Rychlewski, J. (1984). On Hooke's law. Journal of Applied Mathematics and Mechanics, 48(3), 303-314 2.1

[2] Bertram, A., & Glüge, R. (2015). Solid mechanics. Berlin: Springer 2.1

[3] Kaw, A. K. (2005). Mechanics of composite materials. CRC press 2.1, 2.2

[4] Sander, D. (1999). The correlation between mechanical stress and magnetic anisotropy in ultrathin films. Reports on Progress in Physics, 62(5), 809 2.2

[5] Royer, D., & Valier-Brasier, T. (2021). Ondes élastiques dans les solides 1: Propagation (Vol. 1). ISTE Group 2.4.1, 2.4.2

[6] Valier-Brasier, T., & Royer, D. (2021). Ondes élastiques dans les solides 2: Rayonnement, diffusion, génération (Vol. 2). ISTE Group 2.4.1, 2.4.2

[7] Farnell, G. W., & Adler, E. L. (2012). Elastic wave propagation in thin layers. Physical acoustics, 9, 35-127

[8] Robin, M. (2019). Contribution à l'étude de l'adhérence des structures du type couche sur substrat par modes de Rayleigh générés et détectés par sources laser (Doctoral dissertation, Université de Valenciennes et du Hainaut-Cambresis) 2.4.1, 2.4.2

[9] Landau, L. D., Pitaevskii, L. P., Kosevich, A. M., & Lifshitz, E. M. (2012). Theory of elasticity: volume 7 (Vol. 7). Elsevier 2.4.1

[10] Rayleigh, L. (1885). On waves propagated along the plane surface of an elastic solid. Proceedings of the London mathematical Society, 1(1), 4-11 2.4.2

[11] Sezawa, K., & Kanai, K. (1935). Discontinuity in dispersion curves of Rayleigh-waves. Proceedings of the Imperial Academy, 11(1), 13-14 2.4.2

[12] Sezawa, K., & Kanai, K. (1939). The range of possible existence of Stoneley waves. Bull. Earthq. Res. Inst, 17(1), 25 2.4.2

[13] Anderson, D. L. (1962). Love wave dispersion in heterogeneous anisotropic media. Geophysics, 27(4), 445-454 2.4.3

3 Elements of micromagnetism

Contents

This chapter explores the foundational principles of micromagnetism, highlighting its significance in both natural and technological contexts. Magnetism, a fundamental and universal phenomenon arising from electron motion, originates from the combined effects of intrinsic spin and orbital momentum, which together define both atomic and macroscopic magnetic moments. With the continuous advancement of information technology, particularly in nanoscience, micromagnetism has become increasingly relevant due to its

ability to leverage the vectorial nature of magnetization at the nanoscale. At the core of this framework is the Landau-Lifshitz-Gilbert (LLG) equation, which describes the dynamics of magnetization by incorporating multiple energy contributions, including:

- Exchange interaction, which governs the short-range coupling between spins,
- Zeeman energy, arising from external magnetic fields,
- Magnetocrystalline anisotropy, which reflects the dependency of magnetization on crystalline symmetry,
- Magnetostatic interactions, which involve long-range dipolar effects,
- Magnetoelastic effects, which account for the coupling between magnetic and mechanical properties.

The chapter further examines the dynamics of spin precession, distinguishing between propagating and non-propagating modes. These dynamics are probed through experimental techniques such as ferromagnetic resonance (FMR) and Brillouin light scattering (BLS), which provide critical insights into spin wave behavior. Finally, the chapter introduces the concept of magnonic crystals, emphasizing how periodicity influences spin wave dispersion. The discussion outlines the conditions necessary to engineer magnonic properties in structured magnetic materials, paving the way for potential applications in spintronics and magnon-based computing.

3.1 Preamble

Magnetism is a fundamental property that acts and exists at every scale in the universe. The Earth (like many celestial bodies) generates its own magnetic field that protects all living things from solar wind, and we use magnetism on a human scale in our everyday lives (fridge magnets, magnetic resonance imaging, motors, hard drives....). Magnetism comes essentially from the movement of electrons around the nucleus of the atom and comprises two contributions: the angular momentum of the electrons (intrinsic spin) and the orbital momentum [1]. The sum of the magnetic moments of electrons defines the atomic magnetic moment, and the sum of all the atomic magnetic moment defines the magnetic moment of the whole solid, which is referred to as the magnetization. As modern information technology increasingly relies on the electronic properties of solids at the nanoscale (10 nm – 1 µm), it was a natural progression to extend its development to nano- and micromagnetism. Like traditional electronics, micromagnetism is fundamentally based on electronic interactions, but it offers the advantage of leveraging the vectorial nature of magnetization, as opposed to the scalar nature of electron flow [1, 2].

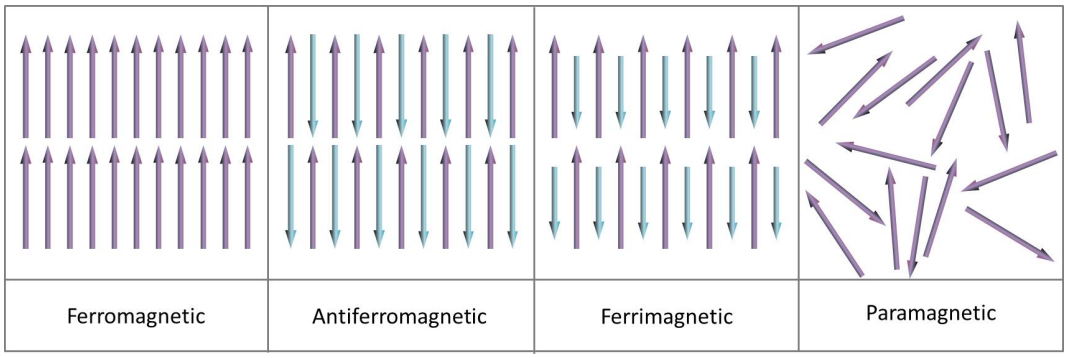

Figure 3.1: Scheme of the four magnetic orders. Paramagnetic materials exhibit randomly oriented magnetic moments in the absence of an applied field. Antiferromagnetic materials have an antiparallel alignment of neighboring spins, resulting in zero net magnetization. Ferromagnetic materials feature a parallel alignment of moments, leading to spontaneous magnetization. Ferrimagnetic materials also show an antiparallel spin alignment, but with unequal moments, producing a nonzero net magnetization.

Magnetic materials exhibit various magnetic phases, as illustrated in figure 3.1. They can be broadly classified based on their effective magnetization in the absence of an external magnetic field:

- Paramagnetic and antiferromagnetic materials exhibit zero effective magnetization,
- Ferromagnetic and ferrimagnetic materials exhibit a nonzero effective magnetization.

While antiferromagnetic and ferrimagnetic materials are of great interest in the micromagnetism community, particularly for their role in spintronic devices, this work focuses exclusively on ferromagnetic materials. These materials are well understood and offer greater

numerical simplicity, making them more suitable for computational modeling and simulations.

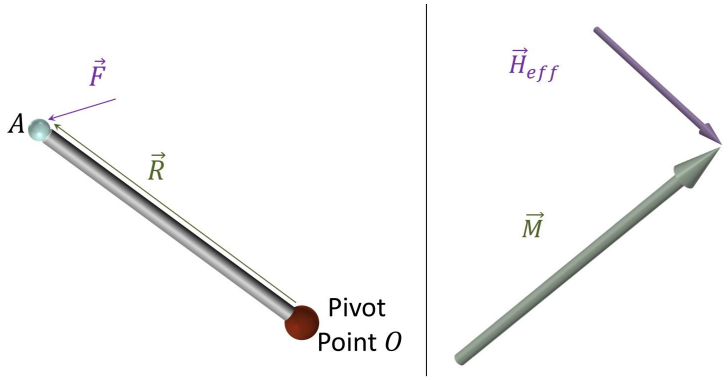

Figure 3.2: Scheme illustrating the analogy between the mechanical torque exerted on a rigid body (left) and the magnetic torque applied to magnetization by a magnetic field (right). In the mechanical case, an external force generates a torque, causing rotational motion around a fixed axis. In the magnetic case, the applied magnetic field exerts a torque on the magnetization vector, leading to its precessional motion around the field direction.

3.2 Landau-Lifshitz-Gilbert equation of motion

Solid mechanics and micromagnetism are closely related not only through magnetoelasticity, but also because the theory of micromagnetism was originally inspired by the rotational motion of rigid bodies. A clear analogy can be drawn between the mechanical dynamics of a rigid body and the magnetization dynamics governed by the Landau-Lifshitz-Gilbert equation. To illustrate this, let us consider an object attached to a pivot point O, as shown in figure 3.2. The torque applied to the object results in rotational motion around the pivot, much like how an applied magnetic field exerts a torque on the magnetization, leading to its precessional motion.

A force $\vec{F}$ applied to a point A generates a torque $\vec{T}$:

$$\vec{T} = \vec{OA} \times \vec{F} = \frac{d\vec{L}}{dt} \tag{3.1}$$

where $\vec{L}$ is the angular momentum. An analogous relation can then be written for the spin momentum $\vec{S}$:

$$\vec{T} = \frac{d\vec{S}}{dt} = \frac{1}{\gamma}\frac{d\vec{M}}{dt} = \vec{M} \times \vec{H}_{eff} \tag{3.2}$$

where $\vec{M} = \gamma\vec{S}$ is the magnetic moment γ being the gyromagnetic ratio and $\vec{H}_{eff}$ is the effective magnetic field applied to $\vec{M}$. This effective field includes multiple contributions of

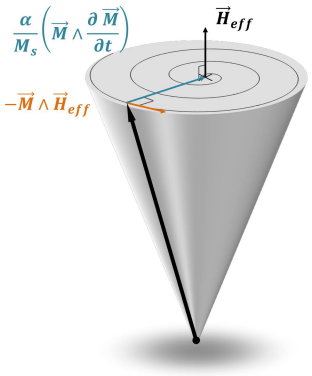

Figure 3.3: Diagram illustrating the precession cone described by the out-of-equilibrium magnetization. When subjected to an external magnetic field, the magnetization vector does not align immediately but instead undergoes precessional motion around the equilibrium direction. This motion follows a cone-like trajectory, characteristic of the Landau-Lifshitz-Gilbert dynamics, with damping gradually aligning the magnetization along the field direction.

the total magnetic energy of the system that will be developed in the following sections. This equation, known as the Landau-Lifshitz equation, was later refined by T. Gilbert, who introduced a damping term based on mechanical analogies with the behavior of rigid bodies [3, 4]:

$$\frac{d\vec{m}}{dt} = -\gamma \vec{m} \times \vec{H}_{eff} + \alpha \vec{m} \times \frac{d\vec{m}}{dt} \tag{3.3}$$

where $\vec{m} = \begin{pmatrix} m_x \\ m_y \\ m_z \end{pmatrix} = \frac{1}{M_s} \begin{pmatrix} M_x \\ M_y \\ M_z \end{pmatrix}$ is the normalized magnetization, meaning that $||\vec{m}|| = 1$ and α is a dimensionless constant called the damping factor.

The Landau-Lifshitz-Gilbert (LLG) equation is fundamental for describing the spatio-temporal evolution of magnetization. While alternative formulations exist to account for specific effects—such as the Landau-Lifshitz-Gilbert-Slonczewski (LLGS) equation for spin transfer torque [5, 6] or the second-time derivative of magnetization to capture nutation phenomena [7, 8, 9])—the standard LLG equation remains the most widely used model for magnetization dynamics. The LLG equation consists of two distinct terms, as illustrated in figure 3.3:

$$-\gamma \vec{M} \times \vec{H}_{eff} \tag{3.4}$$

describes the Larmor precession, where the magnetization precesses around the effective magnetic field

$$\alpha \frac{\vec{M}}{M_s} \times \frac{d\vec{M}}{dt} \tag{3.5}$$

represents damping, which causes the magnetization to gradually align with the effective field, leading to an equilibrium state in the absence of external excitation. This equation is crucial for understanding magnetization dynamics in nanostructures, including spin waves, domain wall motion, and magnetization switching processes.

3.3 Energetic approach

As with all physical systems, a magnetic system naturally evolves toward a state of minimal energy. The total magnetic energy density arises from multiple contributions, each exerting a distinct influence on magnetization dynamics. In the LLG equation, the effect of energy on magnetization is incorporated through the effective magnetic field:

$$\vec{H}_{eff} = -\frac{1}{\mu_0 M_s}\frac{\partial F_{tot}}{\partial \vec{m}} \tag{3.6}$$

where the total magnetic energy density is expressed as [10, 11, 12, 13]:

$$F_{tot} = F_{ex} + F_{Zee} + F_{an} + F_{ms} + F_{me} \tag{3.7}$$

Each term on the right-hand side represents a different contribution to the system's energy:

- F_{ex} : Exchange energy, which favors parallel alignment of neighboring spins.
- F_{Zee} : Zeeman energy, arising from the interaction with an external magnetic field.
- F_{an}: Magnetocrystalline anisotropy energy, which depends on the crystal structure and preferential magnetization axes.
- F_{ms}: Magnetostatic (demagnetizing) energy, resulting from dipolar interactions within the material.
- F_{me}: Magnetoelastic energy, which describes the coupling between magnetization and mechanical stress.

These five energy terms play a crucial role in magnetization dynamics and are the primary contributions considered in our experiments and simulations.

3.3.1 Exchange interaction

The exchange energy is responsible for the coupling at the atomic scale between the neighboring spins and, consequently, responsible for the magnetic order of the magnetic medium. In ferromagnetic, materials this energy keeps the neighboring spins parallel to each other, whereas in antiferromagnetic and ferrimagnetic materials it keeps them antiparallel. Exchange interaction between spin can occur in multiple ways and can take multiple forms. Among them we can mention the direct exchange which is a short distance effect that we are going to consider for the model development, the super-exchange that has a "long"

distance effect thanks to paramagnetic ions that act as intermediaries between two ferromagnetic ions, and the indirect exchange in which the exchange between spins is mediated by the conduction electrons [14, 15, 16] (see figure 3.4).

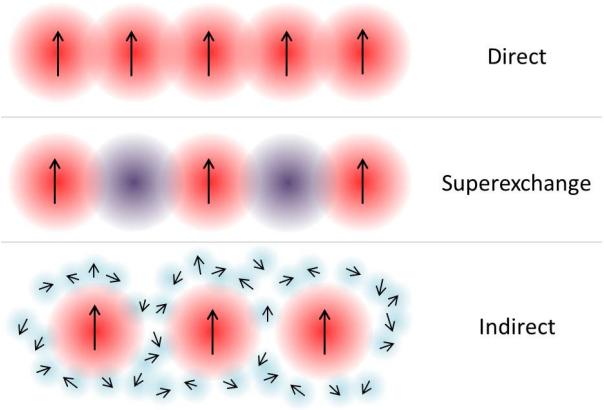

Figure 3.4: Schematic representation of different types of exchange interactions. The red spheres represent magnetic atoms, the purple spheres correspond to paramagnetic ions, and the blue spheres depict conduction electrons. The diagram illustrates various exchange mechanisms, including direct exchange, where magnetic atoms interact *via* overlap of their wavefunctions; superexchange, where interaction is mediated through paramagnetic ions; and RKKY (Ruderman-Kittel-Kasuya-Yosida) exchange, which occurs *via* conduction electrons in metallic systems.

The theory of direct interaction has been described in the Heisenberg model as the overlap of the wave functions of the magnetic atoms or ions:

$$\mathcal{H} = -\sum_{ij} J_{ij} \vec{S}_i \cdot \vec{S}_j \tag{3.8}$$

where $\mathcal{H}$ is the Hamiltonian of the spin interaction, $\vec{S}_i$ and $\vec{S}_j$ are two distinct spins and J_{ij} is the exchange integral, which sign determines the magnetic order, it is positive $J > 0$ for ferromagnetic media and negative $J < 0$ for antiferromagnetic media. As the exchange integral is dependent of the distance between the spins, it becomes quickly negligible after the first neighbors. This Hamiltonian generalized to the continuous media considered in micromagnetism can be expressed as:

$$F_{ex} = A_{ex} \left(\vec{\nabla} \cdot \vec{m} \right)^2 \tag{3.9}$$

where A_{ex} (in J.m^{-1}) is the exchange stiffness. Thus, we can associate an effective field $\vec{H}_{ex}$ to this magnetic energy density:

$$\vec{H}_{ex} = \frac{2A_{ex}}{\mu_0 M_s} \vec{\nabla}^2 \vec{m} \tag{3.10}$$

where μ_0 is the vacuum permeability and M_s is saturation magnetization.

3.3.2 Zeeman energy

The Zeeman interaction corresponds to the effect of an external magnetic field $\vec{H}$ applied to the magnetic moments.

$$\vec{H}_{Zee} = \vec{H} \tag{3.11}$$

$$F_{Zee} = -\mu_0 M_s \vec{H} \cdot \vec{m} \tag{3.12}$$

In the absence of other energy contributions, the Zeeman interaction forces the magnetization to align with the applied magnetic field $\vec{H}$, minimizing the system's energy.

3.3.3 Magnetocrystalline anisotropy

Magnetocrystalline anisotropy is an energy contribution coming directly from the crystalline configuration of the material. Due to the anisotropic spatial distribution of atoms the spin-orbit coupling takes preferential orientations according to the crystallographic axes. This phenomenon gives birth to easy and hard axis for the magnetization depending on what direction minimizes the total energy of the system. Hence, the magnetocrystalline anisotropy energy term takes different forms depending on the type of anisotropy. As the alloys we consider have very small grain sizes, the average behavior of the material is quasi isotropic or slightly anisotropic according one direction due to deposition conditions. Figure 3.5 is showing the energy surface for the uniaxial and cubic cases, which energy takes the following forms [11]:

$$F_{ani} = K_1 \sin^2 \theta \tag{3.13}$$

in the case of a uniaxial anisotropy and [11]:

$$F_{ani} = K_1 \left(\alpha^2\beta^2 + \beta^2\gamma^2 + \alpha^2\gamma^2\right) + K_2\alpha^2\beta^2\gamma^2 \tag{3.14}$$

in the case of a cubic anisotropy. Here, $\alpha = \sin\theta\cos\varphi$, $\beta = \sin\theta\sin\varphi$ and $\gamma = \cos\theta$ where θ and φ are the spherical coordinates angles whereas K_1 and K_2 are called magnetocrystalline constants [17]. Generally speaking, an *ad hoc* uniaxial anisotropy term can be written as:

$$F_u = K(\vec{m} \cdot \vec{u})^2 \tag{3.15}$$

where $\vec{u}$ is the anisotropy axis. Considering this form, the anisotropy field becomes :

$$\vec{H}_{ani} = \frac{2K}{\mu_0 M_s}(\vec{m} \cdot \vec{u}) \cdot \vec{u} \tag{3.16}$$

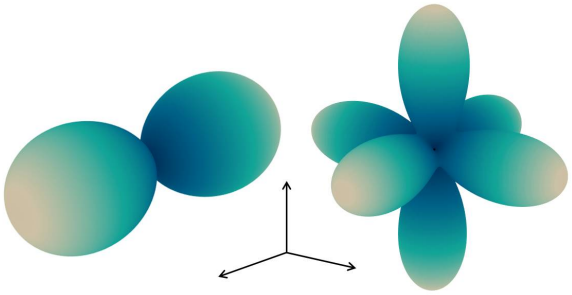

Figure 3.5: Modeling of the anisotropy energy surfaces for uniaxial magnetocrystalline anisotropy (left) and cubic magnetocrystalline anisotropy (right). In the uniaxial case, the energy depends on the angle between the magnetization and the easy axis, forming a double-well potential with two equivalent minima along the preferred direction. In the cubic case, the energy landscape exhibits four or sixfold symmetry, depending on the crystallographic structure, with multiple easy axes corresponding to the lowest energy states.

3.3.4 Magnetostatic interaction

When discussing magnetostatic interactions, two distinct contributions must be considered [18, 20]. A magnetized object, such as a ferromagnet, becomes polarized according to its magnetization orientation, generating a magnetostatic dipolar field outside the magnetic medium. This field obeys Maxwell's laws and is given by:

$$\vec{H}_{dip} = M_s \iiint \rho_{mag} \frac{\vec{OP}}{||\vec{OP}||^3} d\tau + M_s \iint \sigma_{mag} \frac{\vec{OP}}{||\vec{OP}||^3} d\Sigma \tag{3.17}$$

where the $\vec{OP}$ is the position vector and τ and Σ are the volume and the surface respectively. ρ_m and σ_{mag} are the so-called volumetric magnetic charge density and the surface magnetic charge density defined as:

$$\rho_{mag} = -\vec{\nabla} \cdot \vec{m} \tag{3.18}$$

and

$$\sigma_{mag} = \vec{n} \cdot \vec{m} \tag{3.19}$$

where $\vec{n}$ is the normal vector. Due to the continuity of the magnetic induction, a field is induced within the magnetic object, opposing the magnetization. This demagnetizing effect is often difficult to quantify, as it depends on the geometry of the object. However, for ellipsoidal geometries, the demagnetizing field can be determined analytically [19]:

$$\vec{H}_{dem} = M_s \overline{\overline{N}} \vec{m} \tag{3.20}$$

with:

$$F_{dem} = \frac{1}{2} \mu_0 M_s^2 \left(N_{xx} m_x^2 + N_{yy} m_y^2 + N_{zz} m_z^2 \right) \tag{3.21}$$

One can define $\overline{\overline{N}}$ as the demagnetizing tensor and N_{xx}, N_{yy}, N_{zz} the diagonal components of this tensor such as $N_{xx} + N_{yy} + N_{zz} = 1$. Thus, the magnetostatic field is expressed as:

$$\vec{H}_{ms} = \vec{H}_{dem} + \vec{H}_{dip} \tag{3.22}$$

Those two magnetostatic contributions are shown in the simulated ellipsoid in figure 3.6.

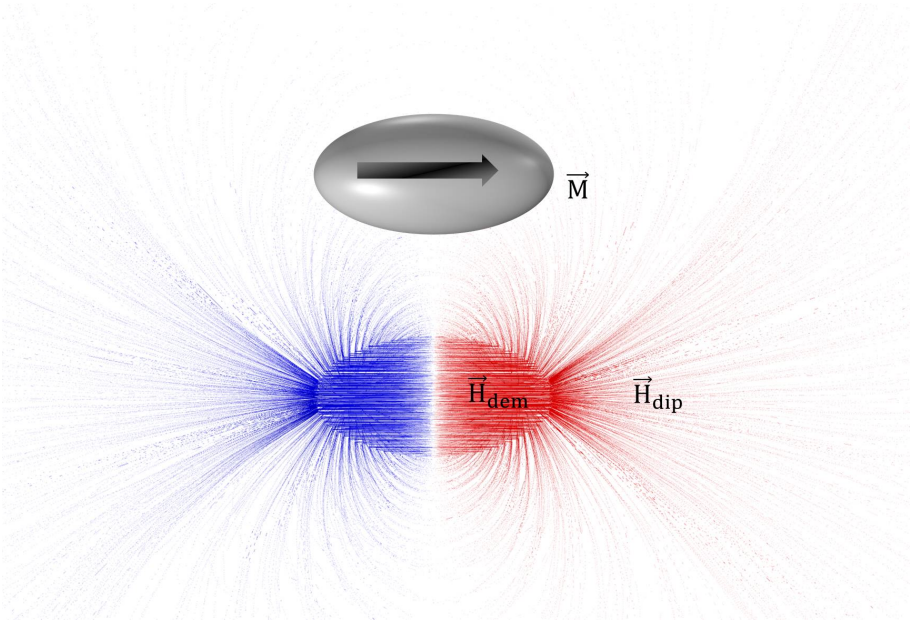

Figure 3.6: Simulated dipolar and demagnetizing fields in a 3D ellipsoidal object, using the Comsol Multiphysics® model developed in this work (further detailed in the next chapters). The dipolar field results from the long-range interaction between magnetic moments, while the demagnetizing field arises from the internal distribution of magnetization within the ellipsoid. These simulations provide insights into the spatial variation of magnetic fields and their influence on magnetization dynamics.

3.3.5 Magnetoelastic anisotropy

The magnetoelastic energy, as discussed in the introduction, arises when a magnetic object is subjected to mechanical stress. This stress induces a lattice deformation, leading to the emergence of magnetocrystalline anisotropy. Figure 3.7 illustrates this effect schematically, distinguishing between the direct and inverse magnetoelastic effects.

- Direct effect: When the magnetization orientation changes under an applied magnetic field, the dimensions of an initially isotropic object are modified. If the magnetostriction coefficient λ is positive, the object undergoes a small elongation along the magnetization direction, while it contracts along the other two axes.

- Inverse effect: When mechanical stress is applied, the magnetization rotates towards the direction of applied strain (for positive λ). The resulting strain is significantly larger than in the direct effect—typically 0% to 0.2% in the elastic regime, compared to $\sim$ 0.001% for the direct effect.

The magnetoelastic energy density in the elastic regime is given by:

$$F_{me} = \underline{\underline{\varepsilon}}^{el} : \underline{\underline{\underline{\underline{C}}}} : \underline{\underline{\varepsilon}}^{el} = \varepsilon_{ij}^{el}\sigma_{ij} \tag{3.23}$$

where $\underline{\underline{\underline{\underline{C}}}}$ is the elastic constants tensor and σ_{ij} are the components of the stress tensor. This expression accounts for both the direct and inverse magnetoelastic effects, through the elastic strain:

$$\underline{\underline{\varepsilon}}^{el} = \underline{\underline{\varepsilon}} - \underline{\underline{\varepsilon}}^{m} \tag{3.24}$$

where the magnetostrictive strain tensor $\underline{\underline{\varepsilon}}^{m}$ in a cubic crystal is expressed as:

$$\underline{\underline{\varepsilon}}^{m} = \frac{3}{2}\left[\lambda_{100}\begin{pmatrix} m_x^2 - \frac{1}{3} & m_x m_y & m_x m_z \\ m_x m_y & m_y^2 - \frac{1}{3} & m_y m_z \\ m_x m_z & m_y m_z & m_z^2 - \frac{1}{3} \end{pmatrix} + (\lambda_{111} - \lambda_{100})\begin{pmatrix} 0 & m_x m_y & m_x m_z \\ m_x m_y & 0 & m_y m_z \\ m_x m_z & m_y m_z & 0 \end{pmatrix}\right] \tag{3.25}$$

with λ_{100} and λ_{111} the magnetoelastic constants and ε_m the strain tensor induced by the magnetization in the case of a cubic crystal.

Magnetoelastic Energy in Terms of Magnetoelastic Coupling Coefficients

More generally, the magnetoelastic energy density F_{me} can also be expressed in terms of the magnetoelastic coupling coefficients B_i. In the case of a cubic crystal, the magnetoelastic anisotropy energy is often given by [22]:

$$\begin{aligned} F_{me} = {} & B_1\left(\alpha_1^2\varepsilon_1 + \alpha_2^2\varepsilon_2 + \alpha_3^2\varepsilon_3\right) \\ & + B_2\left(\alpha_2\alpha_3\varepsilon_4 + \alpha_1\alpha_3\varepsilon_5 + \alpha_1\alpha_2\varepsilon_6\right) + B_3(\varepsilon_1 + \varepsilon_2 + \varepsilon_3) \end{aligned} \tag{3.26}$$

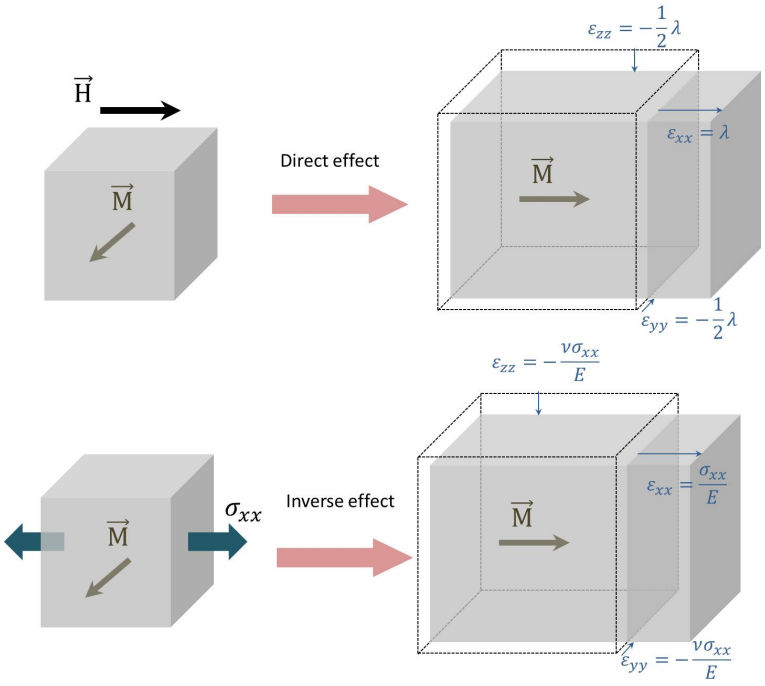

Figure 3.7: Schematic representation of the direct an indirect magnetoelastic effects occurring in a 3D isotropic object.

where: α_1, α_2, α_3 are the magnetization direction cosines; ε_1, ε_2 and ε_3 are the normal strain components; ε_4, ε_5 and ε_6 are the shear strain components; B_1, B_2 and B_3 are the magnetoelastic coupling coefficients.

The parameters α_i represent the direction cosines of the magnetization relative to the cubic axes, while the strains ε_i are measured along these axes. The magnetoelastic energy is typically expressed in terms of magnetostriction coefficients, which requires establishing relationships between magnetostrictive strains, magnetoelastic coupling coefficients, and elastic constants. When stress is applied, the crystal deforms until the magnetoelastic energy F_{me} is in equilibrium with the elastic energy F_{el} (defined in the previous chapter). The equilibrium strains are obtained by minimizing the total energy:

$$F_{tot} = F_{me} + F_{el} \tag{3.27}$$

which leads to the following equations:

$$\frac{\partial E_{tot}}{\partial \varepsilon_1} = C_{11}\varepsilon_1 + C_{12}(\varepsilon_2 + \varepsilon_3) + B_1\alpha_1^2 + B_3 = 0 \tag{3.28}$$

$$\frac{\partial E_{tot}}{\partial \varepsilon_2} = C_{11}\varepsilon_2 + C_{12}(\varepsilon_1 + \varepsilon_3) + B_1\alpha_2^2 + B_3 = 0 \tag{3.29}$$

$$\frac{\partial E_{tot}}{\partial \varepsilon_3} = C_{11}\varepsilon_2 + C_{12}(\varepsilon_1 + \varepsilon_3) + B_1\alpha_3^2 + B_3 = 0 \tag{3.30}$$

$$\frac{\partial E_{tot}}{\partial \varepsilon_4} = C_{44}\varepsilon_4 + B_2\alpha_2\alpha_3 = 0 \tag{3.31}$$

$$\frac{\partial E_{tot}}{\partial \varepsilon_5} = C_{44}\varepsilon_5 + B_2\alpha_1\alpha_3 = 0 \tag{3.32}$$

$$\frac{\partial E_{tot}}{\partial \varepsilon_6} = C_{44}\varepsilon_6 + B_2\alpha_1\alpha_2 = 0 \tag{3.33}$$

When equations 3.28, 3.29 and 3.30 are added together, a homogeneous expansion Δ is obtained. This expansion is independent of the magnetization direction cosines and represents a fundamental change in the volume of the ferromagnet.

$$\Delta = \varepsilon_1 + \varepsilon_2 + \varepsilon_3 = \frac{-B_1 + 3B_3}{C_{11} + 2C_{12}} \tag{3.34}$$

If we neglect this variation, we find:

$$\varepsilon_{1,2,3} = \frac{-B_1\alpha_{1,2,3}^2}{C_{11} - C_{12}} - C_{12}\Delta \simeq \frac{-B_1\alpha_{1,2,3}^2}{C_{11} - C_{12}} \tag{3.35}$$

$$\varepsilon_{4,5,6} = \frac{-B_2\alpha_{2,1,1}\alpha_{3,3,2}}{C_{44}} \tag{3.36}$$

We then introduce the direction cosines (β_1, β_2 and β_3) between the cubic crystal and the crystallographic axes. The relative variation is given by:

$$\frac{\delta\ell}{\ell} = \sum_{i,j} \varepsilon_{ij}\beta_i\beta_j \tag{3.37}$$

The following relation is deduced:

$$\begin{aligned}\frac{\delta\ell}{\ell} = {} & \frac{-B_1}{C_{11} - C_{12}}\left(\alpha_1^2\beta_1^2 + \alpha_2^2\beta_2^2 + \alpha_3^2\beta_3^2 - \frac{1}{3}\right) \\ & + \frac{-B_2}{C_{44}}(\alpha_2\alpha_3\beta_2\beta_3 + \alpha_1\alpha_3\beta_1\beta_3 + \alpha_1\alpha_2\beta_1\beta_2)\end{aligned} \tag{3.38}$$

We found the well known magnetostrictive coefficients (λ_{100} and λ_{111}) as function of the coefficients B_1 and B_2 by evaluating the above equation when the crystal is respectively magnetized along $< 100 >$ and $< 111 >$:

$$\lambda_{100} = -\frac{2}{3}\frac{B_1}{C_{11} - C_{12}} \tag{3.39}$$

and

$$\lambda_{111} = -\frac{B_2}{3C_{44}} \tag{3.40}$$

These expressions highlight the influence of the elastic properties of the material on magnetostriction and confirm the central role of the magnetoelastic coupling coefficients B_1 and B_2 in describing magnetoelastic anisotropy. They are widely used in the modeling of ferromagnetic materials to predict their response to mechanical stress and their behavior in applications such as energy conversion, spin-wave control, and magnetoelastic sensors.

3.4 Propagating and non propagating spin waves

In this work, magnetic samples are characterized using two complementary techniques that provide information on the spin precession frequency. Ferromagnetic resonance (FMR) is used to probe non-propagating spin-wave modes, while Brillouin light scattering (BLS) allows the characterization of propagating spin-wave energies. Since results are obtained on both continuous media and nanostructured samples, special effort is made to predict the magnetic behavior across different geometries. This is achieved through micromagnetic simulations and macrospin modeling, which are systematically compared with experimental data to enhance the understanding of spin-wave dynamics.

3.4.1 Magnetostatic formulation for spin precession

In most cases the study of spin precession is limited to the linear regime corresponding to small harmonic oscillations. This consideration is almost always valid, because the nonlinear regime is only achieved when forced using a strong enough excitation field or perturbation. In the linear regime we can consider that:

$$\vec{m}(x, y, z, t) = \begin{pmatrix} 1 \\ m_y e^{i\omega t} \\ m_z e^{i\omega t} \end{pmatrix} \tag{3.41}$$

if we consider a saturated magnetization along the x-axis. Here ω is the pulsation of the spin precession. Thus, the magnetization along the x-axis remains constant over time, meaning that the magnetization norm is $\|\vec{m}\| \geq 1$, which is not really problematic for small angles (for a precession cone angle of 5° the norm would be less than 1.01). This approximation allows one to write the total magnetization and the field contributions as the sum of a static part and a dynamic part such as:

$$\vec{m}(x, y, z, t) = \vec{m}_0(x, y, z) + \widetilde{\vec{m}}(x, y, z, t) \tag{3.42}$$

$$\vec{H}(x, y, z, t) = \vec{H}_0(x, y, z) + \widetilde{\vec{h}}(x, y, z, t) \tag{3.43}$$

with

$$\widetilde{\vec{m}}(x, y, z, t) = \vec{m}(x, y, z)e^{i\omega t} \tag{3.44}$$

$$\widetilde{\vec{h}}(x,y,z,t) = \vec{h}(x,y,z)e^{i\omega t} \tag{3.45}$$

at equilibrium, supposing that $\vec{m}_0(x,y,z) \gg \widetilde{\vec{m}}(x,y,z,t)$ and $\vec{H}_0(x,y,z) \gg \widetilde{\vec{h}}(x,y,z,t)$, the Landau-Lifshitz equation becomes :

$$\frac{i\omega}{\gamma}\widetilde{\vec{m}} = -\vec{m}_0 \times \widetilde{\vec{h}}_{eff} - \widetilde{\vec{m}} \times \vec{H}_{0\,eff} \tag{3.46}$$

In practical terms, expressing the vectors in spherical coordinates is more advantageous as many measurement setups and energy terms are dependent on angular parameters. In the spherical coordinate system the magnetization direction defines the radial unit vector such as

$$\vec{m} = \vec{e}_r \tag{3.47}$$

and

$$\frac{d\vec{m}}{dt} = \dot{\theta}\vec{e}_\theta + \dot{\varphi}\sin\theta\vec{e}_\varphi \tag{3.48}$$

which is represented in figure 3.8 (left).

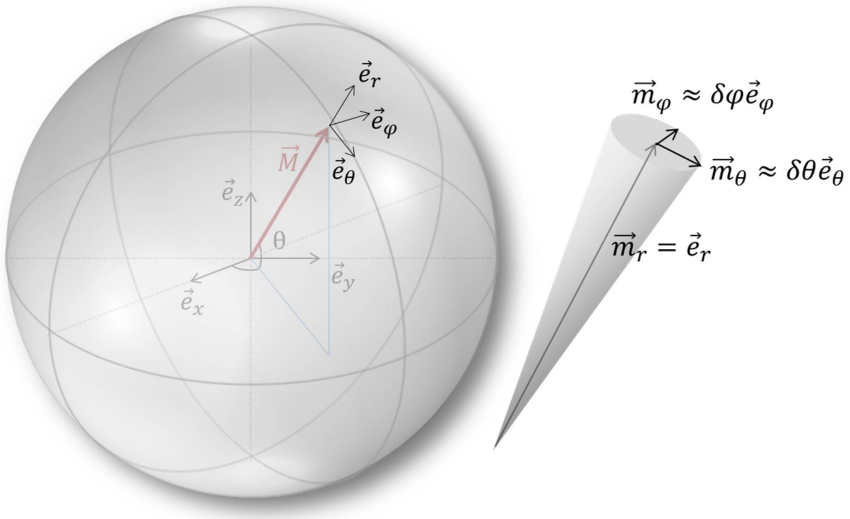

Figure 3.8: Scheme of the magnetization unit vectors in the spherical coordinate system (left). The cone on the right illustrates the decomposition of the magnetization unit vector into its spherical components $\vec{m}_\varphi$, $\vec{m}_\theta$ and $\vec{m}_r$. In the case of small variations of the angles θ and φ denoted as $\delta\theta$ and $\delta\varphi$ respectively, the perturbation of the magnetization is shown within the precession cone, highlighting the contribution of each component.

By neglecting the effect of damping, the LLG becomes:

$$\frac{1}{\gamma}\begin{pmatrix} 0 \\ \dot{\theta} \\ \dot{\varphi}\sin\theta \end{pmatrix} = \frac{1}{\gamma}\begin{pmatrix} 0 \\ i\omega\delta\theta(t) \\ i\omega\delta\varphi(t)\sin\theta \end{pmatrix} = \frac{1}{\mu_0 M_s}\begin{pmatrix} 0 \\ -\frac{1}{\sin\theta}\frac{\partial F}{\partial\varphi} \\ \frac{\partial F}{\partial\theta} \end{pmatrix} \tag{3.49}$$

Let us now define the equilibrium angles of the magnetization as θ_0 and φ_0 such as:

$$\frac{\partial F}{\partial \theta} = \frac{\partial F}{\partial \varphi} = 0 \tag{3.50}$$

for these equilibrium angles and:

$$\begin{cases} \theta = \theta_0 + \delta\theta e^{i\omega t} \\ \varphi = \varphi_0 + \delta\varphi e^{i\omega t} \end{cases} \tag{3.51}$$

$\theta = \theta_0 + \delta\theta$. We can write the Taylor expansion of the energy as:

$$F(\theta, \varphi) = F(\theta_0, \varphi_0) + \frac{1}{2}\left(\frac{\partial^2 F(\theta_0, \varphi_0)}{\partial \theta^2}\theta^2 + \frac{\partial^2 F(\theta_0, \varphi_0)}{\partial \varphi^2}\varphi^2 + 2\frac{\partial^2 F(\theta_0, \varphi_0)}{\partial \theta \partial \varphi}\theta\varphi\right) \tag{3.52}$$

$$\begin{cases} \frac{\partial F}{\partial \theta} = -i\omega\frac{\mu_0 M_s}{\gamma}\delta\theta \sin\theta = \frac{\partial^2 F(\theta_0,\varphi_0)}{\partial \theta^2}\delta\theta + \frac{\partial^2 F(\theta_0,\varphi_0)}{\partial \theta \partial \varphi}\delta\varphi \\ \frac{\partial F}{\partial \varphi} = i\omega\frac{\mu_0 M_s}{\gamma}\delta\varphi \sin\theta = \frac{\partial^2 F(\theta_0,\varphi_0)}{\partial \varphi^2}\delta\varphi + \frac{\partial^2 F(\theta_0,\varphi_0)}{\partial \theta \partial \varphi}\delta\theta \end{cases} \tag{3.53}$$

Solving this pair of equations allows one to easily express $\delta\theta$ and $\delta\varphi$. The final expression we obtain for the precession pulsation is:

$$\omega = \frac{\gamma}{\mu_0 M_s \sin\theta}\sqrt{\frac{\partial^2 F(\theta_0, \varphi_0)}{\partial \theta^2}\frac{\partial^2 F(\theta_0, \varphi_0)}{\partial \varphi^2} - \left(\frac{\partial^2 F(\theta_0, \varphi_0)}{\partial \theta \partial \varphi}\right)^2} \tag{3.54}$$

This expression known as the Smit-Beljers equation (or as the Smit-Suhl equation) [24, 25] is used for analytical macrospin modeling of ferromagnetic resonance, especially in the in plane configuration ($\theta = \frac{\pi}{2}, \varphi = 0$):

$$\omega = \gamma\mu_0\sqrt{H\left(H + M_s\right)} \tag{3.55}$$

and in the out-of-plane configuration ($\theta = 0, \varphi = 0$) where the singularity has to be removed in order to obtain the following expression:

$$\omega = \gamma\mu_0\left(H - M_s\right) \tag{3.56}$$

3.4.2 Spin wave formulation in continuous media

The Smit-Beljers equation describes precisely the behavior of non-propagating spin waves in continuous media, but one of the key aspects of spin waves (as all waves), is that they can propagate over space. This is made possible thanks to both the dipolar field and the anisotropy field that make the close spin directions interdependent [10, 11, 12, 13, 26].

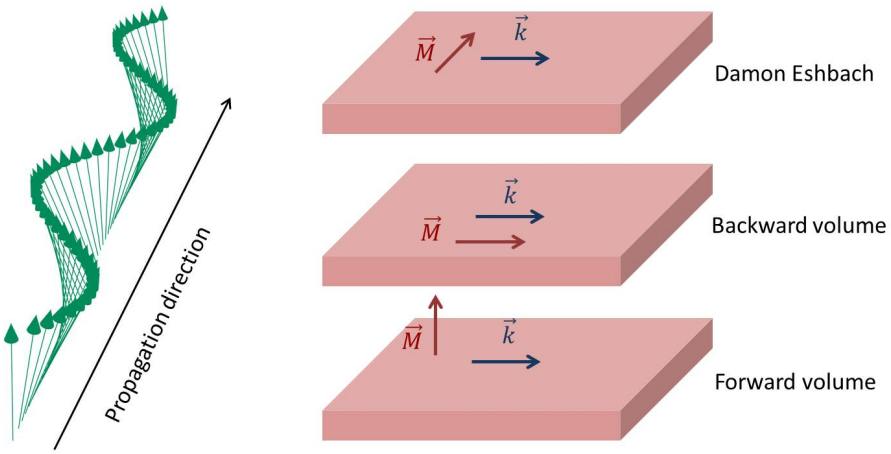

Figure 3.9: Spin waves are collective magnetization oscillations whose propagation depends on the relative orientation of the wave vector $\vec{k}$ and the magnetization $\vec{M}$. On the left, the schematic illustrates spin wave propagation, where each arrow represents an individual magnetic moment precessing collectively.On the right, the diagram shows the three main spin wave configurations: the backward volume mode ($\vec{k} \parallel \vec{M}$), the Damon-Eshbach mode ($\vec{k} \perp \vec{M}$, surface-localized), and the forward volume mode ($\vec{k} \perp \vec{M}$, bulk-propagating).

This propagation can be defined for the spin waves but also for the local effective field as the dipolar field will contain a small dynamical part that is carried away by the spin wave. It is, in this sense, convenient to define a potential for the dipolar field such as:

$$\vec{h}_{dip} = \vec{\nabla}\left(\phi e^{i\omega t - \vec{k}.\vec{r}}\right) \tag{3.57}$$

Incorporating this dynamical component for the effective magnetic field adds up a new wave vector dependency for the spin waves frequencies. The vectorial nature of the magnetization field makes the spin wave dispersion highly dependent on the angle between the magnetization direction and the spin wave propagation direction, hence it is convenient to define typical configurations as presented in figure 3.9.

3.4.2.1 Damon Eshbach configuration

The so-called Damon-Eshbach (DE) spin waves are surface waves propagating perpendicularly to the in-plane magnetization ($\vec{k} \perp \vec{m}$) . This mode is assimilated with the uniform mode when the wave vector is equal to zero. The DE frequency can be written as [27]:

$$\left(\frac{\omega_{DE}}{\mu_0 \gamma}\right)^2 = H\left(H + M_s\right) + \frac{M_s^2}{4}\left(1 - e^{-2kd}\right) \tag{3.58}$$

This kind of propagation configuration leads to an inhomogeneous profile as the wave amplitude is evanescent over the surface of the sample.

3.4.2.2 Backward volume configuration

As opposite to the DE configuration, the spin waves in the backward volume (BV) configuration are volume waves that have an symmetrical profile over the thickness of the film and propagates in the direction of the magnetization orientation ($\vec{k} \parallel \vec{m}$). Similarly to the previous configuration this wave is assimilated to the uniform mode when the wave vector is equal to 0. The analytical formula for the BV spin wave frequency can be written as:

$$\left(\frac{\omega_{BV}}{\mu_0 \gamma}\right)^2 = H^2 + \frac{HM_s\left(1 - e^{-kd}\right)}{kd} \tag{3.59}$$

3.4.2.3 Forward volume configuration

The forward volume mode (FV) propagates perpendicularly to the magnetization direction when saturated out-of-plane [28]. This mode is rarely studied and will also be ignored through this work. The analytical formula for the FV spin wave frequency can be written as:

$$\left(\frac{\omega_{BV}}{\mu_0 \gamma}\right)^2 = H^2 + HM_s\left(1 - \frac{\left(1 - e^{-kd}\right)}{kd}\right) \tag{3.60}$$

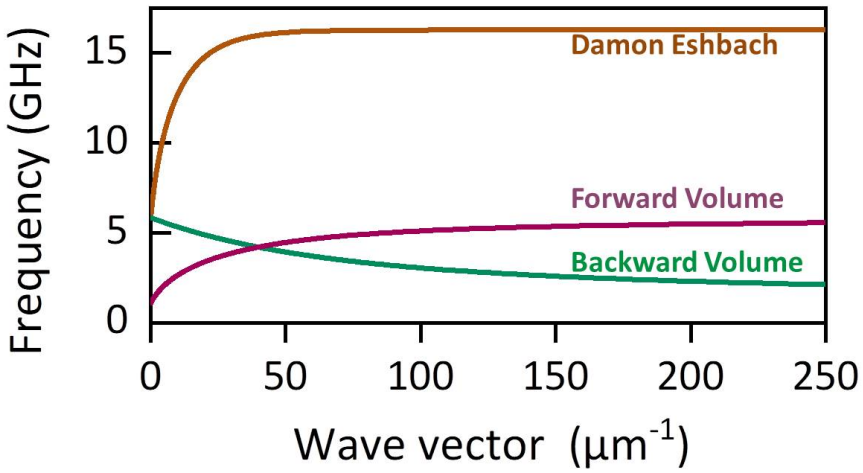

Figure 3.10: pin wave dispersion of the forward volume, backward volume, and Damon-Eshbach modes in continuous ferromagnetic films. The dispersion relations are computed using the parameters: $\gamma = 1.95{\times}10^{11}$rad.Hz.T^{-1} , $M_s = 7.8{\times}10^5 A.m^{-1}$, $\mu_0 H = 35$ mT and a film thickness of $d = 40$ nm.

These three spin wave modes are represented in the dispersion diagram in figure [3.10. As observed in the experimental results, the energies of these spin waves can be tuned by applying a static strain to the ferromagnetic medium. For instance, Karboul et al. studied

the variation of the Damon-Eshbach (DE) mode under the effect of a static strain applied to a thin nickel film [29]. This energy shift is attributed to the magnetoelastic energy induced by the strain, which modifies the effective field in the Landau-Lifshitz-Gilbert (LLG) equation. As a result, the energies of these propagating spin wave modes can be controlled by adjusting the applied strain, offering potential for strain-mediated magnonic devices.

3.5 Interaction with phonons

The coupling between magnons and phonons originates from magnetoelastic interactions [30] and involves both direct and inverse magnetostriction. When dynamic magnetization varies, it induces dynamic stress in the material due to the magnetostrictive effect. Simultaneously, the strain associated with an acoustic wave produces a dynamic magnetic field, illustrating the inverse magnetostrictive effect. If the frequency and wavelength of the stress induced by the spin wave match those of the magnetic field generated by the acoustic wave, the resonance condition for dynamic magnetostrictive coupling is fulfilled. This interaction between magnons and phonons has been studied in semi-infinite films, notably by Kittel [30, 31]. In this work, we investigate such coupling in thin films and arrays of nanostructures. The following equations illustrate the mechanisms governing the interaction between acoustic waves and spin waves, providing a theoretical framework for understanding the dynamics of coupled systems.

3.5.1 Coupled equations for magnon-phonon interaction

For a spin wave propagating along the x-direction (with saturation magnetization aligned along z), the Landau-Lifshitz-Gilbert (LLG) equation leads to the following system:

$$\frac{1}{\gamma}\frac{\partial m_x}{\partial t} = \mu_0 H m_y - \frac{2A}{M_S}\frac{\partial^2 m_y}{\partial x^2} \tag{3.61}$$

$$\frac{1}{\gamma}\frac{\partial m_y}{\partial t} = -\mu_0 H m_x + \frac{2A}{M_S}\frac{\partial^2 m_x}{\partial x^2} \tag{3.62}$$

Similarly, for an acoustic wave propagating along x, characterized by the displacement field u_z, the equation of mechanical motion is given by:

$$\rho\frac{\partial^2 u_z}{\partial t^2} = C\frac{\partial^2 u_z}{\partial x} \tag{3.63}$$

Where C is a component of the elastic tensor. When magnetoelastic anisotropy is considered, the LLG equation and the mechanical wave equation become coupled:

$$\frac{1}{\gamma}\frac{\partial m_y}{\partial t} = -\mu_0 H m_x + \frac{2A}{M_S}\frac{\partial^2 m_x}{\partial x^2} - \gamma B\frac{\partial u_z}{\partial x} \tag{3.64}$$

and

$$\rho\frac{\partial^2 u_z}{\partial t^2} = C\frac{\partial^2 u_z}{\partial x} + \frac{B}{M_S}\frac{\partial m_x}{\partial x} \tag{3.65}$$

These coupled equations illustrate the bidirectional interaction between spin waves and acoustic waves, demonstrating how they can influence each other's dynamics [30, 31].

3.5.2 Physical interpretation and applications

The above equations highlight how a propagating spin wave induces an elastic strain field through the magnetostrictive effect. In turn, this strain modifies the effective magnetic field, leading to a feedback effect that alters the spin wave propagation. This reciprocal interaction is key to understanding how magnons and phonons couple in structured materials. In continuous thin films, such interactions lead to hybrid magnon-phonon modes, which can be detected experimentally through techniques like Brillouin light scattering (BLS). In nanostructured systems, the geometry and periodicity of the structures play a crucial role in defining the strength and nature of the coupling.

Controlling magnon-phonon interactions has significant implications for magnonics and phononics, where strain-mediated effects can be used to tune spin-wave dispersion and even enable strain-based logic devices. By engineering magnetoelastic coupling, it is possible to design reconfigurable magnonic circuits, where external strain can be used to modulate spin-wave propagation without the need for additional magnetic fields. Moreover, these interactions can be harnessed in hybrid quantum systems, where magnons serve as an interface for phonon-mediated information transfer in quantum technologies. The ability to dynamically control spin-wave behavior through acoustic excitations opens new avenues for strain-controlled magnonic transistors, phonon-driven magnonic memory, and energy-efficient computing devices.

3.6 Spin waves in a periodic medium: magnonic crystals

As discussed in the introduction, when the magnetic properties or the geometry of a material are periodically modulated, the propagation of spin waves is significantly altered, giving rise to magnonic crystals. These structures, analogous to photonic or electronic crystals, exhibit band gaps where certain spin-wave frequencies are forbidden. In the following, we introduce the magnonic character of such periodic media using a simplified approach based on the Landau-Lifshitz-Gilbert (LLG) equation in two-dimensional magnonic crystals [10, 32, 33, 34].

We consider a thin ferromagnetic layer, uniformly magnetized along the x-direction, and neglect the exchange interaction, assuming a sufficiently small wave vector k. Under these conditions, the linearized LLG equation takes the form:

$$\begin{aligned} i\left(\tfrac{\omega}{\mu_0 H\gamma}\right) m_y - m_z + \left(\tfrac{M_S}{H}\right) h_z &= 0 \\ i\left(\tfrac{\omega}{\mu_0 H\gamma}\right) m_z + m_y - \left(\tfrac{M_S}{H}\right) h_y &= 0 \end{aligned} \tag{3.66}$$

where we assume a perturbative approach, writing the magnetization as:

$$\vec{m}(x, y, z, t) = \vec{m}_0(x, y, z) + \widetilde{\vec{m}}(x, y, z, t) \tag{3.67}$$

with

$$\left\|\widetilde{\vec{m}}(\vec{r},t)\right\| \ll \left\|\vec{m}_0(\vec{r})\right\| \tag{3.68}$$

and an oscillatory solution of the form:

$$\widetilde{\vec{m}}(\vec{r},t) = \vec{m}(\vec{r})e^{i\left(\omega t - \vec{k}\cdot\vec{r}\right)} \tag{3.69}$$

Similarly, we assume a magnetic potential of the form:

$$\phi(z,t) = \phi(z)e^{i\left(\omega t - \vec{k}\cdot\vec{r}\right)} \tag{3.70}$$

From this formalism, we can recover the expressions for Damon-Eshbach (DE) modes and Backward Volume (BV) modes in continuous films by solving the system of equations.

3.6.1 Periodic structures and spin-wave band gaps

In an approximate approach, we can determine forbidden frequency bands for spin waves by considering that the magnetic parameters of the medium—such as $\vec{m}(\vec{r},t)$ and $\phi(\vec{r},t)$—are periodic functions of the in-plane position vector:

$$\vec{r} = (x,y) - \text{for bi-dimensional magnonic crystals} \tag{3.71}$$

$$\vec{r} = (x,0) - \text{for uni-dimensional magnonic crystals} \tag{3.72}$$

with a lattice periodicity given by:

$$\vec{R} = n_1\vec{a}_1 + n_2\vec{a}_2 \tag{3.73}$$

where $\vec{R}$ is an arbitrary translation vector of the Bravais lattice; $\vec{a}_1$ and $\vec{a}_2$ are the primitive vectors of the lattice while n_1 and n_2 are integers. This periodicity allows us to express:

$$\begin{aligned}\vec{m}(\vec{r}+\vec{R}) &= \vec{m}(\vec{r})\\ \phi(\vec{r}+\vec{R}) &= \phi(\vec{r})\end{aligned} \tag{3.74}$$

Since these functions are periodic, they can be expanded in a Fourier series:

$$\begin{aligned}\vec{m}(\vec{r}) &= \textstyle\sum_{\vec{G}_p} \vec{m}(\vec{G}_p)e^{i\vec{G}_p\cdot\vec{r}}\\ \phi(\vec{r}) &= \textstyle\sum_{\vec{G}_p} \phi(\vec{G}_p)e^{i\vec{G}_p\cdot\vec{r}}\end{aligned} \tag{3.75}$$

Where $\vec{G}_p$ represents a reciprocal lattice vector, defined as:

$$\vec{G}_p = p_1\vec{b}_1 + p_2\vec{b}_2 \tag{3.76}$$

where $\vec{b}_1$ and $\vec{b}_2$ are the basis vectors of the reciprocal lattice, satisfying:

$$\vec{a}_i \cdot \vec{b}_j = 2\pi\delta_{ij} \tag{3.77}$$

3.6.2 Bloch theorem and spin-wave band gaps

The Bloch wave vector $\vec{k} = (k_x, k_y)$ describes spin waves in a periodic magnetic structure. According to Bloch's theorem, the spin-wave solutions can be expressed as Bloch functions, meaning that the spin waves can be restricted to the first Brillouin zone without loss of generality. Indeed, in periodic media, the interplay between wave interference and periodicity leads to the formation of band structures, similar to those found in electronic crystals. In such systems, Bragg reflection occurs when the spin-wave wavelength becomes comparable to the periodicity of the structure, leading to constructive or destructive interference. This results in eigenfrequency splitting, which gives rise to band gaps—frequency ranges where spin-wave propagation is prohibited. These magnonic band gaps are direct analogs of photonic and electronic band gaps, where the propagation of light or electrons is prevented in certain energy ranges due to the periodic potential of the system. In the case of magnonic crystals, the periodic modulation of the magnetic properties (such as saturation magnetization, exchange interaction, or anisotropy) or the geometry (such as periodic arrays of nanostructures) creates an effective periodic potential for spin waves.

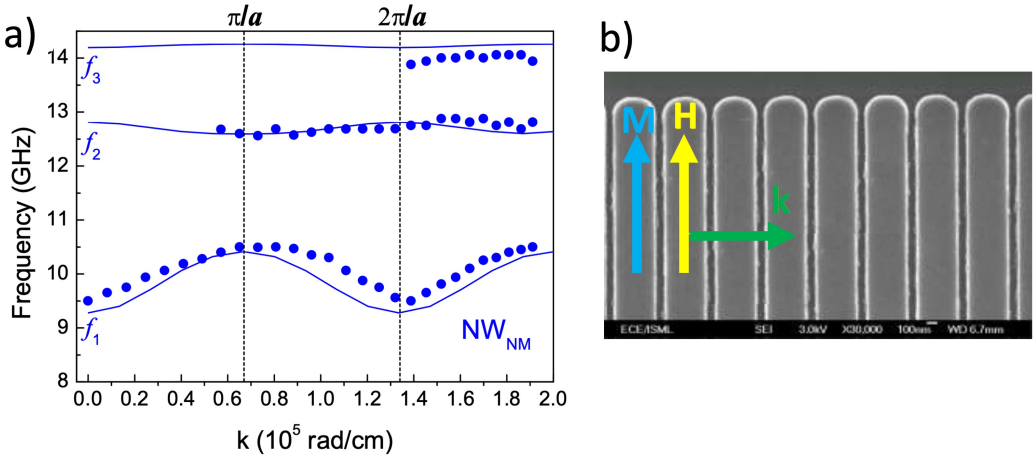

Figure 3.11: Experimental and simulated frequency dispersion for a uniaxial magnonic crystal under an applied field of $\mu_0 H = 500$ mT. The experimental data (symbols) were obtained using BLS, while the simulated dispersion curves (solid lines) were computed using micromagnetic modeling. The vertical dashed lines indicate the first two Brillouin zones, highlighting the periodicity-induced modifications in the spin-wave spectrum. Figures adapted from [35].

3.6.3 Experimental observations and computed results

To illustrate these periodic phenomena, we present in figure 3.11 the experimental results obtained by Gubbiotti et al. [35] for a one-dimensional magnonic crystal, consisting of a permalloy nanowire array with a width of 350 nm and a periodicity of 470 nm, as shown in figure 3.11-b). The experimental data, measured *via* Brillouin light scattering (BLS), are

shown as symbols in figure 3.11-a), while the computed magnonic dispersion curves, obtained using a method similar to the one discussed earlier, are shown as solid lines. The presence of Brillouin zones in the dispersion is a clear signature of the periodicity-induced magnonic behavior, fundamentally modifying the spin-wave excitations in the crystal.

To illustrate these periodic phenomena, we present in figure 3.11 the experimental results obtained by Gubbiotti et al. [35] for a one-dimensional magnonic crystal, consisting of a permalloy nanowire array with a width of 350 nm and a periodicity of 470 nm, as shown in figure 3.11-b). The experimental data, measured via Brillouin light scattering (BLS), are represented by symbols in figure 3.11-a), while the computed magnonic dispersion curves, obtained using a Fourier-based method, are shown as solid lines. The clear periodicity observed in the dispersion relations is a hallmark of magnonic band formation, demonstrating the influence of artificial structuring on spin-wave propagation. One of the most striking features in the experimental data is the presence of Brillouin zones, which indicate periodicity-induced band gaps in the spin-wave spectrum. These zones alter the natural dispersion relation of spin waves, leading to modifications in group velocity, wavelength selectivity, and mode hybridization. Such effects are crucial for tailoring spin-wave transport properties in magnonic devices. Additionally, the agreement between theoretical predictions and experimental results highlights the reliability of current micromagnetic modeling techniques. These computational approaches, based on solving the LLG equation in periodic media, allow us to predict and optimize magnonic band structures, ensuring that experimental designs meet targeted frequency response requirements.

3.6.4 Interplay between periodicity and magnetic coupling

However, simply arranging magnetic objects periodically does not automatically result in a magnonic crystal [120]. The elements must be sufficiently interconnected magnetically, either through: i) dipolar interactions, or ii) a thin magnetic layer acting as a coupling medium.

To illustrate this, we present BLS measurements from this thesis on modulated nanowire arrays (SEM image in figure 3.12-a). These arrays are analyzed under a 50 mT applied field along the long axis of the nanowires, allowing us to probe transverse spin wave propagation. A typical BLS spectrum at $k = 19.35\ \mu\text{m}^{-1}$ is shown in figure 3.12-b), while the full experimental dispersion is presented in figure 3.12-c). Notably, the observed spin-wave modes appear nearly dispersionless, suggesting quantized modes in the nanowire cross-section. Our initial objective was to identify potential magnonic effects from the nanowire cross-section modulation, as shown in figure 3.12-d). When a 100 mT saturating field is applied along the nanowire cross-section, we observe a weak effect near the first Brillouin zone ($10\ \mu\text{m}^{-1}$), indicating a pseudo-magnonic behavior, albeit less pronounced than in figure 3.11.

In summary, while periodicity is essential for magnonic behavior, it is not sufficient. The elements must be strongly coupled, as demonstrated by our BLS measurements on modulated nanowire arrays, where we observed nearly dispersionless modes and a slight pseudo-magnonic effect.

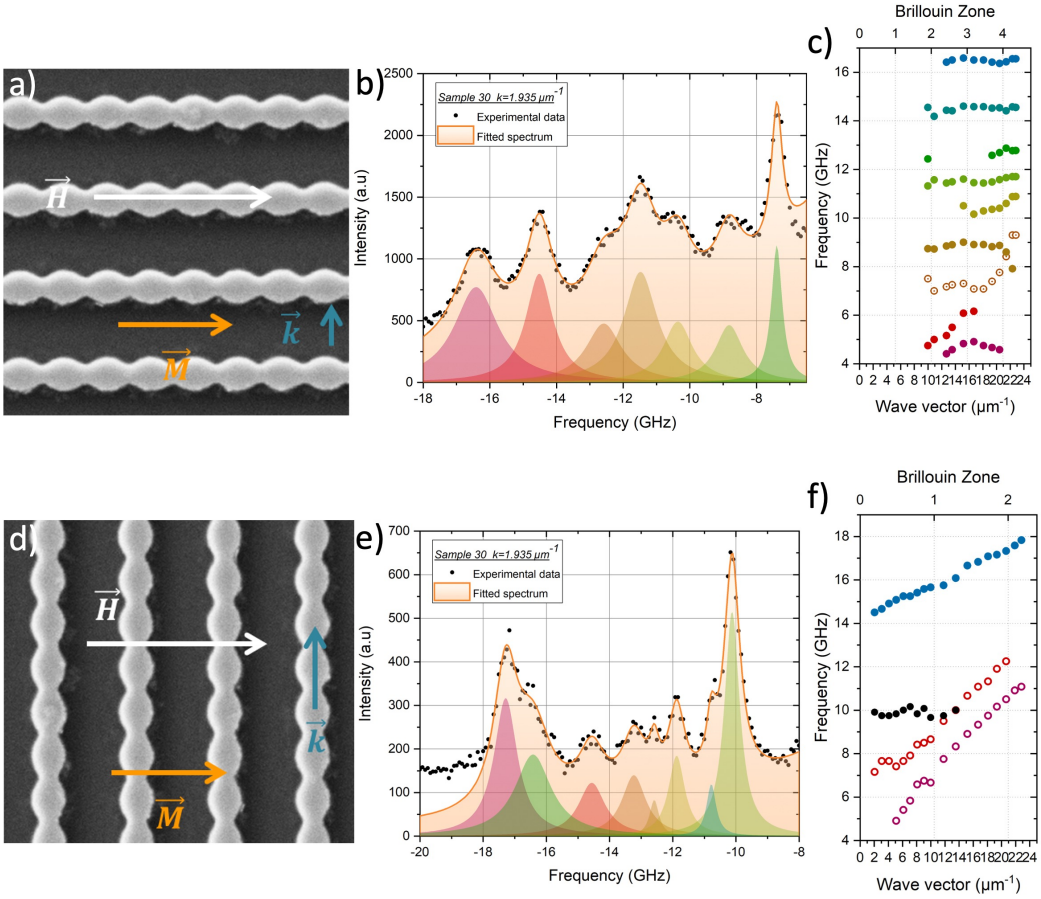

Figure 3.12: a), d) SEM images showing the array of modulated nanowires and the experimental configuration used for Brillouin light scattering (BLS) measurements. (b, e) Typical anti-Stokes BLS spectra (symbols). The orange region under the spectrum represents a fit using multiple Lorentz-Gaussian functions, with individual peaks highlighted in different colors (ranging from red to green). (c) Spin-wave dispersion relation obtained under an applied field of $\mu_0 H = 100$ mT. The vertical dashed lines indicate the first two Brillouin zones, emphasizing the influence of periodicity on the spin-wave behavior.

Bibliography

[1] Getzlaff, M. (2007). Fundamentals of magnetism. Springer Science & Business Media 3.1

[2] Coey, J. M. D. (1978). Amorphous magnetic order. Journal of Applied Physics, 49(3), 1646-1652 3.1

[3] Gilbert, T. L. (2004). A phenomenological theory of damping in ferromagnetic materials. IEEE transactions on magnetics, 40(6), 3443-3449 3.2

[4] Landau, L. A. L. E., & Lifshitz, E. (1935). On the theory of the dispersion of magnetic permeability in ferromagnetic bodies. Phys. Z. Sowjetunion, 8(153), 101-114 3.2

[5] Slonczewski, J. C. (1996). Current-driven excitation of magnetic multilayers. Journal of Magnetism and Magnetic Materials, 159(1-2), L1-L7 3.2

[6] Giordano, A., Finocchio, G., Torres, L., Carpentieri, M., & Azzerboni, B. (2012). Semi-implicit integration scheme for Landau–Lifshitz–Gilbert-Slonczewski equation. Journal of Applied Physics, 111(7) 3.2

[7] Böttcher, D., & Henk, J. (2012). Significance of nutation in magnetization dynamics of nanostructures. Physical Review B—Condensed Matter and Materials Physics, 86(2), 020404 3.2

[8] Thibaudeau, P., & Nicolis, S. (2021). Emerging magnetic nutation. The European Physical Journal B, 94, 1-8 3.2

[9] Li, Y., Naletov, V. V., Klein, O., Prieto, J. L., Muñoz, M., Cros, V., ... & De Loubens, G. (2019). Nutation spectroscopy of a nanomagnet driven into deeply nonlinear ferromagnetic resonance. Physical Review X, 9(4), 041036 3.2

[10] Demokritov, S. O., & Slavin, A. N. (Eds.). (2012). Magnonics: From fundamentals to applications (Vol. 125). Springer Science & Business Media 3.3, 3.4.2, 3.6

[11] Coey, J. M. (2010). Magnetism and magnetic materials. Cambridge university press 3.3, 3.3.3, 3.3.3, 3.4.2

[12] Gurevich, A. G., & Melkov, G. A. (2020). Magnetization oscillations and waves. CRC press 3.3, 3.4.2

[13] Morrish, A. H. (2001). The Physical Principles of Magnetism 3.3, 3.4.2

[14] Iwahara, N., & Chibotaru, L. F. (2015). Exchange interaction between J multiplets. Physical Review B, 91(17), 174438 3.3.1

[15] Moriya, T. (1960). Anisotropic superexchange interaction and weak ferromagnetism. Physical review, 120(1), 91 3.3.1

[16] Kittel, C. (1969). Indirect exchange interactions in metals. Solid state physics, 22, 1-26 3.3.1

[17] Darby, M., & Isaac, E. (1974). Magnetocrystalline anisotropy of ferro-and ferrimagnetics. IEEE Transactions on Magnetics, 10(2), 259-304 3.3.3

[18] Albanese, R., & Rubinacci, G. (1990). Magnetostatic field computations in terms of two-component vector potentials. International journal for numerical methods in engineering, 29(3), 515-532 3.3.4

[19] Osborn, J. A. (1945). Demagnetizing factors of the general ellipsoid. Physical review, 67(11-12), 351 3.3.4

[20] Smith, A., Nielsen, K. K., Christensen, D. V., Bahl, C. R. H., Bjørk, R., & Hattel, J. (2010). The demagnetizing field of a nonuniform rectangular prism. Journal of Applied Physics, 107(10) 3.3.4

[21] Preis, K., Bardi, I., Biro, O., Magele, C., Renhart, W., Richter, K. R., & Vrisk, G. (1991). Numerical analysis of 3D magnetostatic fields. IEEE Transactions on Magnetics, 27(5), 3798-3803

[22] Wedler, G., Walz, J., Greuer, A., & Koch, R. (2000). The magnetoelastic coupling constant B2 of epitaxial Fe (001) films. Surface science, 454, 896-899 3.3.5

[23] Kittel, C. (1949). Physical theory of ferromagnetic domains. Reviews of modern Physics, 21(4), 541

[24] Cherkasskii, M., Barsukov, I., Mondal, R., Farle, M., & Semisalova, A. (2022). Theory of inertial spin dynamics in anisotropic ferromagnets. Physical Review B, 106(5) 3.4.1

[25] Tomczak, P., & Puszkarski, H. (2018). Ferromagnetic resonance in thin films-cross-validation analysis of numerical solutions of Smit-Beljers equation. Application to GaMnAs. arXiv preprint arXiv:1808.01347 3.4.1

[26] Prabhakar, A., & Stancil, D. D. (2009). Spin waves: Theory and applications (Vol. 5). Springer US 3.4.2

[27] Damon, R. W., & Eshbach, J. R. (1961). Magnetostatic modes of a ferromagnet slab. Journal of Physics and Chemistry of Solids, 19(3-4), 308-320 3.4.2.1

[28] Zighem, F., Roussigné, Y., Chérif, S. M., & Moch, P. (2008). Non-conventional interaction contributions in permalloy/NiO composite thin films deduced from their static and dynamic magnetization behavior. Journal of Physics: Condensed Matter, 20(12), 125201 3.4.2.3

[29] Karboul-Trojet, W., Faurie, D., Roussigné, Y., Chérif, S. M., Renault, P. O., & Goudeau, P. (2011). Journal of Physics D: Applied Physics, 44(15), 155002 3.4.2.3

[30] Kittel, C. (1958). Interaction of spin waves and ultrasonic waves in ferromagnetic crystals. Physical Review, 110(4), 836 3.5, 3.5.1

[31] Comstock, R. L., & Auld, B. A. (1963). Journal of Applied Physics, 34(5), 1461-1464 3.5, 3.5.1

[32] Lenk, B., Ulrichs, H., Garbs, F., & Münzenberg, M. (2011). The building blocks of magnonics. Physics Reports, 507(4-5), 107-136 3.6

[33] Rezende, S. M. (2020). Fundamentals of magnonics (Vol. 969, p. 301). Cham: Springer 3.6

[34] Chumak, A. V. (2019). Magnon spintronics: Fundamentals of magnon-based computing. In Spintronics Handbook, Second Edition: Spin Transport and Magnetism (pp. 247-302). CRC Press 3.6

[35] Gubbiotti, G., Xiong, L. L., Montoncello, F., & Adeyeye, A. O. (2017). Collective spin waves in arrays of permalloy nanowires with single-side periodically modulated width. Applied Physics Letters, 111(19) 3.11, 3.6.3, 10.2.3

4 Development of numerical method for fully coupled magneto-mechanical studies

Contents

The numerical simulation of magnetoelastic phenomena remains relatively uncommon in the magnetism community, mainly due to the lack of numerical frameworks capable of handling both complex magnetic and mechanical behaviors simultaneously. Existing studies often focus on simple geometries like continuous films and rely on phenomenological approximations rather than fully coupled models. In this chapter, we present a multiphysics numerical method that fully couples micromagnetism and solid mechanics. Unlike conventional micromagnetic software, which lacks mechanical modeling capabilities,

our approach is implemented in Comsol Multiphysics® [2], requiring the explicit implementation of the LLG equation. We detail the energy contributions involved, along with the boundary conditions essential for accurate simulations. The method accounts for both static strain and dynamic acoustic waves, enabling the study of strain-induced anisotropies and magnon-phonon interactions. This work builds upon Nabil Challab's thesis [1], where he implemented the time-dependent LLG equation coupled with static mechanics. Here, we extend this approach to dynamic mechanical effects, providing a versatile tool for investigating strain-controlled magnetism and hybrid magnonic-phononic systems.

4.1 Implementation of the micromagnetic formalism

The numerical model presented in this chapter builds on the theoretical framework described previously, incorporating the key energy contributions governing magnetoelastic interactions. The total energy density considered in our model is given by:

$$F_{tot} = F_{ex} + F_{Zee} + F_{ms} + F_{me} \tag{4.1}$$

with the Zeeman energy density $F_{Zee} = -\mu_0 M_s \vec{H} \cdot \vec{m}$ where $\vec{H}$ corresponds to the applied magnetic field, the exchange energy $F_{ex} = A_{ex} \left(\vec{\nabla} \cdot \vec{m}\right)^2$, the magnetostatic energy $F_{ms} = \frac{1}{2}\mu_0 M_s \left(\vec{H}_{dem} + \vec{H}_{dip}\right) \cdot \vec{m}$, where the demagnetizing field $\vec{H}_{dem}$ and dipolar field are derived from the magnetic potential ϕ. The magnetocrystalline anisotropy is not defined as the crystalline state of our material is not studied in depth and exhibits a quasi-isotropic behavior. When an anisotropy is needed we choose to either ignore it (as it is often very small) or to generate it virtually with a magnetic field applied along the right direction. The magnetoelastic field can be written as:

$$F_{me} = \underline{\underline{\varepsilon}}^{el} : \underline{\underline{\underline{\underline{C}}}} : \underline{\underline{\varepsilon}}^{el} = \varepsilon_{ij}^{el} \sigma_{ij} \tag{4.2}$$

where where the elastic strain $\underline{\underline{\varepsilon}}^{el}$ is given by:

$$\varepsilon^{el} = \varepsilon^{tot} - \varepsilon^{mag} \tag{4.3}$$

This relation captures the bidirectional coupling between magnetism and solid mechanics: the magnetically induced strain alters the mechanical response (direct effect), while elastic deformations modify the magnetic energy, leading to changes in magnetic behavior (indirect effect). Since micromagnetic solvers are not inherently designed for solid mechanics, this method has been implemented in Comsol Multiphysics® [2], which required the explicit implementation of the Landau-Lifshitz-Gilbert (LLG) equation in its weak formulation [3]:

$$\int_\Omega \left(\frac{d\vec{m}}{dt} + \gamma \vec{m} \wedge \vec{H}_{eff} - \alpha \vec{m} \wedge \frac{d\vec{m}}{dt} \right) \vec{w} d\Omega = 0 \tag{4.4}$$

where Ω is the volume and w is a test function.

4.1.1 Frequency response simulations in Comsol Multiphysics®

Studying the frequency response of a magnetic system can be performed in three different ways inside Comsol Multiphysics.

1. Time-domain study: i) applies an external excitation and solves for the magnetization dynamics over time. ii) While conceptually simple, this method is computationally expensive and impractical when scanning multiple parameters (e.g., field strength, frequency).

2. Eigenfrequency study (preferred method): i) Solves for the natural resonance modes of the system without requiring an external excitation. ii) The time dependency in the LLG equation is replaced by a frequency dependence using:

$$\vec{m}(x, y, z, t) = \vec{m}_0(x, y, z) + \vec{m}(x, y, z)e^{i\omega t} \tag{4.5}$$

   iii) This method is fast and provides direct access to the system's resonance frequencies, making it well suited for our study.

3. Frequency-domain study: i) Requires a harmonic excitation to probe the system at desired frequencies. ii) Used in this work for simulations of ferromagnetic resonance (FMR) and Brillouin light scattering (BLS) spectra, allowing us to compute the system's frequency response over a broad range.

These three methods can be applied to both the homemade micromagnetic approach and the existing solid mechanics module, allowing these two physics to be computed simultaneously and interact with each other.

4.1.2 Handling non-local fields: exchange and magnetostatic terms

Most energy terms are straightforward to implement, but some require special treatment due to their mathematical complexity: i) exchange field and ii) magnetostatic field. Indeed, in the case of the exchange field $\vec{H}_{ex} = -\frac{2A_{ex}}{\mu_0 M_s}\vec{\nabla}^2 \cdot \vec{m}$, it is necessary to balance the derivative order of the unknown variable $\vec{m}$ and the test function $\vec{w}$. Additionally, the magnetostatic field can also be challenging to formulate, as it is a non-local term with a demagnetizing contribution inside the magnetic object and a dipolar contribution radiating outside the magnetic body. This dipolar field is often the most time-consuming part of micromagnetic simulations, and various methods can be used to handle it. In this work, we chose to calculate it accurately by simulating a portion of the universe surrounding the magnetic object. We hence calculate a dipolar potential ϕ such as:

$$\begin{cases} \vec{\nabla} \cdot \vec{H}_{dem} = -\Delta\phi = -M_s\vec{\nabla} \cdot \vec{m} & \Omega_M \\ \vec{\nabla} \cdot \vec{H}_{dip} = -\Delta\phi = 0 & \Omega_U \end{cases} \tag{4.6}$$

where Ω_M is the magnetic volume and Ω_U is the volume around the magnetic domain (i.e. the volume occupied by the universe). This set of equation simply comes from the definition of the magnetic induction $\vec{B} = \mu_0(\vec{H} + \vec{M})$ and the Maxwell Gauss' law $\vec{\nabla} \cdot \vec{B} = 0$.

4.1.3 Boundary conditions

In addition, the following boundary conditions have to be applied:

- The continuity of the normal component of the magnetization:

$$\begin{cases} \vec{n} \cdot \vec{\nabla}\phi = M_s\vec{m} \cdot \vec{n} & \partial\Omega_M \\ \vec{n} \cdot \vec{\nabla}\phi = 0 & \partial\Omega_{innerU} \end{cases} \tag{4.7}$$

where $\partial\Omega_M$ and $\partial\Omega_{innerU}$ are the boundaries of the magnetic domain and the inner boundaries of the universe domain respectively.

- Decay condition for demagnetizing field at infinity:

$$\frac{\partial\phi}{\partial\vec{r}} = \vec{n}\cdot\vec{\nabla}\phi = -2\frac{\phi}{r} \tag{4.8}$$

This accounts for the long-range dipolar decay, ensuring that the field vanishes at large distances. This condition comes from the fact that the magnetic object can be seen as a dipole at a long range, implying that

$$\phi = \frac{\mu_0}{4\pi}\frac{\vec{M}\cdot\vec{r}}{r^3} = \frac{\mu_0}{4\pi}\frac{M\cos\theta}{r^2} \tag{4.9}$$

with θ is the angle between the position vector $\vec{r}$ and the dipole surface. This condition is applied at the outer border of the universe $\partial\Omega_{outerU}$[4].

- Continuity of the demagnetizing potential at the interface between the universe and the magnetic object

$$\phi(\partial\Omega_M) = \phi(\partial\Omega_{innerU}) \tag{4.10}$$

- Conservation of the magnetization norm inside the magnetic domain Ω_M:

$$||\vec{m}|| = 1 \tag{4.11}$$

- Periodic boundary conditions for spin waves in a computational unit cell

$$\begin{cases} \vec{m}_{destination} = \vec{m}_{source}e^{ik\}\cdot(\vec{r}_{desination}-\vec{r}_{source})} \\ \vec{\phi}_{destination} = \vec{\phi}_{source}e^{ik\}\cdot(\vec{r}_{desination}-\vec{r}_{source})} \end{cases} \tag{4.12}$$

This condition is applied on opposites faces of a computational unit cell in order to map the magnetization and the potential from a face to another. The k value is used to force a phase shift between this faces and is used as a wave vector for the spin wave propagation calculation. using $k = 0$ means that the magnetization is periodically repeated over space like in the case of continuous films and periodic nanostructures.

4.1.4 Validation Strategy

It is worth mentioning that to validate our numerical approach, we chose to simulate reference studies and compare the results with experimental data and/or analytical models. It should be noted that some validation concerning the time domain study have been performed in the past by Nabil Challab during his PhD thesis [1, 4], where he has meticulously verified the Larmor precession, the magnetostatic field and the static strain applied on a self supported nanostructure by comparing his simulations with analytical studies and Nmag simulation. In the following sections, we are going to focus on the validation of the eigenfrequency study and frequency domain studies with experimental and numerical studies performed on ferromagnetic continuous films.

4.2 Periodic boundary conditions and magnetostatic field

It has been established earlier that the magnetostatic field was separated into two contributions corresponding to the demagnetizing field inside the magnetic object and the dipolar field in the universe around it. It is then necessary to incorporate a part of the universe into the computation which takes the form a sphere in the case of a finite object as shown in figure 4.1-a). When incorporating the periodic boundary conditions it is not possible to define the universe as a sphere as the universe needs to belong to the periodic cell. We decided, for this matter, to define the universe only above and under the object as represented in figure 4.1-b).

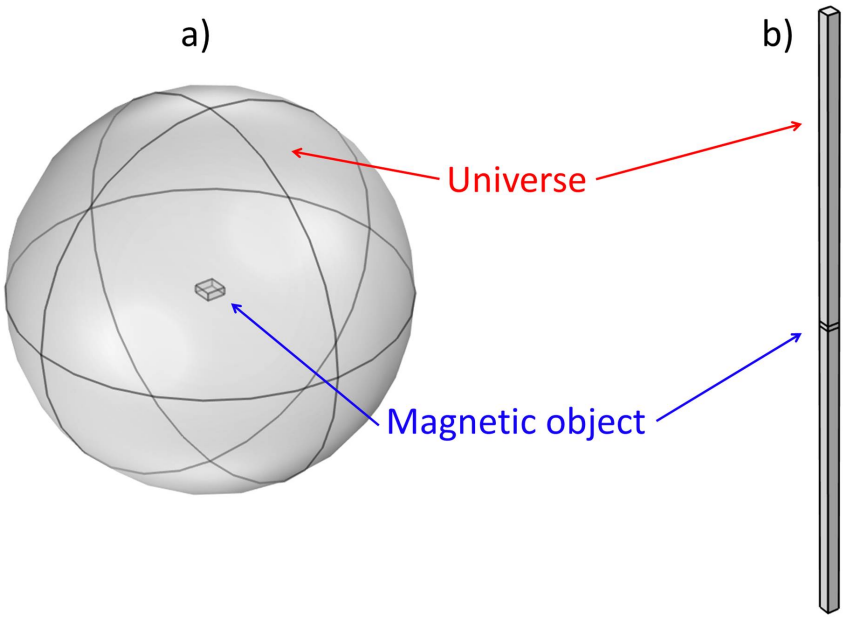

Figure 4.1: a) Geometry used to simulate a finite square dot. b) Unit cell used when periodic boundary conditions are applied.

4.2.1 Implementation of Periodic Boundary Conditions (PBCs)

The application of PBCs is illustrated in figure 4.2., demonstrating their role in simulating a small portion of an infinite thin film, thereby significantly reducing computation time. For example, in Figure [Figure: Thin_Film_Static]-(a), we simulate a single unit cell (200×200×80 nm^3) in the absence of elastic strain and with zero applied magnetic field. To ensure accurate modeling, the automatic meshing algorithm of Comsol Multiphysics® was used to generate the finite element mesh. A key aspect of this meshing process is maintaining the nodal

spacing at the same order of magnitude as the exchange length:

$$\ell_{ex} = \sqrt{\frac{2A}{\mu_0 M_S^2}} \tag{4.13}$$

Extensive verification was conducted to ensure that further reducing the mesh size did not influence the results—except for increasing computation time.

Without PBCs (right side of figure 4.2-(a)), the structure behaves as a single square dot, where the magnetic moment distribution naturally forms a vortex configuration due to the shape anisotropy [5]. In contrast, when PBCs are applied to the four faces of the (x, z) and (y, z) planes, we successfully replicate the behavior of a semi-infinite thin film with an 80 nm thickness, preserving the expected magnetic behavior.

4.2.2 Magnetization response under applied fields

A key feature of periodic boundary conditions is their ability to reproduce the expected magnetic response of a thin film with no in-plane anisotropy. This is demonstrated in Figure [Figure: Thin_Film_Static]-(b), where a small magnetic field (10 mT) is applied in two different directions: i) along the x-axis and ii) at 45° in the (x, y) plane. In both cases, the equilibrium magnetization distribution aligns perfectly with the applied field, as expected for a thin film with negligible in-plane anisotropy. However, saturating the magnetization along the out-of-plane (z) direction proves significantly more difficult due to the demagnetizing field. This effect is illustrated in figure 4.2-(c), where strong out-of-plane magnetic fields of 500 mT and 1500 mT are applied. Even under these high fields, full magnetization saturation along z is challenging to achieve, reflecting the strong demagnetization effects inherent in thin magnetic films.

In summary, the implementation of PBCs in our simulations enables a computationally efficient method for studying magnetic thin films and periodic structures. By accurately modeling both demagnetizing effects and dipolar interactions, we ensure that our numerical framework correctly reproduces the expected magnetization behavior under different external field conditions. These considerations are critical for obtaining realistic micromagnetic simulations, especially in the presence of magnetoelastic coupling and spin-wave dynamics in periodic media.

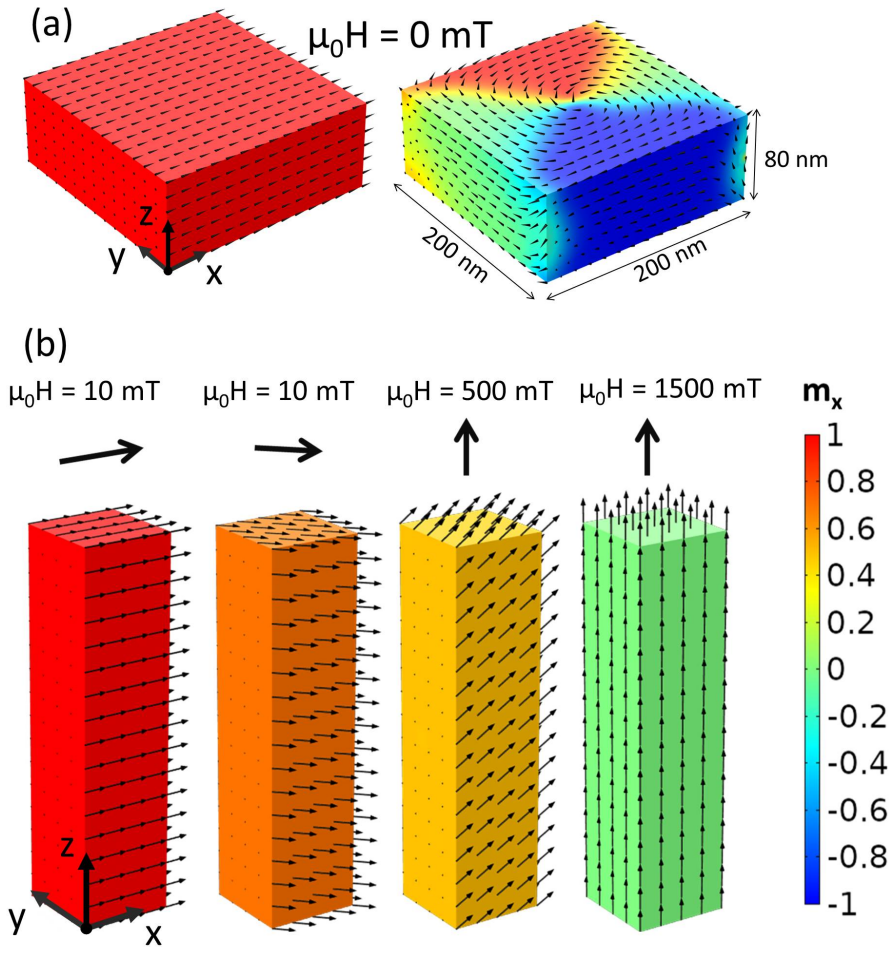

Figure 4.2: In all images, colors encode $x-$component of the normalized magnetization from -1 to +1, see color bar. (a) Calculated magnetic moment distributions at zero applied magnetic field and at equilibrium for a unit cell $200 \times 200 \times 80$ nm^3 obtained with (left) or without (right) the defined periodic boundary conditions (PBC). The PBC have been applied at the 4 surfaces of the (x, z) and (y, z) planes. (b) Magnetic moment distributions calculated in presence of a 10 mT in-plane magnetic field applied either along x or at 45° with respect to x axis. (c) Magnetic moment distribution calculated in presence of an out-of-plane magnetic field (500 mT and 1500 mT, respectively).

4.3 In-plane frequency dependency of non-propagating modes inside continuous films

Choosing ferromagnetic resonance experiments is extremely relevant in our case because it is a frequency-resolved technique that we are going to use throughout our whole work. The

case of continuous films is easy to model in various configurations (from in-plane to out-of-plane) thanks to Kittel's equation and more generally thanks to Smit Beljers' equation [6, 7]. We are going to focus, in a first step, on the case of an 80 nm thick permalloy (Py, $Ni_{80}Fe_{20}$) film deposited on a Si substrate. We started by studying the frequency to field ($f(H)$) dependency in the in-plane configuration. The applied magnetic field has been swept from 0 mT to 220 mT for frequencies going from 0 GHz to 20 GHz.

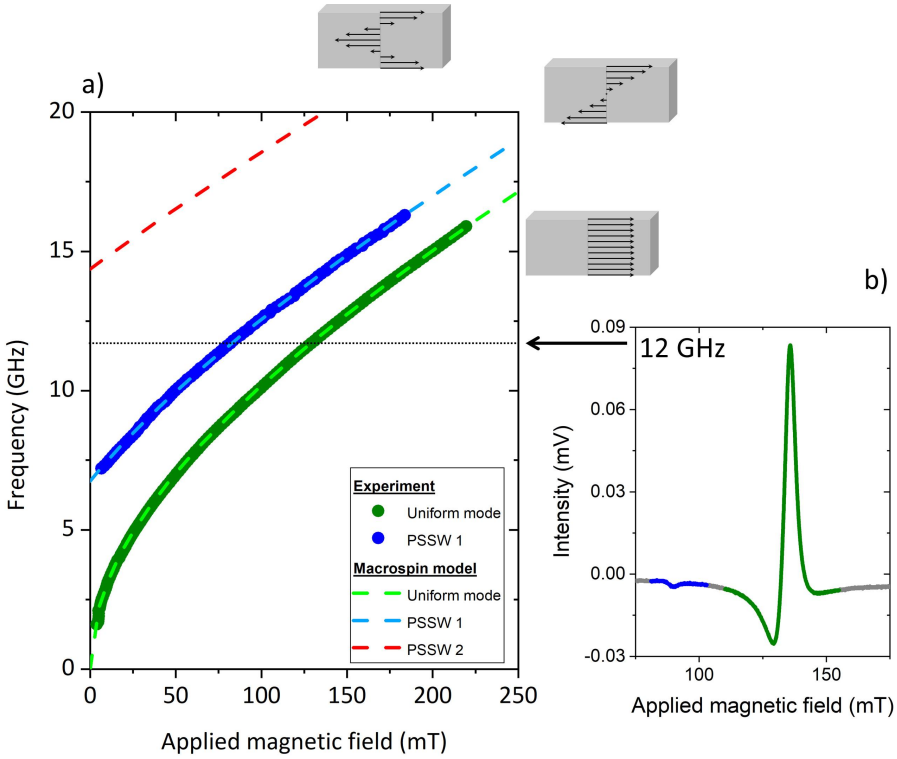

Figure 4.3: a) In-plane FMR measurements obtained on Py continuous film. The thick dots represent the experimental uniform mode (green) and the PSSW1 mode (blue). The dashed lines represent the fitted macrospin model for the uniform (green), PSSW1 (blue) and PSSW2 (red) modes. The insert schemes represent the profile of each move over the thickness of the film. b) Typical experimental spectrum obtained at a driving frequency of 12 GHz.

Figure 4.3 shows the experimental results obtained along with the analytical macrospin model used to fit the magnetic constants of our sample. The equations used are the following:

$$f_{uniform} = \frac{\gamma\mu_0}{2\pi}\sqrt{H\left(H + 4\pi M_s\right)} \tag{4.14}$$

$$f_{PSSW1} = \frac{\gamma\mu_0}{2\pi}\sqrt{\left(H + \frac{2A}{\mu_0 Ms} \times \left(\frac{\pi}{d}\right)^2\right)\left(H + M_s + \frac{2A}{Ms} \times \left(\frac{\pi}{d}\right)^2\right)} \tag{4.15}$$

$$f_{PSSW2} = \frac{\gamma \mu_0}{2\pi} \sqrt{\left(H + \frac{2A}{\mu_0 Ms} \times \left(\frac{2\pi}{d}\right)^2\right)\left(H + M_s + \frac{2A}{Ms} \times \left(\frac{2\pi}{d}\right)^2\right)} \tag{4.16}$$

where d stands for the thickness of the sample[8]. It is worth noting that even though a very small uniaxial anisotropy was measured (about 0.5 mT of amplitude), it was neglected in the analytical and FEM models as its value is small enough to not be relevant. From these results we extracted a saturation magnetization $M_s = 8 \times 10^5$ A.m^{-1} an exchange stiffness $A = 12$ pJ.m^{-1} and a gyromagnetic ratio $\gamma = 1.92 \times 10^{11}$ Hz.T^{-1}. These constants have been incorporated into our FEM model to accurately simulate the behavior of our specific sample. The damping constant used is $\alpha = 0.01$ which what is typically found in the literature for $Ni_{80}Fe_{20}$. We started with the eigenfrequency approach by applying the magnetic field along the x axis leading to a precession according to the yz plane. As continuous films are perfectly homogeneous over space, we chose to simulate a small unit cell ($20 \times 20 \times 80$ nm^3 arbitrarily chosen).

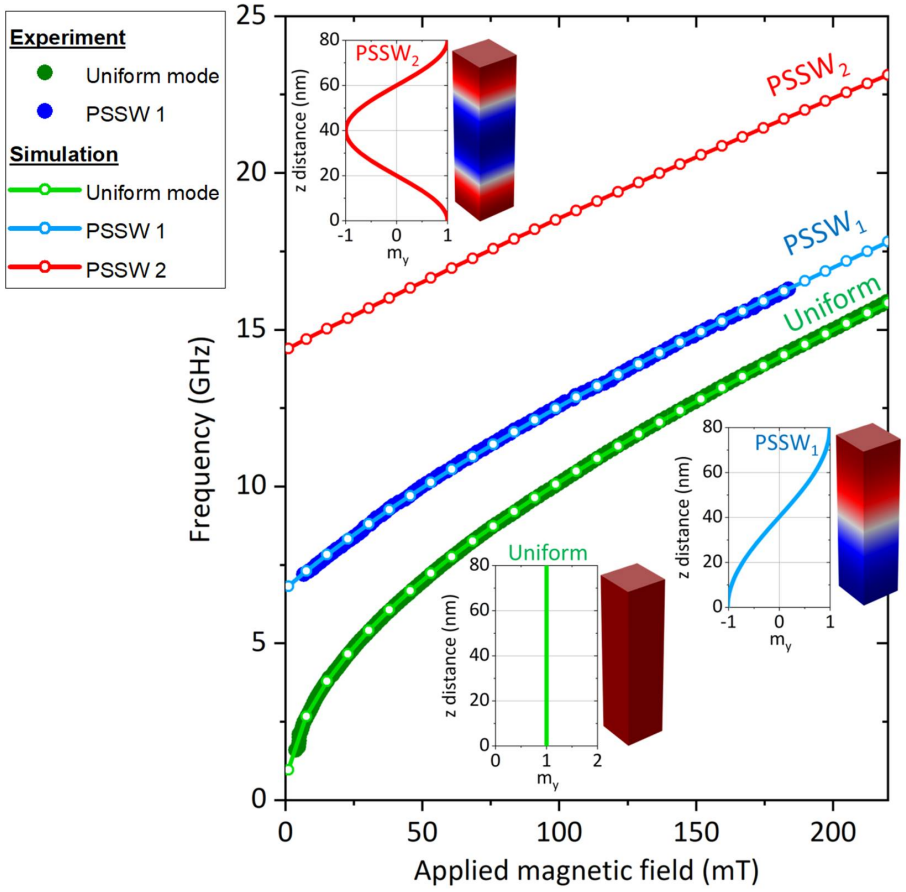

Figure 4.4: Comparison between the experimental data (thick colored dots) with the eignenfrequency simulation (linked colored circles). Insert figures represent the simulated mode profile over the thickness of the 3D unit cell. The color encode the m_y component of the magnetization.

The results shown in figure 4.4 exhibit a very good qualitative and quantitative agreement between the simulations and the experiments. The calculated frequencies fit almost perfectly the experimental set of data and the mode profiles exhibit a homogeneous profile for the uniform mode, and one and two modes for the first and second perpendicular standing spin waves respectively as it is expected. One can observe that the $PSSW_2$ has been simulated even though it has not been measured experimentally. In reality all the possible eigenmodes can be calculated using this method independently of the possibility of observing them experimentally.

For the frequency domain study, we can map the magnetization response according to a chosen harmonic excitation. To be as close as possible to experimental conditions we applied the static magnetic field along the x-axis and the dynamical excitation along the y axis (0.1 mT). We varied the driving frequency from 0 GHz to 20 GHz by steps of 0.1 GHz while the magnetic field was swept from 0 mT to 220 mT by steps of 1 mT.

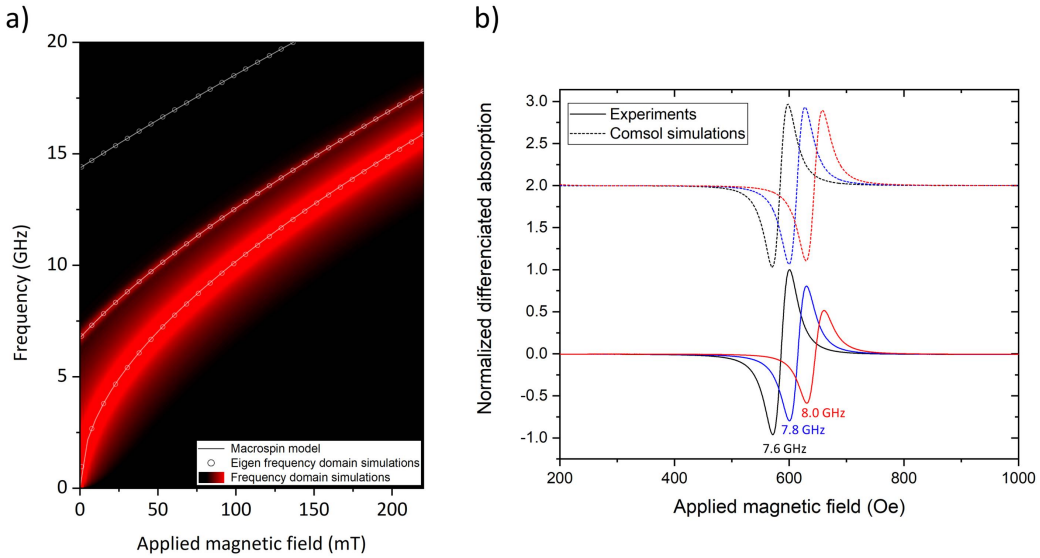

Figure 4.5: a) Comparison between the frequency domain study (mapping) the eigenfrequency study (open circles) and the macrospin model (lines). The mapping encodes the response of the m_y component of the magnetization. b) Comparison between the normalized simulated FMR spectra (dashed lines) using the frequency domain study and the experimental ones (lines) for driving frequencies of 7.6 GHz (black), 7.8 GHz (blue) and 8 GHz (red).

The results obtained are presented in figure 4.5-a) and show once again good agreement with the previous approach and the macrospin model. On the mapping, the red color shows the presence of two modes. The intense one corresponds to the uniform mode and the less intense one corresponds to the PSSW1. Even though the $PSSW_2$ was observed in the simulated profiles at the right frequencies, its m_y responds is too small to be visible on the mapping, which also explains why this mode has not been observed experimentally. It is important to precise that the relative intensity between the uniform mode and the PSSW

may not be entirely representative due the pinning conditions not being well known that have a high effect on the standing modes. Figure 4.5-b) shows the normalized simulated FMR spectra (dashed lines) along with the experimental ones (lines) for multiple frequencies. The simulation performed with a damping $\alpha = 0.01$ exhibit a line-width close to what is observed experimentally. As expected the relative intensity decreases as the frequency increases. This decrease is however smaller than the decrease observed experimentally. This is mostly due to the experimental setup and especially to the copper microstrip line which is less efficient for some frequencies. From this study it is clear that the numerical model we developed allows one to quite precisely simulate the resonance behavior of a continuous film in the in-plane configuration. As this configuration is the simplest (the least influenced by the magnetostatic field) and the most natural for the magnetization, the same study will be undertaken for other configurations in the next sub-sections for further validation.

4.4 Out-of-plane frequency dependency of non-propagating modes inside continuous films

The out-of-plane configuration is an interesting case to study for our model validation as the magnetization is forced along a hard axis (z axis), which lead to the creation of an intense demagnetizing field. As for the in-plane case a simple model can be used to fit the three different magnetic modes:

$$f_{uniform} = \frac{\gamma \mu_0}{2\pi} (H - M_s) \tag{4.17}$$

$$f_{PSSW1} = \frac{\gamma \mu_0}{2\pi} \left(H + \frac{2A}{\mu_0 M s} \left(\frac{\pi}{d} \right)^2 - M_s \right) \tag{4.18}$$

$$f_{PSSW2} = \frac{\gamma \mu_0}{2\pi} \left(H + \frac{2A}{\mu_0 M s} \left(\frac{2\pi}{d} \right)^2 - M_s \right) \tag{4.19}$$

These equations are only applicable when the magnetization is aligned along the out-of plane field which corresponds to an applied magnetic field $\mu_0 H = \mu_0 M_s \approx 1000$ mT.

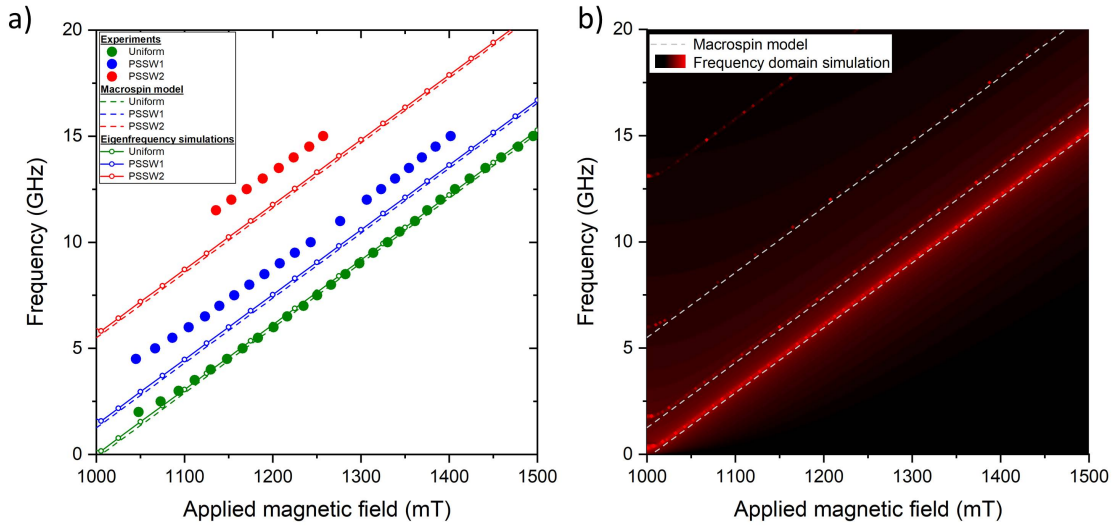

Figure 4.6: a) Out-of-plane FMR measurements fitted with the macrospin model and compared with the eignenfrequency domain simulations. b) Frequency domain simulations compared with the macrospin model. The color encodes the modes relative intensity.

Figure 4.6-a) shows the FMR experimental (dots) results along the macrospin model (dashed line) and the eigenfrequency FEM simulations. One can observe that although we managed to fit the uniform mode and to obtain the right tendency for the standing modes, it remains a frequency shift between the modeled standing modes and the experimental ones. It has been tried to change the magnetic constants in order to correct this discrepancy, but no better set of constants was found. This may be corrected by adding a pinning term to our equations, however we do not have a definitive explanation for these results. Even though we observed this shift we still used the model's magnetic constants for the micromagnetic simulations for both eigenfrequency method represented by the linked circles in figure 4.6-a) and the frequency domain method represented by the colormap on figure 4.6-b). Similarly to the previous study, the macrospin model and the FEM simulations agree very well. The colormap shows a prominent uniform mode with multiple low intensity standing modes.

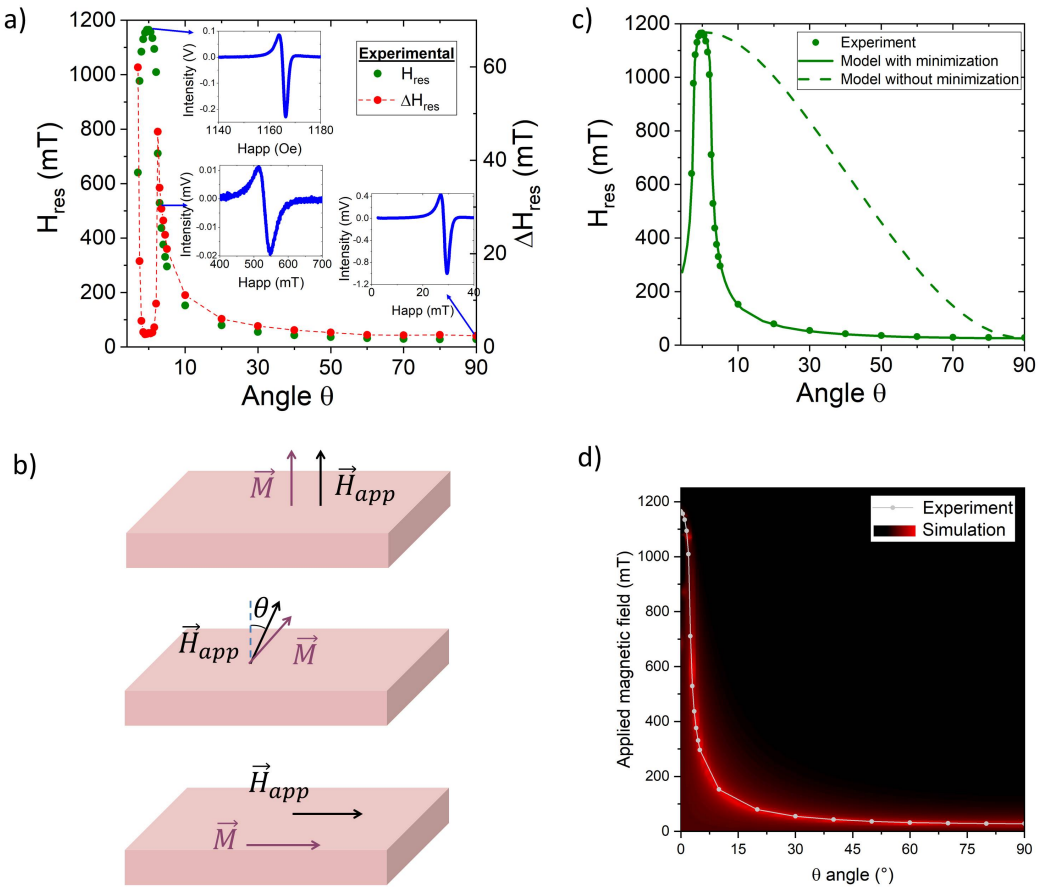

Figure 4.7: a) Fmr measuments performed on the continuous film for a driving frequency of 5 GHz. The green set of data represents the resonance frequency with respct to the out-of-plane angle while the red set of data represents the resonance peak width. b) Schematic of the magnetization and applied field configuration. c) Comparison between the experimental data (dots), the macrospin model without energy minimization (dashed line) and the macrospin model with energy minimization. d) Comparison between experiments (line and dots) and frequency domain simulation.

4.5 In-plane to out-of-plane angular dependency of non-propagating modes in continuous films

The two previous studies use very simple and straightforward models. With the equations used we assume that the magnetization is aligned along the applied magnetic field, which is a valid assumption in the in-plane and out-of-plane configurations. The in-between configurations necessitate to determine the angle between the applied field and the magnetization as illustrated on figure 4.7-b), which is done by minimizing the total magnetic energy of the system[9].

The results obtained on figure 4.7-a) were obtained for a fixed driving frequency of 5GHz. The magnetic field was applied at an angle θ from the normal of the sample's surface going from 0° to 90°. It is clear that the resonance field H_{res} decreases very quickly in a first regime from 0° to 10° and then continues to decrease slowly in a second regime from 10° to 90°. The FWHM referred to as ΔH_{res} is the smallest at a 0° and increases highly when changing slightly the angle, reaching high values between 2.5° and 10°. This can be observed directly on the 4.7-a) inserts where very thin spectra are obtained at 0° and 90° while a wide spectrum is obtained at 2.5°. We fitted these results (dots) in figure 4.7-c) with an energy minimization based macrospin model represented by the continuous line. This has been done by expliciting the resonance frequency and the total energy with respect to the applied magnetic field, the applied field angle and the magnetization angle. We fixed the angle of the resonance field while the magnetization angle was interactively adjusted using a dichotomous approach. We show the importance of minimizing the energy by comparing it with the model without minimization. It is clear that not minimizing is only acceptable in the in-plane and out-of-plane configurations, as this approach diverges very quickly from reality. For this study, the eigenfrequency approach is not possible as we have to fix the resonance frequency at 5 GHz. As we know that the magnetization is aligned with the direction of the magnetic field only at 0° and 90° it is necessary to perform a temporal simulation of the system in order to obtain the exact magnetization equilibrium position for each magnetic field value, which makes this kind of study time consuming. Figure 4.7-d) shows the experimental data (white dots and line) superimposed on the frequency domain simulation. The calculated dependency follows exactly the experimental tendency and the signal width increases greatly from 90° to 5° before decreasing quickly around 0°.

Those studies under multiple FMR configuration allowed us to validate our numerical approach for the magnetic frequency response.

4.6 Direct magneto-elastic effects inside continuous films

Although the direct effect is not easy to highlight experimentally for small samples like ours, it is simple to compare our simulations with the theoretical values of the magnetically induced strain. The strain depends on the magnetization direction and is proportional to the magnetoelastic constant:

$$\varepsilon_{xx}^{m} = \lambda \tag{4.20}$$

$$\varepsilon_{yy}^{m} = -\frac{1}{2}\lambda \tag{4.21}$$

when the magnetization is aligned along the x-axis. More generally the magnetic strain is written:

$$\underline{\underline{\varepsilon}}^m = \frac{3}{2}\left[\lambda_{100}\begin{pmatrix} m_x^2 - \frac{1}{3} & m_x m_y & m_x m_z \\ m_x m_y & m_y^2 - \frac{1}{3} & m_y m_z \\ m_x m_z & m_y m_z & m_z^2 - \frac{1}{3} \end{pmatrix} + (\lambda_{111} - \lambda_{100})\begin{pmatrix} 0 & m_x m_y & m_x m_z \\ m_x m_y & 0 & m_y m_z \\ m_x m_z & m_y m_z & 0 \end{pmatrix}\right] \tag{4.22}$$

This term has been integrated inside Comsol by adding a contribution to the total strain and by modifying the native integrated equations.

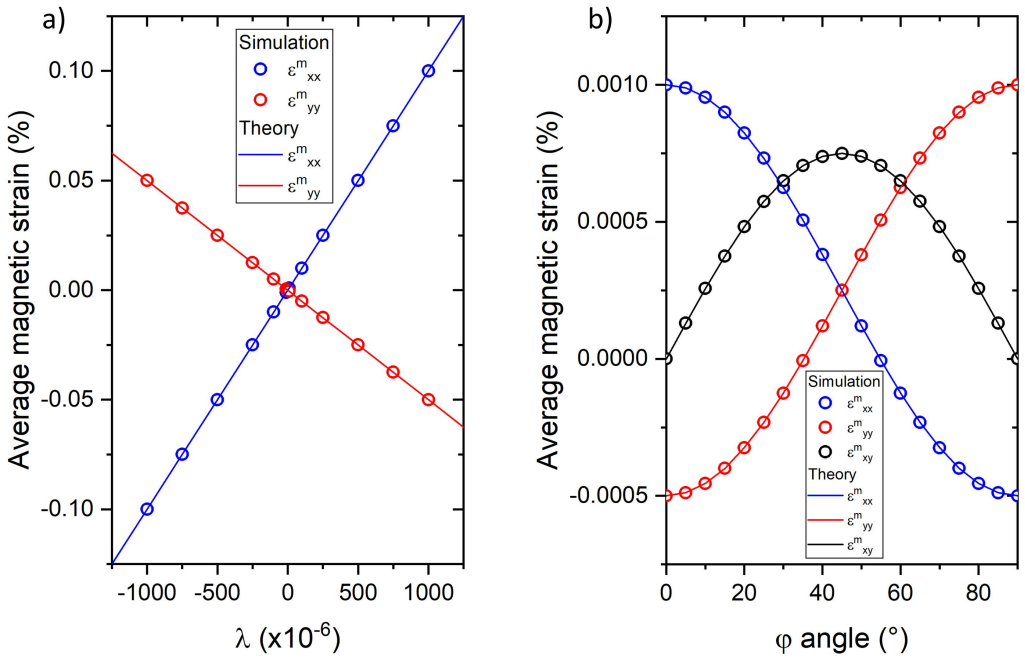

Figure 4.8: Average simulated magnetic strain (circles) compared with the calculated theoretical value (lines) inside the unit cell with respect to a) the magnetoelastic constant λ and b) the in-plane angle between the applied magnetic field and the x axis for $\lambda = 1 \times 10^{-5}$.

We verified the good integration of the direct magnetoelastic effect by applying numerically an external magnetic field on a continuous film. As this effect only depends on the magnetoelastic constant λ and the magnetization direction, we varied these two parameters. Figure 4.8-a) shows the effect of the magnetoelastic constant over the magnetic strain tensor components ε^m_{xx} and ε^m_{yy}. The simulations (circles) follow perfectly the theoretical values (line) with a linear behavior showing the expected slopes $s_{\varepsilon^m_{xx}} = 1$ and $s_{\varepsilon^m_{yy}} = -0.5$. The magnetization direction dependency is plotted on figure 4.8-b) where φ represents the in-plane angle between the magnetization and the x-axis. These results obtained for $\lambda = 1 \times 10^{-5}$ follow once again perfectly the expected values for ε^m_{xx}, ε^m_{yy} and ε^m_{yx}.

4.7 Indirect magneto-elastic effects inside continuous films

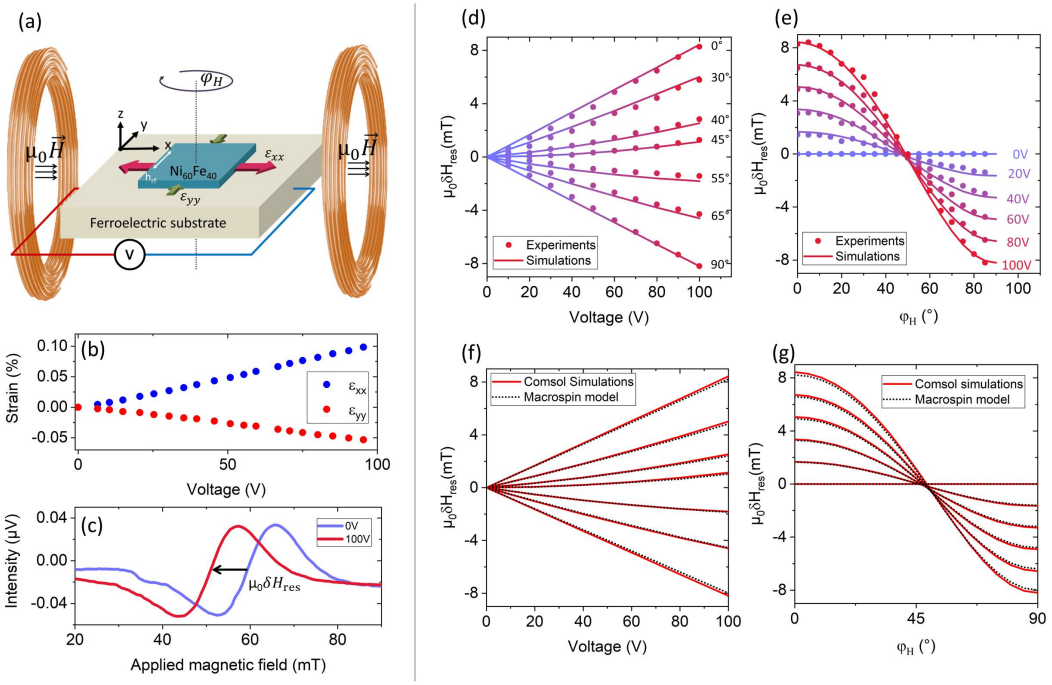

Figure 4.9: (a) Schematic of $Ni_{60}Fe_{40}$ film/ferroelectric substrate system. $\mu_0\vec{H}$ corresponds to the applied magnetic field. (b) Ferroelectric substrate strain calibration curve. (c) FMR spectra obtained at 0V (blue) and 100V (red). (d) Resonance field shift ($\mu_0\delta H_{res} = \mu_0 H_{res}(0) - \mu_0 H_{res}(V)$) as function of the applied voltage. The experimental data are represented by symbols while numerical results are represented by conbtinuous lines. (e) Resonance field shift ($\mu_0\delta H_{res}$) as function of the in-plane φ_H. (f-g) Simulations (red lines) superimposed to the macrospin model (black dashed lines) (g).

The simplest application of magnetoelastic effects is the case of a continuous thin film subjected to strains from various sources (flexible substrate under tension or bending [11], ferroelectric substrate subjected to a voltage [12], effects of epitaxial interfaces [13], ...). In this section, we show how our numerical approach described allows to take into account these effects, whether they concern the static or the dynamic properties of the magnetization. More precisely, we have simulated a magnetoelectric system composed of a ferroelectric substrate on which a ferromagnetic thin film is deposited. The interest of this example is that we were able to confront the calculations to *in situ* FMR experiments (voltage applied to the substrate) [5]. The ferroelectric substrate is composed of polycrystalline PZT, more details can be found in ref. [15]. Thus the imposed elastic strains by the substrate are transmitted to the thin film which is itself magnetostrictive. Thus, this example allows to show

a first study taking into account of the magnetoelastic coupling in micromagnetic calculations. Here, a macroscopic strain state is imposed on the edges of the substrate (along x and y), and its distribution (in this case homogeneous) is determined numerically.

Figure 4.9-(a) shows a schematic of the studied system. A $Ni_{60}Fe_{40}$ thin film (20 nm) is deposited on a ferroelectric substrate whose $\varepsilon_{xx}(V)$ and $\varepsilon_{yy}(V)$ are experimentally known thanks to digital image correlation measurements, more details are given in reference [16]. ε_{xx} and ε_{yy} vary almost linearly between 0 V and 100 V and respectively reach values of 1×10^{-3} and -0.5×10^{-3}, their evolution are presented in figure 4.9-(b). Indeed, ε_{xx} is found to be positive whereas ε_{yy} is found to be negative with a ratio $\varepsilon_{yy}/\varepsilon_{xx} \simeq -0.5$ making the mechanical traction slightly biaxial. These in-plane strains will then be injected in the micromagnetic simulations performed with a Young's modulus $Y_{N_{60}Fe_{40}} = 180$ GPa and a Poisson ratio $\nu = 0.3$. Figure 4.9-(a) presents the sweep-field FMR experiments: a static magnetic field $\mu_0\vec{H}$ is applied in the plane of the film. The angle φ_H between $\mu_0\vec{H}$ and the main direction of traction (x) can vary from 0 to 90 degrees. On the schematic, we have also represented the radio-frequency field (h_{rf}) imposed inside the film which allows to excite the magnetic moments and thus probe the non-propagating modes (here only the uniform mode is concerned). The complete study of the uniform precession mode by FMR allowed us to determine the magnetic parameters of the $Ni_{60}Fe_{40}$ thin film, namely $M_s = 0.95 \times 10^6$ A.m^{-1}, $A = 1.2 \times 10^{-11}$ J.m^{-1} and $\gamma = 1.76 \times 10^{11}$ rad.s^{-1}.T^{-1}. Those parameters will be used for the numerical simulations. Figure 4.9-(c) shows typical experimental spectra at 8 GHz for two applied voltages (0 V and 100 V). The magnetic field is applied along the main traction ($\varphi_H = 0^\circ$) and the driven frequency is fixed at 8 GHz. We observe a shift of the resonance field $\mu_0\delta H_{res} = \mu_0 H_{res}(0) - \mu_0 H_{res}(V)$ equal to $\sim +8$ mT. This shift is physically linked to the magnetoelastic field $\mu_0\vec{H}_{me}$ induced by the imposed in-plane strains from the substrate deformation. The positive sign of $\mu_0\delta H_{res}$ allows to deduce that the magnetostriction coefficient of the $Ni_{60}Fe_{40}$ film $\lambda_{Ni_{60}Fe_{40}}$ is positive. Indeed, in this case, $\mu_0\vec{H}_{me}$ is aligned with x, which decreases the resonance field (making x an easy axis). The complete experimental evolution (open symbols) of $\mu_0\delta H_{res}$ as a function of V is shown in figure 4.9-(d) for several φ_H angle. One can observe that $\mu_0\delta H_{res} \sim -8$ mT for $\vec{H}$ applied at 90° that is coherent with a uniaxial magnetoelastic field aligned along x. The complete in-plane variations of $\mu_0\delta H_{res}$ are presented in figure 4.9-(e) for several applied voltage. We recognize the signature of a second order anisotropy axis, which is directly linked to the voltage induced magneto-elastic anisotropy. It is clear that this magnetoelastic anisotropy is greater the more voltage is applied. The variations presented in figures 4.9-(d) and 4.9-(e) allow us to determine the magnetostriction coefficient for the thin film; by adjusting it, we found a value of $\lambda_{Ni_{60}Fe_{40}} \simeq +12 \times 10^{-6}$, as already found in reference [10]. To verify this value we compared our simulation with a macrospin model taking into consideration the magnetoelastic energy:

$$F_{Me} = -\frac{3}{2}\lambda\left[\left(\sin^2\theta\cos^2\varphi - \frac{1}{3}\right)\sigma_{xx} + \left(\sin^2\theta\sin^2\varphi - \frac{1}{3}\right)\sigma_{yy}\right] \tag{4.23}$$

$$\|H_{Me}\| = \frac{3\lambda}{M_s}\sqrt{(\sin\theta\cos\varphi\sigma_{xx})^2 + \left(\sin\theta\sin\varphi\sigma_{yy}\right)^2} \tag{4.24}$$

with θ and φ corresponding to the spherical angles associated with the magnetization direction. As the magnetization is not necessarily align along the applied magnetic field it is necessary to minimize the magnetic energy if the magnetic field is not strong enough which has been done in figure 4.9-f,g). We can observe a quasi perfect agreement with the simulations, confirming the correct implementation of the indirect magnetoelastic formalism.

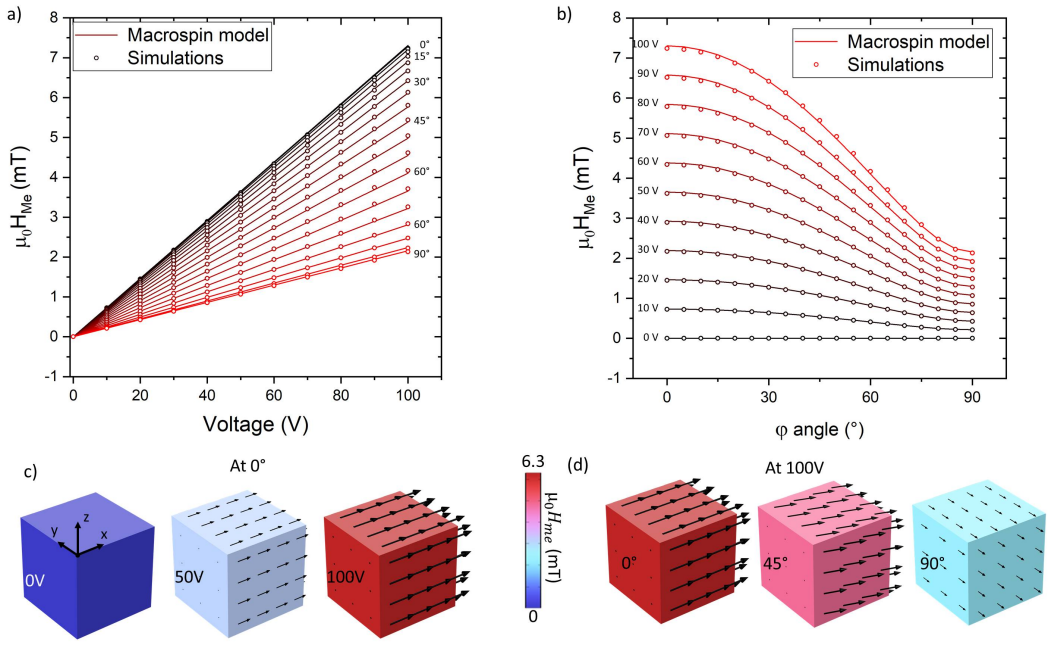

Figure 4.10: (a) Simulated (open circles) and modelled (lines) magnetoelastic field values with respect to the applied voltage for multiple directions of the applied magnetic field. (b) Simulated (open circles) and modelled (lines) magnetoelastic field values with respect to the applied field angle for multiple values of the applied voltage. (c-d) Magnetoelastic field (arrows) and its module map calculated for different values of the applied voltage at $\varphi_H = 0^\circ$ (c) and for different angle at 100 V (d).

Finally, we simulated the magneto-mechanical behavior of this thin film subjected to homogeneous strains. For this purpose, a unit cell like the one presented in the previous section was used. The dimensions of the unit cell are $20\times20\times20$ nm^3. The PBC were applied on the four faces of the (x, z) and (y, z) planes to simulate a semi-infinite film in the (x, y) plane. We verified that our results remained unchanged by considering larger unit cells (along x and y). As expected, the application of PBC in the mechanical equations leads well to homogeneous induced strain fields in the film. The calculated induced magnetoelastic fields are also homogeneous for the different considered strain states. In this regard, figure 4.10-(a,c) (resp. 4.10-(b,d)) corresponds to the calculated induced static magnetoelastic field for different applied voltage (resp. in-plane angle φ_H) at $\varphi_H = 0^\circ$ (resp. at 100 V) and at zero applied magnetic field. The lines in the graph correspond to the modelization

while the open circles show the FEM simulations. The 3D cellcolors encode $x-$component of the magneto-elastic field $\mu_0 H_{me}$ while the arrows show its distribution in the volume. In figure 4.10-(c), we observe that the amplitude of $\mu_0\vec{H}_{me}$ increases with the applied voltage as shown by the arrow sizes on the 3D views. One can note that $\left\|\mu_0\vec{H}_{me}\right\| \simeq 6.3$ mT at 100 V that is different to the +8 mT found for $\mu_0\delta H_{res}$ at 100 V. This is due to the slightly biaxial in-plane stress state induced by the ferroelectric substrate, due to the Poisson's ratio mismatch between substrate and thin film [16]. In addition, the same observation can be done in the images of figure 4.10-(d). We notice that the $\mu_0\vec{H}_{me}$ is weak but not zero at 90°, which would have been the case for a uniaxial stress state. We have indeed verified that when we impose a uniaxial stress state, the $\mu_0\vec{H}_{me}$ cancels for $\varphi_H = 90°$. In order to compare more directly our simulations to the experimental results, we proceeded to calculations of eigen-modes as done in the previous section but in the presence of a mechanical stress in the film. So, we added a magneto-elastic anisotropy term to the total energy density which is dependent on the mechanical stresses calculated in parallel with the resolution of the LLG equation. The magnetic parameters that have been used correspond to the values extracted from FMR experiments. Therefore, we simulated several frequency as function of the applied magnetic field $f(H)$ curves by applying magnetic field varying from 0 to 250 mT (by steps of 10 mT) for different φ_H angle and at the different mechanical stress states. We then measured on these numerically $f(H)$ curves the field shifts between these curves at a specific fixed frequency, which allows us to determine a shift similar to the one measured experimentally ($\mu_0\delta H_{res}$). We are thus in the same conditions as the *in situ* sweep-field FMR experiments. The continuous lines in figures 4.9-(d) and 4.9-(e) are thus the numerical $\mu_0\delta H_{res}$ variations. Note that no fit parameters have been used. A very good agreement is found for both the $\mu_0\delta H_{res}$-variations at fixed φ_H (figure 4.9-d)) and at fixed applied voltage (figure 4.9-e)). These results validate our approach which combines mechanical calculations with the resolution of the LLG equation in the presence of a magnetoelastic term.

Bibliography

[1] Challab, N. (2021). Contrôle du champ magnétoélastique local dans des réseaux de nanostructures pour des applications de straintronic (Doctoral dissertation, Paris 13). 4, 4.1.4

[2] COMSOL Multiphysics® v. 6.1. www.comsol.com. COMSOL AB, Stockholm, Sweden. 4, 4.1

[3] Szambolics, H., Buda-Prejbeanu, L. D., Toussaint, J. C., & Fruchart, O. (2008). Finite element formalism for micromagnetism. COMPEL-The international journal for computation and mathematics in electrical and electronic engineering, 27(1), 266-276. 4.1

[4] N. Challab, A. D. Aboumassound, F. Zighem, D. Faurie and Haboussi, J. Phys. D: Applied Physics **52**, 355004 (2019). 4.1.3, 4.1.4

[5] Wang, J., Li, G. P., Shimada, T., Fang, H., & Kitamura, T. (2013). Control of the polarity of magnetization vortex by torsion. Applied Physics Letters, 103(24). 4.2.1

[6] Fuentes, G. P., Silva, D. B. O., & Padrón-Hernández, E. (2022). FMR in thin films with finite extension. 4.3

[7] Li, Y., Li, C., Du, Q., Shi, K., Zhou, Z., Liu, M., & Pan, J. (2022). Thickness-dependence of magnetic damping related to two-magnon scattering in ultrathin Ni0. 81Fe0. 19 films. Journal of Physics D: Applied Physics, 55(24), 245001. 4.3

[8] Capku, Z., & Yildiz, F. (2021). Spin wave modes observation in YIG thin films with perpendicular magnetic anisotropy. Journal of Magnetism and Magnetic Materials, 538, 168290. 4.3

[9] Xu, X., Huang, H., Jin, L., Wen, T., Liao, Y., Tang, X., ... & Zhong, Z. (2023, March). Out-of-plane ferromagnetic resonance and surface spin wave modes in Ni80Fe20 film on ripple-patterned sapphire substrate. In Journal of Physics: Conference Series (Vol. 2459, No. 1, p. 012034). IOP Publishing. 4.5

[10] N. Challab, D. Faurie, M. Haboussi, A. O. Adeyeye and F. Zighem, ACS Applied Materials & Interfaces **13**, 29906-29915 (2021). 4.7

[11] M. Gueye, B. M. Wague, F. Zighem, M. Belmeguenai, M.S. Gabor, Jr. T. Petrisor, C. Tiusan, S. Mercone, D. Faurie, App. Phys. Lett. **105**, 062409 (2014) 4.7

[12] M. Gueye, F. Zighem, D. Faurie, M. Belmeguenai, S. Mercone, Appl. Phys. Lett. **105**, 052411 (2014) 4.7

[13] S. Goel, S. Ohya and M. Tanaka, Phys. Rev. B **99**, 014431 (2019). 4.7

[14] M. Gueye, P. Lupo, F. Zighem, D. Faurie, M. Belmeguenai and A. O. Adeyeye, Europhys Lett. **114**, 17003 (2016). 4.7, 7.1

[15] T. Sadat, D. Faurie, P. Godard, D. Thiaudière, P.-O. Renault and F Zighem, J. Phys. D: Appl. Phys. 53, 145001 (2020) 4.7

[16] F. Zighem, M. Belmeguenai, D. Faurie, H. Haddadi, J. Moulin, Rev. Sci. Inst. **85**, 103905 (2014) 4.7, 4.7

5 Experimental methods

Contents

This chapter explores the principles and experimental techniques surrounding ferromagnetic resonance (FMR) and Brillouin light scattering (BLS), two fundamental and complementary methods in magnetism research. FMR, a widely implemented technique, remains a cornerstone for studying magnetization dynamics, providing crucial insights into magnetic parameters through the interaction of microwave radiation and magnetic fields. Its sensitivity to damping mechanisms and magnetic anisotropy makes it an indispensable tool for characterizing both bulk materials and nanostructures. A comprehensive description of our experimental setup is provided, detailing broadband FMR techniques and the use of lock-in amplification to optimize signal-to-noise ratios, allowing for precise extraction of resonance conditions and linewidth variations. The chapter also delves into the BLS technique, emphasizing its ability to probe spin wave dynamics and analyze the interactions of magnons and phonons in thin films and nanostructures. Unlike FMR, which provides global information on magnetization dynamics, BLS offers spatial and wavevector-resolved insights, making it particularly valuable for investigating confined and propagating spin waves. The discussion includes the physical principles of light interaction, the role of inelastic light scattering in resolving spin wave spectra, and the setup for BLS using tandem Fabry-Pérot interferometry, which enables high spectral resolution and selective detection of scattered light.

5.1 Ferromagnetic resonance

Ferromagnetic resonance is a long time known technique that was first discussed theoretically in 1921 [1] and has been developed experimentally by Griffiths in 1946 [2] and further theorized by Kittel in 1947 [3]. Although it is an established technique, it remains highly effective and versatile for studying magnetization dynamics, and it continues to be one of the most widely used characterization methods in modern magnetism research. By combining in-plane and out-of-plane behavior, one can especially determine some magnetic parameters such as the saturation magnetization, the gyromagnetic ratio, the anisotropy constant and the exchange in the case of sufficiently thick films. The working principle lies on the excitation of the magnetic moment *via* the application of an external power. This forced spin precession can be achieved by putting the magnetic sample in a resonant microwave cavity which is then supplied at the frequency of one of its resonant modes. Looking at the reflected intensity with respect to the applied magnetic field allows one to see the evolution of the absorbed power, which is maximum when the resonance field is reached. This technique is sensitive enough to measure signals from very thin films (few nanometers) but is limited by the fixed working frequencies of the cavity, and is difficult to adapt other *in situ* studies. Our setup uses another method called broad-band FMR which is more versatile (more space for *in situ* strain application) and allow to perform measurements on a large window of frequency.

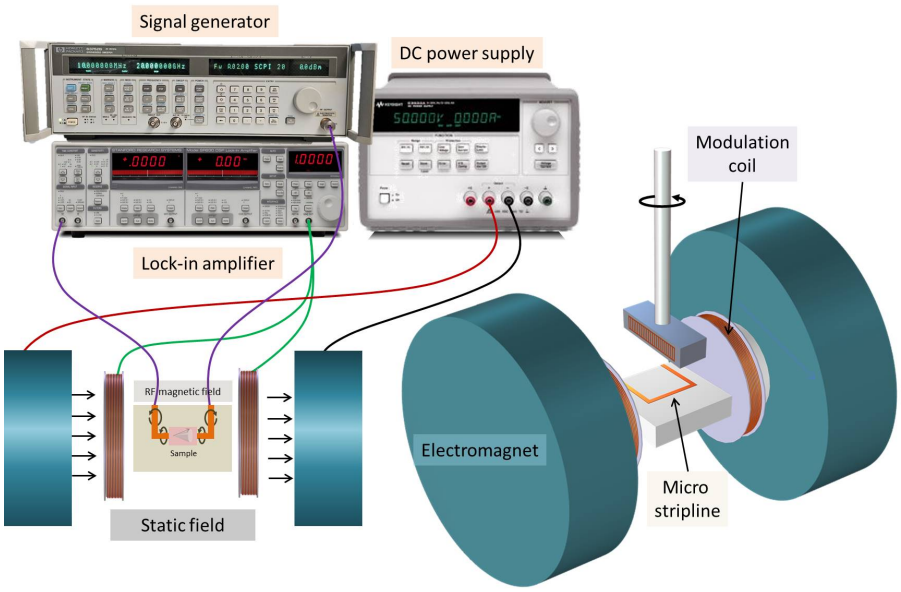

Figure 5.1: Schematic representation of the FMR setup, depicting the electromagnet, power supply, radio-frequency synthesizer, and lock-in amplifier. The diagram on the right highlights the modulation coils, the microstrip line, and the rotation rod, which allows the sample to be adjusted within its plane. In this setup, the sample consists of a ferroelectric actuator, designed to accommodate a magnetic layer either through deposition or bonding.

5.1.1 Experimental setup characteristics

Our experimental setup (shown in figure 5.1) consists of an electromagnet powered by an Agilent E3633A DC power supply, enabling the application of a static magnetic field ranging from 0 to 220 mT. The spin excitation is induced by placing the magnetic sample in contact with a copper microstrip line, which is connected to a Hewlett-Packard 83752B Synthesized Sweeper generating signals in the 10 MHz to 20 GHz range. The setup also includes an SR830 Stanford Research Systems lock-in amplifier for signal detection. The RF current flowing through the microstrip line generates a radio-frequency magnetic field, which is oriented perpendicular to the applied static field. This configuration drives the precessional motion of the magnetization, leading to a variation in the transmitted power through the strip line. At resonance, the absorbed power reaches its maximum, causing a characteristic dip in the transmission spectrum. To detect the transmitted power, the output current from the strip line is passed through a Schottky diode, which converts the high-frequency signal into a voltage proportional to the transmitted power. However, due to small variations in the output signal caused by changes in the static field, the measured signal is often buried in noise and background signals. To enhance signal detection, we employ a modulation technique: a small alternating magnetic field ($\left\|\vec{h}_{AC}\right\| = 0.5$ mT at 170 Hz) is superimposed on the static field using modulation coils. This modulated signal is fed into the lock-in amplifier, which extracts the component at 170 Hz, significantly improving the signal-to-noise ratio. Finally, our measurements yield the derivative of the transmitted power with respect to the applied static field, $\frac{dV}{dH_{AC}}$.

5.1.2 Lock-in amplification

The lock-in amplification technique is used in order to increase the FMR signal to noise ratio. The lock-in amplifier converts an input AC signal V_{in} into a DC signal by multiplying it with a reference AC signal V_{ref}:

$$V_{in}(t) = V_{in}\sin(\omega_{in}t) \tag{5.1}$$

$$V_{ref}(t) = V_{ref}\sin(\omega_{ref}t + \phi) \tag{5.2}$$

where ω_{in} and ω_{ref} are the frequencies of the input and reference signal respectively, and ϕ is the phase shift of the reference signal.

Multiplying 5.1 and5.2 gives the output signal:

$$V_{out} = \frac{V_{in}V_{ref}}{2}\left[\cos\left((\omega_{in} - \omega_{ref})t + \phi\right) - \cos\left((\omega_{in} + \omega_{ref})t + \phi\right)\right] \tag{5.3}$$

The signal being integrated over a time far larger than the input signal and the reference signal frequencies (300 ms in our case). In this case, the maximum amplification is reached when $\omega_{in} = \omega_{ref}$ with a signal close to 0 $\omega_{in} \neq \omega_{ref}$ as represented in figure5.2, meaning that

the non modulated signal is suppressed. For $\omega_{in} = \omega_{ref}$, the output amplitude integrated over a long time gives:

$$V_{out} = \frac{V_{in} V_{ref}}{2} \cos \phi \tag{5.4}$$

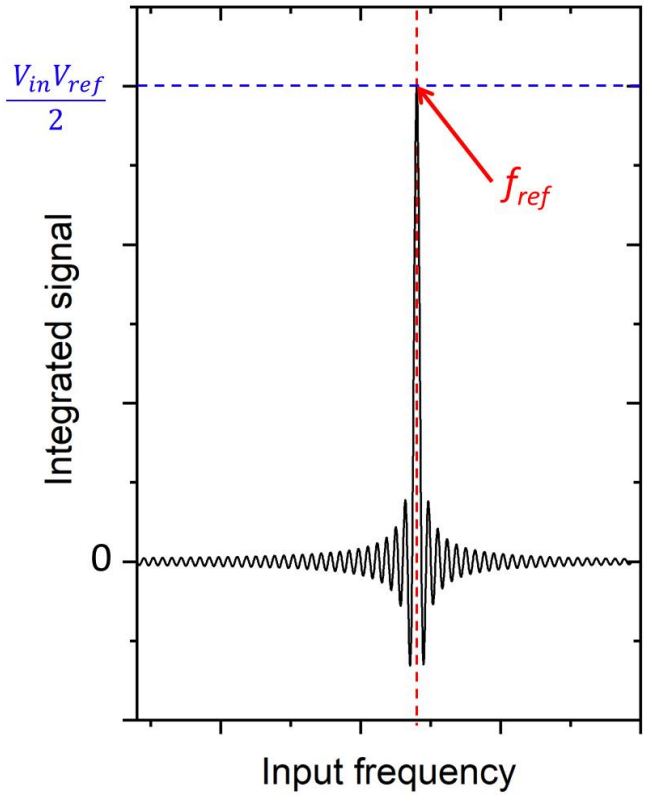

Figure 5.2: Integrated output signal over 300 ms with respect to the input frequency for a phase shift $\phi = 0$.

As the modulation is applied on the static field, the total field applied to the sample is:

$$H = H_{DC} + h_{AC} \sin(\omega_{mod} t) \tag{5.5}$$

where ω_{mod} is the modulation pulsation. The output voltage measured by the FMR setup depends on the applied modulated magnetic field:

$$V_{FMR}(H(t)) = V(H_{DC} + h_{AC} \sin(\omega_{mod} t)) \tag{5.6}$$

The output voltage given by expression 5.6 can be developed into the first-order Taylor expansion such as:

$$V_{FMR}(H(t)) = V(H_{DC}) + \frac{dV(h_{AC})}{dH} \sin(\omega_{mod} t) \tag{5.7}$$

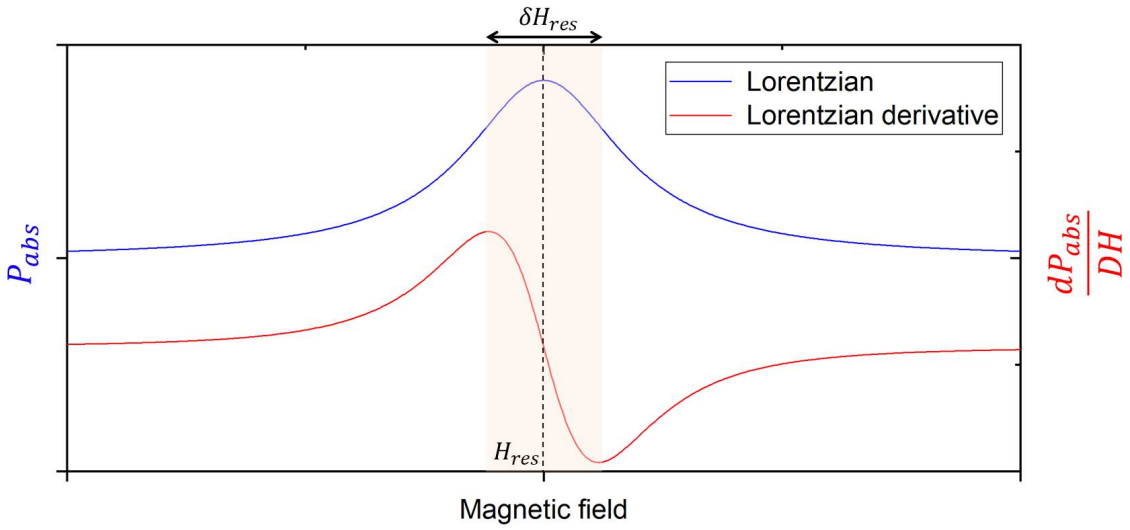

Figure 5.3: Comparison between the typical Lorentzian power absorption signal (blue) and its derivative, as measured by FMR (red). The blue curve represents the absorbed power, following a Lorentzian profile, while the red curve corresponds to the first derivative of the Lorentzian, which is the actual signal detected in FMR experiments. This derivative signal provides direct access to key magnetic parameters such as the resonance field and the linewidth (FWHM), essential for determining damping properties.

which is then multiplied by the reference signal:

$$V_{FMR}(H(t)) \times V_{ref} = V(H_{DC}) \times V_{ref} \sin(\omega_{mod} t + \phi) + \frac{dV(h_{AC})}{dH} \sin(\omega_{mod} t) \times V_{ref} \sin(\omega_{ref} t + \phi) \quad (5.8)$$

The FMR signal multiplied by the reference signal comes down one part that multiplies a constant signal $V(H_{DC})$ signal to the reference AC signal, that becomes 0 when integrated over time, and a second part corresponding to the multiplication of two AC signals that is described by equations 5.3 and 5.4. Ultimately, when $\omega_{mod} = \omega_{ref}$ the output amplified FMR signal is:

$$\frac{dV(h_{AC})}{dH} \times \frac{V_{ref}}{2} \cos\phi \quad (5.9)$$

This means that the typical FMR spectra measured with this technique do not give information on the absorbed power, but instead on the variation of the absorbed power with respect to the applied static field.

Figure 5.3 shows the difference between the absorbed power signal (blue) which is a lorentzian and the FMR measured signal (red) which is a Lorentzian derivative. From these signals, it is very easy to extract the resonance field and the FWHM (respectively H_{res} and δH_{res}) which can be helpful in some circumstances to determine the Gilbert damping constant. Fitting the experimental spectra allows one to numerically determine theses values

by considering an asymmetric Lorentzian in the form of:

$$V = V_s \times \frac{\delta H_{res}^2}{(H - H_{res})^2 + \delta H_{res}^2} + V_a \times \frac{\delta H_{res}\,(H - H_{res})}{(H - H_{res})^2 + \delta H_{res}^2} \tag{5.10}$$

$$\frac{dV}{dH_{res}} = \frac{2V_s(H - H_{res})\delta H_{res}^2}{\left((H - H_{res})^2 + \delta H_{res}^2\right)^2} + \frac{2V_a(H - H_{res})^2\delta H_{res}}{\left((H - H_{res})^2 + \delta H_{res}^2\right)^2} - \frac{V_a\delta H_{res}}{(H - H_{res})^2 + \delta H_{res}^2} \tag{5.11}$$

where V_s and V_a are respectively the symmetric and anti-symmetric contribution amplitudes [4, 5, 6]. This approach provides a precise characterization of magnetic damping and anisotropy, making it a powerful tool for studying magnetization dynamics in thin films and nanostructures. By analyzing the extracted parameters, such as the linewidth broadening and resonance field shifts, one can gain deeper insights into intrinsic and extrinsic damping mechanisms, spin-orbit interactions, and the influence of strain or interfacial effects.

5.2 Brillouin light scattering

Similarly to the ferromagnetic resonance technique, the Brillouin light scattering technique (BLS) is one of the most used techniques by the magnonic community. BLS is an optical technique that is useful for characterizing the magnetization dynamics like FMR, but has the advantage of probing the propagating behavior (wave vector $k \neq 0$ m^{-1} of waves in solids in the gigahertz range (order of 1 GHz-500 GHz) such as spin waves and acoustic waves (atomic lattice vibrations), which makes this technique also popular in the acoustic community. A lot of information can be extracted from BLS measurements which makes it a popular in various domains of magnetism such as magnonics [7], magnetoelastic interactions [8], interfacial Dzyaloshinskii-Moriya interaction [9] and more. The spin waves can be excited using this technique *via* a radio frequency pumping, but can also be measured without any external excitation as they exist naturally thanks to intrinsic thermal fluctuations in the solid that excite them randomly. Although the second approach leads to a weaker signal, it has the advantage of being simpler and to be easier to adapt for various wave vector configurations, which is our does not use any external excitation.

5.2.1 Physical principle

The BLS technique is an optical technique that is based on the inelastic interaction between light and matter to probe the intrinsic matter properties. Incident photons coming from a laser source interact with phonons and magnons in the solid and is then diffused by these waves. These magneto-optical and opto-mechanical inelastic interactions lead to a change of the photon energy after diffusion which can be translated as a wavelength/frequency shift.

The wavelength shift can occur according to two different processes presented in figure 5.4. The Stoke process results in the annihilation of a phonon or a magnon, which energy

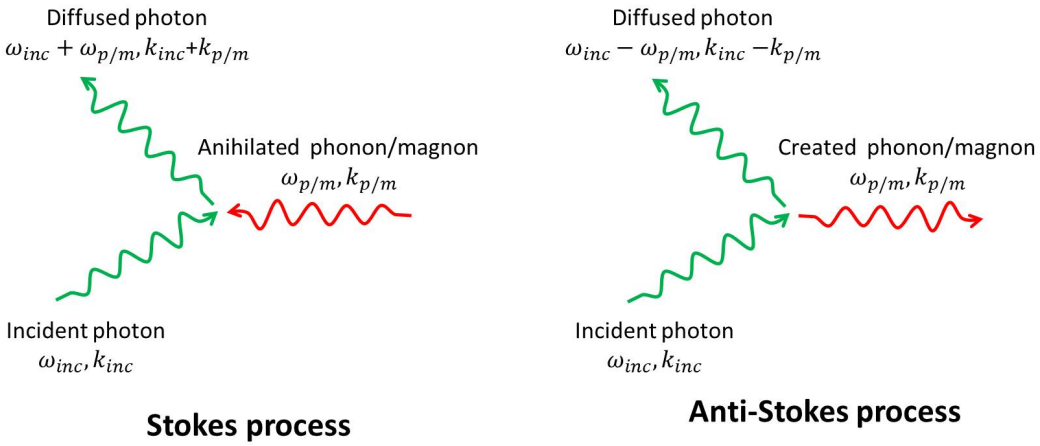

Figure 5.4: Stokes and anti-Stokes inelastic diffusion process occurring during BLS measurements.

is entirely transferred to the diffused photon that, consequently, has a positive frequency shift. As opposite, the anti-Stokes process results in the the creation of a phonon or magnon. Part of the incident photon energy is transferred to this new wave, which translates into a negative frequency shift. The magnons and phonons created have a frequency that is dependent on their wave vector. It is experimentally easy to select the wave vector of interest as the light is diffused in all directions. In most of BLS setups (if it is not all setups) the collected light is diffused in the direction of the incident beam as presented in figure 5.5.

The scheme shows the light focused on the solid with an angle θ formed with the normal of the surface. As the phonons/magnons creation/annihilation is due to the thermal fluctuation, this makes is a "rare" event, meaning that only a few of the incident photons are scattered. The remaining of the light is reflected and lost. The only exploitable light is the collected diffused light that goes back in the incident beam direction. In this configuration the different wave vectors can be written as:

$$\begin{cases} \vec{k}_{inc} = k\left(\sin\theta\vec{x} - \cos\theta\vec{y}\right) \\ \vec{k}_{ref} = k\left(\sin\theta\vec{x} + \cos\theta\vec{y}\right) \\ \vec{k}_{dif} = k\left(-\sin\theta\vec{x} - \cos\theta\vec{y}\right) \\ \vec{k}_{mag} = \vec{k}_{inc} - \vec{k}_{dif} = 2k\sin\theta \end{cases} \tag{5.12}$$

As the light wave vector only depends on laser wavelength that is fixed, the magnon wave vector is simply $\vec{k}_{mag} = \frac{4\pi\sin\theta}{\lambda}$. It is important to keep in mind that this wave vector is not entirely well defined as the angle of collection $\delta\theta$ is typically between 5° and 10°.

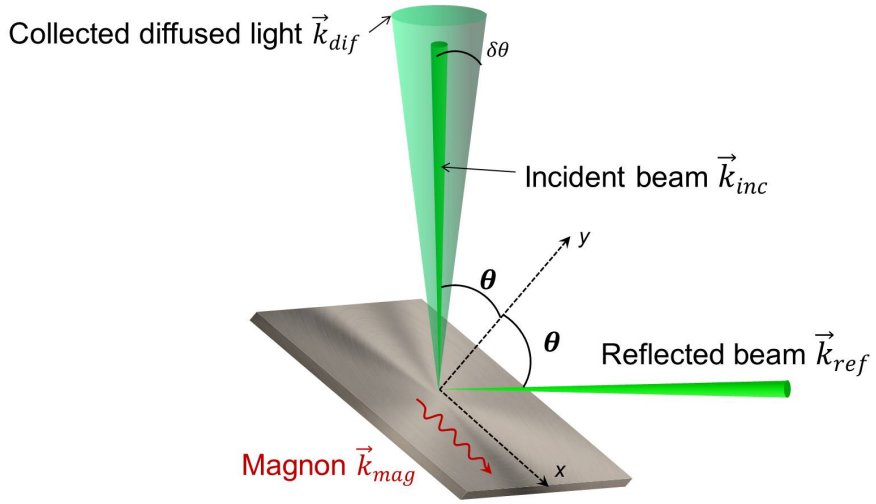

Figure 5.5: This figure illustrates the interaction of light with a solid surface in the context of Brillouin light scattering (BLS), which probes magnon dynamics.The incident beam ($\vec{k}_{inc}$) is directed onto the surface at an angle θ relative to the normal. Part of the light is reflected ($\vec{k}_{ref}$) at the same angle θ, following the law of reflection. A portion of the incident light interacts with magnons ($\vec{k}_{mag}$) within the material, leading to inelastic scattering. This interaction results in a frequency shift in the scattered light, which carries information about the spin wave dynamics in the material. The collected diffused light ($\vec{k}_{diff}$) is scattered at an angle $\delta\theta$ relative to the incident beam and is analyzed to extract information on magnon properties. This schematic represents a typical backscattering geometry used in BLS experiments, where the wavevector of the incident photons couples to the spin waves inside the material, allowing for the study of magnon dispersion and interactions in thin films and nanostructure.

5.2.2 Experimental setup

The BLS setup installed for this work is a tandem Fabry-Perot interferometer (TFP-2) which is used both for magnon and phonon characterization.

The experimental environment is illustrated and shown in figure 5.6-a) and b-e) respectively. We use a 150 mW 532 nm continuous Torus laser source with a possibility of switching with a 50 mW 473 nm continuous Spectra Physics laser source. The incident light is first split with a glass plate (95% transition, 5% reflection). The reflected light is attenuated and used as a reference beam while the transmitted light is guided towards the sample thanks to two mirrors and focused on the sample surface thanks to a plano-concave lens. The backscattered light is then collected by the same lens and collimated towards a second one that focuses the light on a set of two mirrors used to guide and align the beam inside the interferometer pinhole entrance. For this setup, we decided to design a compact sample environment by using permanent magnets. Our prototype presented on figure 5.6-b-e) can hold a maximum of three magnets on each side of the sample for the application of a

maximum of 130 mT more or less homogeneous over the whole sample surface. The whole sample holder is able to rotate according to the in-plane φ angle and out-of-plane θ angle and can be translated in the x, y and z directions. This setup presents some advantages and inconvenient, indeed, it is usually complicated to perform measurements in other configurations than the Damon Eshbach one because it is necessary to change the angle between the applied magnetic field and the incident angle. The use of electromagnets is a limiting factor as they occupy a lot of space and end up blocking the laser beam. Our compact permanent magnets can rotate at 360° without blocking the laser for $\theta = 0 - 65^{\circ}$. One of the drawbacks of this setup is the limited magnetic field that it is possible to reach, as it is fixed by the permanent magnets. It is also more difficult to tune the applied field. In our prototype we can only tune it by changing the number of magnets, but the next version of this setup which is in the process of fabrication will allow us to change mechanically the space between the two blocks of magnets. The other drawback is the slight inhomogeneity of the magnetic field that can lead to small differences of the measured spectra depending on the probed surface spot.

5.2.3 Fabry-Pérot interferometer

The Brillouin Light Scattering technique takes advantage of the small energy shift of the backscattered light. Even though the principle is similar to the Raman spectroscopy, the probed frequencies (a few GHz) are a few order of magnitude smaller than the Raman ones (a few THz). Hence, the BLS is a very sensitive technique as the reference light frequency is 563.5 THz, meaning that a shift of 1 GHz represent only a change of 0.0002 %. In order to achieve such resolution, this technique uses Fabry-Pérot interferometry (FPI). FPI uses a set of two parallel mirrors spaced by a distance L_1 that dictates the transmitted wavelength such as:

$$T = \frac{F_T}{1 + \left(\frac{2\Delta\lambda}{\pi\delta\lambda}\right)^2 \sin^2\left(\frac{2\pi L_1}{\lambda}\right)} \tag{5.13}$$

where $\Delta\lambda = \frac{\lambda^2}{2L_1}$ is the free spectral range (FSR) corresponding to the interval between two transmitted wavelength and $\delta\lambda$ the transmission peak width. The transmission equation 5.13 plotted in figure 5.7 shows that only the wavelength that satisfies the condition $L_1 = \frac{1}{2}n\lambda$ are transmitted, where n is an integer number. The F_T factor is the maximum transition that is fixed by the instrument intrinsic loss ($F_T < 1$), especially due to the mirror reflectance.

In order to improve the frequency shift range, a second FPI is used in addition to the first one. The spacing L_2 of the second FPI is slightly different from L_1, such as $L_2 = L_1 \cos\phi$, where ϕ represents the angle the angle between the two FPI. This way if the transmission peaks are superimposed for $n\lambda$,the next peaks will not coincide. The two FPI used in a tandem configuration TFP, are working as a spectrometer by changing simultaneously the L_1 and L_2 mirror spacing [10, 11, 12].

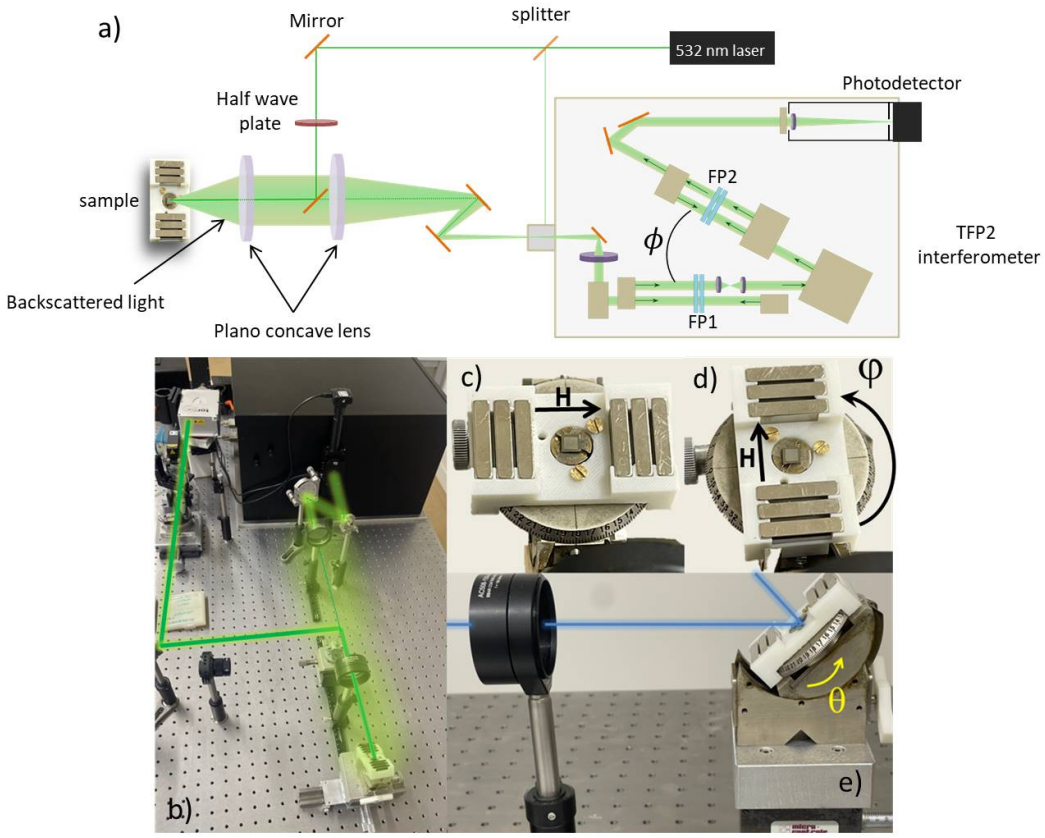

Figure 5.6: Experimental setup for Brillouin Light Scattering (BLS) measurements using a tandem Fabry-Pérot interferometer (TFP-2). (a) Schematic representation of the optical setup: a 532 nm laser is directed onto the sample, and the backscattered light is collected and focused using plano-concave lenses. A half-wave plate is used for polarization control. The collected light is directed towards a Fabry-Pérot interferometer (TFP-2), which consists of two interferometric cavities (FP1 and FP2) for high-resolution spectral analysis. The photodetector records the signal. (b) Photograph of the actual experimental setup showing the laser path and optical components.(c) Close-up view of the sample holder, where the external magnetic field ($\vec{H}$) is applied in a fixed direction. (d) Configuration allowing the in-plane rotation of the sample by an angle φ, enabling measurements at different orientations relative to the applied magnetic field. (e) Tilted configuration of the sample, allowing control over the incidence angle (θ) of the laser, which influences the detected wavevector of the scattered light.

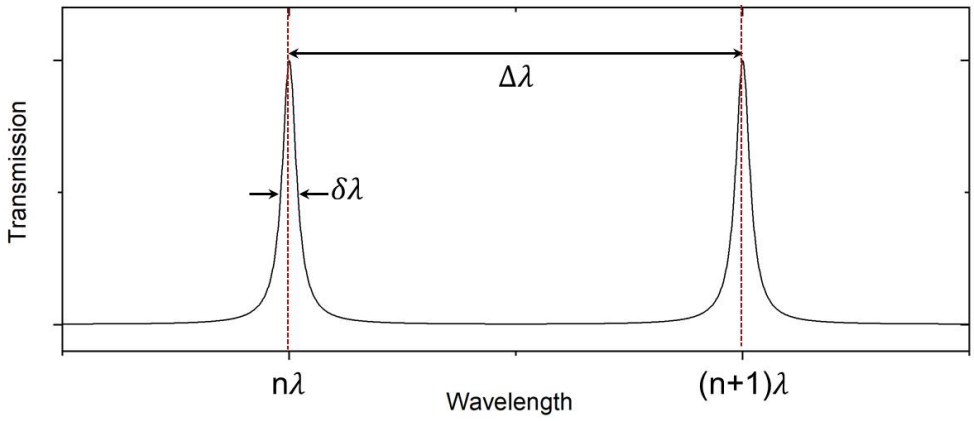

Figure 5.7: Transmission curve illustrating the spectral selectivity of the Fabry-Pérot interferometer (FPI). The peaks correspond to the resonant transmission wavelengths at integer multiples of the cavity length ($n\lambda$ and $(n+1)\,\lambda$. $\delta\lambda$ represents the linewidth (FWHM) of the transmission peak, which determines the spectral resolution of the interferometer. $\Delta\lambda$ denotes the free spectral range (FSR), the wavelength separation between two consecutive transmission maxima. A high finesse Fabry-Pérot interferometer, characterized by narrow linewidth ($\delta\lambda$) and large FSR ($\Delta\lambda$), enables precise spectral filtering, making it essential for applications such as Brillouin light scattering (BLS) and high-resolution optical spectroscopy.

5.3 Nanofabrication techniques

For this work, all the studied samples were fabricated abroad, by the group of Prof. Adeyeye Adekunle at the National University of Singapore and Durham University, in a cleanroom environment. The deposition was performed either by evaporation or sputtering, depending on the sample series. The critical step in the nanofabrication process is the nano-patterning stage. In our samples, two lithographic nano-patterning techniques were used, which will be discussed in this section. Even though none of the samples analyzed in this work were fabricated locally, a significant part of this thesis was dedicated to developing an in-house nano-patterning technique within the cleanroom of Université Sorbonne Paris Nord.

5.3.1 Deep UV lithography

The most recent samples fabricated by Pr. Adeyeye's team used the deep UV (DUV) lithography technique at Durham University. This technique which is widespread relies on the projection of the pattern of a photomask onto a photoresist coated on the substrate. The photoresist is sensitive to the wavelength of the light source which is in the low UV range in the case of the deep UV technique (typically $200-280$ nm). The exposed part of the resist

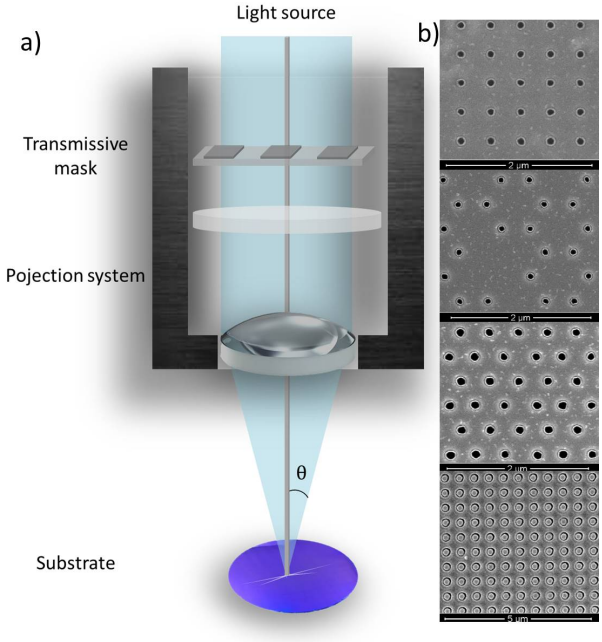

Figure 5.8: Deep UV (DUV) lithography process and resulting nanostructures. (a) Simplified schematic of the DUV lithography technique. A high-intensity light source illuminates a transmissive mask containing the desired pattern. The light is then focused and projected onto a photoresist-coated substrate through an optical projection system. The exposure angle (θ) and the numerical aperture of the system determine the resolution of the patterned structures. (b) Scanning Electron Microscopy (SEM) images of nanostructures fabricated using DUV lithography. The images show arrays of antidots and nanorings, demonstrating the capability of this technique to produce high-resolution periodic patterns over large areas with excellent uniformity.

will then be removed during the development step of the process (in the case of a positive photoresist, opposite for a negative resist). This technique has the advantage of being much faster than the electron beam lithography (EBL) while allowing one to obtain smaller patterns than the usual photolithography. The resolution r of this technique depends mainly on the light wavelength λ and on the numerical aperture NA of the optical system:

$$r = \beta \frac{\lambda}{NA} \tag{5.14}$$

where β is a factor that takes other contribution like the resist quality. A simplified schematic of a DUV system is presented in figure 5.8-a). The incident light coming from the light source is transmitted through the mask with the desired pattern. The light is then passed through a complex system of mirrors and lenses (that have been simplified largely on the scheme) that is called the projection system, that projects the pattern onto the surface

of the substrate covered by the photoresist [13, 14, 15]. The numerical aperture is defined by θ the projection half angle and n the refractive index of the media between the substrate and the projection system such as:

$$NA = n\sin(\theta) \tag{5.15}$$

Some of the fabricated samples, designed and prepared by Jay Scott at Durham University, are presented in figure 5.8-b). These samples feature arrays of antidots, which are periodic arrangements of nanoholes with varied geometries and spacing, tailored to investigate their influence on magnetic and spin-wave properties. The fabrication process ensures high precision and uniformity, making these structures particularly suitable for magnonic and spintronic applications. The last image in the series displays a distinct variation of these patterns, showing an array of anti-rings, where circular openings with a defined central core introduce additional degrees of freedom in controlling the magnetic response of the system.

5.3.2 Development of an interference lithography setup

Some of the former samples used in this work have been fabricated at the NUS in Singapore thanks to a nano-patterning technique called interference lithography (IL) [16]. This technique presents the advantage of not needing physical masks in order to induce periodic patterns. Instead, the system uses interference of light in order to create exposed and unexposed regions on the photoresist. This technique, though less common than DUV lithography, can still achieve much smaller patterns compared to conventional photolithography. Another advantage is the significantly simpler optical setup required, making it feasible for custom, homemade design.

During this thesis, we designed and installed our own setup which will be used for future thesis sample nano-patterning. Some setups in the literature use two laser sources that will interfere together as illustrated in figure 5.9-a) [17, 18]. In our case we took the Lloyd's mirror approach that uses a single laser source that interacts with itself [16]. Figure 5.9-b) shows a photography ot the experimental setup of the interference lithography system situated within the clean room at Université Sorbonne Paris Nord. The laser is a 355 nm Cobalt Zouk® laser that have the advantage of having a long coherence length. The beam is expanded thanks to a lens that have a short focal length (3 mm in our case) which allow us to obtain a spot that have a diameter close to 10 cm. We installed a pinhole behind this lens in order to filter part of the noise of the light. A collimating lens is placed after the first lens to correct the beam's divergence and ensure a parallel beam path. The beam then reaches a substrate holder composed of two rotating planes. The first plane serves as the primary substrate holder, onto which half of the beam spot is directed. The second half of the spot hits the second plane that holds a Lloyd's mirror which is an extremely flat mirror (Valumax broadband mirror, 50.8×50.8 mm^2, $\lambda/10$, 250-600 nm) that reflects the light to the sample. Finally, the sample is hit by the incident beam and the reflected beam that act as two laser sources that interfere together. The scheme of the setup is shown in figure 5.9-d). It is important to note that the Lloyd's interferometer was custom-built by Noël Girodon-Boulandet. The initial design is illustrated in figure 5.9-c), highlighting the various degrees

of freedom related to rotation and translation, which are essential for achieving precise alignment and optimal interference patterns during the lithography process.

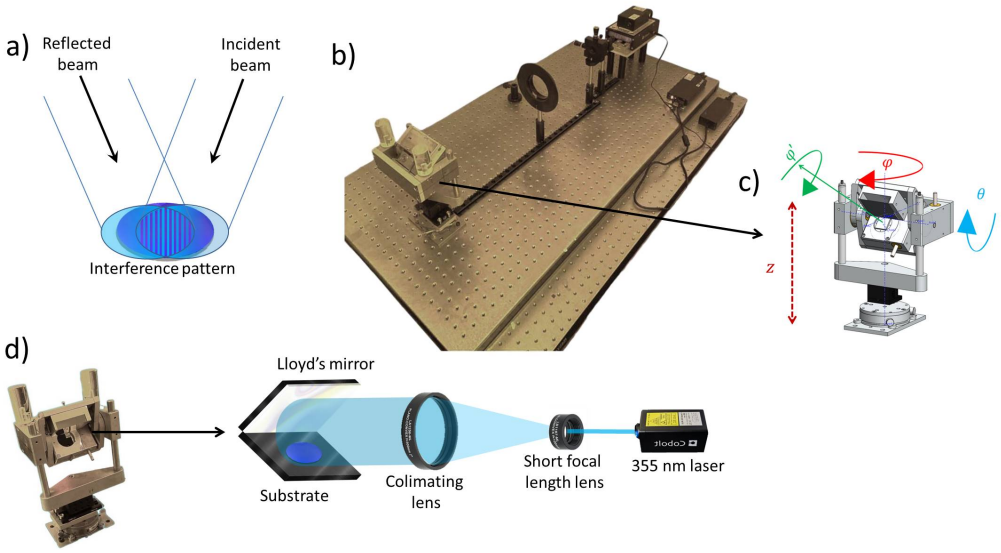

Figure 5.9: a) Basic principle of interference lithography. The incident laser beam is split into two paths: one is directly illuminating the substrate, while the other is reflected by Lloyd's mirror. The superposition of these two beams generates an interference pattern, which defines the periodic structure on the photoresist. b) Photograph of the experimental interference lithography setup, installed in the cleanroom at Université Sorbonne Paris Nord. The image highlights the key optical components and their arrangement, essential for achieving high-precision periodic nanostructures. c) Mechanical design of Lloyd's interferometer. This schematic illustrates the multiple degrees of freedom in the system, including rotation (φ), tilt (θ), and vertical translation (z), which are crucial for fine-tuning the interference pattern and optimizing the exposure conditions. d) Optical path and interference mechanism. This diagram provides a detailed overview of the beam path in the setup. A 355 nm Cobalt Zouk® laser is used as the coherent light source. The beam is expanded using a short focal length lens and collimated to ensure a uniform interference pattern. The Lloyd's mirror, positioned at 90° to the substrate, creates an interference pattern by reflecting part of the beam onto the photoresist-coated sample, enabling the fabrication of highly periodic nanostructures over large areas.

The IL is a quite cheap and versatile technique that can be use only for periodic structures patterning. A large area can be covered depending on the spot size and homogeneity in just a few minutes. It is possible to realize more complex patterns than just lines depending on the number of exposition, the in plane angle of the substrate and the exposition duration.

This technique is already giving good results, and is currently under calibration (led by Walid Mnasri who has a post-doc position in the team) in order to optimize the lift-off step of nano-fabrication. Some patterned we obtained are shown in figure 5.10 with

SEM images (top), AFM images (middle) and simulation (bottom) using a simple model of overlapping electromagnetic waves that interfere. We can see that it is possible to obtain simple 1D arrays like the nanowires array (figure 5.10-a)) and 2D patterns with square dots and antidots (figure 5.10-b and c)) obtained with two expositions at 0° and 90°. With even more exposition it is possible to complicate the variety of pattern. An example is shown in figure 5.10-d) where the patterned was used using three expositions at 0°, 45° and 90°. The angle between the mirrors defines the periodicity of the array and can be changed between each exposition in order to create more exotic patterns. It is also possible to imagine a translation system that allows one to change the position of the substrate in order to change the position of the interference on the surface. A few examples of simulated "more exotic" geometry can be seen in figure 5.10-e) [17, 18, 19, 20].

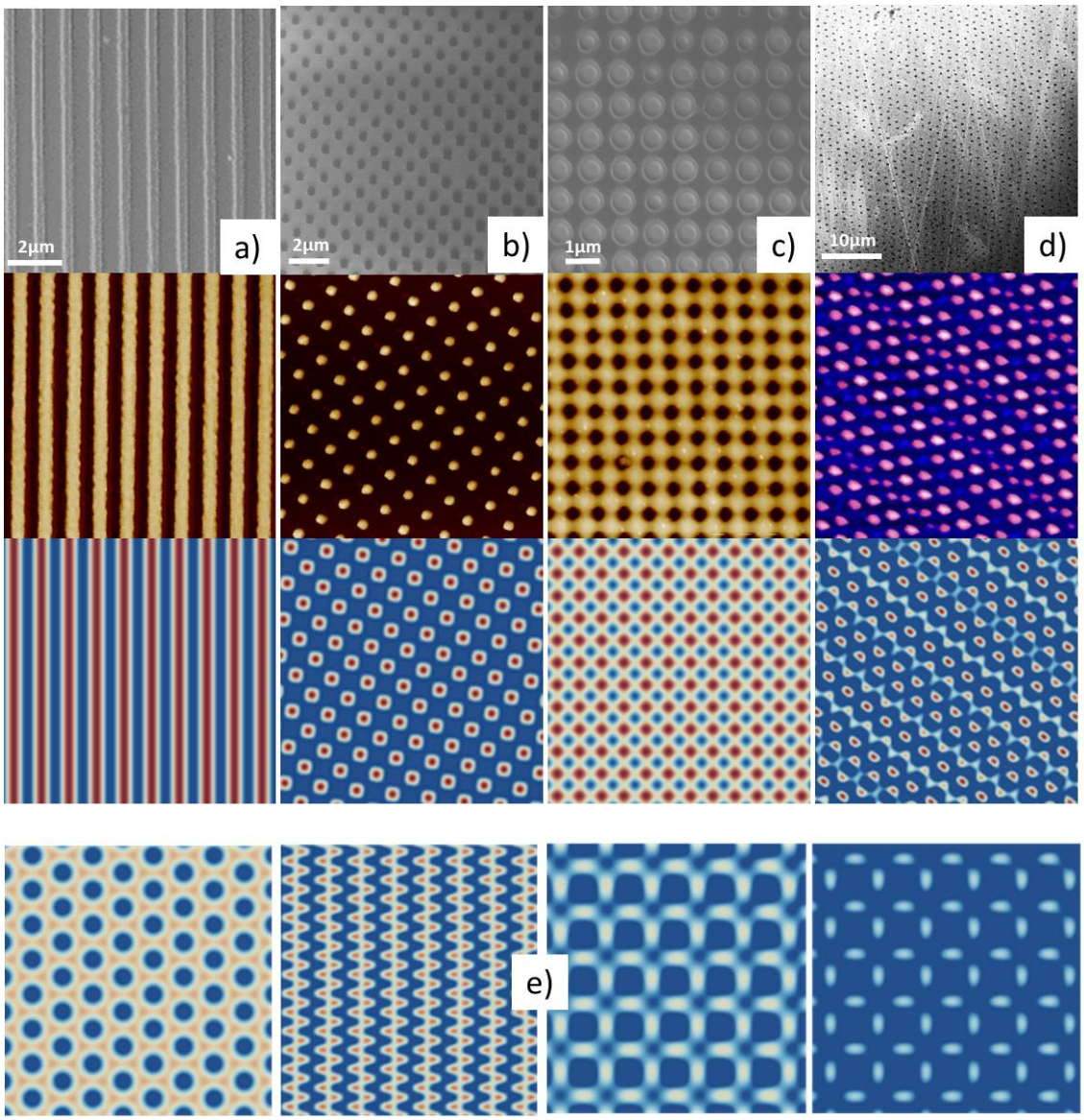

Figure 5.10: Nanopatterns fabricated using the developed interference lithography (IL) technique, with experimental and simulated results. The images showcase various periodic structures obtained using IL, demonstrating the technique's ability to generate well-ordered nanoscale patterns. (a–d) Comparison of experimental and simulated results for different nanopatterns. Top row: Scanning Electron Microscopy (SEM) images of the fabricated patterns. Middle row: Atomic Force Microscopy (AFM) images, providing topographical details of the structures. Bottom row: Simulated patterns, based on the interference of multiple laser exposures. The different patterns include: (a) Nanowire (line) arrays, obtained with a single exposure. (b) Dot arrays, formed by two perpendicular exposures. (c) Antidot arrays, where periodic holes are structured within a continuous film. (d) "Lace" patterns, created by superimposing multiple exposures at different angles. (e) Simulated interference lithography patterns showcasing additional complex structures that can be generated by varying the number of exposures, angles, and periodicities. These simulations illustrate the potential of IL for fabricating exotic nanostructures beyond simple periodic arrays.

Bibliography

[1] Gans, R., & Loyarte, R. G. (1921). Die Permeabilität des Nickels für schnelle elektrische Schwingungen. Annalen der Physik, 369(3), 209-249 5.1

[2] Griffiths, J. H. (1946). Anomalous high-frequency resistance of ferromagnetic metals. Nature, 158(4019), 670-671 5.1

[3] Kittel, C. (1947). Interpretation of anomalous Larmor frequencies in ferromagnetic resonance experiment. Physical Review, 71(4), 270 5.1

[4] Lo, C. K. (2013). Instrumentation for ferromagnetic resonance spectrometer. Ferromagnetic Resonance-Theory and Applications, 186 5.1.2

[5] Vaseghi, S. V. (2008). Advanced digital signal processing and noise reduction. John Wiley & Sons 5.1.2

[6] Reijerse, E. J. (2010). High-frequency EPR instrumentation. Applied magnetic resonance, 37, 795-818 5.1.2

[7] Gubbiotti, G., Tacchi, S., Madami, M., Carlotti, G., Adeyeye, A. O., & Kostylev, M. (2010). Brillouin light scattering studies of planar metallic magnonic crystals. Journal of Physics D: Applied Physics, 43(26), 264003 5.2

[8] Bozhko, D. A., Vasyuchka, V. I., Chumak, A. V., & Serga, A. A. (2020). Magnon-phonon interactions in magnon spintronics. Low Temperature Physics, 46(4), 383-399 5.2

[9] Stashkevich, A. A., Belmeguenai, M., Roussigné, Y., Cherif, S. M., Kostylev, M., Gabor, M., ... & Hehn, M. (2015). Experimental study of spin-wave dispersion in Py/Pt film structures in the presence of an interface Dzyaloshinskii-Moriya interaction. Physical Review B, 91(21), 214409 5.2

[10] Lindsay, S. M., Anderson, M. W., & Sandercock, J. R. (1981). Construction and alignment of a high performance multipass vernier tandem Fabry–Perot interferometer. Review of scientific instruments, 52(10), 1478-1486 5.2.3

[11] Anderson, M. W. (1982). Tandem interferometry of the low-frequency two-phonon difference spectrum of silicon. Arizona State University 5.2.3

[12] Scarponi, F., Mattana, S., Corezzi, S., Caponi, S., Comez, L., Sassi, P., ... & Fioretto, D. (2017). High-performance versatile setup for simultaneous Brillouin-Raman microspectroscopy. Physical Review X, 7(3), 031015 5.2.3

[13] Nalamasu, O., Cheng, M., Timko, A. G., Pol, V., Reichmanis, E., & Thompson, L. F. (1991). An overview of resist processing for deep-UV lithography. Journal of Photopolymer Science and Technology, 4(3), 299-318 5.3.1

[14] Totzeck, M., Ulrich, W., Göhnermeier, A., & Kaiser, W. (2007). Pushing deep ultraviolet lithography to its limits. nature photonics, 1(11), 629-631 5.3.1

[15] Bogaerts, W., Wiaux, V., Taillaert, D., Beckx, S., Luyssaert, B., Bienstman, P., & Baets, R. (2002). Fabrication of photonic crystals in silicon-on-insulator using 248-nm deep UV lithography. IEEE Journal of selected topics in quantum electronics, 8(4), 928-934 5.3.1

[16] Zighem, F., Faurie, D., Belmeguenai, M., Garcia-Sanchez, A., Lupo, P., & Adeyeye, A. O. (2017). Large area periodic ferromagnetic nanowires deposited onto a polymer substrate. Applied Physics Letters, 111(5) 5.3.2

[17] van Wolferen, H. A., & Abelmann, L. (2011). Laser interference lithography. In Lithography: Principles, processes and materials (pp. 133-148). Nova Publishers 5.3.2, 5.3.2

[18] Lu, C., & Lipson, R. H. (2010). Interference lithography: a powerful tool for fabricating periodic structures. Laser & Photonics Reviews, 4(4), 568-580 5.3.2, 5.3.2

[19] Seo, J. H., Park, J. H., Kim, S. I., Park, B. J., Ma, Z., Choi, J., & Ju, B. K. (2014). Nanopatterning by laser interference lithography: applications to optical devices. Journal of nanoscience and nanotechnology, 14(2) 1521-1532. 5.3.2

[20] Hung Jr, Y., Chang, H. J., Chang, P. C., Lin, J. J., & Kao, T. C. (2017). Employing refractive beam shaping in a Lloyd's interference lithography system for uniform periodic nanostructure formation. Journal of Vacuum Science & Technology B, 35(3) 5.3.2

6 Characterization and simulation of periodic arrays of nanostructures

Contents

This chapter focuses on the characterization and simulation of periodic arrays of nanostructures, specifically investigating the magnetic properties of nanoscale antidot arrays and width-modulated nanowires. Utilizing our numerical model, we demonstrate the behavior of continuous films under static strain, validating our approach through comparisons with experimental results, literature, and other micromagnetic simulation software. The section on antidot arrays highlights the intricate dynamics of ferromagnetic resonance (FMR) in systems with varied thickness, revealing complex magnetic modes influenced by structural geometries. The findings indicate a significant interplay between thickness and magnetic behavior, with distinct modes identified, including Damon-Eshbach and backward volume modes. Furthermore, we explore width-modulated nanowires, emphasizing the correlation between localized magnetization inhomogeneities and mode frequency.

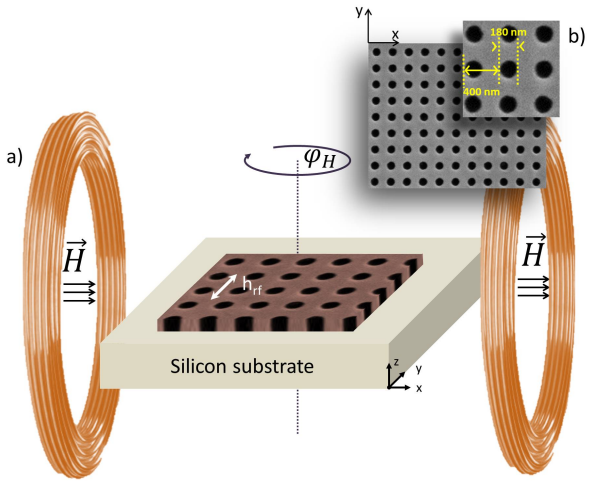

Figure 6.1: a) Schematic illustrating the array of $Ni_{80}Fe_{20}$ antidot under investigation. The h_{rf} denotes the radiofrequency pumping field while φ_H represents the in-plane angle between the applied magnetic field $\vec{H}$ and $\vec{h}_{rf}$. b) A scanning electron microscopy image depicting the studied array, which has a periodicity of 400 nm and a hole radius of 90 nm.

6.1 Magnetic arrays of antidots

6.1.1 Ferromagnetic resonance characterization

Nanoscale antidot arrays with a fourfold symmetry were fabricated on Si(001) substrates using DUV lithography at 248 nm [1]. The process involved applying an anti reflective layer, depositing $Ni_{80}Fe_{20}$ films and performing lift-off in unexposed areas. The completion of the lift-off process was confirmed through scanning electron microscopy and atomic force microscopy inspection. An example of scanning electron microscopy image of the samples can be seen in figure 6.1-b). Additionally, reference samples were prepared as continuous films during the same deposition run. Two different thicknesses, 40 nm and 80 nm, were chosen for this study. At 40 nm, the system can be considered as predominantly 2D, where the magnetization tends to remain in the plane even without the presence of an applied magnetic field. In contrast, at 80 nm, the system could exhibit a more intricate behavior. In particular, the non-propagating modes exhibit diverse profiles across the thickness, adding complexity to their characteristics.

While the magnetic modes in continuous thin films can often be straightforwardly predicted and described using the well-established Smit-Beljers relation [2], the scenario becomes considerably more intricate when dealing with periodic arrays of antidots due to the presence of holes. In these antidot arrays, the magnetostatic waves do not exhibit homogeneous behavior across the entire surface; instead, they become localized within specific regions of the lattice [3, 4, 5, 6, 7, 8]. To illustrate this phenomenon, we present in figure 6.2

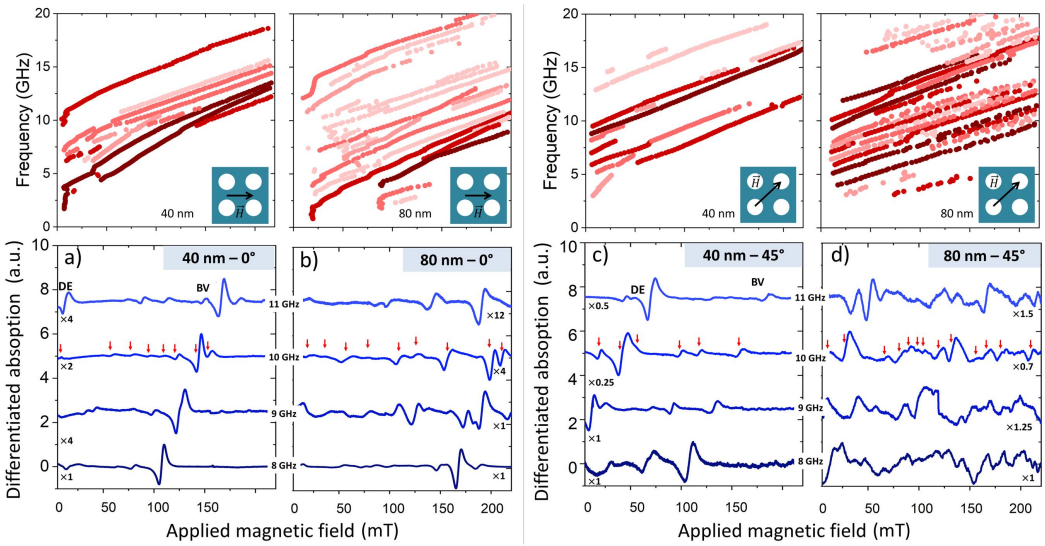

Figure 6.2: FMR spectra recorded at different frequencies from the two studied arrays (40 nm and 80 nm) with $\varphi_H = 0^\circ$ (a-b) and $\varphi_H = 45^\circ$ (c-d). The red arrows in the 10 GHz spectra indicate the presence of a magnetostatic mode. The amplitude of some spectra has been multiplied by a coefficient for clarity.

a set of typical spectra obtained for two thicknesses of identical antidot geometries. This figure presents spectra obtained from both arrays, recorded at various frequencies and for two specific angles, $\varphi_H = 0^\circ$ and $\varphi_H = 45^\circ$. The spectra reveal the presence of multiple modes, indicative of complex dynamic magnetic behaviors within these arrays. For clarity, red arrows have been added to the spectra measured at 10 GHz, highlighting mode positions. The amplitudes of certain spectra have been scaled by a coefficient to enhance clarity, this coefficient is indicated in each spectrum. Focusing on the 40 nm array at an angle of $\varphi_H = 0^\circ$, we can distinguish two prominent modes. The first mode appears at a low magnetic field and is designated as the DE-like mode, which stands for Damon-Eshbach like-mode. The second notable mode occurs at a higher magnetic field and is referred to as the BV-like mode, which is short for Backward volume mode. The Damon-Eshbach and backward volume mode designation is usually used in the case of propagating spin waves in continuous films in order to differentiate the spin waves propagating in the in-plane direction perpendicular to the magnetization (DE) and along the direction of the magnetization (BV). In our case we are considering two modes which can be seen as standing waves with an effective wave vector k_{eff} perpendicular to the magnetization (DE-like mode) or along the magnetization (BV-like mode). In addition to these dominant modes, the spectra also exhibit several less intense modes situated between the DE-like and BV-like modes. For example, in the spectrum recorded at 11 GHz, “the DE-like” mode can be observed around a magnetic field of approximately 15 mT, while the “BV-like” mode appears at a significantly higher field of around 160 mT. Moreover, the resonance fields of both the DE-like and BV-like modes shift with changing frequency. If we focus on the 80 nm array, a larger number

of modes become apparent. The prominence of certain modes compared to others is much less clear. However, the frequency dependence of the modes is rather similar. The fact that only the thickness varies between these two arrays leads to conclude that these additional modes result from the larger thickness, providing the modes a greater freedom to spread across the thickness.

6.1.2 OOMMF and COMSOL micromagnetic simulations

Micromagnetic simulations under OOMMF software were conducted to investigate the magnetic modes and their frequency dependencies in a square array of antidots [9, 10]. The array consisted of 100 antidots (10×10 holes) with a diameter of 180 nm and a periodicity of 400 nm. Cuboid cells with a volume of $5\times5\times5$ nm^3 were used for the simulations. The simulation parameters were determined from the ferromagnetic resonance (FMR) analysis of the reference continuous films, including the saturation magnetization ($M_s = 8\times10^5$ A.m^{-1}), gyromagnetic ratio ($\gamma = 1.91$ rad.s^{-1}T^{-1}) and exchange stiffness ($A = 13\times10^{-12}$J.m^{-1}). Indeed, the intrinsic magnetic parameters of the samples were determined by investigating the magnetization dynamics of $Ni_{80}Fe_{20}$ thin films of similar thicknesses (40 nm and 80 nm) than the studied arrays of antidots using FMR technique [2, 11]. By employing the Landau-Lifshitz-Gilbert (LLG) equation solved in spherical coordinates, we conducted an analysis to fit our experimental data and extract the magnetic parameters that govern the behavior of the films. In the simulations, the Landau-Lifshitz-Gilbert equation was solved with a damping constant (α) of 0.5 for both the continuous film and square array systems. The equilibrium states were obtained by applying a static magnetic field ranging from 20 to 220 mT along the x-axis. The dynamic response of the systems was then studied by perturbing the equilibrium state with a short magnetic field pulse applied orthogonally. The relaxation of the system was governed by the Landau-Lifshitz-Gilbert equation with a damping constant of $\alpha = 0.008$. The magnetic pulse was defined as $\widetilde{h} = h_0 \cdot \mathrm{sinc}[2\pi f_{cut}(t - t_0)]$, where f_{cut} was set to 25 GHz and the sampling frequency (f_s) was 200 GHz.

Each dynamic simulation was performed over a duration of 20 ns, divided into 4000 stages using the Runge-Kutta algorithm. The magnetization configuration was recorded for each elementary volume and stage, and the Fourier transform method was applied to obtain the resonance frequencies associated with the different magnetic modes. The magnetization component $m_y = M_y/M_s$ was used for the Fourier transform, where M_y represents the y-component of magnetization and M_s is the saturation magnetization. To obtain the profiles of each mode, the system was excited by applying a cosine function at the frequency of each respective mode. This excitation allowed us to capture the dynamic behavior and visualize the spatial distribution of the magnetization. The resulting data were processed using image analysis techniques to extract the detailed profiles of the modes. By analyzing these profiles, we gained insights into the spatial localization and intensity variations of the non-propagating modes within the system.

Figure 6.3 presents the complete dependencies of the mode frequencies as a function of the applied magnetic field for both arrays and φ_H angles. The experimental data extracted from the spectra partly presented in figure 6.2 are represented by symbols (orange circles)

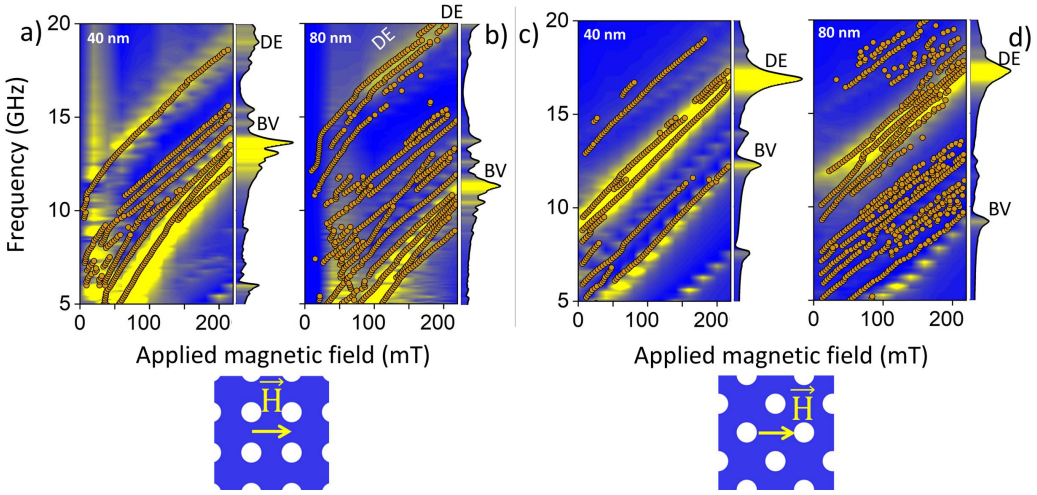

Figure 6.3: Experimental (symbols) and numerical results (colormaps) are presented with a magnetic field applied along 0° (a-b) and 45° (c-d) for the two studied systems. The colors represent the relative power spectral density obtained through micromagnetic simulations, while the symbols correspond to the experimental data. A typical simulated spectrum (at $H = 220\,\mathrm{mT}$) is shown for each graph. In addition, a small sketch of the studied systems shows the direction of the applied field.

while the colormaps are generated from micromagnetic simulations. The colormaps provide frequency positions and relative intensities and correspond to simulated spectra for various applied magnetic field strengths. The two schematics correspond to the experimental configurations used, illustrating measurements at $\varphi_H = 0^\circ$ (figures 6.3-a) and 6.3-b)) and $\varphi_H = 45^\circ$ (figures 6.3-c) and 6.3-d)). At $\varphi_H = 0^\circ$, we have the confirmation that the number of observed modes is significantly influenced by the thickness of the array.

Specifically, in the 40 nm array, the spectra clearly display the primary modes: a solitary mode for DE-like mode and several accompanying modes for the BV-like one. In contrast, the 80 nm array exhibits a less distinct separation between the DE- and BV-like modes, as previously shown in the experimental spectra (see figure 6.2). Notably, modes persist between 5 and 10 GHz for magnetic fields exceeding 200 mT, contrasting sharply with the absence of such modes in the 40 nm array under similar conditions. A simulated spectrum at 220 mT is provided alongside each colormap to demonstrate the relative intensity distribution of modes. The simulations effectively delineate distinct mode clusters, particularly highlighting the DE-like and BV-like modes within the 40 nm array. The relative intensities and frequency positions derived from these simulations fit well with experimental observations.

To determine the origin of each mode in both systems, we determine the spatial profiles of each mode by exciting the systems with a cosine function at the frequency of each mode. The main results are presented in figure 6.4. The simulation results revealed a wide range of possible spatial distributions for the modes. The colormap represents m_y component

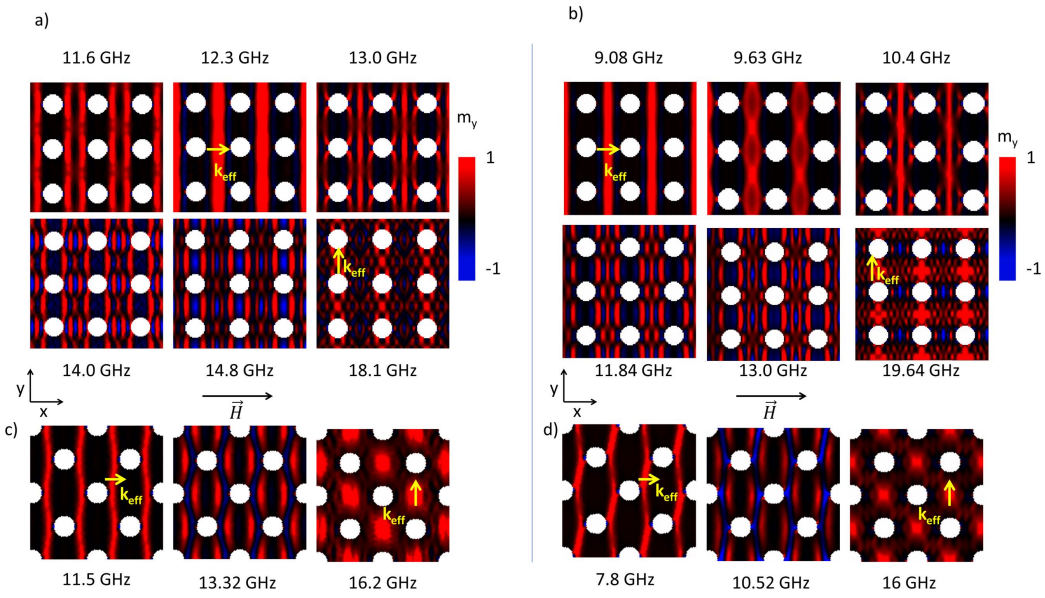

Figure 6.4: Spin precession amplitudes determined at $H = 200$ mT (applied along the x-axis) obtained through micromagnetic simulations. The color coding represents m_y component of the magnetization: red and blue areas indicate high precession amplitudes, while black areas indicate zero precession amplitudes. The k_{eff} vector in some profiles indicate an effective wave-vector that can be associated to the mode. a) and b) correspond to profiles calculated at $\varphi_H = 0^\circ$ while c) and d) are profiles obtained at $\varphi_H = 45^\circ$.

of the magnetization, the applied magnetic field being applied along x direction, red and blue areas indicate high precession amplitudes, while black areas indicate zero precession amplitudes. All the presented mode profiles in figure 6.4 are determined for a magnetic field of 200 mT, meaning that the static magnetization configuration is almost saturated along the x-axis. In figure 6.4 -a), which pertains to the 40 nm sample with an applied magnetic field angle $\varphi_H = 0^\circ$, we have illustrated effective wave vectors $\vec{k}_{eff}$ on two of the mode profiles: one at 12.3 GHz and the other at 18.1 GHz. These two profiles correspond to what we have previously referred to as the BV-like mode and the DE-like mode. In the first case, we observe that the wave vector is oriented along the direction of the applied magnetic field, (i. e. along the static magnetization). In contrast, in the second case, the wave vector is perpendicular to the applied field. This observation is interesting as it aligns with the characteristics of the DE and BV modes typically found in magnetic thin films. The BV-like mode represents a situation where the spin waves propagate along the direction of the static magnetization. On the other hand, the DE-like mode depicts a scenario where spin waves propagate perpendicular to the magnetization direction. The other modes between DE-like and BV-like modes correspond to a mix between them in terms of spatial area. A similar behavior can be observed in figure 6.4 -b) for the 80 nm array at $\varphi_H = 0^\circ$. The BV-like mode and the DE-like are however slightly shifted in frequency and the difference

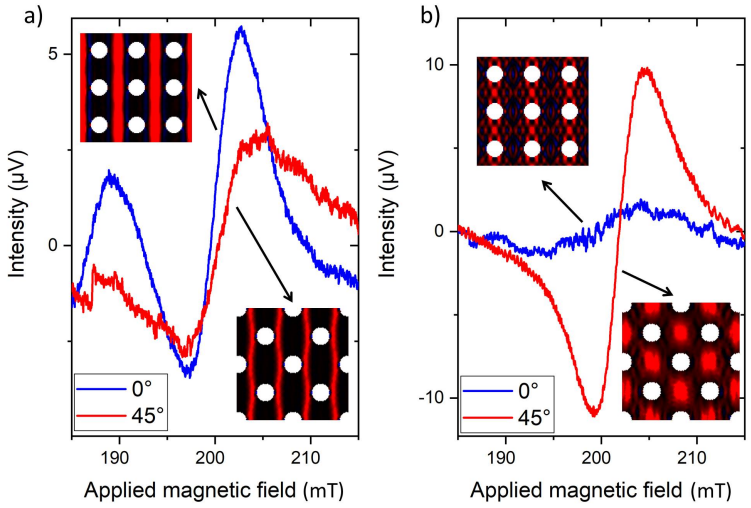

Figure 6.5: a) BV-like mode measured by FMR at 0° and 45° for the 40 nm sample. Spectra where the resonance field was equal (12 GHz at 0° and 14 GHz at 45°) are shown to compare their intensity for an equivalent static configuration. Mode profiles were calculated for this applied magnetic field (i.e., 200 mT). b) DE-like mode measured by FMR at 0° and 45° for the 40 nm sample. Spectra where the resonance fields coincide at 200 mT were measured at frequencies of 18 GHz (0°) and 17 GHz (45°).

between this mode is higher (around 6 GHz for the 40 nm array and 10 GHz for the 80 nm at 200 mT). Moreover, the 80 nm array exhibits a significantly larger number of intermediate modes between the DE- and BV-like modes. These intermediate modes (not all of which are displayed) often exhibit lower amplitudes. They represent a combination or hybridization of the DE-like and BV-like modes. This indicates a complex interplay between different types of spin wave modes within the array, resulting in a richer and more intricate spectrum of magnetic behaviors.

At $\varphi_H = 45^\circ$, the DE- and BV-like modes are still present for both thickness. It is interesting to note that the spatial area occupied by the BV-like mode is now lesser than the DE-like mode. This explains what we have observed in the FMR experimental spectra; namely, an inversion of the relative intensities between these two main modes occurs when the sample is rotated by 45°. To go further, we have calculated the intensity ratio ($r = \frac{I_{0^\circ}}{I_{45^\circ}}$) of the mode intensities for the 40 nm array along the two different directions (see figure 6.5). The experimental value of this ratio (r_{exp}) has been calculated from the amplitude of FMR peaks and the simulated (r_{sim}) one has been extracted from the simulated spectral density:

Mode	r_{exp}	r_{sim}
mode	0.31	0.33
BV-like mode	1.6	1.4

The comparison between the experimental and simulated intensity ratios indicated a

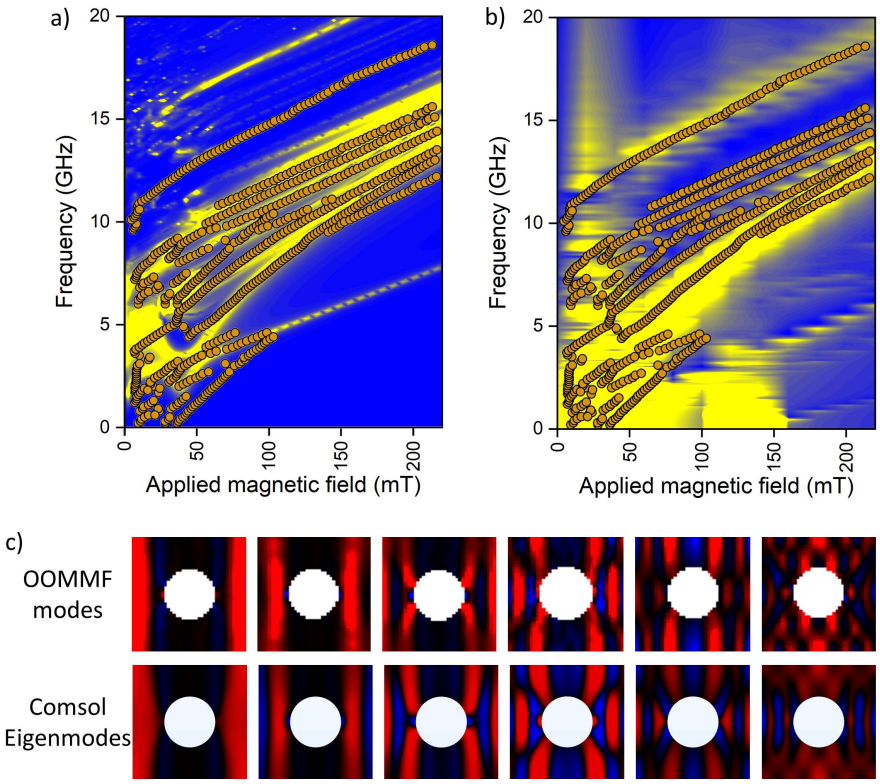

Figure 6.6: Comparison between a) Comsol simulations performed with the frequency domain solver and b) the OOMMF simulations. c) The mode profiles obtained with the eigenfrequency solver were compared with the mode profiles calculated with OOMMF.

high level of agreement for both modes. Micromagnetic simulations allowed us to determine both the positions of the peaks as well as their relative intensities. They highlighted the simultaneous measurement of DE and BV modes within the antidot arrays. It confirmed that the additional modes in the 80 nm array were due to a larger thickness. The presence of numerous magnetic modes in magphonic crystals benefits the magnon-phonon coupling [12, 13, 14]. When phonon and magnon branches intersect, new forbidden bands can emerge, controlling wave propagation within the material. This capability could support applications like frequency filtering and enhanced spintronic devices, using these new properties for advanced signal processing.

The modes calculated with OOMMF allow us to have a reference in order to verify our Comsol simulations[15, 16]. The comparison is shown in figure 6.6 where we started to reproduce the FMR simulations. We can see on the $f(\mu_0 H)$ mapping (figure 6.6-a,b)) that the results obtained with our Comsol simulations are very close to the experiments and seem more consistent than the OOMMF ones. This could be due to the lack of periodic boundary conditions in our OOMMF model. It is interesting to see that our highest experimental mode in terms of frequency seems to badly reproduce by the Comsol simulation. The main modes profile have then been compared with both software in figure 6.6-c). Their correspondence

is almost perfect, which confirms the accuracy of our model.

6.2 Width modulated nanowires

In order to further the comparison of our approach with experiments, we have conducted FMR measurements on more complex objects. For this purpose, a 20 nm thick $Ni_{80}Fe_{20}$ periodic array of width-modulated nanowires [17, 18] deposited on Si have been studied. A scanning electron microscope image is presented as an insert in figure 6.7-a), one can note the width modulation of the nanowire which makes this array more complex from a geometrical point of view. Thus, the width is modulated so that the largest part is 230 nm wide and the thinnest part is 150 nm.while the periodicity of the array is around 600 nm (along y) and the modulation periodicity is 280 nm (along x). This modulation creates local inhomogeneities in the magnetization which creates several possibilities for the localized magnetic modes as compared to a uniform nanowire geometry.

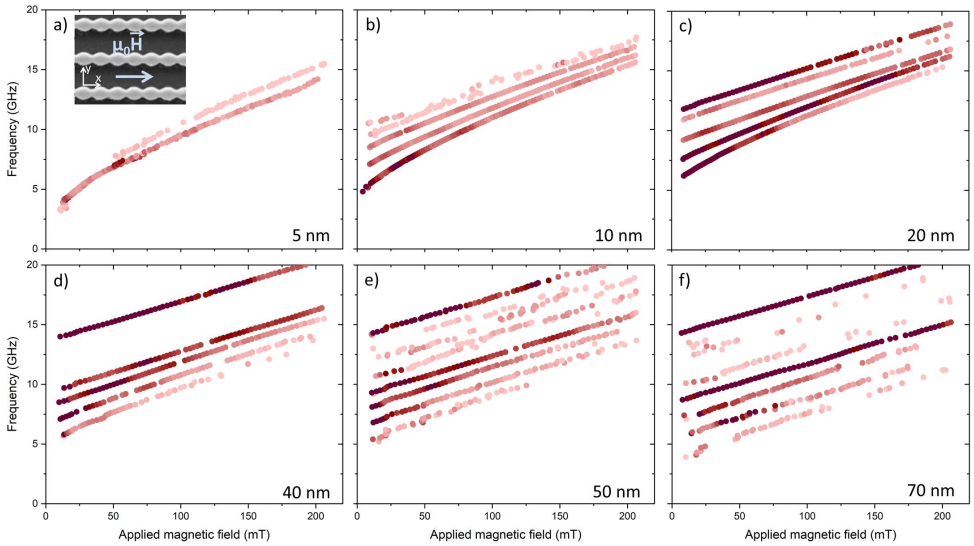

Figure 6.7: FMR results obtained for the same array of width modulated nanowires for thicknesses of a) 5 nm, b) 10 nm, c) 20 nm, d) 40 nm, e) 50 nm and f) 70 nm. The dot colors indicates the relative intensity of the modes. The darker the modes, the more intense they are.

Figure 6.7-a-f) shows the influence of the thickness on the number of modes, but also on their quality. The 5 nm thick sample showed only two modes very close in frequency that had a very small intensity. As the thickness increases, other modes appear and the signal gets stronger. For the 50 nm and 70 nm thick samples a lot of modes can be measured (between 7 and 8 modes) but the signal starts deteriorating. For this part of the study we chose to focus on the sample that gave us the best signal which is the 20 nm thick sample presented in figure 6.7-c).

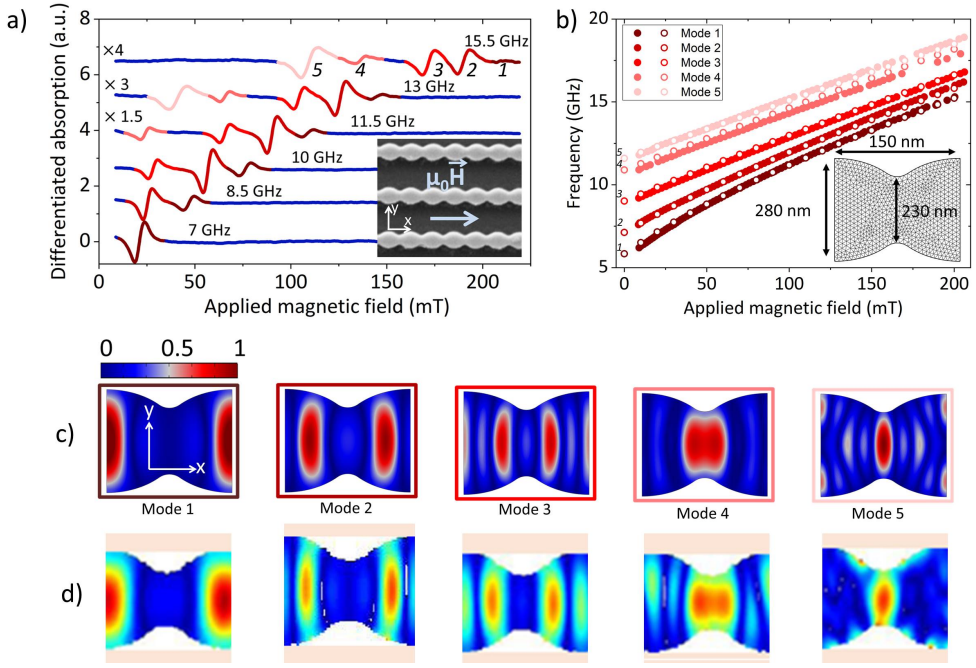

Figure 6.8: a) Typical sweep-field FMR spectrum recorded at a different driven frequency (from 7 to 15.5 GHz) in a 20 nm thick $Ni_{80}Fe_{20}$ width-modulated array of nanowires with a magnetic field applied along the nanowires (along x direction). The insert shows a scanning electron microscopy image of this array: the periodicity of the array is 600 nm along y while the width-modulation periodicity is 280 nm (larger width is 230 nm and the thinnest is 150 nm). b) Experimental (filled symbols) and simulated frequency (open symbols) variations of the mode frequencies as function of the magnetic field of array of nanowires. The insert shows a typical mesh of the representative elementary volume used for the simulations. c) Top view of the calculated 3D magnetic mode profiles where colors encode m_y (see scale-bar). d) Edited result from [18]

Figure 6.8-b) presents typical spectra obtained for a magnetic field applied along the nanowires (along x) at multiple driven frequencies. One can clearly note the presence of at least five distinguishable modes of different amplitudes and of different linewidths. Similar to the thin film, we have first defined a representative elementary volume which is presented as an insert in 6.8-c). The magnetic mode energies and their 3D profiles have been then calculated. We have been able to identify the five experimental modes by comparing the numerical and experimental variations of their frequencies (see open symbols in figure 6.8-c)). Typical extracted 3D modes are presented in 6.8-c); we found a good correlation between the experimental magnetic mode amplitudes and their calculated profiles: the larger the spin precession region, the larger the amplitude. This correlation is also valid for the experimental linewidth of the modes: the larger the region involved by the precession of the mode, the larger the experimental linewidth. Figure 6.8-d) shows the work of L. L. Xiong & al. in which they studied similar samples. The profile presented here were

obtained by them in the paper presented in [18] in which they used LLG micromagnetic simulator to perform their simulations. They did not simulate a 20 nm thick geometry but we selected a mix of what they obtained for 10 nm and 30 nm. We can easily see that the profiles obtained in our work with our numerical method are very consistent with what is obtained with more conventional micromagnetic softwares as they are almost identical as those calculated by this other group with LLG micromagnetic simulator and by us with the previous OOMMF study.

In the following chapter, the magnetoelastic energy term is incorporated into the LLG finite element resolution to account for the indirect magnetoelastic effect induced by the presence of external strain.

Bibliography

[1] Adeyeye, A. O., & Singh, N. (2008). Large area patterned magnetic nanostructures. Journal of Physics D: Applied Physics, 41(15), 153001 6.1.1

[2] Farle, M. (1998). Ferromagnetic resonance of ultrathin metallic layers. Reports on progress in physics, 61(7), 755 6.1.1, 6.1.2

[3] Bali, R., Kostylev, M., Tripathy, D., Adeyeye, A. O., & Samarin, S. (2012). High-symmetry magnonic modes in antidot lattices magnetized perpendicular to the lattice plane. Physical Review B—Condensed Matter and Materials Physics, 85(10), 104414 6.1.1

[4] Wang, C. C., Adeyeye, A. O., & Singh, N. (2006). Magnetic antidot nanostructures: effect of lattice geometry. Nanotechnology, 17(6), 1629 6.1.1

[5] Tacchi, S., Madami, M., Gubbiotti, G., Carlotti, G., Adeyeye, A. O., Neusser, S., ... & Grundler, D. (2010). Angular dependence of magnetic normal modes in NiFe antidot lattices with different lattice symmetry. IEEE transactions on magnetics, 46(6), 1440-1443 6.1.1

[6] Tacchi, S., Madami, M., Gubbiotti, G., Carlotti, G., Adeyeye, A. O., Neusser, S., ... & Grundler, D. (2010). Magnetic normal modes in squared antidot array with circular holes: A combined Brillouin light scattering and broadband ferromagnetic resonance study. IEEE Transactions on Magnetics, 46(2), 172-178 6.1.1

[7] D. H. Y. Tse, S. J. Steinmuller, T. Trypiniotis, D. Anderson, G. A. C. Jones, J. A. C. Bland, and C. H. W. Barnes, Physical Review B 79, 054426 (2009) 6.1.1

[8] Tse, D. H. Y., Steinmuller, S. J., Trypiniotis, T., Anderson, D., Jones, G. A. C., Bland, J. A. C., & Barnes, C. H. W. (2009). Static and dynamic magnetic properties of Ni 80 Fe 20 square antidot arrays. Physical Review B—Condensed Matter and Materials Physics, 79(5), 054426 6.1.1

[9] Mu, C. P., Wang, W. W., Zhang, B., Liu, Q. F., & Wang, J. B. (2010). Dynamic micromagnetic simulation of permalloy antidot array film. Physica B: Condensed Matter, 405(5), 1325-1328 6.1.2

[10] Magadeev, E. B., Vakhitov, R. M., & Kanbekov, R. R. (2022). Stability of nontrivial magnetic structures in ferromagnetic films with antidots. Journal of Physics: Condensed Matter, 35(1), 015802 6.1.2

[11] Zighem, F., Roussigné, Y., Chérif, S. M., Moch, P., Youssef, J. B., & Paumier, F. (2010). Magnetic properties of exchange biased and of unbiased oxide/permalloy thin layers: a ferromagnetic resonance and Brillouin scattering study. Journal of Physics: Condensed Matter, 22(40), 406001 6.1.2

[12] Trzaskowska, A., Graczyk, P., Babu, N. K. P., Zdunek, M., Głowiński, H., Kłos, J. W., & Mielcarek, S. (2022). The studies on phonons and magnons in [CoFeB/Au] N multilayers of different number of repetitions. Journal of Magnetism and Magnetic Materials, 549, 169049 6.1.2

[13] Graczyk, P., & Krawczyk, M. (2017). Coupled-mode theory for the interaction between acoustic waves and spin waves in magnonic-phononic crystals: Propagating magnetoelastic waves. Physical Review B, 96(2), 024407 6.1.2

[14] Babu, N. K., Trzaskowska, A., Graczyk, P., Centała, G., Mieszczak, S., Głowiński, H., ... & Kłos, J. W. (2020). The interaction between surface acoustic waves and spin waves: The role of anisotropy and spatial profiles of the modes. Nano letters, 21(2), 946-951 6.1.2

[15] Challab, N., Aboumassound, A. D., Zighem, F., Faurie, D., & Haboussi, M. (2019). Micromagnetic modeling of nanostructures subject to heterogeneous strain fields. Journal of Physics D: Applied Physics, 52(35), 355004 6.1.2

[16] COMSOL Multiphysics® v. 6.1. www.comsol.com. COMSOL AB, Stockholm, Sweden. 6.1.2

[17] Xiong, L. L., & Adeyeye, A. O. (2016). Dynamic behavior of Ni80Fe20 nanowires with controlled periodic width modulation. Applied Physics Letters, 108(26) 6.2

[18] Xiong, L. L., Kostylev, M., & Adeyeye, A. O. (2017). Magnetization dynamics of Ni 80 Fe 20 nanowires with continuous width modulation. Physical Review B, 95(22), 224426 6.2, 6.8, 6.2, 10.2.3

7 Elastic strain effects in periodic arrays of nanostructures

Contents

The previous chapters presented measurements obtained on thin films, antidots array and modulated nanowires arrays free of strain as well as experiments performed on strained continuous films. In this chapter, periodic nanostructures submitted to strain will be studied experimentally in a first step and then by purely numeric simulations.

7.1 Magnetic arrays of antidots under static strain

For this study a 20 nm thick array of antidot made of a $Ni_{60}Fe_{40}$ alloy was deposited on a 127.5 µm thick polyimide substrate (also known as Kapton®) by interference lithography. The resulting array presented holes with a diameter $D = 250$ nm separated by a period of $a = 600$ nm as represented on figure 7.1-a). The experimental setup used for the *in situ* strain and measurement was the same as what has been presented for the continuous film strain experiment [1, 2]. The polymer substrate was then glued on the same type of ferroelectric actuator on which voltage was applied in order to transmit strain from the actuator to the substrate and the periodic structure.We extracted the mechanical and magnetic constants from previous work and from literature, meaning that they are close to our materials characteristics but not entirely accurate. Indeed, characterizing the mechanical properties of metamaterials and especially with such small thickness is not trivial. For the mechanical aspect we used Poisson' ratios $\nu_{Ni_{60}Fe_{40}} = 0.3$ and $\nu_{\text{Kapton}} = 0.3$, and Young's moduli $Y_{Ni_{60}Fe_{40}} = 205$ GPa and $Y_{\text{Kapton}} = 4$ MPa. For the magnetic constants we used and exchange constant $A_{ex} = 13$ pJ.m^{-1}, a saturation magnetization $M_s = 9.5 \times 10^5$ A.m^{-1}, a gyromagnetic ratio $\gamma = 1.76 \times 10^{11}$ rad.Hz.T^{-1} and a magnetostriction at saturation of $\lambda = 12 \times 10^{-6}$.

The ferroelectric actuator calibration for the ε_{xx} and ε_{yy} with respect to the applied voltage was implemented inside our mechanical model in order perform a biaxial mechanical stress. Periodic and anti-periodic boundary conditions for the mechanical displacement were applied on opposite faces of the unit cell, as illustrated by the arrows on figure 7.1-a), such as:

$$\begin{cases} u_{src} = -u_{dst} \\ v_{src} = v_{dst} \end{cases} \tag{7.1}$$

for faces aligned along the x axis and:

$$\begin{cases} u_{src} = u_{dst} \\ v_{src} = -v_{dst} \end{cases} \tag{7.2}$$

for faces aligned along the y axis, with the displacement vector $\begin{pmatrix} u \\ v \\ w \end{pmatrix}$. It is worth mentioning that using only one unit cell for the mechanical test led to some inaccuracy for the calculated values in mesh elements close to the cell borders. These inaccuracy where not present for the magnetism aspect of the simulation. In order to overcome this issue, we decided to use a 3×3 cell only for the mechanical part, which lead to accurate values of the strain field in the center cell in which we perform the magnetic simulations. Unlike the case of continuous films, the presence of the holes lead to a heterogeneous strain and stress field as shown in the 7.1-b) calculated ε_{xx} (top) and ε_{yy} (bottom) profiles. We can see that the heterogeneity are concentrated over the whole thickness of the magnetic layer and quickly start to vanish in the polymer substrate until it becomes entirely homogeneous in depth. Having these heterogeneity led to an average strain lower to what is applied on the substrate as it is shown on figure 7.1-c). The average strain field still evolve linearly with

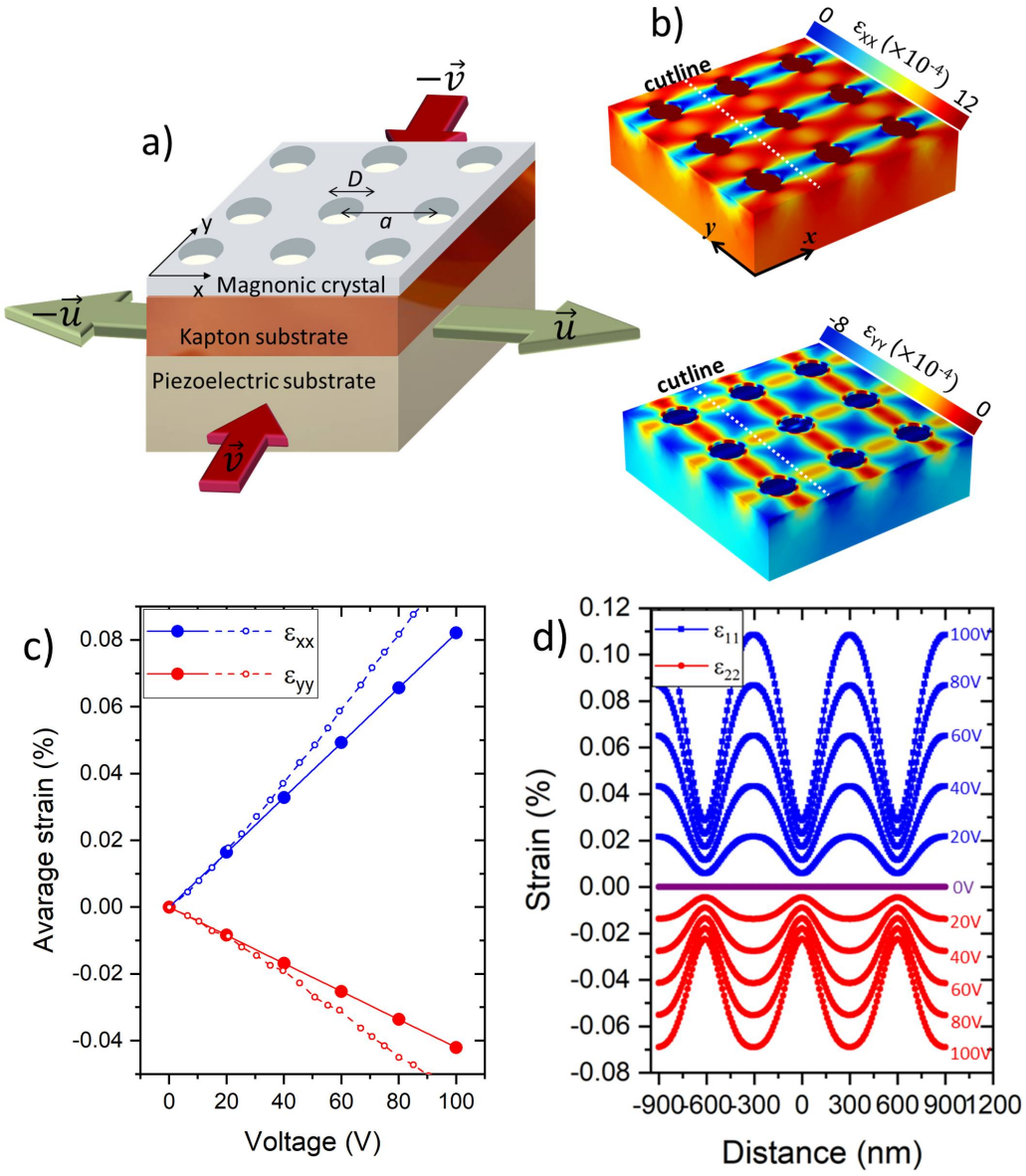

Figure 7.1: a) Schematic illustrating the array of $Ni_{60}Fe_{40}$ /polymer/ferroelectric substrate stacking The arrows show how the strain is applied. b) Profile of the ε_{xx} and ε_{yy} strain field calculated in the 3×3 geometry. c) Comparison between the ferroelectric substrate voltage calibration and the simulated average strain field components. d) Profile of the simulated ε_{xx} (blue) and ε_{yy} (red) components of the strain tensor along the cutline represented by the white dashed lines in b).

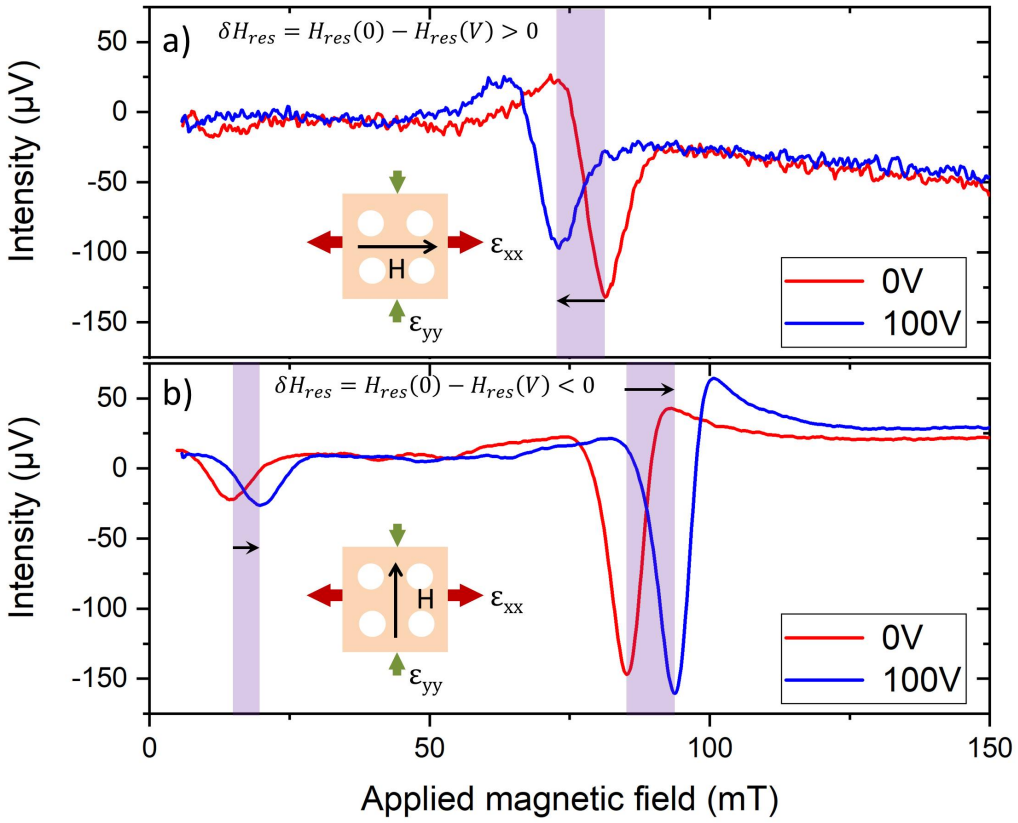

Figure 7.2: FMR spectra obtained at $0V$ (red) and $100V$ (blue) for a magnetic applied along the a) x direction and b) the y direction, for a driving frequency of 8 GHz.

respect to the applied voltage but due to the lower strain transmission that can observed on figure 7.1-d) and the mechanical contrast between the polymer and the metal, it is not possible to obtain the average strain in these two layers. Similar experiments were performed by N. Challab et al. in multiple directions between the applied magnetic field and the main strain direction [2].

For this study we focused on the results obtained at a 0° angle and 90° angle between the applied magnetic field and the x direction which we define as the principal strain direction. Figure 7.2-a) shows the comparison between the FMR spectrum obtained at 0V in red lines and the spectrum obtained when applying 100V in blue lines with the magnetic field applied along the y direction. One can observe a clear decrease of the resonance fields of approximately 8.4 mT, which is characteristics of materials with a positive magnetostrictive constant [1, 2, 3, 4, 5]. The opposite happens in figure 7.2-b) where the magnetic field is applied along the x axis, meaning that we observe an increase of the resonance field by changing the applied voltage from $0V$ to $100V$. This behavior is characteristic of materials with a positive magnetostrictive constant λ, which creates an easy direction for the magnetization in the direction of the tensile strain while creating a hard plane in the perpendicular direction. It is worth noting that the spectra on figure 7.2-b) exhibit a better signal than fig-

ure 7.2-a) and show two different modes. It is possible that the second mode also exists in figure 7.2-a) but are covered by the noisy background. We can also see a small difference of the resonance field of the two 0 V spectra. This could be explained by the possible presence of an anisotropy that could be either intrinsic of the material deposited or generated by residual strain after the gluing of the Kapton on the piezoelectric substrate [5]. In both cases we can ignore these effect by not plotting the resonance field but the resonance field shift defined as:

$$\delta H_{res} = H_{res}(0) - H_{res}(V) \tag{7.3}$$

It is interesting to notice that the main mode in figure 7.2-b) has a resonance field shift almost two times higher than the second mode, meaning that the voltage-induced strain do not affect all the magnetic modes the same way.

The static configuration of the magnetization influences highly the magnetoelastic field which has been represented by the arrows in figures 7.3-a) and 7.3-b) for angles of 0° and 90° respectively. The color-map represents the norm of the magnetoelastic field over the surface of the array of antidots defined as:

$$\vec{H}_{me} = \frac{3\lambda}{M_s} \begin{pmatrix} m_x\sigma_{xx} + m_y\sigma_{xy} + m_z\sigma_{xz} \\ m_x\sigma_{xy} + m_y\sigma_{yy} + m_z\sigma_{yz} \\ m_x\sigma_{xz} + m_y\sigma_{zy} + m_z\sigma_{zz} \end{pmatrix} \tag{7.4}$$

where σ_{ij} are the components of the stress tensor. As the stress and strain field are heterogeneous, the magnetoelastic field perceived by the magnetization is also heterogeneous. The experimental and numerical resonance field shift has been represented on figure 7.3-c) where the positive shift (in red) has been obtained for a 0° angle and the negative shift (in blue) for a 90° angle. The corresponding calculated mode profile has been inserted in front of each curve, and we managed to obtain very consistent results between experiments and simulation. The difference in shift between the different modes can be seen experimentally and numerically and have, according to us, two main origins that are the heterogeneous magnetoelastic field that influences differently the modes depending on their spatial localization and the slope at the driving frequency of each mode in the $f(H_{app})$ dependency. The simulation obtained are close to what was expected for material mechanical and magnetic constants found in the literature that could be refined slightly to obtain even better results. Nonetheless this tool we developed is consistent enough to be used for magneto-mechanical studies on complex geometries, which is why some work that we could not realize experimentally are going to be presented on a purely numerical aspect in the following sections and chapters.

7.2 Control of magnetic mode energies in a modulated array of nanowires

The previous case was characterized by a homogeneous strain field, thus simpler to solve in terms of induced magnetoelastic field. However, in modern objects of nanomagnetism, the presence of strain gradients related to complex geometries requires a numerical modeling

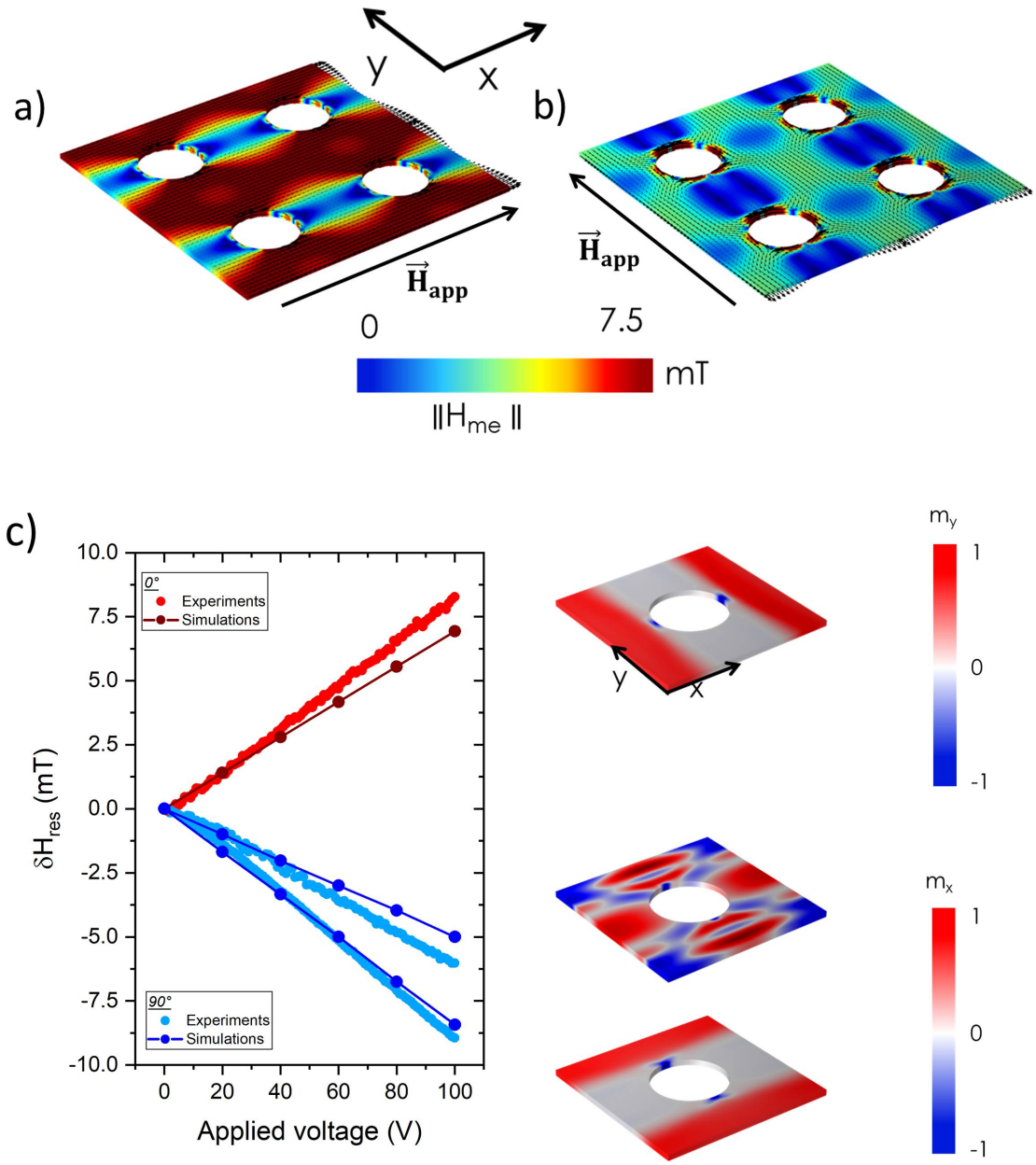

Figure 7.3: The magnetoelastic field is calculated for a field applied along b) the x axis and c) the y axis at 100V. d) Resonance field shift obtained experimentally (light dots) and numerically (dark light and dots) for the magnetic field applied at a 0 degree angle with the x axis (red) and at a 90° angle (blue) for a resonance frequency of 8GHz.

taking into account the heterogeneous localization of the strains and thus the associated magnetoelastic field [4, 14, 15, 16, 17, 18, 19, 6, 7, 8, 9, 10, 11, 12, 13]. The approach developed here allows to perform this kind of resolution and will be illustrated in this section by the numerical study of the magneto-mechanical properties of modulated nanowires already discussed.

For this study, we employed the same magnetic parameters as presented in figure 7.1. Since $Ni_{80}Fe_{20}$ is non-magnetostrictive, we opted to use a magnetoelastic constant λ of 3×10^{-5}, which is typical for ferromagnetic polycrystalline thin films. Additionally, we utilized a Young's modulus Y of 180 GPa and a Poisson ratio ν of 0.3 for the purpose of this study. These chosen parameters provide a reasonable approximation for the magnetoelastic behavior in the absence of direct experimental measurements.

Modulated nanowires were numerically submitted to external strains along their main axis (x). PBC were adopted so that the representative unit cell (identical to that used in the previous chapter) allows the determination of the whole behavior. Different external strains were applied (from 0% to 0.2% with 0.05% step). Figure 7.4-(a) shows the in-plane strain (ε_{xx}, ε_{yy}) maps at the top surface of the unit cell (right images) for a macroscopic applied strain of $\overline{\varepsilon}_{xx} = 0.2\%$. We observe that the strain fields are heterogeneous in (x, y) plane but homogeneous over the thickness. This is due to the width modulation of the nanowires; indeed, nanowires without modulation would have presented much more homogeneous strain fields. These inhomogeneities are illustrated on the left graph where we have represented a cut along the nanowire (dashed line in the maps). It is interesting to note that the variations of ε_{xx} and ε_{yy} are respectively located around +0.2 and -0.06 which correspond to the macroscopic values of $\overline{\varepsilon}_{xx}$ and $\overline{\varepsilon}_{yy}$.

These heterogeneous values naturally give rise to a heterogeneous magnetoelastic field. This is illustrated in figure 7.4-(b) where the amplitude of $\mu_0\vec{H}_{me}$ has been calculated from the strain fields presented in figure 7.4-(a) and the equilibrium magnetization distribution (see left map of figure 7.4-(b)) obtained in the absence of the applied magnetic field for a macroscopic strain $\overline{\varepsilon}_{xx} = 0.2\%$. It should be mentioned that H_{me} and the magnetization distribution are obtained in a self-consistently scheme. This magnetoelastic field configuration is thus directly linked to the strain field configuration and more particularly to that of ε_{xx} since the magnetic moment are mostly oriented in the x direction. We have followed the evolution of the frequencies of the different magnetic modes identified in the previous section at different macroscopic strain values. Figure 7.5 (left graph) shows the frequency shift ($\delta f = f(0) - f(\overline{\varepsilon}_{xx})$) obtained for an applied macroscopic strain of 0.2%, for increasing applied magnetic field. It is interesting to note that not all modes show the same frequency shift for a given magnetic field. Moreover, the lower frequency modes have the largest δf. For instance, at zero applied field mode 1 has a frequency shift of $\delta f \sim 2.4$ GHz while it is twice as low for mode 5 ($\delta f \sim 1.2$ GHz). These lowest frequency modes δf are also the most affected by the applied magnetic field. In order to emphasize this phenomenon we plotted the δf evolution of each mode with respect to the applied macroscopic strain at 0 mT and 100 mT. In figure 7.5 (right graphs), we observe an almost linear dependency of the modes to the applied strain which has been experimentally observed in the elastic regime in saturated magnetic configurations [4, 2]. These graphs show that the lowest

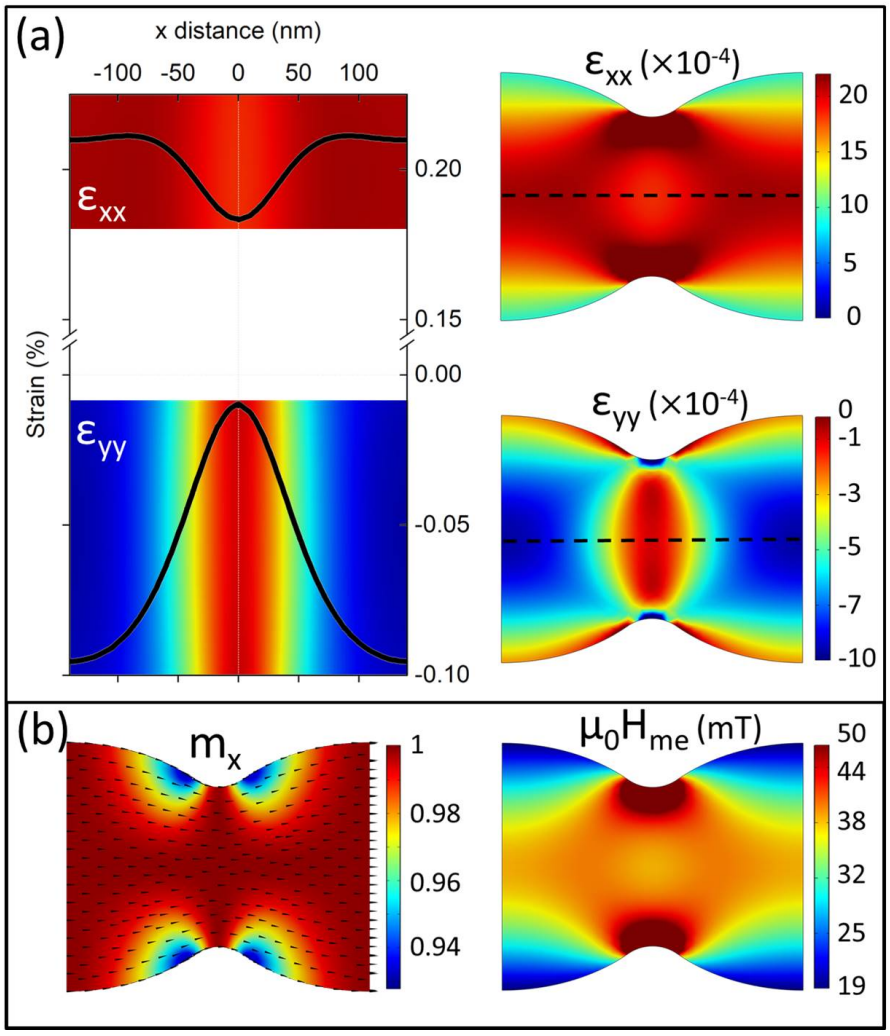

Figure 7.4: (a) Top view of the spatial distribution of the induced in-plane strains ε_{xx} and ε_{yy} inside the nanowires for a macroscopic applied strain of $\overline{\varepsilon}_{xx} = 0.2\%$. Cross-sections are shown on the right side of these strain maps. They were obtained from the black dotted lines on the mapping images, the colors correspond to a single pixel stretched along y and serves as a guide for the eyes. (b) Top view of the spatial distribution of the amplitude of the induced magnetoelastic field calculated in absence of applied magnetic field ($\left\|\mu_0 \vec{H}_{me}\right\|$). The corresponding magnetic moment distribution is also represented.

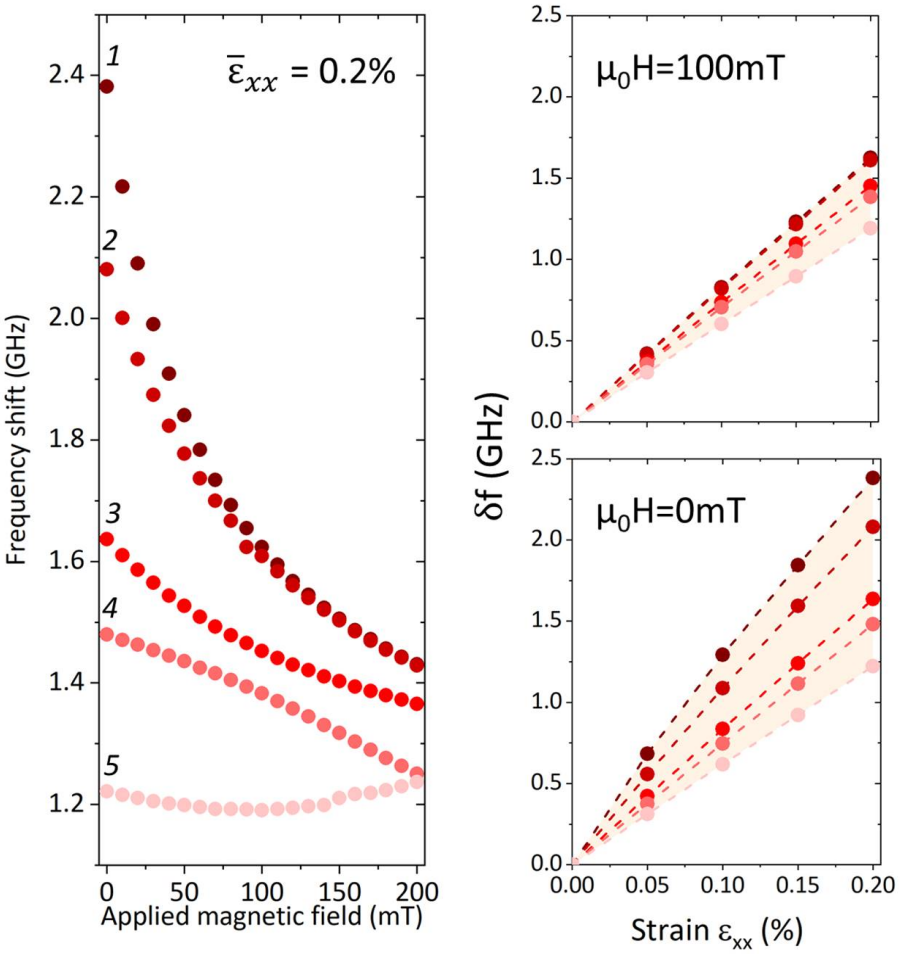

Figure 7.5: Left graph: frequency shift as function of the applied magnetic field; the frequency shift corresponds to the difference between the mode energies calculated at $\varepsilon_{xx} = 0.2$ % and at $\varepsilon_{xx} = 0$ %. Right graphs: frequency shift of the different magnetic modes as function of ε_{xx} for an applied field of 100 mT along the nanowires (i. e. along x) and in absence of applied field.

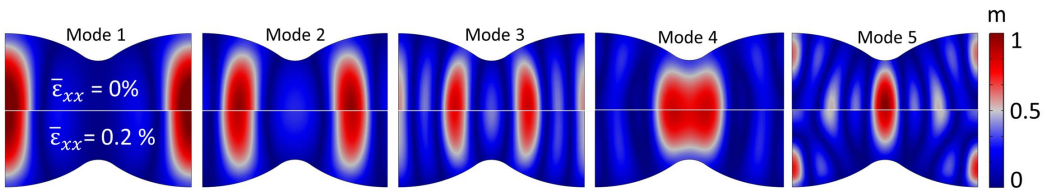

Figure 7.6: Top view of the spatial distribution of the magnetic modes calculated at $\varepsilon_{xx} = 0.2$ % and at $\varepsilon_{xx} = 0$ %. The upper (resp. lower) section of each map has been computed with a strain of 0% (resp. 0.2%).

frequency modes are getting closer to the higher modes behavior as the magnetic field increases, which can be related to the experimental and numerical data shown in figure 7.2-(c). Indeed, we observe in this figure that the mode evolution slopes are different for each mode at low magnetic field which gives birth to a differentiated mode control with the applied strain. As the applied field increases, the slopes tend to equalize which explains the tightening evolution of all the modes as function of $\overline{\varepsilon}_{xx}$. To understand the observation of such a difference at low applied field, we scrutinized the spatial distribution of each magnetic modes at minimum ($\overline{\varepsilon}_{xx} = 0$) and maximum applied strain ($\overline{\varepsilon}_{xx} = 0.2\%$). The different spatial distributions of the five modes are presented in figure 7.6; the upper (resp. lower) half corresponds to maps obtained at a strain of 0% (resp. 0.2%). It is interesting to notice that the lowest frequency modes (especially modes 1 and 2) show a clear variation of their spatial distribution whereas the higher frequency modes remain mainly in the same spatial region. This is most probably related to the progressive saturation of the magnetization close to the borders of the modulated nanowires and would explain why at high applied field the lowest frequency modes δf is highly reduced. These modes frequency shift are only observable thanks to the coupling between the LLG and the equations of mechanics in the case of magnetostrictive materials. In the case an infinite non magnetostrictive material ($\lambda = 0$) no shift is observed numerically, however in the case of the modulated nanowires array a very small shift (negligible compared to the magnetoelastic effect) is observed due to the slight shape modification induce by the strain.

Bibliography

[1] Gueye, M., Zighem, F., Faurie, D., Belmeguenai, M., & Mercone, S. (2014). Optimization of indirect magnetoelectric effect in thin-film/substrate/piezoelectric-actuator heterostructure using polymer substrate. Applied Physics Letters, 105(5) 7.1, 7.1

[2] Challab, N., Faurie, D., Haboussi, M., Adeyeye, A. O., & Zighem, F. (2021). Differentiated strain-control of localized magnetic modes in antidot arrays. ACS Applied Materials & Interfaces, 13(25), 29906-29915 7.1, 7.1, 7.1, 7.2

[3] Zighem, F., Belmeguenai, M., Faurie, D., Haddadi, H., & Moulin, J. (2014). Combining ferromagnetic resonator and digital image correlation to study the strain induced resonance tunability in magnetoelectric heterostructures. Review of Scientific Instruments, 85(10) 7.1

[4] Challab, N., Faurie, D., Haboussi, M., & Zighem, F. (2021). Effects of Heterogeneous Strain on the Magnetization Processes in Magnetic Nanomembranes. physica status solidi (RRL)–Rapid Research Letters, 15(8), 2100149 7.1, 7.2, 7.2

[5] Gueye, M., Lupo, P., Zighem, F., Faurie, D., Belmeguenai, M., & Adeyeye, A. O. (2016). Unambiguous magnetoelastic effect on residual anisotropy in thin films deposited on flexible substrates. Europhysics Letters, 114(1), 17003 4.7, 7.1

[6] Cañón Bermúdez, G. S., & Makarov, D. (2021). Magnetosensitive E-Skins for Interactive Devices. Advanced Functional Materials, 31(39), 2007788 7.2

[7] Ha, M., Cañón Bermúdez, G. S., Kosub, T., Mönch, I., Zabila, Y., Oliveros Mata, E. S., ... & Makarov, D. (2021). Printable and stretchable giant magnetoresistive sensors for highly compliant and skin-conformal electronics. Advanced Materials, 33(12), 2005521 7.2

[8] Jaris, M., Yang, W., Berk, C., & Schmidt, H. (2020). Towards ultraefficient nanoscale straintronic microwave devices. Physical Review B, 101(21), 214421 7.2

[9] Chavez, A. C., Schneider, J. D., Barra, A., Tiwari, S., Candler, R. N., & Carman, G. P. (2019). Voltage-controlled ferromagnetic resonance of dipole-coupled Co 40 Fe 40 B 20 nanoellipses. Physical Review Applied, 12(4), 044071. 7.2

[10] Münzenrieder, N., Karnaushenko, D., Petti, L., Cantarella, G., Vogt, C., Büthe, L., ... & Tröster, G. (2016). Entirely flexible on-site conditioned magnetic sensorics. Advanced Electronic Materials, 2(8), N-A 7.2

[11] Melzer, M., Makarov, D., & Schmidt, O. G. (2020). A review on stretchable magnetic field sensorics. Journal of Physics D: Applied Physics, 53(8), 083002 7.2

[12] Zighem, F., & Faurie, D. (2021). A review on nanostructured thin films on flexible substrates: links between strains and magnetic properties. Journal of Physics: Condensed Matter, 33(23), 233002 7.2

[13] Faurie, D., Adeyeye, A. O., & Zighem, F. (2021). Prospects toward flexible magnonic systems. Journal of Applied Physics, 130(15) 7.2

[14] Makarov, D., & Sheka, D. D. (Eds.). (2022). Curvilinear micromagnetism: from fundamentals to applications (Vol. 146). Springer Nature 7.2

[15] Yershov, K. V., & Sheka, D. D. (2023). Control of magnetic response in curved stripes by tailoring the cross section. Physical Review B, 107(10), L100415 7.2

[16] Raftrey, D., Hierro-Rodriguez, A., Fernandez-Pacheco, A., & Fischer, P. (2022). The road to 3-dim nanomagnetism: Steep curves and architectured crosswalks. Journal of Magnetism and Magnetic Materials, 563, 169899 7.2

[17] Makarov, D., Volkov, O. M., Kákay, A., Pylypovskyi, O. V., Budinská, B., & Dobrovolskiy, O. V. (2022). New dimension in magnetism and superconductivity: 3D and curvilinear nanoarchitectures. Advanced Materials, 34(3), 2101758. 7.2

[18] Sheka, D. D., Pylypovskyi, O. V., Landeros, P., Gaididei, Y., Kákay, A., & Makarov, D. (2020). Nonlocal chiral symmetry breaking in curvilinear magnetic shells. Communications Physics, 3(1), 128 7.2

[19] Makushko, P., Kosub, T., Pylypovskyi, O. V., Hedrich, N., Li, J., Pashkin, A., ... & Makarov, D. (2022). Flexomagnetism and vertically graded Néel temperature of antiferromagnetic Cr2O3 thin films. Nature Communications, 13(1), 6745 7.2

8 Spin wave dispersion

Contents

This chapter explores spin wave dispersion in both strained and strain-free magnetic structures, beginning with experimental validation using ferromagnetic resonance (FMR) and Brillouin light scattering (BLS). We measure a 40 nm permalloy continuous film, confirming our simulations' accuracy, particularly for phonons and spin waves in Damon-Eshbach and backward volume configurations. We then investigate the impact of static strain on spin wave dispersion in magnonic crystals, employing BLS on a 20 nm $Ni_{60}Fe_{40}$ antidot array. The experimental results show significant frequency shifts, validating our numerical simulations. Next, we examine the effects of uniaxial strain on antidots deposited on a ferroelectric substrate (PZT), demonstrating how strain alters the magnonic band structure and frequency modes. Finally, we simulate square magnetic dots on polymer substrates, revealing that increased separation reduces interactions and affects spin wave quantization. This chapter lays the groundwork for understanding how mechanical strain influences magnonic properties in various magnetic structures.

8.1 Experimental validation of the model

The results obtained in the previous chapters where obtained using the FMR technique. As the excitation is applied homogeneously over the whole surface, the measured magnetic modes are excited in a static manner. Simulating this behavior was easily done by simply applying continuous periodic boundary conditions such as $\vec{m}_{dst} = \vec{m}_{src}$. This condition cannot be applied when working with propagating waves like spin waves and acoustic waves. These two types of waves can be measured simultaneously with the Brillouin light scattering, which make it convenient to simulate them also simultaneously [1, 2, 3]. Some study in the literature use Comsol Multiphysics in order to simulate the acoustic behavior of phononic crystals using the solid mechanics module (or directly the acoustic module) [4, 5], but none of the work found where performed on continuous films, except in the paper of Babu et al. [6] where they simulate both magnon and phonon an their coupling in thin films. Even though our work is not directly focused on acoustic waves, it is important for us to first verify the reliability of this numerical approach firstly because we drew inspiration from the acoustic wave calculation for our spin wave simulations, and secondly because it can be interesting to study both waves together in order to couple them through magnon-phonon interaction [7, 1, 2, 3, 4, 5], which will be the subject of the next chapter. The way the acoustic wave are calculated in Comsol is close to the approach we use for our magnetostatic modes, but instead of continuous boundary conditions, Floquet Boundary conditions are used [13]. These conditions more often qualified as Bloch conditions impose a phase shift on opposite faces of the unit cell such as the displacement field $\vec{u}$ is written [14]:

$$\vec{u}_{dst} = \vec{u}_{src} e^{-i\vec{k}\cdot(\vec{r}_{dst}-\vec{r}_{src})} \tag{8.1}$$

This way it is easy to control numerically the wave vector $\vec{k}$ of the acoustic wave. This is a rather simple but efficient method that allows one to simulate the phonon behavior using the eigenfrequency approach. The displacement field is only dependent on the material properties and the applied load, follows simply the second Newton's law

$$\sum \vec{F} = m\vec{a} \tag{8.2}$$

which, in terms of solid mechanics, is more frequently written:

$$-\omega^2 \rho \vec{u} = \vec{\nabla} \cdot \underline{\underline{\sigma}} + \vec{F}_V \tag{8.3}$$

where ω is the pulsation, ρ is the material mas density, $\underline{\underline{\sigma}}$ is the strain tensor and $\vec{F}_V$ are volume forces that are not considered in our case. In order to account for spin waves and acoustic waves at the same time was convenient to apply the same boundary conditions for the magnetization, which we integrated inside Comsol Multiphysics such as:

$$\vec{m}_{dst} = \vec{m}_{src} e^{-i\vec{k}\cdot(\vec{r}_{dst}-\vec{r}_{src})} \tag{8.4}$$

As the term $\vec{r}_{dst} - \vec{r}_{src}$ finally corresponds to the period of the unit cell, it becomes evident that the calculation lead to folded branches in the dispersion curves that we have no method

to unfold numerically. It is then only relevant to perform the simulations inside the limit of the first Brillouin zone.

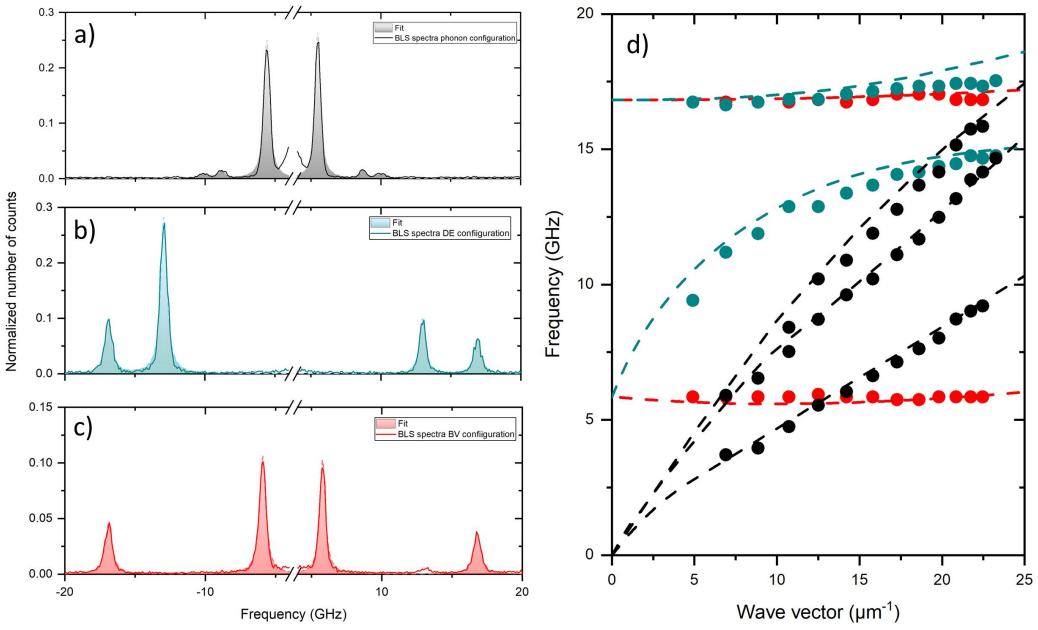

Figure 8.1: BLS spectra obtained with a 532 nm wavelength for a wave vector of 12.5 μm^{-1} for the a) phonon analysis configuration, b) spin waves analysis in Damon-Eshbach configuration and c) spin waves analysis in backward volume configuration. The experimental spectra are represented in bold lines while the colored area represent the fitted spectra. d) Entire dispersion curves obtained for the corresponding phonons (black), DE configuration magnons (blue) and BV configuration magnons (red). The dots represent the data extracted from experimental spectra while the dashed lines represent the simulations.

In order to have a reference to confront with this approach to reality we performed BLS measurement on a 40 nm Py continuous film deposited on a SiO_2/Si substrate. Our TFP2 BLS setup allows us to selectively analyze phonon and magnon by changing the incident light polarization and to shift from a backward volume configuration to Damon-Eshbach one by rotating our permanent magnets. The results obtained are shown in figure 8.1. We can see that using a *P* polarized incident light in figure 8.1-a) and *S* polarized incident light in figures 8.1-b) and 8.1-c) allowed to completely isolate the signal coming from phonons and magnons, respectively. It is quite interesting to see that three peaks can be observed in the phonons spectrum in figure 8.1-a) which we expected to correspond to the Rayleigh and first two Sezawa acoustic modes.

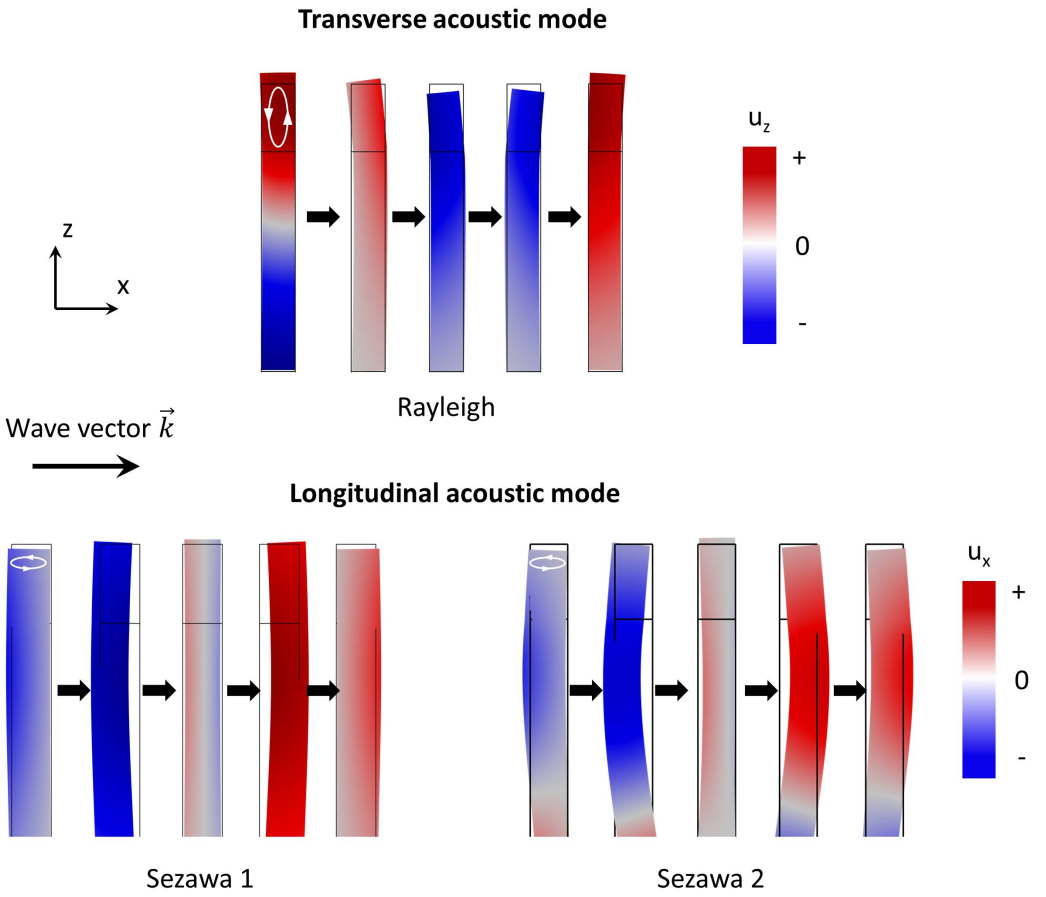

Figure 8.2: Mode profile of the calculated quasi-transverse acoustic wave (Rayleigh) and the two quasi-longitudinal acoustic waves (Sezawa 1 and 2). The color encodes the z-component of the displacement field in the case of the transverse wave and the x-component of the displacement field in the case of the longitudinal wave.

Looking at the simulations of the acoustic waves represented by black dashed lines in figure 8.1-d) which modes profiles are represented in figure 8.2 we can affirm that these modes were indeed correspond to Rayleigh and Sezawa [6]. It is important to note that forth one corresponding to the Love acoustic wave was also simulated but not represented as it is difficult to be observe with this technique [15]. The simulations performed are very accurate and reproduced almost exactly the behavior of the Rayleigh mode which has a polarization mainly transverse to the surface normal, and the Sezawa modes that are longitudinal waves with a polarization mainly in-plane in the direction of propagation. The quantitative agreement between simulations and experiment is also comforting because the acoustic study is trickier than the magnetic one. Indeed, the results depend highly on the materials stacking ($Ni_{80}Fe_{20}$(40 nm)/SiO_2(400 nm)/Si) and their mechanical properties which cannot be extracted easily experimentally and that can be highly affected by other parameters like the layers adhesion. For these simulations we used values found in the literature and presented in table 8.1:

	$Ni_{80}Fe_{20}$	SiO_2	Si
ν	0.3	0.17	0.28
C_{11}(GPa)	275	75.2	166
C_{12}(GPa)	118	15.4	64
C_{44}(GPa)	78	29.9	80

Table 8.1: Mechanical properties of the materials composing the sample.

These results obtained for the phonons are in themselves not very important in the context of this chapter, but still allow us to verify this approach in thin films, which has not been extensively done in the literature. We then simulated the spin wave dispersion using this approach adapted for the micromagnetic formalism we implemented for the DE configuration ($\vec{k} \perp \vec{m}$) and for the BV configuration ($\vec{k} \parallel \vec{m}$). In both cases, we manage to measure two modes corresponding to the DE and first PSSW in figure 8.1-b) and to the BV and first PSSW in figure 8.1-c). The magnetic constants have been determined experimentally using FMR and are given in table 8.2.

γ (rad.Hz.T^{-1})	$M_s(A.m^{-1})$	A(J.m^{-1})
1.95×10^{11}	7.8×10^5	13×10^{-12}

Table 8.2: Magnetic properties of the 40 nm thick permalloy continuous film

One can see that the measured spin waves in figure 8.1-d) are nicely reproduced by our FEM model using the Floquet boundary conditions. The DE mode frequency in blue (experiments in dots and simulation in dashed lines) starts around 6 GHz and increases very quickly with the wave vector and starts to reach an asymptotic value of approximately 15 GHz, and we can observe a slight increase of the standing mode around 17 GHz in blue. This behavior was reproduced numerically (dashed lines) but seems to be slightly overestimated by the model. We tried changing the mesh refinement and the unit cell size in order to verify if this overestimation was due to the model or to computing inaccuracy, however changing these parameters lead to the same PSSW evolution. Figure 8.3-a) show the profile of these two modes in the Damon-Eshbach configuration at multiple states of the wave half period. As expected the DE mode has an evanescent profile of the m_x component of the magnetization which is at the origin of the experimental intensity asymmetry observed at around 7.5 GHz in figure 8.1-b) between the Stokes and anti Stokes part of the spectrum [16]. The experimental backward configuration represented in red dots in 8.1-d) is very well reproduce by the simulations in red dashed lines. Unlike the DE mode, the calculated BV mode profile presented in figure 8.3-b) has a completely homogeneous intensity over the thickness of the continuous film, which is coherent with the symmetric intensity measured in figure 8.1-c) [16].

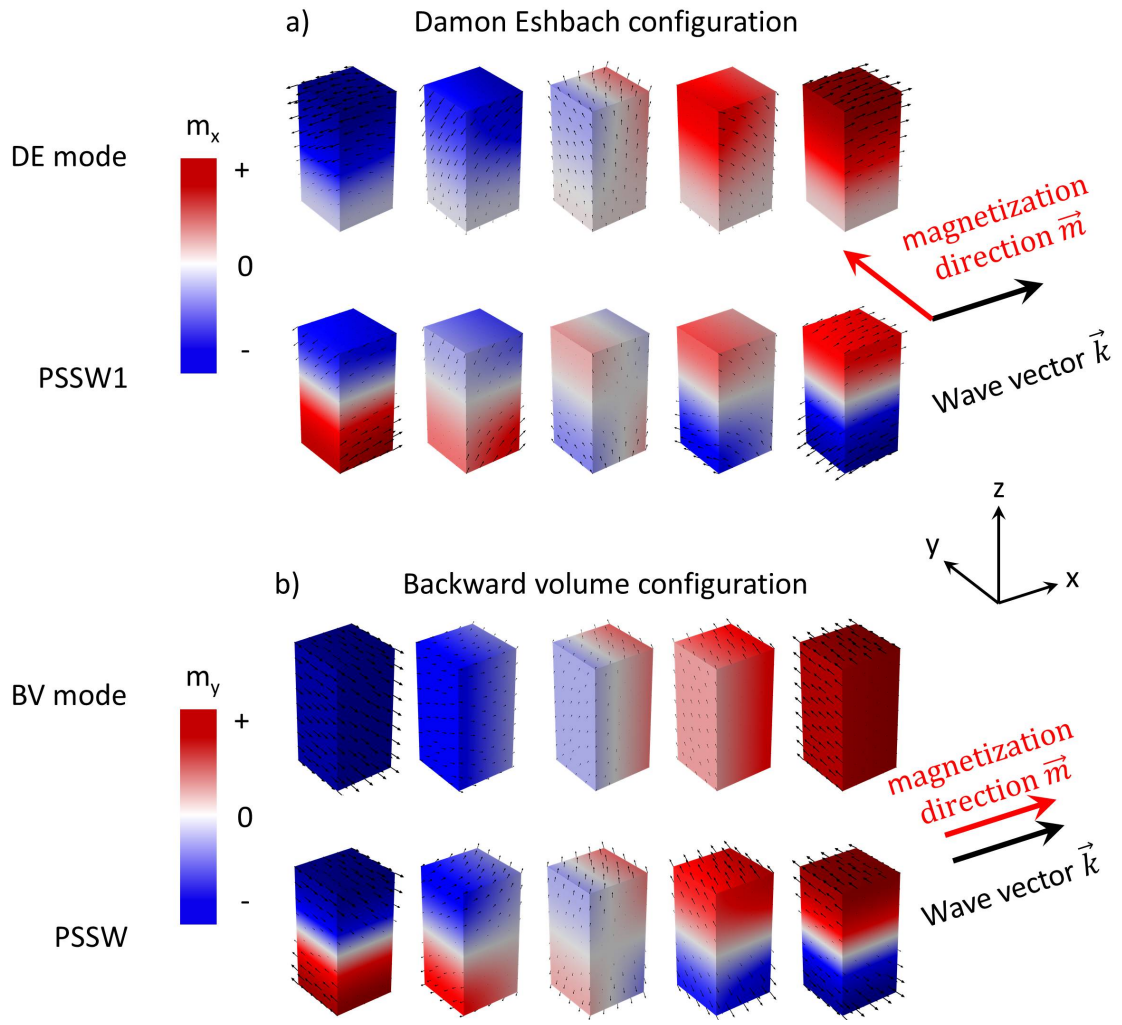

Figure 8.3: Mode profile of the calculated spin waves in the Damon Eshbach and backward volume configurations. a) The color encodes the m_x component of the magnetization in the case of the Damon Eshbach configuration and b) the $m_y$component in the case of the backward volume configuration.

As for the FMR measurements shown in the previous chapters we compared our simulations to analytical models presented in figure 8.4. In this graph we compared the simulation in dashed lines for the different modes with a model where the effect of exchange is not taken into account (thin dashed line) and an other where the exchange is taken into account. For the backward volume mode we observe a clear agreement with the exchange model with an increase of the frequencies at high wave vector, while the other show only a decrease of the frequencies. The PSSW in this configuration slightly diverges at high wave vector. In the case of the DE mode we can clearly see a divergence between the exchange model and the simulations that seems to follow the non-exchange model. The PSSW in this configuration also increases more quickly than the model at high wave vector similarly to what we saw with the experimental data. Despite these slight discrepancies we managed

to adapt the phonon approach to the magnon frequency calculation which will allow us to study the case of magnonic crystals in the following studies.

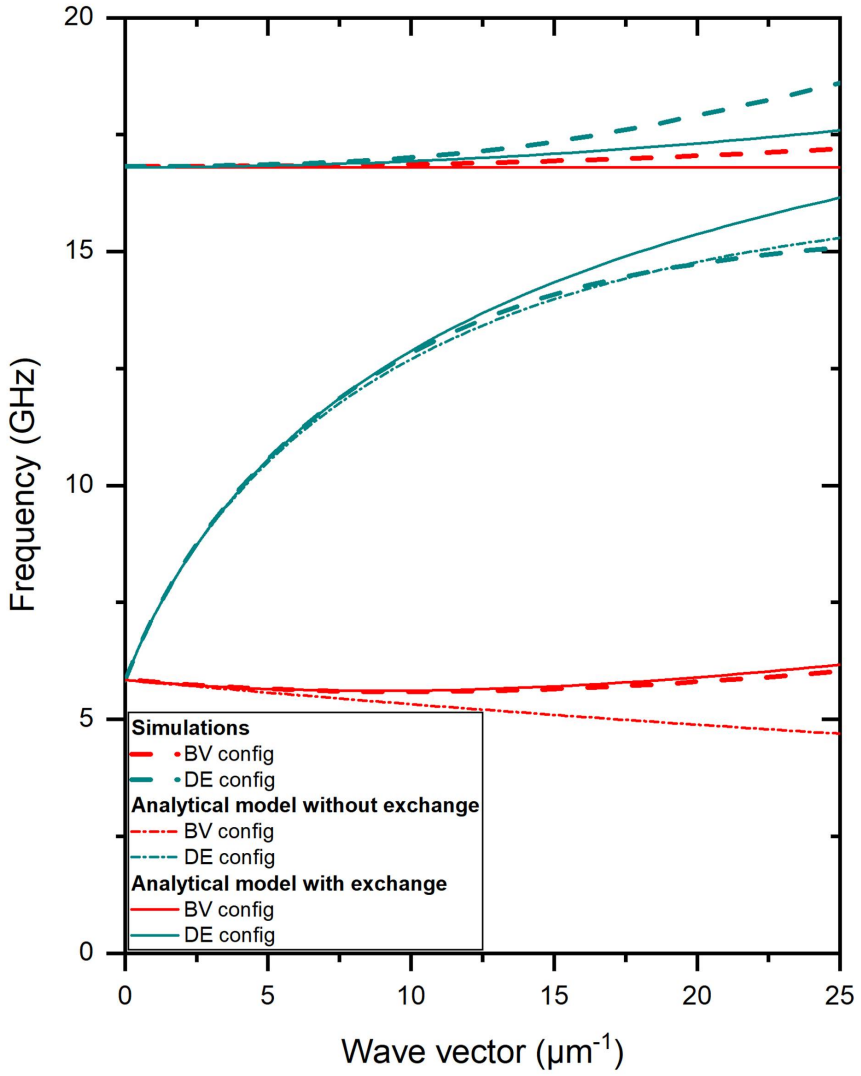

Figure 8.4: Comparison between the simulations in thick dashes lines and analytical models taking into consideration the effect of the exchange in continuous lines and analytical models without the effect of the exchange.

8.2 Magnonic crystal dispersion

8.2.1 Comparison between BLS measurements and simulations

In this section, we focus on the effect of static strain on the spin wave dispersion of magnonic crystals. Since these studies will be entirely numerical, it is first necessary to validate our

computational approach by comparing the simulated dispersion relations with experimental data. To this end, we performed Brillouin Light Scattering (BLS) measurements in the Damon-Eshbach configuration, which is particularly well suited for observing magnonic band structures. The studied sample consists of a 20 nm thick $Ni_{60}Fe_{40}$ antidot array, with hole radii of 70 nm and a lattice period of 420 nm (see figure 8.5). The magnetic parameters were determined using ferromagnetic resonance (FMR) measurements on a continuous film fabricated under the same conditions, and the extracted values are summarized in Table 8.3.

γ (rad.Hz.T^{-1})	$M_s(A.m^{-1})$	A(J.m^{-1})
1.88×10^{11}	12×10^{5}	8×10^{-12}

Table 8.3: Magnetic properties of the $Ni_{60}Fe_{40}$ used for the magnonic crystal

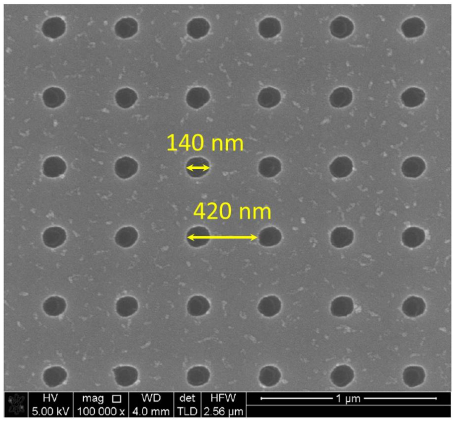

Figure 8.5: Scanning Electron Microscopy (SEM) image of the studied antidot magnonic crystal. The sample consists of a 20 nm thick $Ni_{60}Fe_{40}$ film patterned into a square lattice of circular antidots. The hole diameter is 140 nm, and the lattice period is 420 nm, as indicated by the yellow annotations.

Experimental Spectra and Data Processing

Studying magnonic crystals via BLS leads to more complex spectra, similar to FMR measurements, but requires significantly longer acquisition times. This is due to the fact that, in structured systems, each spin wave mode occupies a much smaller magnetic volume compared to uniform modes in continuous films. Figure 8.6-a) presents a typical BLS spectrum obtained from the sample (light gray curve), where four distinct modes can be observed in both the Stokes and anti-Stokes regions. To extract these modes, we numerically fitted the spectrum using a convolution of eight Lorentzian functions (colored dashed lines), with the resulting fit shown in colored areas. The experimental dispersion relation, extracted from BLS measurements, is shown in figure 8.6-b) (red dots). This dataset is superimposed onto the simulated band structure, which was obtained for a magnonic crystal with the same structural and magnetic parameters as the experimental sample.

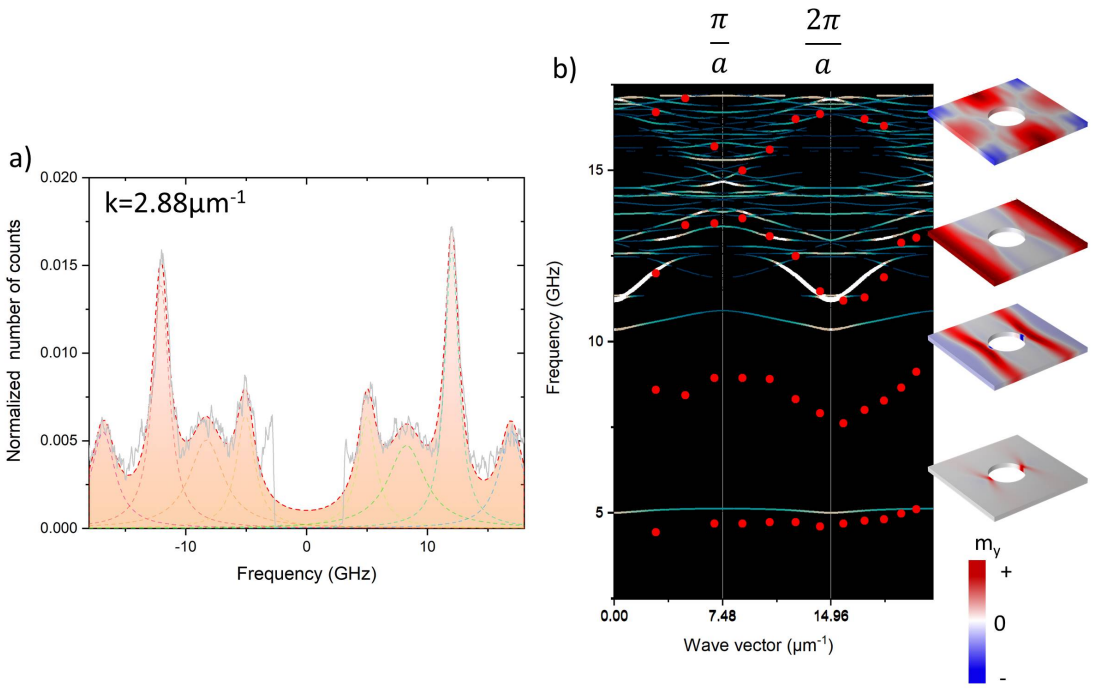

Figure 8.6: a) Brillouin Light Scattering (BLS) spectrum measured in the Damon-Eshbach configuration $\left(\vec{k} \perp \vec{m}\right)$ at an applied magnetic field of 110 mT, for a wave vector $k = 2.88\ \mu m^{-1}$. The experimental spectrum (gray curve) reveals multiple spin wave modes. The peaks were fitted using a superposition of eight Lorentzian functions (dashed lines), with the resulting fit shown as the shaded area. b) Comparison between experimental and simulated spin wave dispersion. The red dots represent the BLS-extracted dispersion relation, superimposed on the simulated magnonic band structure (color map). The relative intensity of the simulated spin wave modes is encoded in color and data point size (brighter/larger markers correspond to stronger intensity). The inset mode profiles correspond to the experimentally observed modes, represented at $k = 0\ \mu m^{-1}$. The red and blue contrast illustrates the dynamic magnetization component (m_y), indicating the spatial distribution of each mode within the antidot lattice.

Comparison Between Experiment and Simulation

As described earlier in this manuscript, the simulations were computed only for $k \in \left[0; \frac{\pi}{a}\right]$, and the data were mirrored to reconstruct the full Brillouin zone. This approach reduces computational time, as the Floquet boundary conditions naturally enforce band folding. The simulated band structure is presented as a color map in figure 8.6-b), where the relative intensity is encoded in both color scale and data point size (brighter/larger points indicate stronger intensity).

By comparing the simulated and experimental dispersion relations, we observe a strong agreement between both datasets, confirming the validity of our computational approach. The profiles associated with each experimentally detected mode were analyzed at $k = 0$ μm^{-1} for clarity. The first mode (~5 GHz) is localized at the edges of the antidots and is highly sensitive to the exchange interaction strength. This mode exhibits minimal wavevector dependence. The two higher-frequency modes correspond to: i) a Damon-Eshbach-like (DE-like) mode (~16 GHz) and ii) a Backward Volume-like (BV-like) mode (~12 GHz), previously identified in an earlier chapter. Both modes are accurately reproduced by simulations, in terms of frequency positioning and relative amplitude.

However, a fourth mode (~8 GHz) is detected in BLS but does not clearly correspond to any visible feature in the simulations. Its nature and origin remain unclear. One possibility is that it may correspond to a computed mode near 10 GHz, whose profile is also shown in figure 8.6. While this hypothesis appears reasonable—since the amplitude of the experimental mode is comparable to the simulated branch—we cannot fully confirm this interpretation. The unexpectedly low frequency of this mode remains unexplained. Nonetheless, the overall agreement between experiment and simulation is remarkably strong, validating our computational approach and providing a solid foundation for the subsequent numerical studies on strain-induced effects in magnonic crystals.

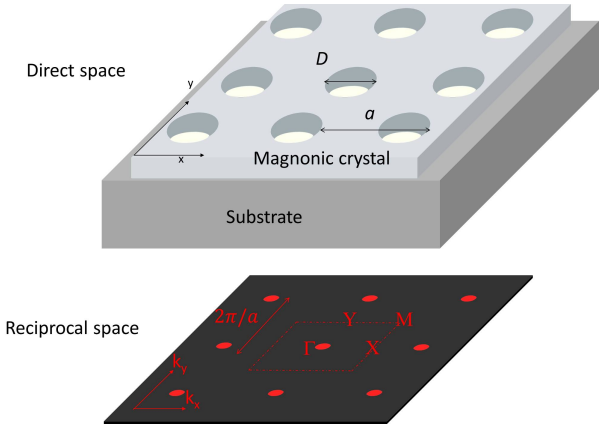

Figure 8.7: Schematic representation of the sample in the direct space and in the reciprocal space.

8.2.2 Effect of static strain on magnonic crystal

Previous studies have demonstrated that applying strain to control static magnetic modes is an efficient method for tuning spin wave frequencies. Both numerical simulations and experimental results have confirmed that strain-induced modifications lead to significant frequency shifts of various spin wave modes. The modes observed in FMR at $k = 0$ µm^{-1} correspond to the initial points of dispersion curves at the Γ point of the reciprocal space (see figure 8.7). This implies that the entire magnonic band structure should be affected by static strain, leading to a global shift of the magnonic branches.

Our initial plan was to perform BLS measurements on the same sample previously studied using FMR. However, we encountered significant technical challenges when switching to BLS. The sample structure consisted of a 20 nm thick antidot array deposited on Kapton®, a polymer substrate that was glued onto a piezoelectric substrate. While Kapton® is widely used for flexible electronics and strain experiments, its strong acoustic signature in BLS spectra posed a major issue.

As shown in figure 8.8 , we performed BLS measurements on an antidot array deposited on Kapton®, using two different configurations: one in a magnon-detection configuration (red spectrum), where a half-wave plate was used to isolate the magnetic signal, and another in a phonon-detection configuration (black spectrum), where the acoustic phonon signal was directly measured. The results reveal that both spectra exhibit similar features, indicating that the strong phonon background completely masks the magnetic signal, even when using optical polarization filtering. Although the magnon-sensitive configuration attenuates the phonon signature, the residual acoustic contribution remains too dominant, making it impossible to reliably extract small frequency shifts due to strain.

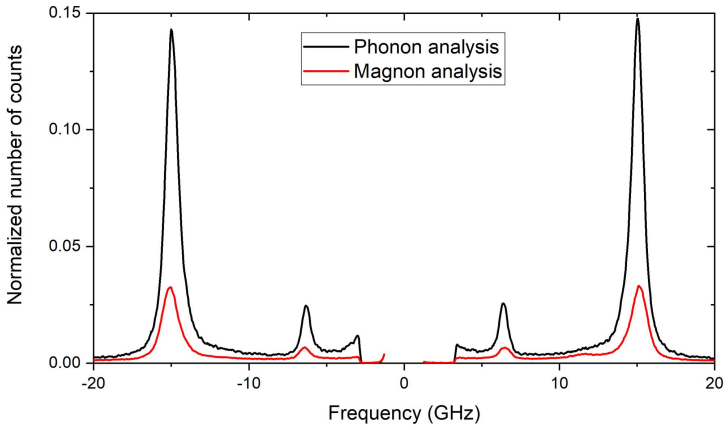

Figure 8.8: BLS signal obtained on nanostructures deposited on Kapton. The black spectrum show the signal in the phonon analysis configuration while the red spectrum show the signal obtained in the magnon analysis configuration.

Another limiting factor is the low thermal resistance of polymer substrates, which restricts the laser power that can be used in BLS experiments. This results in extremely long acquisition times, making the measurement process impractical. To mitigate these issues,

several alternative approaches were considered. One option was to increase the magnetic layer thickness to at least 200 nm, which would enhance the magnetic signal relative to the substrate's acoustic background. However, thicker films exhibit lower strain transmission, reducing the effectiveness of strain-induced magnon tuning. Another option was to replace the polymer substrate with a ferroelectric material, allowing direct deposition of the nanostructures onto a rigid piezoelectric substrate. This would eliminate the phonon noise from Kapton® and enable a clearer magnetic signal in BLS spectra. Unfortunately, such samples could not be fabricated within the timeframe of this PhD.

Given these challenges, we opted to focus on numerical simulations to investigate the effect of static strain on magnonic crystals, which is discussed in the following section.

8.2.3 Numerical Study of Magnonic Crystals on a Ferroelectric Substrate

Using a ferroelectric substrate in order to control the magnonic branches has been discussed for a few years but has never really been realized experimentally nor numerically. Using our numerical model we can now easily see the effect of an heterogeneous strain field in complex structures. For this study we numerically decided to simulate an antidot with magnetic properties close to what can be found in the literature for CoFeB alloys that tend to be more magnetostrictive than NiFe alloys. This magnonic crystal is deposited on top of a PZT substrate which is not numerically used for its piezoelectric properties but for its mechanical properties. Indeed, even though it is possible to easily apply a real voltage with these simulations with Comsol's AC/DC module, we decided to only apply an artificial uniaxial strain on the substrate. The reason for this is that adding another level of complexity with a third module increases the computing time for probably not much added value to the results. The geometry has a period $a = 400$ nm and holes diameter $D = 160$ nm. We limited the study to uniaxial strain in the range $\varepsilon = [0\% - 0.2\%]$ applied to the substrate which corresponds to the typical elastic range of metals (above this value the antidot would be plastically deformed) and which can be realistically reached using ferroelectric substrates.

	CoFeB	PZT
ν	0.28	0.3
C_{11}(GPa)	250	135
C_{12}(GPa)	100	68
C_{44}(GPa)	75	22

γ (rad.Hz.T^{-1})	$M_s(A.m^{-1})$	A(J.m^{-1})	$\lambda(\times 10^{-6})$
1.88×10^{11}	10×10^{5}	10×10^{-12}	20

Table 8.4: Mechanical and magnetic properties of the materials composing the sample

As for the previous chapter study, the magnetic features are calculated in the unit cell represented in figure 8.9-a) at the center of the 3×3 geometry. For the whole study the magnetization is saturated along the x-axis thanks to an external magnetic field of 50 mT.

The mechanical properties are computed in the entire 3 × 3 cell represented in figure 8.9-b). The color mapping represents the σ_{xx} and σ_{yy} components of the stress tensor after application of a uniaxial strain of 0.2% (0.1% on each face of the substrate) along the x-axis as represented by the wide arrows. We can see that the stress is quasi uniform in the substrate as it is a continuous media and we can especially see that the σ_{yy} component of the stress tensor is close to 0 GPa even if the ε_{yy} is not 0 due to the conservation of the volume of the solid. Nonetheless, due to the presence of the holes, a σ_{yy} stress is induced in the structure layer leading to a maximum value of 180 MPa in the border of the holes. Figure 8.9-c) show the average value of the ε_{xx} and ε_{yy} of the strain tensor in the magnonic crystal volume. As mentioned the conservation of the volume lead to a non 0 ε_{yy} strain We can also observe that as the strain is applied on the substrate and because we have a mechanical contrast between the substrate and the nano patterned film, the average strain in the magnonic crystal is not 0.2% but closer to 0.17%. Similarly, the average stress tensor main components are plotted in figure 8.9-d). As mentioned earlier the average σ_{yy} is different from 0 GPa thanks to the holes presence, however it is clear that this value is almost insignificant next to σ_{xx} and will not play a great role in the band shifts.

For each applied strain, we used the same method use in the previous section for the magnonic band calculation. As the spin wave behavior vary depending on their propagation direction and the magnetization direction we decided to draw inspiration to the electronic band structure representation and to simulate how the spin wave evolve across the First Brillouin Zone (FBZ) between the four high symmetry points represented in figure 8.10-a). Using the frequency domain method we simulated "pseudo-BLS" spectra (shown in figure 8.10-b)) at those symmetry points in absence of strain (black) and at 0.2% of uni-axial strain (red). The peculiar vectorial nature of spin renders very different the X and Y symmetry points that would be identical for electronic or phononic band structures for example. We can see that at the X point the spin wave response is very close to the behavior at the Γ point in the center of the FBZ forecasting almost no magnonic effect in the case where $\vec{k} \parallel \vec{M}$. As opposite, the Y and M symmetry points present spectra very different from the Γ one which make them a lot more interesting for magnonic purpose.

Comparing the spectra at 0% and 0.2% of strain we observe a clear shift of the spin wave modes in the four symmetry points. Similarly to what has been shown in the previous chapter, the modes are not all shifted the same way, which is made clear by looking at the first two modes of each spectra. The modes profiles associated to the spectrum Γ at 0% of strain are represented in figure 8.10-c). It is quite clear that some of these modes can be grouped by family as their spacial profile are very similar. This is the case of the modes between 8 GHz and 12 GHz and those between 12 GHz and 15 GHZ. Some of these modes are very close in frequency meaning that they would probably overlap in real BLS spectra that have larger spectral with than the calculated ones. It is also interesting to see that there is a progressive evolution of the spatial profile of each consecutive mode.

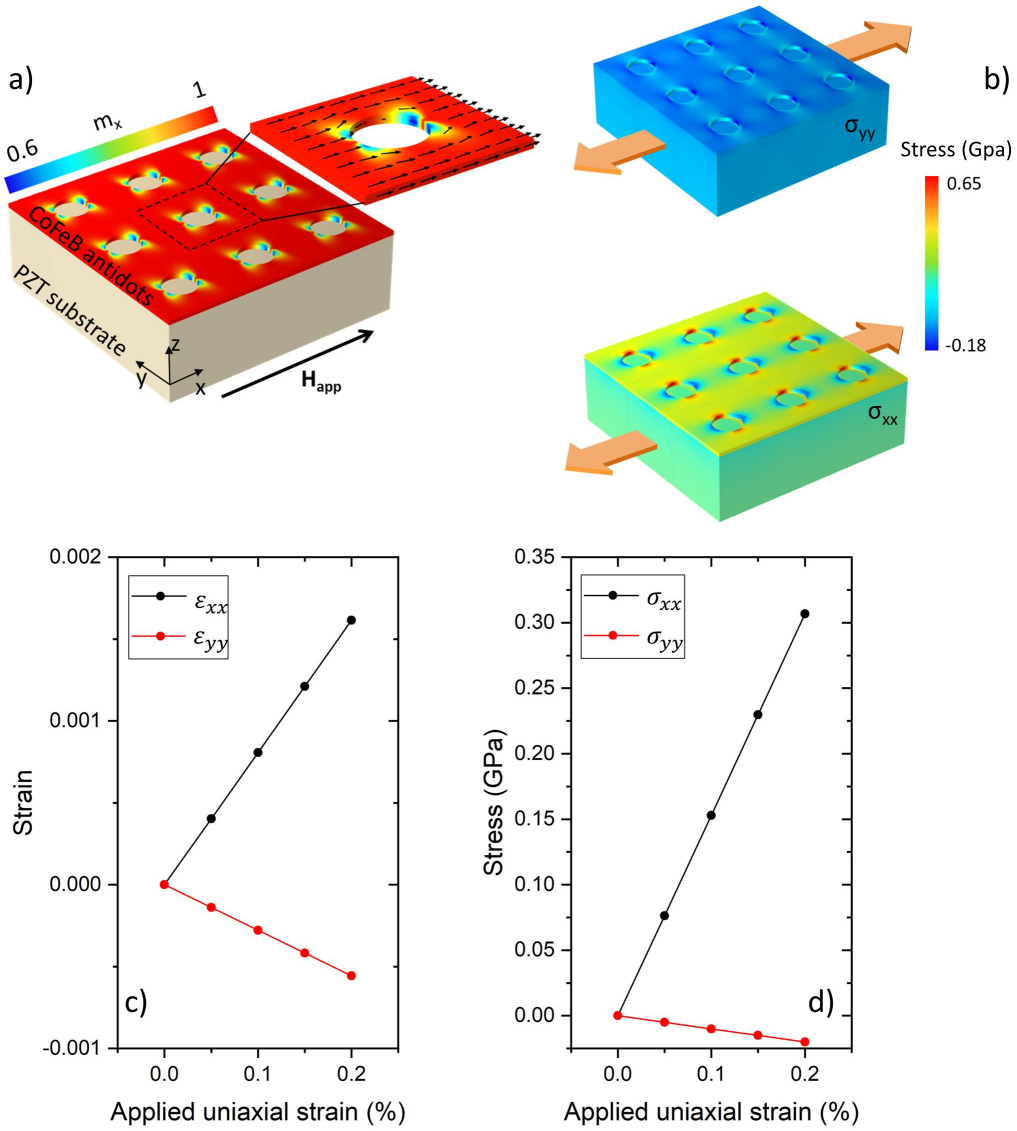

Figure 8.9: a) Equilibrium configuration of the magnetization calculated for the unit cell (delimited by dashed lines). This configuration has then been repeated to a 3×3 cell to show the perfect periodicity of the magnetization. b) σ_{yy} (top) and σ_{xx} (bottom) components of the stress tensor calculated in the 3×3 cell for 0.2% of uniaxial strain applied on the substrate. Associated average c) strain and d) stress in the magnonic crystal unit cell.

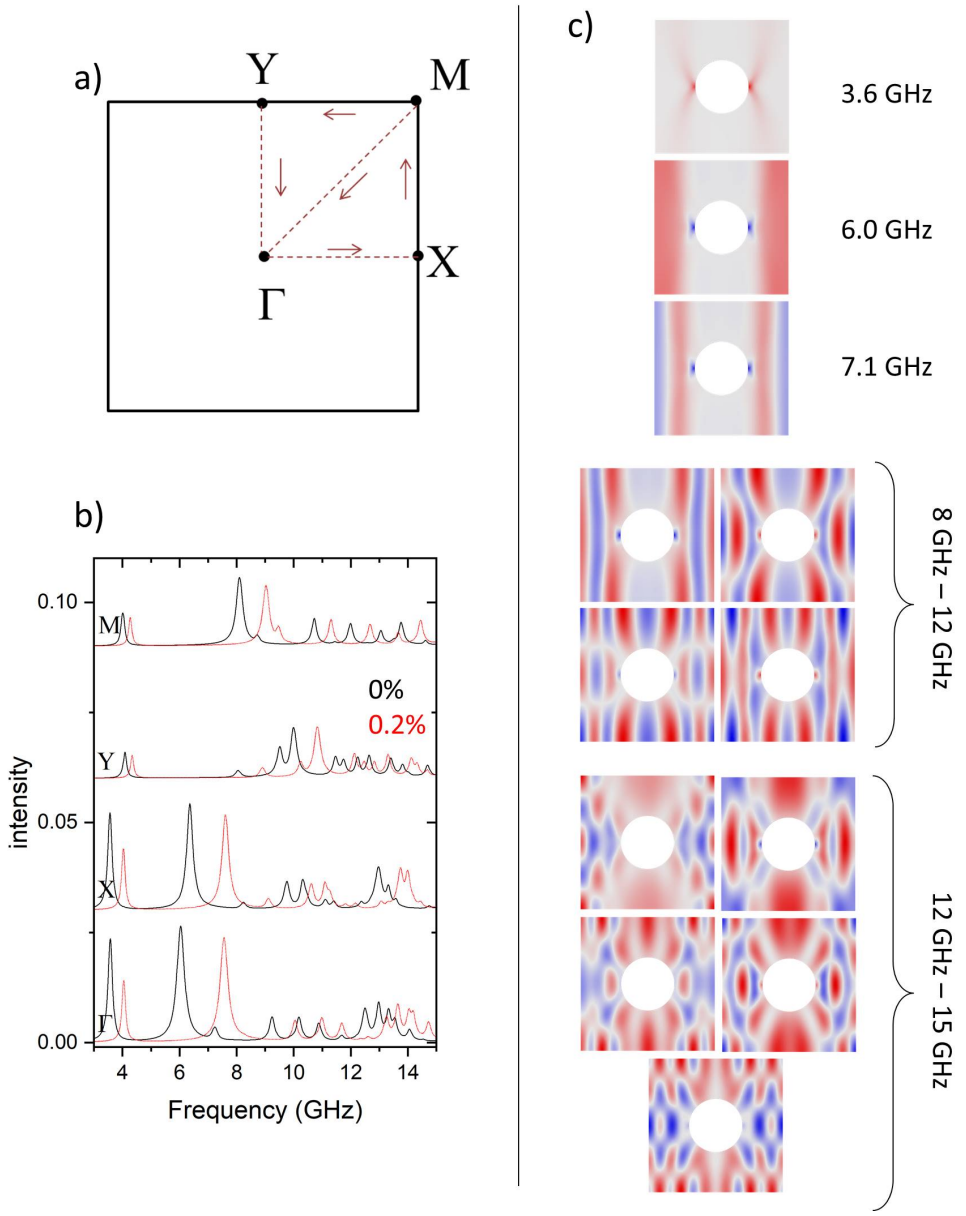

Figure 8.10: a) Representation of the first Brillouin zone (FBZ) showing the simulated $M - Y - \Gamma - X - M - \Gamma$ path. b) Simulated spectra at 0% (black) and 0.2% (red) of applied strain at each high symmetry point of the FBZ. c) Representation of the modes profiles calculated at the Γ point for the unstrained magnonic crystal.

Using the eigenfrequency solver we calculated the modes frequency when moving continuously from each symmetry point to an other. The path taken is $M - Y - \Gamma - X - M - \Gamma$ and is represented by the arrows in figure 8.10-a). The results are plotted in figure 8.11-a) in the case of the unstrained magnonic crystal and in 8.11-b) in the case of 0.2% of applied strain. The dispersion diagrams show clearly that some propagation direction are less suitable for magnonic effects. This is the case for the $\Gamma - X$ direction we mentioned, as we can

observe very few frequency changes for the spin wave in this part of the diagram. We can, however, see strong changes in the modes intensities, meaning that some of the small mode observed in Γ become very prominent in X and vice versa. The same behavior can be seen in the M − Y direction, which is equivalent to the X − Γ direction but shifted at the border of the FBZ. This can be explained by the fact that there is often a dipolar coupling between each nanostructure of a magnonic crystal meaning that the spin waves can propagate in long range trough the dipolar field thanks to small changes of the latter induced by the spin precession . However, in the case where $\vec{k} \parallel \vec{m}$ the propagation direction is perpendicular to the precession cone plane which is not optimal for taking advantage of the dipolar field. This is confirmed by the Y − Γ and the X − M directions corresponding to $\vec{k} \perp \vec{m}$ where the frequency and the intensity of the mode are very dependent on the wave vector. The M − Γ direction is an hybrid of X − M and Y − Γ as the wave propagation direction forms a 45° angle with the magnetization, and it is possible to see some similar features with those two regions. It is important to mention that most of the experimental work found in the literature only focus on the Y − Γdirection for practical reasons. Indeed, the BLS technique is hard to adjust to other directions as they necessitates to rotate the direction of the applied magnetic field, meaning that the electromagnet ends up obstructing the incident beam. The use of the permanent magnets of our setup would prove to be helpful for this specific type of study which will be performed in future work by the team.

By comparing the results at 0% and 0.2% of strain we easily recognize the same type of band structure with a shift of the magnonic branches. In parallel to what was observed in the simulated spectra, we can clearly see a difference in the frequency shit of the different modes. The difference is especially visible when comparing the first two modes in the Γ − X region, as the first mode is only slightly affected by the strain while the second one seems to be the most affected. As a results, the bandgaps between the spin wave modes are not only shifted, but also changed in size. This as been quantified by looking at some of the bandgaps that we identified by the colored areas in figure 8.11-a). The same simulations have also been performed for in between values of applied strain to see the progressive evolution of the bandgaps size. Figure 8.11-c) shows that none of the bandgaps stay still while applying strain. Thanks to the applied strain up to 0.2% we manage to change the size of the bandgaps of a few hundreds of megaHertz, and even 1 GHz for the purple bandgap that seems to be especially sensitive of the energy of the system. It is also interesting to note that positive and negative change of the bandgap size can be observed corresponding respectively to an opening or a closing of the gap. Such behavior could be observed using a static field to change the magnetic system energy (the effect would be slightly different due to the heterogeneity of the strain field), however, what makes this study remarkable is that the use of voltage induced strain is both very energy efficient and compact for significant changes in the band structures [17].

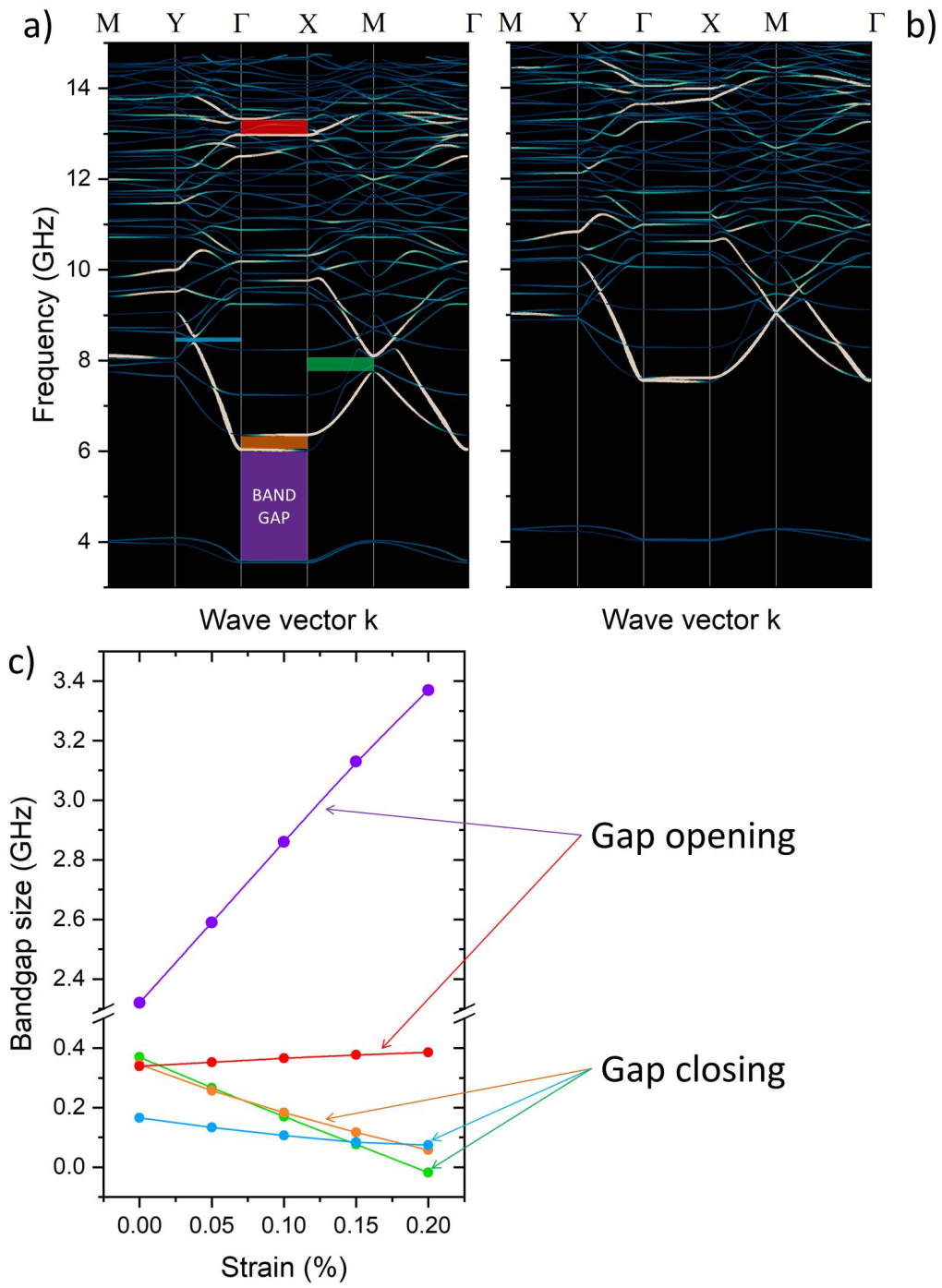

Figure 8.11: a) Magnonic band diagram simulated on the unstrained crystal. The colored rectangles represents the considered bandgaps. b) Same diagram simulated for the crystal strained at 0.2%. The relative intensity of the calculated modes is encoded by the brightness and the size of the plotted data. c) Bandgap size for various strain representing the same bandgaps shown in a).

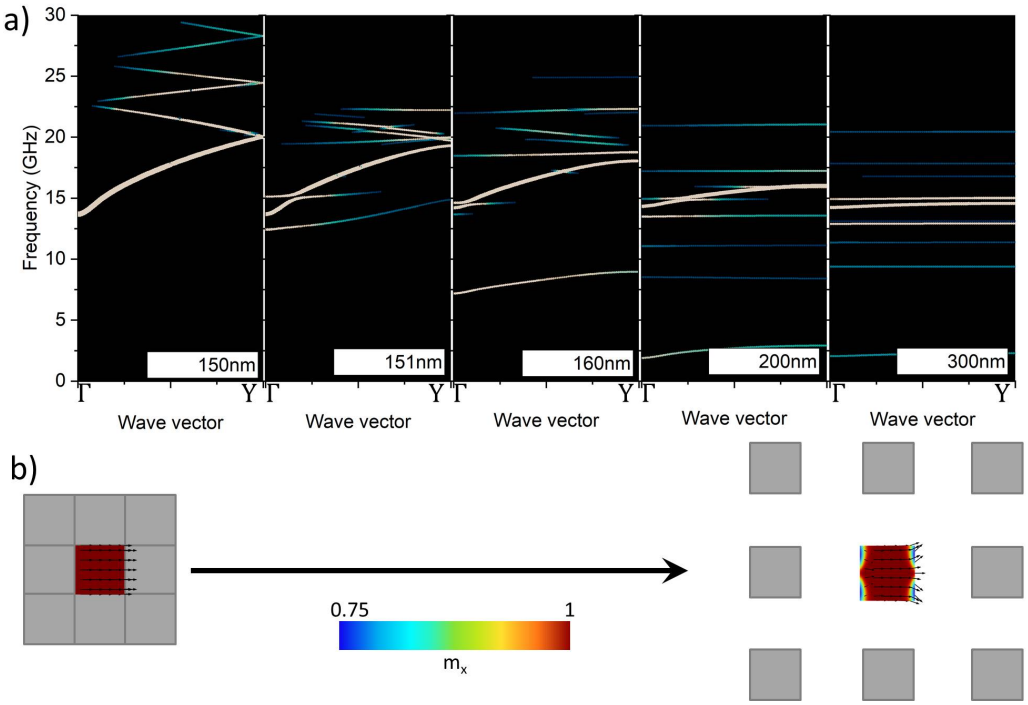

Figure 8.12: a) Dispersion diagram simulated for the $\Gamma - Y$ direction of the FBZ. The legend corresponds to the period of the array. b) Scheme of the array configuration for a period of 150 nm (left) and 300 nm (right). The center of the scheme represents the simulated equilibrium configuration of the magnetization in both cases.

8.2.4 Numerical study of magnonic crystals deposited on a polymer substrate

The use of rigid substrate like in the case of the previous study is common and the most suited for devices. However, this kind of substrate is very limited in terms of maximum strain reachable, due to their brittleness and due to the strain transmitted to the magnetic object that lead to the risk of creating cracks. Choosing a polymer with a high mechanical contrast with the magnetic film could solve both these issues in the case of space nanostructures like magnetic dots [18, 19, 20, 21]. For this study we decided to use the same magnetic material and to simulate square magnetic dots with dimensions $150 \times 150 \times 20$ nm^3. In a first step, before considering applying strain, we started to artificially separate the nanostructures, passing from a continuous film (nanostructures linked together) to completely separated and decoupled nanostructures. We only focus on the $\Gamma - Y$ direction as we saw that it is the most suited direction to observe magnonic branches.

Figure 8.12-a) shows the evolution of the magnonic band structure with the period of the array. The magnetization is in each cases saturated along the x direction using a 150 mT magnetic field. The first diagram show the case of a period of 150 nm which correspond to a case where all the structures are linked as represented on the scheme bellow. The simulations show multiple modes which are joined at the center and at the border of the

FBZ. This "zigzag" band structure is in fact logical and completely expected as it reproduces exactly the behavior of the continuous film DE-mode when the branches are unfolded.

As we start separating the dots, one can immediately see some change in the band structure. Indeed, looking at the 151 nm and 160 nm periods we start seeing gaps appearing between the branches and shift of other modes. The more we continue separating the structures the less they are coupled together as we can see on the 200 nm period where the magnonic branches starts to flatten. Ultimately they become too distant to interact together and the dispersion diagram becomes completely flat as represented for the period of 300 nm. In this last case, we found some quantized spin wave modes in the section of dots.

One can see that the dimension of the array plays a big role, especially in the case of low thicknesses, and quickly transform a completely coupled array of dots to a an array of completely isolated dots, which also can we observed on the static configuration. It is of course not possible to control experimentally the period of a magnonic in this manner. However, the concept of spacing the dots in a specific geometry is quite feasible and could be achieved using very soft polymers like PDMS. Current work is lead in the team to perform such experiments on PDMS substrates (polydimethylsiloxane), which has a very low Young's Modulus ($Y = 750$ kPa, $\nu = 0.49$) compared to the metals. With such materials, it could be possible to reach up to 50% of strain without damaging the array and the substrate, if we manage to obtain good adhesion between the metal and the polymer [17]. This approach would be even more interesting than just changing the period as the direction of the applied strain with respect to the magnetization orientation would also have an impact on the dispersion diagram.

Finally, we simulated the dispersion diagrams in the case where the uniaxial strain is applied along the x-axis and in the case where it is applied along the y-axis, while still saturating the magnetization along the x direction on the structure with a 200 nm period. Figure 8.13 summarize the results in both cases.

The top view of the starting geometry is represented on the left with the strain on the substrate (which is equal to 0 as we start at 0% of strain) and with the static magnetization configuration which is saturated along the x-axis. The final object for 30% of strain is represented on the top right part of the figure. We can observe on the perspective view that the ε_{yy} component of the strain field is, as expected, 0.3 in the substrate but equal to 0 in the magnetic dot. Indeed the mechanical contrast between the two materials is too high to transmit any strain from the polymer to the metal, meaning that the magnetic layer would not be damaged in real experimental conditions. This also means that the change in the spin wave behavior is, this time, not due to magnetoelastic effects but due to purely geometric effects. On the top view we can see a clear elongation of the substrate along the y direction and a contraction along the y direction. This leads to two consequences. Indeed , the contraction leads to a decrease of the distance between the dots along the x-axis which strengthen the magnetization (which can be seen on the top view), leading to an increase of the magnetic modes frequencies. On the other hand, the elongation leads to a increase of the distance of the nanostructures along the y-axis, which decreases the interactions between the dots and leads to a flattening of the dispersion diagram. The exact opposite happens when the strain is applied along the x direction (bottom). The resulting object of

the 30% strain is represented on the bottom right, where we can see on the perspective view that the ε_{xx} component of the strain has exactly the same profile as the ε_{yy} component on the top right object. The top view shows that the elongation and contra contraction are this times inverted. As a result, as the the dots are closer along the y axis and further away along x, the array of dots is starting to behave like an array of isolated nanowires oriented along the y-axis. This can be seen on magnetization static configuration represented on the top view where we can see that the external field is no longer enough to saturate properly the magnetization that wants to rotate along the y direction. This leads in the decrease of the main magnonic branches frequencies (bottom dispersion diagrams). At the same time, as the dots are closer along the y-axis, their dipolar interaction is increase, leading to larger magnonic branches.

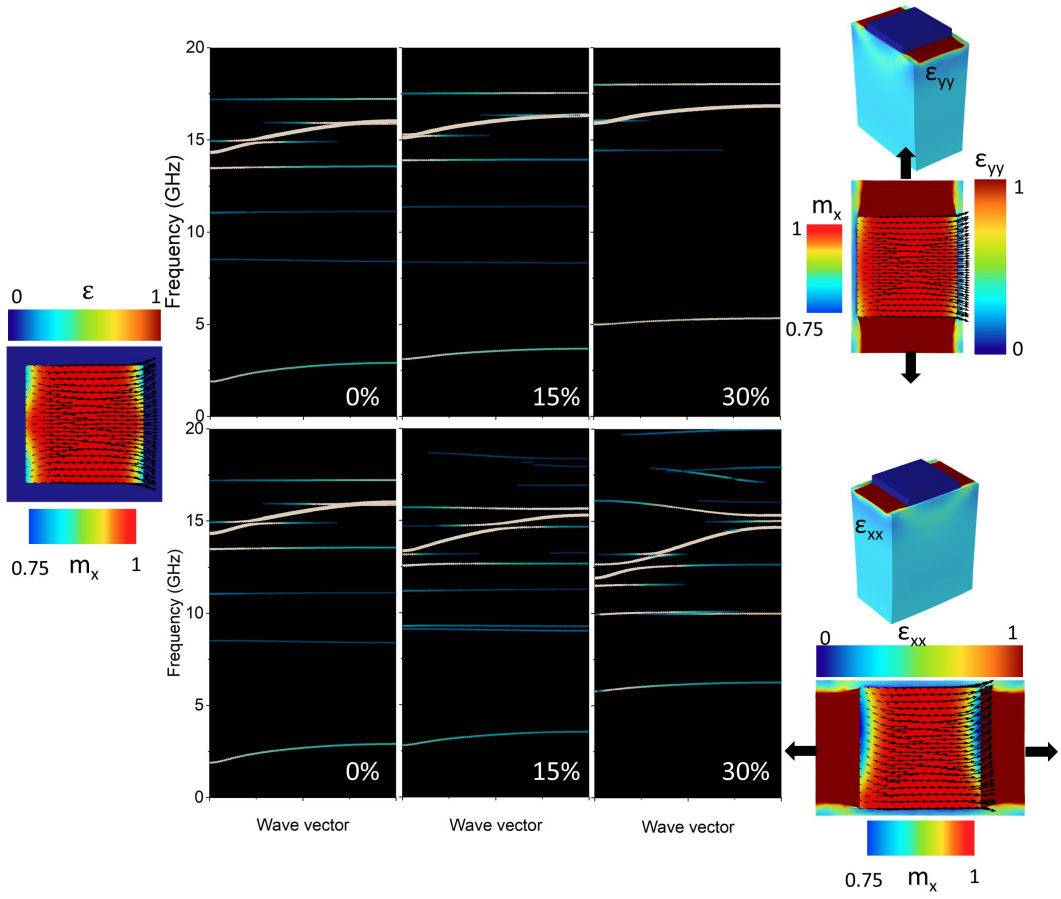

Figure 8.13: Dispersion diagram calculated for 0%(left), 15% (middle) and 30% (right) of strain applied on the PDMS substrate along the y direction (top) and the x direction (bottom). The colors represent the strain values and the m_x component of the magnetization.

This work shows that using strain for spin wave control can be done in multiple ways and lead to different behaviors depending on the sample geometry, the nature of the substrate

and the type of applied strain. We have also shown thanks to simulations that it is possible to have a significant impact on the spin wave behavior by strain induced magnetoelastic effects as discuss throughout this whole manuscript, but also by strain induce geometrical effects, which is a rich field of research that deserves to be further explored.

Bibliography

[1] Olsson, K. S., An, K., & Li, X. (2018). Magnon and phonon thermometry with inelastic light scattering. Journal of Physics D: Applied Physics, 51(13), 133001 8.1

[2] An, K., Olsson, K. S., Weathers, A., Sullivan, S., Chen, X., Li, X., ... & Li, X. (2016). Magnons and phonons optically driven out of local equilibrium in a magnetic insulator. Physical Review Letters, 117(10), 107202 8.1

[3] Agrawal, M., Vasyuchka, V. I., Serga, A. A., Karenowska, A. D., Melkov, G. A., & Hillebrands, B. (2013). Direct Measurement of Magnon Temperature: New Insight into Magnon-Phonon Coupling in Magnetic Insulators. Physical review letters, 111(10), 107204 8.1

[4] Ibarias, M., Zubov, Y., Arriaga, J., & Krokhin, A. A. (2020). Phononic crystal as a homogeneous viscous metamaterial. Physical Review Research, 2(2), 022053 8.1

[5] Sik Ma, P., Eui Kwon, Y., & Young Kim, Y. (2013). Wave dispersion tailoring in an elastic waveguide by phononic crystals. Applied physics letters, 103(15) 8.1

[6] Babu, N. K., Trzaskowska, A., Graczyk, P., Centała, G., Mieszczak, S., Głowiński, H., ... & Kłos, J. W. (2020). The interaction between surface acoustic waves and spin waves: The role of anisotropy and spatial profiles of the modes. Nano letters, 21(2), 946-951 8.1, 8.1

[7] Bozhko, D. A., Vasyuchka, V. I., Chumak, A. V., & Serga, A. A. (2020). Magnon-phonon interactions in magnon spintronics. Low Temperature Physics, 46(4), 383-399. 8.1

[8] Liao, L., Liu, J., Puebla, J., Shao, Q., & Otani, Y. (2024). Hybrid magnon-phonon crystals. npj Spintronics, 2(1), 47 1.1, 1.5, 8.1, 9, 9.1.3, 9.1.3, 9.2.2

[9] Hatanaka, D., Asano, M., Okamoto, H., & Yamaguchi, H. (2023). Phononic crystal cavity magnomechanics. Physical Review Applied, 19(5), 054071 1.1, 1.5, 8.1, 9

[10] Graczyk, P., & Krawczyk, M. (2017). Coupled-mode theory for the interaction between acoustic waves and spin waves in magnonic-phononic crystals: Propagating magnetoelastic waves. Physical Review B, 96(2), 024407 1.1, 1.5, 1.5, 8.1, 9, 9.1.1, 9.2.2

[11] Pan, H., Zhang, V. L., Di, K., Kuok, M. H., Lim, H. S., Ng, S. C., ... & Adeyeye, A. O. (2013). Phononic and magnonic dispersions of surface waves on a permalloy/BARC nanostructured array. Nanoscale research letters, 8, 1-6 1.1, 1.5, 8.1, 9, 9.2.2

[12] Zhang, V. L., Ma, F. S., Pan, H. H., Lin, C. S., Lim, H. S., Ng, S. C., ... & Adeyeye, A. O. (2012). Observation of dual magnonic and phononic bandgaps in bi-component nanostructured crystals. Applied Physics Letters, 100(16) 1.1, 1.5, 8.1, 9, 9.2.2

[13] Hakoda, C., Rose, J., Shokouhi, P., & Lissenden, C. (2018, April). Using Floquet periodicity to easily calculate dispersion curves and wave structures of homogeneous waveguides. In AIP Conference Proceedings (Vol. 1949, No. 1). AIP Publishing 8.1

[14] Ashcroft, N. W., & Mermin, N. D. (1976). Solid state. Physics (New York: Holt, Rinehart and Winston) Appendix C 8.1

[15] Carlotti, G., Colpani, P., Piccolo, D., Santucci, S., Senez, V., Socino, G., & Verdini, L. (2002). Measurement of the elastic and viscoelastic properties of dielectric films used in microelectronics. Thin Solid Films, 414(1), 99-104 8.1

[16] Zighem, F., Roussigné, Y., Chérif, S. M., & Moch, P. (2007). Spin wave modelling in arrays of ferromagnetic thin stripes: application to Brillouin light scattering in permalloy. Journal of Physics: Condensed Matter, 19(17), 176220 8.1

[17] Faurie, D., Adeyeye, A. O., & Zighem, F. (2021). Prospects toward flexible magnonic systems. Journal of Applied Physics, 130(15) 1.1, 1.4, 8.2.3, 8.2.4

[18] Zighem, F., & Faurie, D. (2021). A review on nanostructured thin films on flexible substrates: links between strains and magnetic properties. Journal of Physics: Condensed Matter, 33(23), 233002 1.1, 8.2.4

[19] Melzer, M., Mönch, J. I., Makarov, D., Zabila, Y., Cañón Bermúdez, G. S., Karnaushenko, D., ... & Schmidt, O. G. (2015). Wearable magnetic field sensors for flexible electronics. Advanced Materials, 27(7), 1274-1280 1.1, 8.2.4

[20] Makushko, P., Oliveros Mata, E. S., Cañón Bermúdez, G. S., Hassan, M., Laureti, S., Rinaldi, C., ... & Makarov, D. (2021). Flexible magnetoreceptor with tunable intrinsic logic for on-skin touchless human-machine interfaces. Advanced Functional Materials, 31(25), 2101089 1.1, 8.2.4

[21] Marunchenko, A. A., Baranov, M. A., Ushakova, E. V., Ryabov, D. R., Pushkarev, A. P., Gets, D. S., ... & Makarov, S. V. (2022). Single-Walled Carbon Nanotube Thin Film for Flexible and Highly Responsive Perovskite Photodetector. Advanced Functional Materials, 32(12), 2109834 8.2.4

9 Magnon-phonon interaction

Contents

This chapter examines magnon-phonon interactions, a growing focus in the magnetoelastic field [1, 2, 3, 4, 5, 6, 7]. Initial BLS measurements on magnetic films on silicon were inconclusive due to experimental limitations, such as the narrow anticrossing gap in materials like $Ni_{60}Fe_{40}$ and CoFeB, and the in-plane polarization of Love phonons, which are difficult to observe using BLS. Simulations on a $Ni_{80}Fe_{20}/SiO_2/Si$ system with an adjusted magnetoelastic constant revealed a small coupling gap between BV magnons and Love phonons. Increasing the magnetoelastic constant enhanced this gap, suggesting materials like FeGa or Terfenol-D could improve detection. The chapter also explores how coupling changes with the angle between magnetization and wave vector and investigates strain control to shift magnon-phonon interactions. Finally, coupling was observed in bi-component magphonic crystals, though not in mono-component structures, highlighting the need for further research in this complex area.

9.1 Coupling in unstrained continuous films

9.1.1 Experimental limitations and motivation for simulations

This last chapter is dedicated to the magnon phonon interaction, which importance is growing more and more in the magnetoeslatic field community. We initially carried out a series of BLS measurements in order to observe such coupling inside continuous magnetic films deposited on Si substrate. However, the lack of resolution of our experimental setup has limited our capability of measuring such sensible phenomenon. The first limitation is a physical one. Indeed, the magnon-phonon coupling is characterized by an anti-crossing between the magnon branches and the phonon branches [8]. The more the material is magnetoelastic the wider is the anti-crossing gap [3, 13, 9, 11, 12]. Nonetheless, for commonly used materials likes $Ni_{60}Fe_{40}$ or CoFeB this gap is less than 0.5 GHz. If the modes are too broad (as in our case), it becomes very difficult to observe any mode repulsion between magnons and phonons, even by fitting the BLS spectra. Another physical issue arises from the nature of the phonon that can couple with magnons. The mode that is known to interact well with the BW-magnon in the accessible range of energies and wave-vector by BLS is the Love phonon one, which is ironically also difficult to observe by the BLS technique as its polarization is purely in-plane and thus do not generate any ripple effects needed for the inelastic backscattering of light of opaque materials [14]. The only way of seeing them is at the anti-crossing region where the Love acoustic wave transitions from acoustic to magnetic. Seeing the appearance of a mode close to the magnon is hence a clue that a coupling occurs, but as mentioned, the width of the spin wave mode can completely cover this new mode [8]. In some cases it is possible to also couple the spin wave with the Rayleigh acoustic mode. This coupling is too small to be observed in common configurations (DE and BW) however the gap size is maximum when the magnetization direction and the wave vector form a angle close to 45° [15]. Unfortunately in most cases we could not managed to make these two modes to cross because the spin wave frequency is higher than the acoustic waves in the whole wave-vector range accessible by BLS.

9.1.2 Identifying magnon-phonon coupling via simulations

We decided to numerically look for this kind of coupling by simulated the same thin film composed like $Ni_{80}Fe_{20}/SiO_2/Si$ as in the previous chapter. However, even is the permalloy is supposed to be non magnetostrictive we decided to fix its magnetoelastic constant to $\lambda = 2 \times 10^{-5}$, a value closer to reality, as it is indeed very difficult to obtain $Ni_{80}Fe_{20}$ with strictly zero magnetostriction [16]. Contrary to the situation where magnetic modes can be controlled by strain, the magnetoelastic energy in this case is not strong enough to allow for the observation of significant coupling between the magnetic and elastic components. Indeed, we recall that the energy term is expressed as:

$$F_{me} = \underline{\underline{\varepsilon}}^{el} : \underline{\underline{\underline{\underline{C}}}} : \underline{\underline{\varepsilon}}^{el} = \varepsilon_{ij}^{el}\sigma_{ij} \tag{9.1}$$

and only affects the magnetic behavior when the object is subjected to strain. In order to properly compute this effect it is necessary to modify the solid mechanics equation in order

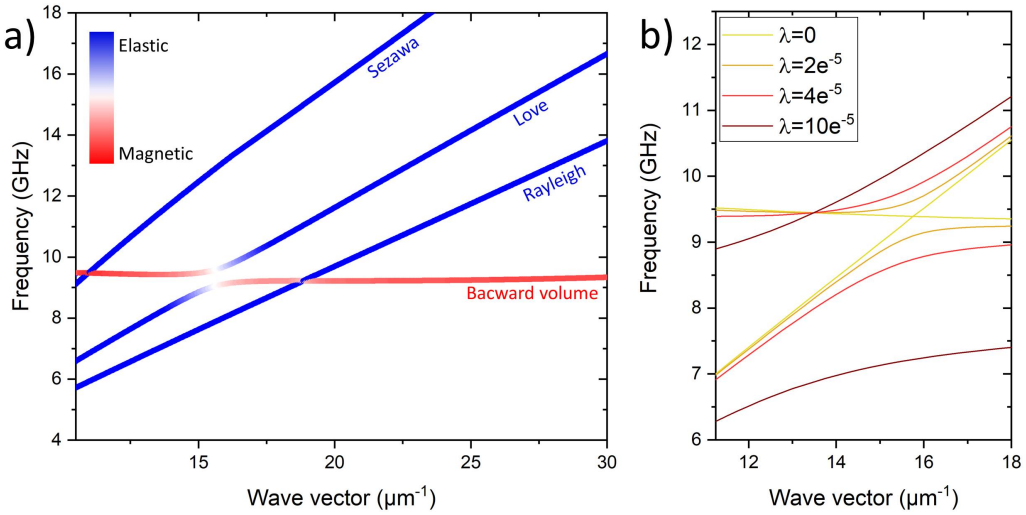

Figure 9.1: a) Simulated dispersion diagram showing both elastic (blue) and magnetic (red) modes for a $Ni_{80}Fe_{20}/SiO_2/Si$ thin film with a magnetostriction constant of $\lambda = 2{\times}10^{-5}$. The backward volume spin wave mode (red) remains nearly flat, whereas the Rayleigh, Love, and Sezawa acoustic modes (blue) exhibit a strong wave vector dependence. The color transition near 10 GHz suggests a magnon-phonon hybridization region, where spin waves and elastic waves interact. b) Effect of magnetostriction on the coupling region. Simulations with different values of the magnetostriction constant (λ) illustrate how increasing magnetoelastic coupling alters the dispersion relations. Higher values of λ lead to stronger mode repulsion and more pronounced hybridization effects in the magnon-phonon interaction zone.

to add the magnetic strain $\underline{\underline{\varepsilon}}^m$ such as the elastic strain can be written $\underline{\underline{\varepsilon}}^{el} = \underline{\underline{\varepsilon}} - \underline{\underline{\varepsilon}}^m$ and:

$$\underline{\underline{\varepsilon}}^m = \frac{3}{2}\left[\lambda_{100}\begin{pmatrix} m_x^2 - \frac{1}{3} & m_x m_y & m_x m_z \\ m_x m_y & m_y^2 - \frac{1}{3} & m_y m_z \\ m_x m_z & m_y m_z & m_z^2 - \frac{1}{3} \end{pmatrix} + (\lambda_{111} - \lambda_{100})\begin{pmatrix} 0 & m_x m_y & m_x m_z \\ m_x m_y & 0 & m_y m_z \\ m_x m_z & m_y m_z & 0 \end{pmatrix}\right] \tag{9.2}$$

Under these conditions, the acoustic waves can be influenced by the spin wave precession and *vice versa*. This means that the surface oscillations generate local stress (and strain) *via* indirect magnetoelastic effects, which affect the spin wave precession. In turn, In turn, this precession generates local stress *via* direct magnetoelastic effects, influencing the surface mechanical oscillations. The simulations presented in figure 9.1-a) show the crossing between the BV magnon and the Sezawa, Love and Rayleigh phonons with an external magnetic field of 100 mT. The color of the plot points is indicative of the elastic aspect in blue and magnetic aspect in red of each mode. Among the three acoustic waves, it is clear that the Love acoustic mode interacts with the spin wave, as evidenced by the repulsion between the two branches. In this configuration, the Sezawa mode appears to show no interaction,

while the Rayleigh mode is only very slightly influenced by the BV mode. The Love/BV gap, although relatively small, has a frequency spacing of approximately 0.4 GHz. In contrast, experimental spectra can extend up to 2 GHz wide, or even wider depending on the damping characteristics of the material. This significant width can complicate the observation of coupling between the modes, making it an extremely delicate task. To enhance the visibility of this coupling and achieve a greater gap, it is essential to select materials that possess higher magnetostriction constants. This necessity is illustrated in the simulation shown in figure 9.1-b), which highlights how different materials can influence the coupling behavior. Indeed, figure 9.1-b) shows the evolution of the gap formed by the coupling between the Love and BV waves when the magnetoelastic constant is varied. We can clearly observe that when $\lambda = 0$, no coupling occurs, demonstrating that this phenomenon is solely attributed to magnetoelastic effects. As the magnetoelastic constant increases, the gap widens in a linear manner, indicating that this coupling could be significantly easier to measure using materials known for exhibiting giant magnetostriction constants, such as FeGa alloys or Terfenol-D. Reports indicate that FeGa alloys can achieve values of approximately 200×10^{-6} [17, 18], while Terfenol-D can reach values around 1000×10^{-6} [19, 20].

9.1.3 Angular dependence of coupling

Furthermore, as previously mentioned, the coupling depends on the spin wave propagation configuration and it is interesting to study how the coupling between the magnons and the Love and Rayleigh evolve with respect to the angle between the magnetization direction and the wave-vector [1, 7]. This angle dependency have been simulated and the results are presented in figure 9.2. In practice, we varied the angle of the applied magnetic field between 0 and 90° relative to the x-direction, without changing the propagation direction of the spin waves being probed. Since the layer lacks any anisotropy (shape or otherwise), the static magnetization aligns along the magnetic field direction. Under these conditions, we probe DE-type waves at 0° and BV-type waves at 90°. In figure 9.2-a), we represented the obtained dispersion of the spin waves and the acoustic ones (Love and Rayleigh waves). The dashed red curves represent the dispersion in each cases without coupling (i. e. obtained with $\lambda = 0$).

We first observe that the only waves affected by the angle of the applied magnetic field are obviously the magnetic modes, or at least for $\lambda = 0$. As expected, the spin waves progressively evolve from the backward behavior to the Damon-Eshbach behavior and crosses the phononic branches at increasing frequencies. The thick dots represent the portion of the dispersion curves near the crossing between the magnon and phonon branches with the coupling phenomena taken into account in the simulations, and their color once again gives indication on the elastic (blue) or magnetic (red) behavior of each mode. One can see that the anti-crossing is extremely dependent on the angle for both the Rayleigh and Love waves. Indeed, in the case of the Love mode, the anti-crossing gap size is maximum at 0° (BV) and progressively decreases until 45° where the gap is almost entirely closed. Above 45° the gap starts to increase again until reaching 90° (DE) which has the second largest gap. In the case of the Rayleigh acoustic wave the exact opposite happens.

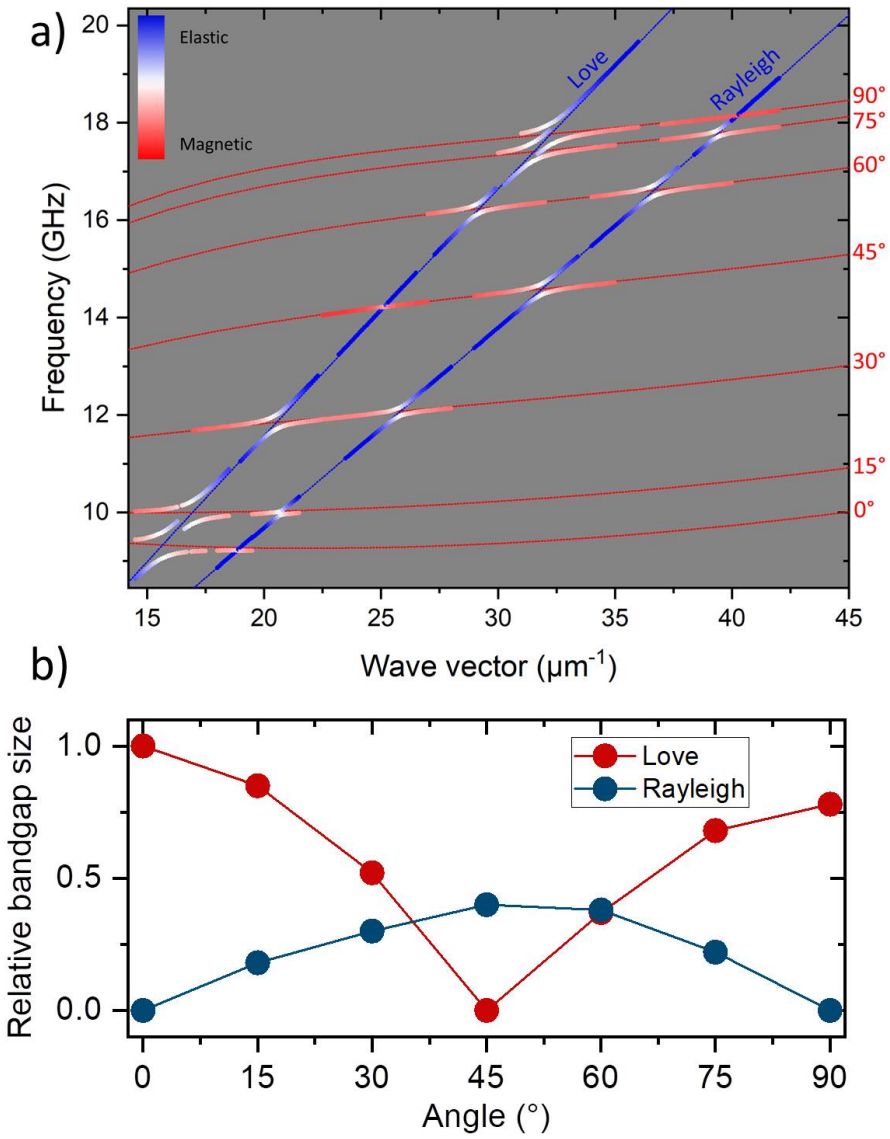

Figure 9.2: a) Numerically calculated dispersion relations for different angles between the magnetization direction and the wave vector. The wave modes are color-coded based on their elastic (blue) or magnetic (red) nature. The Love and Rayleigh acoustic modes are indicated, while multiple spin wave branches interact with them at specific frequencies, leading to magnon-phonon coupling regions (white areas). The angular dependence of these interactions is highlighted on the right. b) Relative bandgap size evolution for the Love and Rayleigh mode interactions as a function of the propagation angle. The bandgap size varies non-monotonically, with Love modes (red) exhibiting maximum coupling at 0° and 90°, while Rayleigh modes (blue) dominate around 45°. This behavior emphasizes the strong anisotropy of magnetoelastic interactions in the system.

At 0° the gap is initially closed and increases until reaching 45° which corresponds to the

largest gap observed for the Rayleigh. Above 45° the gap decreases until it closes entirely again at 90°. These gap variations are shown in figure 9.2-b), where two opposite trends can clearly be observed. Overall, the gap formed between the spin waves and the Love wave is larger than the gap formed with the Rayleigh one. It is worth mentioning that measuring the size of this kind of gap is not ideal, as the two closest points are located at different wave vectors, causing the gap to be tilted. Because of this it is not meaningful to think in terms of frequency gap. Instead we chose to plot the gap size in pixels measured on the graph picture normalized by the largest gap (Love gap at 0°). This approach may not be the most rigorous but still give us insights on the relative band-gap size.

In order to interpret this angle dependency, our first intuition relied on the polarization of each wave which would make sense in the backward case as the magnon and Love have approximately the same polarization, while the Rayleigh phonon have a polarization perpendicular to that of the magnons. However, in the DE case, the opposite should be observed, which in not the case according to our simulations. According to the work of Wang et al., [6] the coupling strength is controlled by the angular momentum of chiral phonons. Other authors like evoke a high dependence of the sense of precession (right-handed or left-handed) which is at the origin of the non reciprocal coupling [1]. A case of the latter phenomenon will be illustrated in the next section. This non reciprocity makes complex and non-trivial the interpretation of the coupling observed in figures 9.2-a) and 9.2-b), that have been obtained for positive angles between ($\vec{k}$ and $\vec{m}$). In order to further understand this phenomena we plan in the future to realize complementary simulations, especially simulations involving magnons and phonons propagating in opposite directions.

9.2 Elastic control of the magnon-phonon interaction

9.2.1 Strain control of the coupling in continuous films

The coupling observed previously rely on magnetoelastic effects naturally present in the material. In addition to this effect, we can consider applying an additional static strain to shift the magnonic band structure while keeping the acoustic band structure unchanged. This approach could potentially enhance the interaction between the two systems and allow for further investigation into their coupling behavior. This method provides the opportunity to manipulate the frequency at which the magnon-phonon interaction takes place. By applying additional static strain, we can effectively shift the resonance conditions, thereby enabling more precise control over the interaction dynamics between the magnons and phonons. Moreover, if the applied saturating magnetic field is sufficiently small (i. e. lesser than the induced magnetoelastic field), it becomes possible to tune the direction of the magnetization by applying elastic strain. This means that one could gradually transition from BV configurations to DE configurations, providing a new degree of freedom for exploring the coupling effects between spin waves and acoustic waves.

In this regard, we simulated the previously studied continuous film, this time applying an external magnetic field of $\mu_0 H = 20$ mT (instead of 100 mT) in the x-direction, along with a magnetoelastic constant of $\lambda = 40 \times 10^{-6}$. This adjustment was made to better visualize the

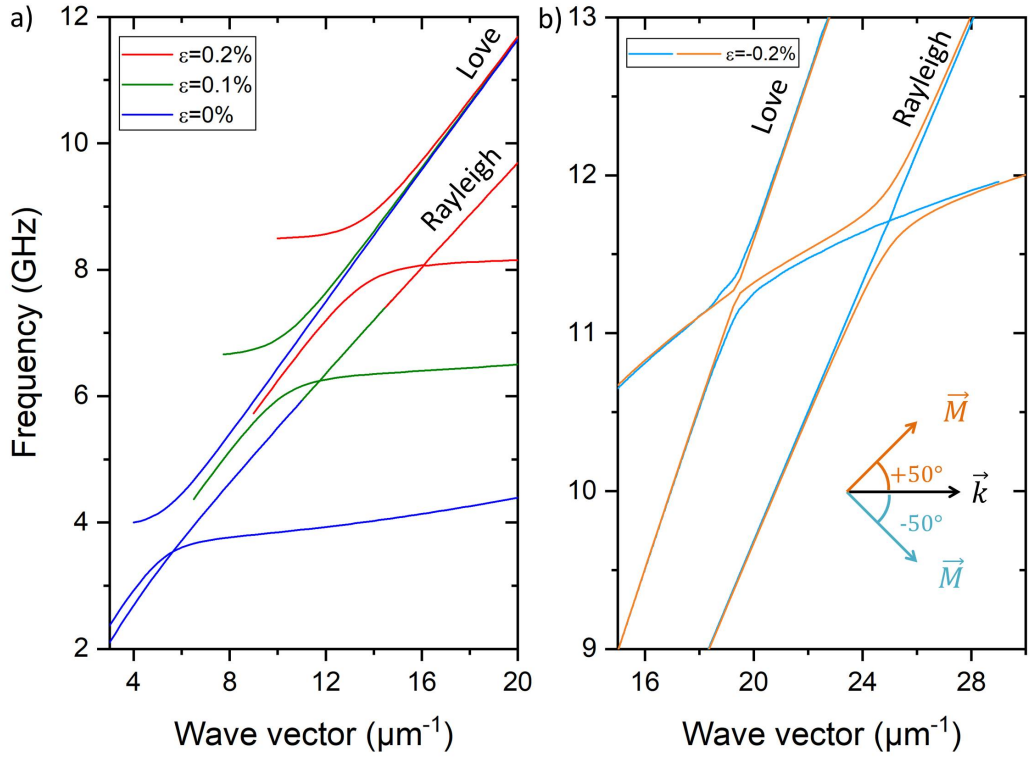

Figure 9.3: a) Simulated dispersion diagram obtained on a strained $Ni_{80}Fe_{20}$ magnetic film at 0% (blue), 0.1% (green) and 0.2% (red) of applied strain. b) Same sample subjected to compression (0.2%). The orange and light blue curves represent respectively the dispersion diagram for a positive or negative angle formed between $\vec{k}$ and $\vec{m}$.

coupling effects between the magnon and phonon modes. With this lower applied magnetic field, it will be possible to change the direction of the static magnetization by applying a negative strain (compression). Precisely, since λ is positive, a positive strain will create an easy axis aligned with the direction of the applied strain, while a negative strain will induce an easy plane that is perpendicular to the direction of the applied strain. If the strain is sufficiently strong to counteract the external magnetic field, the magnetization will rotate towards either the positive or negative y-direction.

In the initial phase, we focused on applying positive strain in the $x-$direction, as depicted in figure 9.3-a). We examined three specific strain values: 0% (dark blue), 0.1% (green), and 0.2% (red). This application of positive strain significantly influences the magnetization in the x-direction, leading to a noticeable shift of the BV magnon toward higher frequencies. As a result of this strain application, we observed that the coupling between the Love phonon and the magnon becomes slightly stronger, indicating an enhanced interaction between these two modes. Conversely, the coupling with the Rayleigh wave remains unaffected and remains at zero throughout this process. This finding suggests that applying positive strain is an energy-efficient method for controlling the frequency at which the cou-

pling occurs. Following the analysis of positive strain effects, we then applied a compressive strain of 0.2% along the x-axis. With the chosen magnetostriction constant ($\lambda = 40 \times 10^{-6}$) and the applied magnetic field ($\mu_0 H = 20$ mT) we manage to make the magnetization rotate (the rotation is induced by the compressive strain) until it reaches equilibrium at a $+50^\circ$ or -50° angle. As we still look at the waves propagating along the $x-$direction, the spin wave do not exhibit a BV behavior, but a behavior close to the 45° discussed in figure 9.2 of the previous section. The results are shown in figure 9.3-b). As there is no preferential direction between $+50^\circ$ (orange) and -50° (light blue) we simulated both. It is interesting to see that even though the absolute values of the angle formed between $\vec{M}$ and $\vec{k}$ are the same, we observe two different coupling behavior while the frequency evolution are identical. This confirms that the complexity of the coupling mechanics is not trivial and that non-reciprocal behaviors of the coupling occur depending on positive or negative precession direction relative to the elastic wave polarization [7].

9.2.2 The peculiar case of magphonic crystals

Lack of coupling in mono-component magnonic crystals

Given the well-established magnon-phonon coupling in thin films, we initially expected a similar interaction to emerge naturally within magnonic crystals, where periodic structuring modifies both magnetic and acoustic wave propagation. However, our simulations consistently failed to reveal any clear coupling between magnon and phonon branches in the studied structures. This absence of interaction persisted across various geometries, including nanowire arrays, suggesting a fundamental limitation in conventional mono-component magnonic crystals. The most plausible explanation lies in the spatial localization mismatch between the magnetic and acoustic modes, which prevents efficient coupling and hybridization [4, 5]. The mode profiles of spin waves and phonons may not overlap sufficiently within the periodic lattice, thereby hindering energy exchange and resonant interactions.

Enhancing magnon-phonon coupling using bi-component structures

To circumvent this issue, we explored an alternative approach by simulating bi-component magnonic crystals, where the unit cell contains two distinct magnetic materials instead of a single homogeneous material [3]. This design eliminates the non-magnetic voids present in traditional antidot or nanowire arrays, thereby increasing the interaction volume for both wave types. As shown in figure 9.4, introducing a bi-component structure successfully restores magnon-phonon coupling, evidenced by the presence of anti-crossing features in the dispersion relations.

For these simulations, we selected CoFeB (matrix) and $Ni_{80}Fe_{20}$ (dots) as representative materials, though we adjusted their magnetoelastic constants artificially to $\lambda_1 = 10 \times 10^{-6}$ and $\lambda_2 = 30{\times}10^{-6}$. to enhance the coupling effects. The analysis of the unstrained dispersion diagram clearly demonstrates the presence of hybridized modes, where magnons in the backward volume configuration strongly interact with a phononic branch corresponding

to the Love acoustic mode in a continuous film. This result confirms that magnon-phonon interactions can be engineered within magnonic crystals, offering new perspectives for strain-mediated wave control in magnetoacoustic devices.

Strain control of magnon-phonon interactions

Furthermore, applying a uniaxial strain to the system selectively shifts the magnonic band structure, while leaving the acoustic bands largely unperturbed. This unique characteristic where strain can modify spin wave dispersion without significantly affecting phonon modes creates opportunities to tune the coupling conditions dynamically, increasing the likelihood of crossing and anti-crossing phenomena. Given the inherent complexity and richness of the band structure in magnonic crystals, such tuning capabilities could pave the way for novel strain-controlled hybrid magnon-phonon systems, which remain largely unexplored.

Perspectives and future research directions

It is essential to highlight that the absence of observable coupling in mono-component magnonic crystals does not imply that such interactions are fundamentally impossible. Instead, it underscores the need for a more systematic investigation of material choices, geometries, and excitation conditions. Magnon-phonon interactions are highly anisotropic, meaning that their manifestation depends critically on magnetization orientation and propagation direction, factors that could potentially reveal coupling in specific configurations that were not explored in this thesis [1].

Future research should therefore aim to refine the design principles of magphonic crystals, including investigations into alternative material systems, complex geometries, and strain engineering strategies. By systematically optimizing coupling conditions, it may be possible to unlock stronger and more versatile magnon-phonon interactions, paving the way for next-generation strain-tunable magnetoacoustic devices.

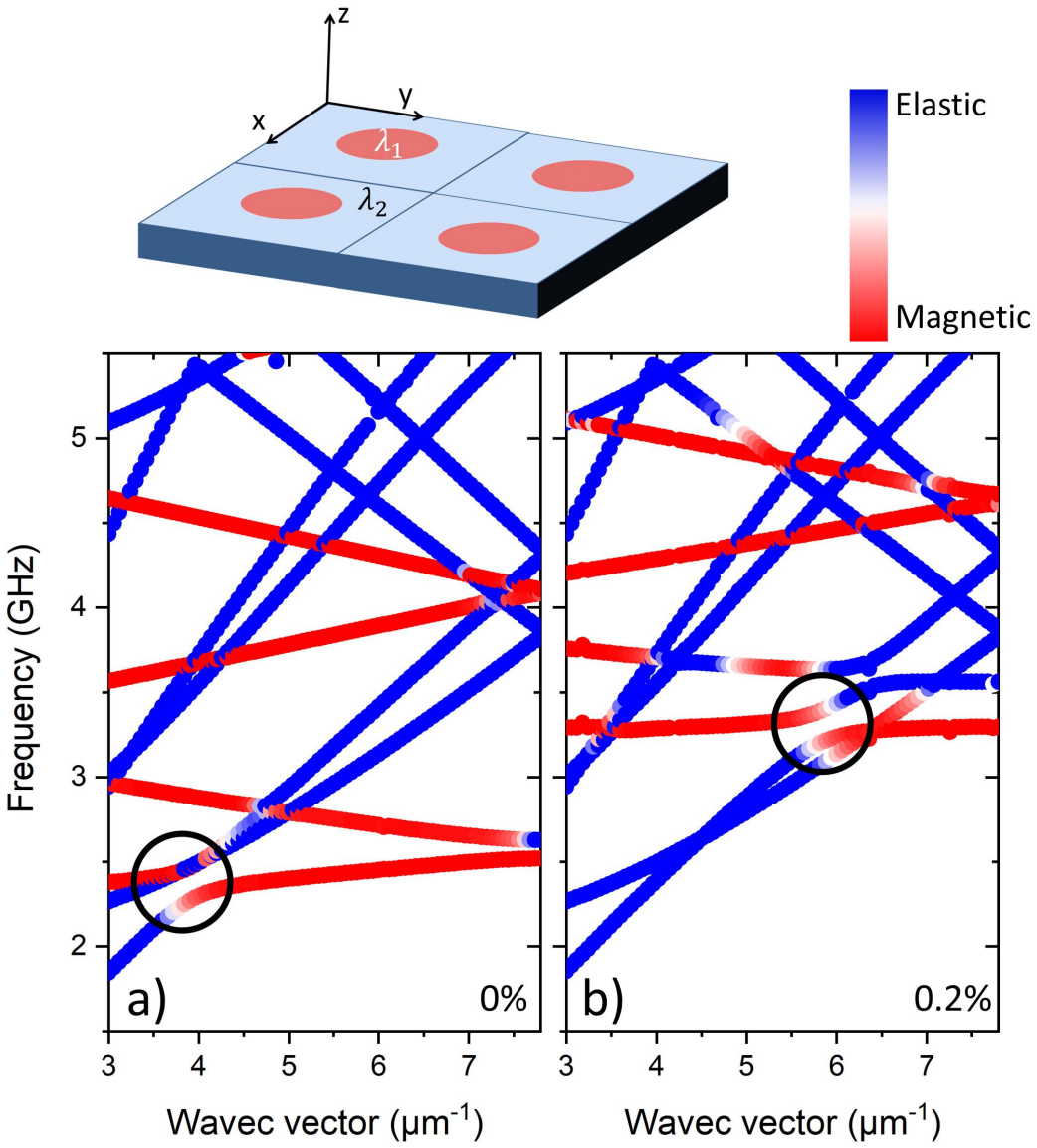

Figure 9.4: Strain-induced modifications in the dispersion of a bi-component periodic structure.The top schematic illustrates the bi-component periodic structure used in simulations, consisting of alternating regions with different magnetostrictive constants (λ_1, λ_2) embedded in a non-magnetic matrix. a) Simulated dispersion diagram at 0% strain, showing the interaction between elastic (blue) and magnetic (red) waves. The circled region highlights a specific coupling point between spin waves and acoustic modes. b) Simulated dispersion diagram at 0.2% applied strain. The introduction of strain modifies the band structure, shifting the coupling regions and altering the hybridization conditions. The circled region shows a displacement of the coupling point compared to the unstrained case, demonstrating the tunability of magnon-phonon interactions through mechanical deformation.

Bibliography

[1] Liao, L., Liu, J., Puebla, J., Shao, Q., & Otani, Y. (2024). Hybrid magnon-phonon crystals. npj Spintronics, 2(1), 47 1.1, 1.5, 8.1, 9, 9.1.3, 9.1.3, 9.2.2

[2] Hatanaka, D., Asano, M., Okamoto, H., & Yamaguchi, H. (2023). Phononic crystal cavity magnomechanics. Physical Review Applied, 19(5), 054071 1.1, 1.5, 8.1, 9

[3] Graczyk, P., & Krawczyk, M. (2017). Coupled-mode theory for the interaction between acoustic waves and spin waves in magnonic-phononic crystals: Propagating magnetoelastic waves. Physical Review B, 96(2), 024407 1.1, 1.5, 1.5, 8.1, 9, 9.1.1, 9.2.2

[4] H. Pan et al., Nanoscale Research Letters 8, 115 (2013) 1.1, 1.5, 8.1, 9, 9.2.2

[5] Pan, H., Zhang, V. L., Di, K., Kuok, M. H., Lim, H. S., Ng, S. C., ... & Adeyeye, A. O. (2013). Phononic and magnonic dispersions of surface waves on a permalloy/BARC nanostructured array. Nanoscale research letters, 8, 1-6 1.1, 1.5, 8.1, 9, 9.2.2

[6] Wang, Q., Liu, S., Long, M. Q., & Wang, Y. P. (2023). Regulation of magnon-phonon coupling by phonon angular momentum in two-dimensional systems. Physical Review B, 108(17), 174426 9, 9.1.3

[7] Lopes Seeger, R., La Spina, L., Laude, V., Millo, F., Bartasyte, A., Margueron, S., ... & Devolder, T. (2024). Symmetry of the coupling between surface acoustic waves and spin waves in synthetic antiferromagnets. Physical Review B, 109(10), 104416 9, 9.1.3, 9.2.1

[8] Babu, N. K., Trzaskowska, A., Graczyk, P., Centała, G., Mieszczak, S., Głowiński, H., ... & Kłos, J. W. (2020). The interaction between surface acoustic waves and spin waves: The role of anisotropy and spatial profiles of the modes. Nano letters, 21(2), 946-951 9.1.1

[9] Trzaskowska, A., Graczyk, P., Babu, N. K. P., Zdunek, M., Głowiński, H., Kłos, J. W., & Mielcarek, S. (2022). The studies on phonons and magnons in [CoFeB/Au] N multilayers of different number of repetitions. Journal of Magnetism and Magnetic Materials, 549, 169049 9.1.1

[10] Cracknell, A. P. (1974). Magnetoelastic waves and a group-theoretical determination of selection rules for magnon-phonon interactions in antiferromagnetic FeCl2. Journal of Physics C: Solid State Physics, 7(23), 4323

[11] Cracknell, A. P. (1974). A group theoretical study of selection rules for magnon-phonon interactions in ferromagnetic hcp metals. Journal of Physics F: Metal Physics, 4(3), 466 9.1.1

[12] Wang, H., Yang, Y., Chen, J., Wang, J., Jia, H., Chen, P., ... & Yu, H. (2023). Long-distance coherent propagation of magnon polarons in a ferroelectric-ferromagnetic heterostructure. Physical Review B, 108(14), 144425 9.1.1

[13] Yamamoto, K., Xu, M., Puebla, J., Otani, Y., & Maekawa, S. (2022). Interaction between surface acoustic waves and spin waves in a ferromagnetic thin film. Journal of Magnetism and Magnetic Materials, 545, 168672 9.1.1

[14] Błachowicz, T. (2003). Sezawa and love modes in Co/Cu superlattices. Open Physics, 1(4), 574-595 9.1.1

[15] Hwang, Y., Puebla, J., Kondou, K., Gonzalez-Ballestero, C., Isshiki, H., Muñoz, C. S., ... & Otani, Y. (2024). Strongly coupled spin waves and surface acoustic waves at room temperature. Physical Review Letters, 132(5), 056704 9.1.1

[16] Gueye, M., Lupo, P., Zighem, F., Faurie, D., Belmeguenai, M., & Adeyeye, A. O. (2016). Unambiguous magnetoelastic effect on residual anisotropy in thin films deposited on flexible substrates. Europhysics Letters, 114(1), 17003 9.1.2

[17] Wu, R. (2002). Origin of large magnetostriction in FeGa alloys. Journal of Applied Physics, 91(10), 7358-7360 9.1.2

[18] Srisukhumbowornchai, N., & Guruswamy, S. (2001). Large magnetostriction in directionally solidified FeGa and FeGaAl alloys. Journal of Applied Physics, 90(11), 5680-5688 9.1.2

[19] Sandlund, L. A. R. S., Fahlander, M. I. R. K. A., Cedell, T. O. R. D., Clark, A. E., Restorff, J. B., & Wun-Fogle, M. (1994). Magnetostriction, elastic moduli, and coupling factors of composite Terfenol-D. Journal of Applied Physics, 75(10), 5656-5658. 9.1.2

[20] McKnight, G. P., & Carman, G. P. (2002). [112] oriented Terfenol-D composites. Materials Transactions, 43(5), 1008-1014. 9.1.2

10 Conclusions and perspectives

Contents

This chapter presents the conclusions of our research on magnetoelastic effects and the strain control of spin wave dynamics, emphasizing the originality of integrating experimental and numerical approaches. We developed a numerical method using COMSOL Multiphysics®, successfully validating it through various experiments involving continuous ferromagnetic films and nano-patterned structures. Our findings demonstrate the potential to significantly influence spin wave frequencies through applied strain, particularly in magnonic crystals, revealing distinct mechanisms of magnetoelastic effects and geometrical phenomena. Looking ahead, we aim to conduct experiments aligned with our simulations, addressing challenges encountered during this thesis. Future work will explore the induction of magnetic textures in multi-component geometries under strain, the effects of mechanically curved objects on magnetization configurations, and the investigation of nutation phenomena under strain.

10.1 Conclusion

This work and more generally the research of the team focuses on magnetoelastic effects and strain control of the spin wave dynamics. Tackling this field of research not only by the experimental prism but also by the numerical approach made this work especially original as it is very rarely done. This lack of numerical support in the field is indeed due to a lack of tool for this type of study coupling the micromagnetism and the solid mechanics problems. Developing the numerical method under Comsol Multiphysics® was in our sense the best option as the solid mechanics physics was already incorporated inside the software, and the latter is developed for such coupled studies. However incorporating the micromagnetism formalism and making sure to correctly couple the equations was a task that needed meticulous validation with experimental and theoretical models support. Our validation process covered in a first step simple cases like continuous ferromagnetic films studied by FMR in multiple configurations, followed by a strain test *in situ* which was perfectly reproduced by the simulations and the macrospin model.Validation was also obtained on nano patterned structures with and without strain. Those experiments showed us that it is possible to significantly control the magnetic modes in a differentiated manner using a voltage applied on a piezoelectric substrate. The experiments shown in this work are mainly obtained on magnetostatic modes as some issues were faced on the sample signal in BLS spectroscopy. Nonetheless a few experiments were lead with this technique on thin films and magnonic crystal in order to validate the spin wave simulations performed using the Floquet-Bloch periodic boundary conditions we incorporated. Overall, all the validations show very close agreement between simulations, models, and experiments which lead us to use this tool to simulated the behavior of the magnonic band structures of an antidot magnonic crystal subjected to up to 0.2% of strain in the case of a regular rigid substrate. Those simulations showed that it is conceivable to significantly change the spin wave frequencies at 0.2% of strain (which can be obtained by applying voltage on a ferroelectric substrate) and to change consequently the magnonic bandgaps due to the differentiated mode frequency shift. We also went up to 30% in the case of a magnonic crystal made of ferromagnetic dots deposited on PDMS (polymer) substrate. This had the effect of changing the overall shape of the crystal, leading to a change in the spin wave dispersion configuration. These two numerical cases involve different mechanisms, as the first one involve purely the magnetoelastic effects, while the second one relies on purely geometrical phenomena. Finally, we saw that it is possible to simulated also the magnon-phonon coupling using our simulations and that by using static strain, we manage to shift the frequency at which this coupling happens. This numerical model we developed is promising for future studies, which is why we would like to address some perspectives for the future.

10.2 Perspectives

As discussed throughout this manuscript we plane to perform all the experiments on all the simulations we performed in this work. Indeed, all that have been simulated was initially thought to be performed experimentally. However, some sample issues, and not anticipated

problems put a stop on the initial plan. We hope that after calibration of the interference lithography setup I developed, it will be straightforward to design locally the samples and to overcome the issues we faced during my PhD. This will be hopefully done during the future PhD of Ulrich Leuga who will be following this work. I would like to share in these perspectives some preliminary studies and work I have been a part of that were made possible using this numerical tool.

10.2.1 Magnetic textures induced by strain

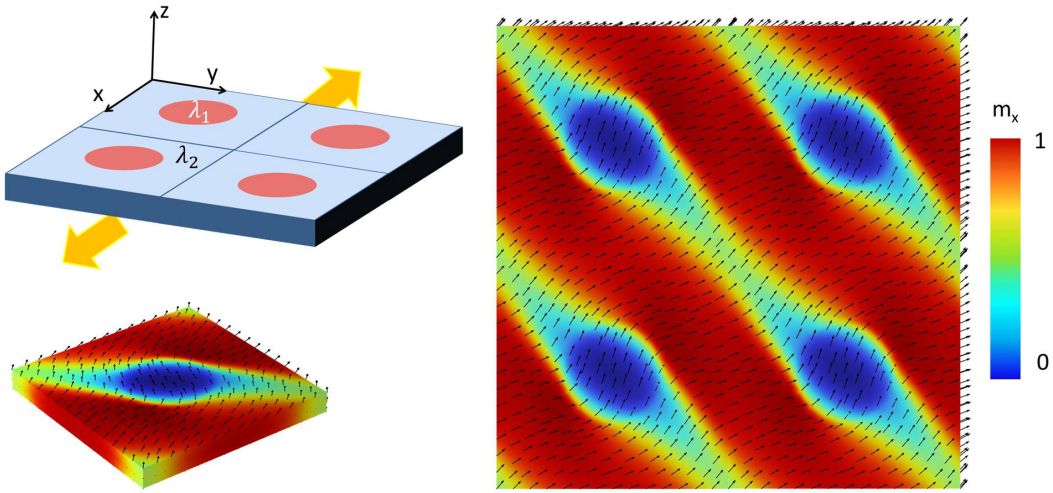

Figure 10.1: Simulations of the equilibrium state of the magnetization in a 20 nm thick of the bi component periodic structure under uniaxial strain ($\varepsilon_{xx} = 0.2\%$) schematized in the top left part of the figure with $\lambda_1 = -2 \times 10^{-5}$ and $\lambda_2 = 2 \times 10^{-5}$.

Through all this manuscript we focused on mono-component geometries for our experiments and simulations. However, in the final part of chapter 9, we explore the potential of bi-component magphonic crystals for magnon-phonon coupling. Beyond this concept, we believe that an even more promising field lies in the manipulation of magnetic textures through strain application in multi-component geometries. Indeed, the possibility of combing materials having positive and negative λ opens the possibility of inducing locally completely opposite behaviors in regard to the applied strain. Let us consider a bi-component geometry initially magnetized along the x direction and subjected to a uniaxial strain along the $x-$axis. For the material with the positive magnetostriction the strain will make the x axis an easy direction for the magnetization, while for the negative magnetostriction material, the strain will create an easy plane for the magnetization perpendicular to the x axis (yz plane). This will result in regions in space where the magnetization wants to point towards the x direction and others where the magnetization wants to align along the $y-$axis.

Figure 10.1 illustrates this effect. We chose to work with the typical $Ni_{80}Fe_{20}$ (cylinder core) and CoFeB (matrix) alloys considered in this manuscript with $\lambda_1 = -20 \times 10^{-6}$ and

$\lambda_2 = +20 \times 10^{-6}$. The period is $a = 400$ nm and the diameter of the core is $d = 180$ nm. A uniaxial strain of 0.2% is applied along the x-axis without any external magnetic field. The competition between the core and the matrix behavior creates these regions in the core where the magnetization is almost along the y axis and regions in the matrix almost aligned along the x axis and in between regions where the magnetization is directed diagonally. As the magnitude of $\|\lambda\|$ increases, these effects become more pronounced.

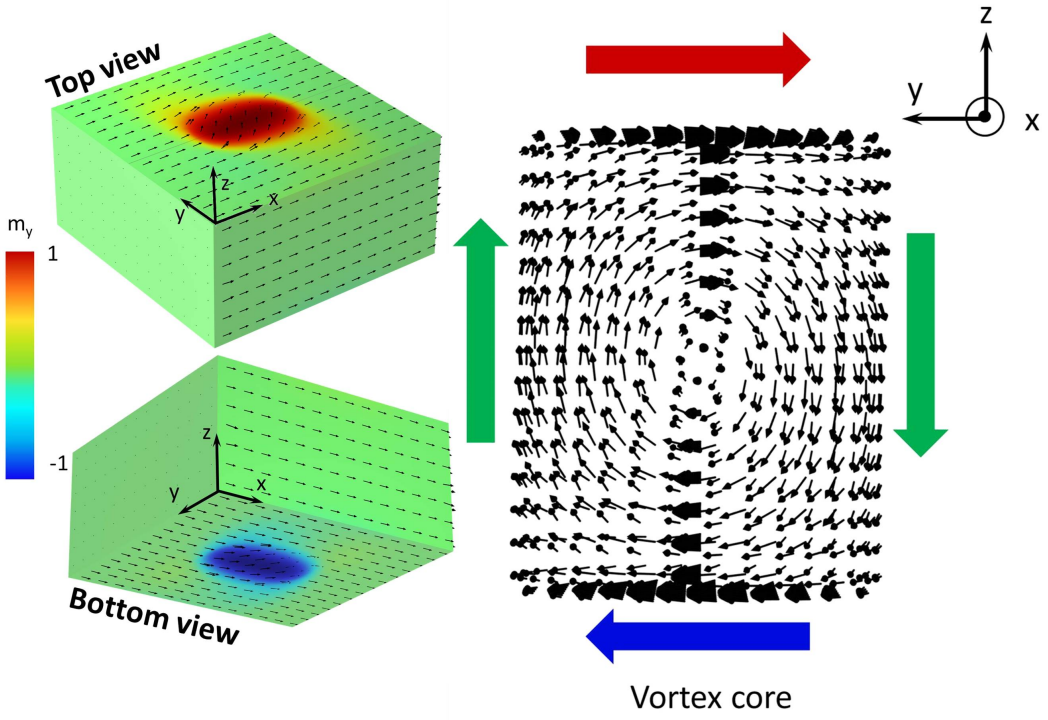

Figure 10.2: Simulations of the equilibrium state of the magnetization in a 200 nm thick of the bi component periodic structure under uniaxial strain ($\varepsilon_{xx} = 0.2\%$) with $\lambda_1 = -100 \times 10^{-6}$ and $\lambda_2 = 100 \times 10^{-6}$. The color mapping on the left encode the y component of the magnetization for the top and bottom view of the unit cell. The arrows on the right part show the configuration of the magnetization inside the cylinder core.

Let us now consider the same object but with a thickness of 200 nm and $\lambda_1 = -100 \times 10^{-6}$ and $\lambda_2 = 100 \times 10^{-6}$ subjected to the same strain. The larger thickness gives more freedom for the magnetization to adopt stable configurations while the larger λ constant amplifies the local magnetoelastic effects in the x direction for the matrix and in the y direction fore the cylinder core. As a result, the magnetization is fully aligned along the x axis in the matrix as represented by the green color in figure 10.2, while in the core the magnetization minimizes its energy by adopting a vortex configuration. This vortex can be seen in the right part of figure 10.2 where the arrows represent the magnetic moments

inside the cylinder core. On the top an bottom view of the color map we can see that the magnetization go in opposite directions in the top and bottom faces in order to minimize the magnetic energy of the system. This is only possible because the magnetoelastic field acts as an anisotropy, meaning that there is no preferential direction between positive and negative in the y-axis. This magnetic texture can be selectively induced or suppressed through precise modulation of the applied strain. It is important to mention that in this study we applied the strain directly on the magnetic object however in a real case the strain would be transmitted from a substrate, which could lead to non negligible strain gradient over the thickness depending on the material used and the thickness of the magnetic layer. Nonetheless we would still expect the apparition of magnetic textures.

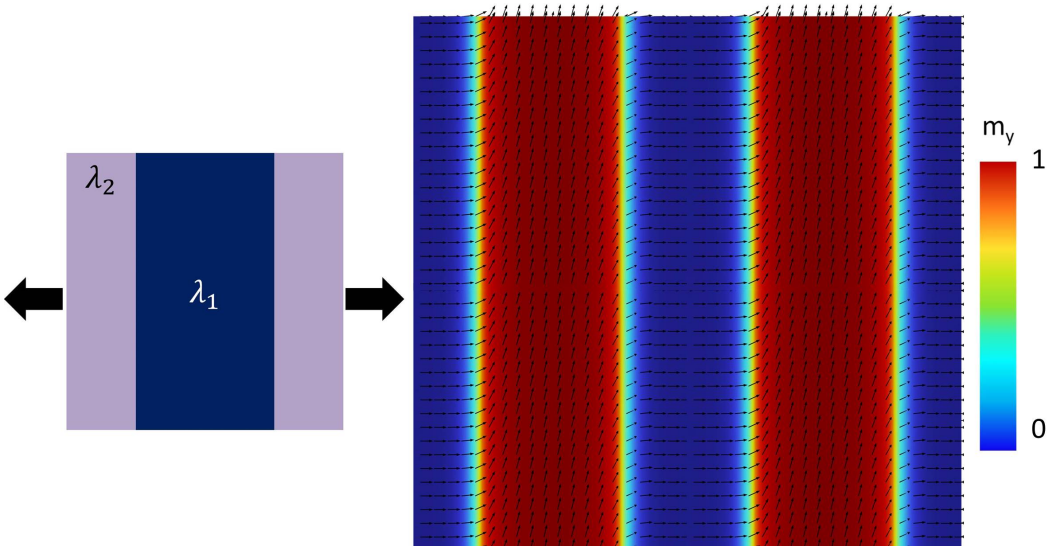

Figure 10.3: Simulations of the equilibrium state of the magnetization in a 20 nm thick of the bi component nanowires array under uniaxial strain ($\varepsilon_{xx} = 0.2\%$) schematized in the left part of the figure with $\lambda_1 = -100 \times 10^{-6}$ and $\lambda_2 = 10 \times 10^{-6}$. The color map on the right encode the y component of the magnetization.

As a last example, we show the case of an array of bi-component nanowires (figure 10.3 made of the same materials as before ($\lambda_1 = -100 \times 10^{-6}$ and $\lambda_2 = 100 \times 10^{-6}$). The array chosen has a thickness of $t = 20$ nm, a periodicity of $a = 600$ nm and each nanowire is 300 nm wide. The simple geometry makes things even more straightforward in this case where the magnetization in the positive λ regions is aligned along the x axis while it is aligned along the y direction the negative λ regions. In this case we imposed the periodicity of the magnetization but is cannot exclude the possibility of having an anti-symmetric configuration in the $y-$direction for consecutive nanowires. If we consider spin waves propagating in this type of structure, we could imagine that the magnonic band structure would be significantly altered by the application of elastic strain. Indeed, with no strain, we would observe a typical band structure for a bi-component nanowire crystal, similar to those studied by Wang et al. (see introduction of the manuscript). However, once

a positive strain is applied, there would be substantial shifts in the bands corresponding to the material whose static magnetization has switched. The opposite effect occurs under negative strain. The band variations, on the order of 5 GHz, are noteworthy from a band structure engineering perspective.

These three examples highlight the wide range of magnetic textures that can be induced through elastic strain, provided the appropriate materials are selected for real-world applications. This could open new avenues for researchers studying magnetic textures and domain walls, and even more so for the field of reconfigurable magnonics. These textures could be switched "on" and "off" by controlling the voltage applied to a ferroelectric substrate, for example, enabling dynamic manipulation of magnonic properties. As mentioned, the case presented in figure 10.3 is particularly compelling because switching the magnetization direction directly affects the magnetic modes and spin wave frequencies. Reversing the magnetization in one material or the other would also result in non-reciprocal changes in the magnetic band structures, due to the differing material properties. This can be achieved by applying either positive strain (switching the negative λ) or negative strain (switching the positive λ). [1, 2, 3, 4, 5, 6, 7, 8]

10.2.2 Mechanically curved objects

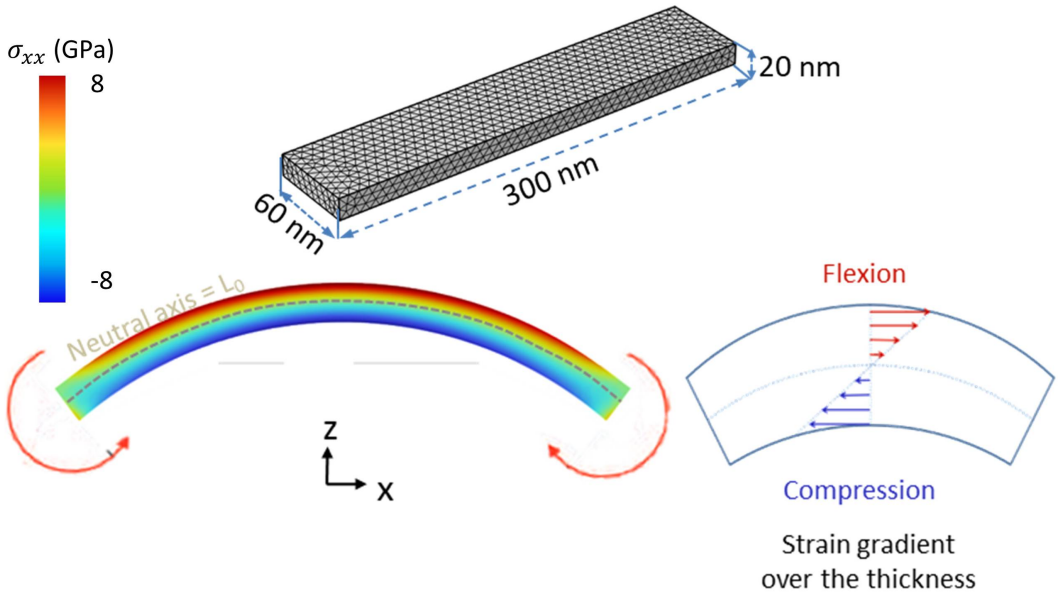

Figure 10.4: Mechanically bended nanowire. The color map encodes the σ_{xx}component of the strain field.

The possibility of coupling the complex mechanical tests and micromagnetism inside our simulations allow us to also study the case of mechanically curved nano-metric or micrometric objects. This topic is already under study in the context of the thesis of Maya Khelif in the team who studies the magnetoelastic and shape effect of magnetic objects curved

mechanically. An example is given in figure 10.4 where an initially flat nanowire is bended mechanically. The bending test generates a gradient of stress over the thickness of the object. The latter is thus subjected to flexion in the top surface (positive stress) and compression in the bottom surface (negative stress). At the center of the nanowire exists a line that is call the neutral axis where the stress is equal to 0 GPa.

As discussed in the previous section, the magnetostrictive material do not react the same way to positive and negative strain and stress which mean that the magnetization can adopt complex configurations if the the magnetoelastic coefficient is sufficient. This has been illustrated by the simulations she performed in figure 10.4 where the use of a high magnetoelastic constant forces the magnetization in perpendicular directions above and below the neutral axis. In the case where $\lambda = -100 \times 10^{-6}$ the magnetization is aligned along y on top and x at the bottom of the wire (figure 10.4-a) while the opposite happens for $\lambda = 100 \times 10^{-6}$ (see figure 10.4-b). This is a simple case that opens a lot of opportunities regarding strain applied to flexomagnetism and curvilinear magnetism. [9, 10, 11, 12, 13, 14]

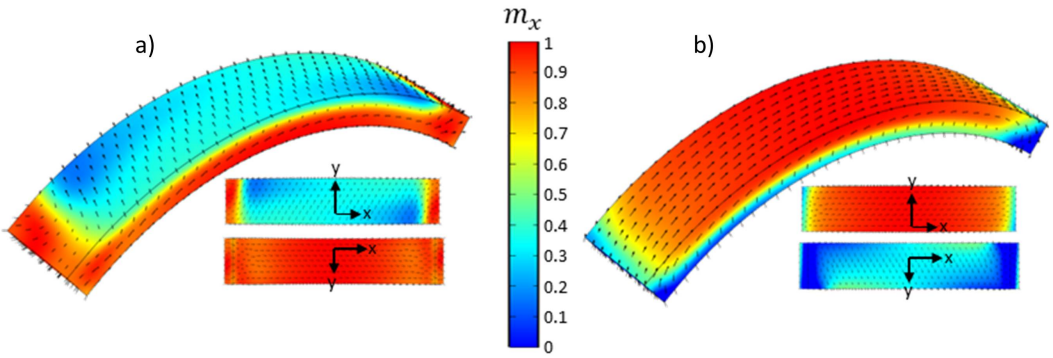

Figure 10.5: Magnetization configuration in the CoFeB bended nanowire for a) $\lambda = -10 \times 10^{-5}$ and b) $\lambda = 10 \times 10^{-5}$. The color encode the m_x component of the magnetization.

10.2.3 Strain control of nutation

Nutation has been a subject of debate since a long time in the community since its formulation as no irrefutable evidence of its existence have been shown. Nonetheless some groups have been publishing some numerical results on this phenomenon and some others try to measure high frequency signals that could be attributed to nutation. This phenomenon, like precession, can be assimilated to the motion of a rigid body like a rotating spinner. In addition to the precession motion , an other higher frequency oscillation can be supposedly happening at very small amplitudes and at frequency in the sub terahertz regime ($\sim 0.1 - 1$ THz). This additional motion can be formulated by adding a nutation term involving the second time derivative of the magnetization in the LLG

$$\frac{d\vec{m}}{dt} = -\gamma \vec{m} \times \vec{H}_{eff} + \alpha \vec{m} \times \frac{d\vec{m}}{dt} + \eta \vec{m} \times \frac{d^2\vec{m}}{dt^2} \tag{10.1}$$

where η is the nutation parameter ($\sim$ 1ps). In the context of an investigation lead on nutation in the team, we decided to implement this phenomenon into our numerical model in order to confront it with a macrospin model. From this study we raised a few points that are worth to be addressed.

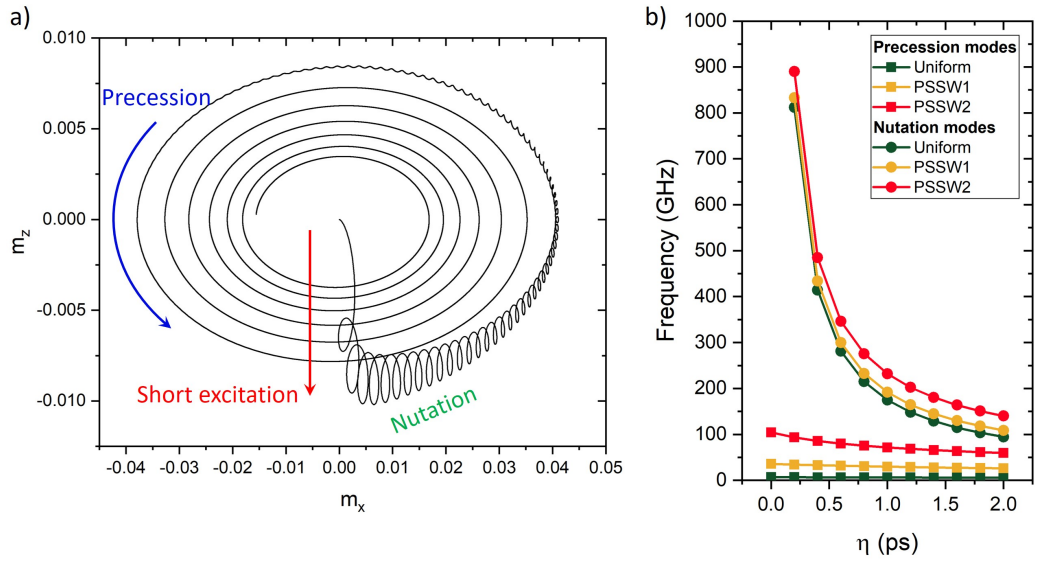

Figure 10.6: a) Evolution of the magnetization over time showing nutation oscillations on top of the precession motion. b) Calculated eigenmodes frequency with respect to the nutation parameter.

Figure 10.6-a) shows the temporal simulation of the magnetization inside a continuous film initially magnetized along the y-axis. At time $t = 0s$ a short excitation out-of-plane is applied in order to initiate precession. As this precession motion starts, it is possible to see very rapid oscillation that attenuate after a short time that are what we call the nutation motion. It becomes evident that the presence of this term gives rise to new eigen modes that we calculated using the eigen solver. The calculated modes with respect to the nutation parameter have been plotted in figure 10.6-b). These six modes have been obtained on a 20 nm thick $Ni_{80}Fe_{20}$ film saturated with an external field of 100 mT. The three lower frequency modes are the uniform and two first PSSW associated with precession, while the three higher frequency modes are the uniform and two PSSW associated with nutation. We can see that for $\eta = 0$ ps the nutation modes are diverging toward infinite frequency meaning that only precession exist. As η increases the nutation frequencies decreases. It is also intriguing to observe that the precession frequencies are also affected by the nutation parameter which has also been observed with the colleagues analytical model. This means that if nutation do exist and if these results are correct, it would imply that the magnetic constants measured without taking into account the nutation parameter are not exact and only compensate its effect of the frequency. To go further we also calculated the effect of strain on the frequencies and the nutation dispersion with $\eta = 1$ ps.

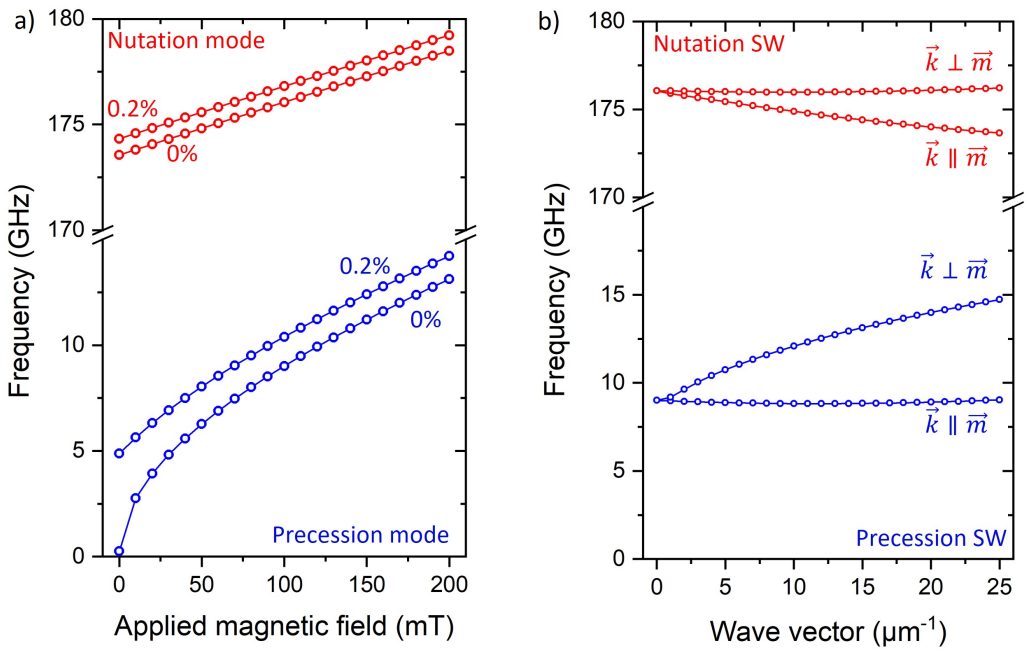

Figure 10.7: a) Simulated FMR frequencies of the precession uniform mode (blue) and the nutation uniform mode (red) for 0% and 0.2% of uniaxial strain. b) Simulated dispersion curve for the precession (blue) and nutation modes (red) in the DE and BV configurations.

Figure 10.7-a) show the frequency with respect to the applied magnetic field (corresponding to typical FMR measurements) at 0% and 0.2% of uniaxial strain along the direction of the magnetization. We can see that the nutation and precession uniform modes evolve approximately the same with the applied magnetic field. By applying strain we manage to shift both modes by a few gigahertz meaning that the nutation is globally affected by the magnetic energy of the system similarly to other usual modes. On the other hand, on figure 10.7-b) we have calculated the dispersion of both modes in the DE and BV configurations. By comparing nutation and precession spin waves, it appears that the nutation spin waves frequencies evolve completely differently. Indeed, in the BV configuration, the frequency decreases faster than the precession spin waves. In the DE configuration, the nutation dispersion show almost no change while the precession mode increases highly.

This behavior has still not be observe with BLS measurements, which explains partially this debate subsisting concerning the existence of magnetic nutation

These perspectives we discussed in this last part of the manuscript allow one to foresee a plethora of future experimental and numerical work around magnetoelastic coupling and strain control of the magnetization dynamics in magnetic structures like magnonic crystals. [15, 16, 17, 18, 19]

Bibliography

[1] H. Yu, J. Xiao, & H. Schultheiss. (2021). Magnetic texture based magnonics. Physics Reports, 905, 1-59. 10.2.1

[2] Z. Shen, S. Dong, & X. Yao. (2023). Manipulation of magnetic topological textures via perpendicular strain and polarization in van der Waals magnetoelectric heterostructures. Physical Review B, 108(14), L140412. 10.2.1

[3] A. Haykal, J. Fischer, W. Akhtar, J. Y. Chauleau, D. Sando, A. Finco, ... & V. Garcia, V. (2020). Antiferromagnetic textures in BiFeO3 controlled by strain and electric field. Nature communications, 11(1), 1704. 10.2.1

[4] H. Merbouche, I. Boventer, V. Haspot, S. Fusil, V. Garcia, D. Gouéré, ... & A. Anane. (2021). Voltage-controlled reconfigurable magnonic crystal at the sub-micrometer scale. ACS nano, 15(6), 9775-9781. 10.2.1

[5] M. Krawczyk, & D. Grundler. (2014). Review and prospects of magnonic crystals and devices with reprogrammable band structure. Journal of physics: Condensed matter, 26(12), 123202. 10.2.1

[6] A. V. Sadovnikov, A. A. Grachev, A. A. Serdobintsev, S. E. Sheshukova, S. S. Yankin, & S. A. Nikitov. (2019). Magnon straintronics to control spin-wave computation: Strain reconfigurable magnonic-crystal directional coupler. IEEE Magnetics Letters, 10, 1-5. 10.2.1

[7] R. Antos, Y. Otani & J. Shibata. (2008). Magnetic vortex dynamics. Journal of the Physical Society of Japan, 77(3), 031004. 10.2.1

[8] J. P. Park & P. A. Crowell. (2005). Interactions of spin waves with a magnetic vortex. Physical review letters, 95(16), 167201. 10.2.1

[9] J. Leng, M. Xu, M. Xu & J. Zhang. (2009). Magnetic field variation induced by cyclic bending stress. NDT & E International, 42(5), 410-414. 10.2.2

[10] Q. Shu, Z. Xu, S. Liu, J. Wu, H. Deng, X. Gong & S. Xuan. (2022). Magnetic flexible sensor with tension and bending discriminating detection. Chemical Engineering Journal, 433, 134424. 10.2.2

[11] E. Shuvaeva, S. Kaloshkin, M. Churyukanova, A. Perminov, I. Khriplivets, A. Mitra, ... & A. Zhukov. (2018). The impact of bending stress on magnetic properties of Finemet type microwires and ribbons. Journal of Alloys and Compounds, 743, 388-393. 10.2.2

[12] D. D.Sheka, O. V. Pylypovskyi, O. M. Volkov, K. V. Yershov, V. P. Kravchuk & D. Makarov. (2022). Fundamentals of curvilinear ferromagnetism: statics and dynamics of geometrically curved wires and narrow ribbons. Small, 18(12), 2105219. 10.2.2

[13] Y. Gaididei, A. Goussev, V. P. Kravchuk, O. V. Pylypovskyi, J. M. Robbins, D. D. Sheka ... & S. Vasylkevych. (2017). Magnetization in narrow ribbons: curvature effects. Journal of Physics A: Mathematical and Theoretical, 50(38), 385401. 10.2.2

[14] C. Garg, S. H. Yang, T. Phung, A. Pushp & S. S. Parkin. (2017). Dramatic influence of curvature of nanowire on chiral domain wall velocity. Science advances, 3(5), e1602804. 10.2.2

[15] P. Thibaudeau & S. Nicolis. (2021). Emerging magnetic nutation. The European Physical Journal B, 94, 1-8. 10.2.3

[16] A. De, J. Schlegel, A. Lentfert, L. Scheuer, B. Stadtmüller, P. Pirro, ... & M. Aeschlimann. (2024). Nutation: separating the spin from its magnetic moment. arXiv preprint arXiv:2405.01334. 10.2.3

[17] D. Böttcher & J. Henk. (2012). Significance of nutation in magnetization dynamics of nanostructures. Physical Review B—Condensed Matter and Materials Physics, 86(2), 020404. 10.2.3

[18] K. M. Salikhov. (2022). A New View on Spin "Nutation". Journal of Experimental and Theoretical Physics, 135(5), 617-631. 10.2.3

[19] M. C. Ciornei, J. M. Rubí & J. E. Wegrowe. (2011). Magnetization dynamics in the inertial regime: Nutation predicted at short time scales. Physical Review B—Condensed Matter and Materials Physics, 83(2), 020410. 10.2.3

List of Figures

List of Tables

Résumé

La straintronique magnétique est un domaine en plein essor, orienté vers le développement de capteurs avancés et de technologies innovantes de traitement et de stockage de l'information, en exploitant des systèmes magnétiques soumis à des contraintes mécaniques. Ce mariage entre mécanique et magnétisme est rendu particulièrement prometteur grâce à la magnétoélasticité, qui se traduit à la fois par une modification des propriétés magnétiques sous l'effet de déformations, et par l'apparition de déformations induites par des variations de la configuration magnétique. L'objectif de ce travail est d'explorer l'évolution des fréquences propres des ondes de spin dans des couches ferromagnétiques continues et dans des structures nanostructurées périodiquement, appelées cristaux magnoniques, lorsqu'elles sont soumises à des déformations. Cette étude est menée expérimentalement via les techniques de résonance ferromagnétique et de spectroscopie par diffusion Brillouin. En parallèle, un modèle numérique par éléments finis est développé, intégrant de manière complète le couplage entre micromagnétisme et mécanique des solides, pour pallier les limitations des logiciels classiques de simulation micromagnétique face aux problèmes complexes liés aux essais mécaniques. Les résultats montrent un contrôle efficace des fréquences et des bandes magnoniques dans le régime élastique, ainsi que la possibilité de prédire des couplages potentiels entre ondes de spin et ondes acoustiques.

Summary

Magnetic straintronics is a rapidly growing field aimed at developing advanced sensors and innovative technologies for information processing and storage by leveraging magnetic systems subjected to mechanical strain. This combination of mechanics and magnetism is particularly promising due to magnetoelasticity, which manifests in two ways: changes in magnetic properties when the system is deformed, and the appearance of deformations caused by changes in the magnetic configuration. The goal of this work is to study the evolution of the eigenfrequencies of spin waves in continuous ferromagnetic films and periodically nanostructured layers, known as magnonic crystals, under mechanical strain. This is investigated experimentally using ferromagnetic resonance and Brillouin light scattering spectroscopy. Additionally, a finite element numerical model is developed to fully couple micromagnetism and solid mechanics, addressing the limitations of conventional micromagnetic simulation software when dealing with complex mechanical testing scenarios. The results demonstrate effective control over these frequencies and magnonic band structures within the elastic regime, as well as the potential for predicting coupling effects between spin waves and acoustic waves.